Middlesex University London

Middlesex University Research Repository:

an open access repository of
Middlesex University research

http://eprints.mdx.ac.uk

Karamanoglu, Mehmet, 1992.
Boundary element analysis of spherical and radome shells.
Available from Middlesex University's Research Repository.

Copyright:

Middlesex University Research Repository makes the University's research available electronically.

Copyright and moral rights to this thesis/research project are retained by the author and/or other copyright owners. The work is supplied on the understanding that any use for commercial gain is strictly forbidden. A copy may be downloaded for personal, non-commercial, research or study without prior permission and without charge. Any use of the thesis/research project for private study or research must be properly acknowledged with reference to the work's full bibliographic details.

This thesis/research project may not be reproduced in any format or medium, or extensive quotations taken from it, or its content changed in any way, without first obtaining permission in writing from the copyright holder(s).

If you believe that any material held in the repository infringes copyright law, please contact the Repository Team at Middlesex University via the following email address:
eprints@mdx.ac.uk

The item will be removed from the repository while any claim is being investigated.

Boundary Element Analysis of Spherical and Radome Shells

A thesis submitted to the Council for National Academic Awards in partial fulfilment of the requirements for the degree of Doctor of Philosophy

Mehmet KARAMANOGLU, BEng (Hons), AMIMechE

School of Mechanical and Manufacturing Engineering
Middlesex Polytechnic
London

April 1992

Dedication

To my wonderful wife Ishil, with love

y94305 29

Site TP BG	MIDDLESEX UNIVERSITY LIBRARY
Accession No.	7187 1160
Class No.	624.17762 KAR
Special Collection ✓	Thesis Coll.

Contents

Abstract viii

Acknowledgements ix

Notation x

1 Introduction 1

2 Boundary Element Method Formulation 7

2.1 - INTRODUCTION 7

2.2 - LINEAR THEORY OF ELASTICITY 8

2.3 - BASIC BEM EQUATIONS 9

2.3.1 - Internal Points: 11

2.3.2 - Boundary Points: 20

3 BEM For A Solid Sphere 23

3.1 - INTRODUCTION 23

3.2 - LINEAR ELEMENTS 24

3.2.1 - Surface Displacements 24

3.2.2 - Numerical Integration 28

3.2.3 - Internal Displacements 31

3.2.4 - Internal Stresses 32

3.3 - EVALUATION OF SINGULAR INTEGRALS 34

3.3.1 - Previous Formulation 34

3.3.2 - Finite-part Integral Formulation 35

3.4 - QUADRATIC ELEMENTS 40

3.4.1 - Surface Displacements - equal elements 40

3.4.2 - Surface Displacements - unequal elements 44

3.4.3 - Internal Displacements 48

3.4.4 - Internal Stresses 50

4 BEM For A Hemisphere 52

4.1 - INTRODUCTION 52

4.2 - BEM IMPLEMENTATION 53

4.3 - PROBLEMS WITH CORNERS 55

4.3.1 - Previous Work 55

4.3.2 - Use of the Double Node Concept 56

4.4 - PROBLEMS WITH INTEGRATION 58

4.4.1 - Integration of the Corner Elements 58

4.4.2 - Integration Over the Base Elements 59

4.5 - RESULTS 61

5 BEM For A Hollow Sphere 65

5.1 INTRODUCTION 65

5.2 BEM IMPLEMENTATION OF A HOLLOW SPHERE 66

5.3 RESULTS OF A THICK WALLED SPHERE 67

5.3.1 - Analytical Formulation 67

5.3.2 - BEM Results For A Thick Sphere 68

5.4 SEMI-CONTINUOUS ELEMENTS 71

5.4.1 - Position of the End Node 71

5.4.2 - Relationship Between Node Position and Gauss Points 81

5.5 INCREASING THE EFFICIENCY 89

5.6 THIN WALLED HOLLOW SPHERE 91

5.6.1 - Element Size Limitation 92

5.6.2 - Limitation of the System Matrix 103

6 BEM For A Cone 104

6.1 - INTRODUCTION 104

6.2 - BEM IMPLEMENTATION OF A CONE 107

6.3 - COORDINATE GENERATION FOR THE CONE 108

6.4 - SURFACE DISPLACEMENTS 111

6.4.1 - BEM Model 111

6.4.2 - FEM Model 114

6.5 - INTERNAL DISPLACEMENTS 115

6.6 - COMPARISON OF BEM AND FEM DISPLACEMENTS 116

6.6.1 - Optimising Node Positions 116

6.6.2 - Wall thickness = 10mm 117

6.6.3 - Wall thickness = 5mm 122

6.6.4 - Various Cone Heights 122

6.7 - INTERNAL STRESSES 128

6.7.1 - Stresses Close To Surface: 130

6.8 - SURFACE STRESSES 133

6.8.1 - Stress - Strain Relationship 133

6.8.2 - Strain - Displacement Relationship 134

6.8.3 - Use of Cubic Spline 141

6.9 - RESULTS 145

6.9.1 - Results - BEM Spline Fit 146

6.9.2 - Results - Various Cone Heights 147

6.9.3 - Results - FEM-BEM Comparison 147

7 Further Developments 161

7.1 - INTRODUCTION 161

7.2 - DBEM APPLIED TO CRACK PROBLEMS 162

7.3 - DBEM APPLIED TO CONE 162

7.4 - NEW INTEGRATION METHODS 164

8 Conclusions 165

Appendix A : Linear Interpolation Formula 172

Appendix B : Formulation Of The Cone Geometry . 174

Appendix C : Effect Of Quadratic Elements 176

Appendix D : Stress Transformations 179

Appendix E : Further Results 184

Appendix F : Published Work 192

References 207

Abstract

This study presents the application of the Boundary Element Method (BEM) to spherical and radome geometries. The boundary of the solution domain was discretized by using both linear and quadratic elements and the validity of the results were compared against other analytical and numerical methods.

Several improvements to the BEM have been presented. These include the efficient evaluation of the singular integrals where new methods have been implemented and compared with other schemes. Improvement is also shown by the implementation of the semi-continuous elements to solve the well known limitation of the *Corner Problems* present in the BEM. Exhaustive numerical experimentation is carried out to establish the optimum collocation point for the semi-continuous elements and to link this to the quadrature rule used for the integration of that element.

The present study also includes the limitations of the BEM in applications involving geometries of long and thin sections. The study shows in detail the circumstances under which accurate results can be expected in the BEM. In this case, the emphasis is placed on the element size and the section thickness. A relationship linking these two parameters in the control of the accuracy of the BEM results is also established.

For the surface stresses and strains of the domain, a detailed implementation of a natural cubic spline is illustrated which greatly improved these surface results.

Acknowledgements

I wish to extend my special thanks to my supervisor, Gerry Beswick, who has 'opened my eyes' to the world of the Boundary Element Method and assisted me with his expertise in every stage of my research.

My special thanks also goes to my director of studies, Dr. Roger Whittaker, who has been a great help to me by asssesing my progress along the way and keeping me on my toes.

I would also like to express my sincere thanks to my parents, who have supported me with their love and help, especially during the preparation of this thesis.

Finally, I would like to thank my wife, Ishil, for her caring, understanding and support and also for the sacrifices she made during this research.

Notation

$\mathbf{A}$	Solution matrix multiplying the unknown vector $\mathbf{x}$
$\mathbf{b}$	Matrix containing known variables
b	Outside base radius of a cone
b_1, b_2, b_3	Cartesian components of the body forces
$B(\varepsilon)$	Spherical ball of radius ε
c_1, c_2	Intercepts of the linear element variation
c_{lk}^{jk}	Rigidity coefficients
d	Offset of the origin for the large arc in a cone geometry
D_{kij}	Third order tensor multiplying the tractions
$\boldsymbol{e}_1, \boldsymbol{e}_2, \boldsymbol{e}_3$	Unit vectors in cartesian directions
$\boldsymbol{e}_\theta, \boldsymbol{e}_r$	Unit normal vectors in θ and r direction
E	Elasticity modulus
h	Offset of the origin of the small arc forming the tip of a cone
h_i	Interval width in spline formulation
H	Cone height
m_1, m_2	Gradients of the linear element variation
M	Number of boundary elements
M_i	Moments in cubic spline formulation

$\boldsymbol{n}$	Unit outward normal vector at the boundary
n_j	Cartesian components of the direction cosines of a unit vector
N_1, N_2, N_3	Lagrangian quadratic shape functions
$p_i, \hat{p}_i$	Surface tractions
p_k^*	Surface tractions corresponding to the w_k^* system
p_{lk}^*	Fundamental solution of the traction kernels
P	Applied pressure
r	Distance between a source point and a field point
r, s	Lower and upper integration limits in the Kutt formula
r_i, r_o	Inner and outer radii of the tip of a cone
R	Radius
R_i, R_o	Inner and outer radii of the body of a cone
s	Arc length
S	Surface area
S_1, S_2, S_3	Boundary surfaces
$S(x)$	Spline function
$S'(x)$	First derivative of the spline function $S(x)$.
$S''(x)$	Second derivative of the spline function $S(x)$.
S_{kij}	Third order tensor multiplying the displacements
t	Factor used in the location of the nodes in semi-continuous elements
t	Wall thickness
$\mathbf{u}$	Displacement vector
u_i	Cartesian displacements
w_i	Weight of the ith intgeration point
w_{lk}^*	Fundamental solution of the displacement kernels

w_k^*	Virtual displacement pattern that satisfies the homogenous boundary conditions
x	Vector containing the unknown variables
x_1, x_2, x_3	Cartesian coordinates
α, ψ	Angles used in Kutt formulation
$\alpha_1, \alpha_2, \alpha_3, \alpha_4$	Local angles used for in the composite mapping
$\alpha_i, \beta_i, \gamma_i$	Parameters used in the linear set of the spline equations
∂B	Surface area of a spherical ball $B(\varepsilon)$
δ_{ij}	Kronecker's delta
ε_{ij}	Cartesian strain tensor
ε_{jk}^*	Strain tensor corresponding to the w_k^* system
ε_{rr}	Radial strain
$\varepsilon_{\theta\theta}$	Hoop strain in θ direction
$\varepsilon_{\varphi\varphi}$	Hoop strain in φ direction
θ_T	Angle of a common tangent for two arcs
λ	Factor used for controlling the singularity order in Kutt formulation
μ	Shear modulus
ν	Poisson's ratio
ξ, η	Intrinsic coordinates
$\xi(x_j), \eta(x_j)$	Functions used to define $\phi(x_j)$
ξ_i	Coordinate of the ith integration point
ρ	Radial distance in local coordinates
σ_e, σ_v	Von Mises equivalent stress

σ_{ij}	Cartesian stress tensor
σ^*_{jk}	Stress tensor corresponding to the w^*_k system
σ_{rr}	Radial stress
$\sigma_{\theta\theta}$	Hoop stress in θ direction
$\sigma_{\varphi\varphi}$	Hoop stress in φ direction
$\phi(x_1,x_2,x_3)$	A function with continuous first derivatives with respect to cartesian coordinates
Ω	Volume of a body
Ω	Volume Ω excluding $B(\varepsilon)$

Chapter

1

Introduction

"In research the horizon recedes as we advance, and is no nearer at sixty than it was at twenty. As the power of endurance weakens with age, the urgency of the pursuit grows more intense... And research is always incomplete."

Mark Pattison

1875

The complexity of practical problems that engineers and scientists have to deal with is sometimes beyond their analytical capability to solve them, and in some past cases the solution time required would have exceed their lifetime. However, thanks to the recent development of numerical techniques and the availability of computer power, it is now possible to tackle these difficult problems. Over the years, engineers and mathematicians worked together to come up with some numerical tools that would provide them with the ability to solve some of their engineering problems. As a result, engineers have now been provided with two different tools which can play major roles in their work: the Finite Difference Method (FDM) and the Finite Element Method (FEM).

The FDM is a direct numerical algorithm used for solving differential equations and is, for example, extensively used in the solution of fluid mechanics problems. Recently, it is becoming a popular tool with its extensive usage in Computational Fluid Mechanics (CFD).

The FEM originated as a method of stress analysis. The method is based upon the piecewise discretization of the problem domain into a number of elements. The governing equation for each element is determined separately and these are then formed into a system of algebraic equations, which are then solved using numerical techniques.

The so called displacement method, commonly used in FEM, gives good results for displacements, but the stresses are less accurate as they are calculated by using the derivatives of the displacements and compounding certain errors. In many engineering problems, particularly in linear elasticity, the major interest is in the determination of the stresses, and very often these are of a particular interest in the surface region. Because of the nature of the Finite Element Method, there is always an excess amount of information that has to be calculated in order to obtain the information required. This could be very expensive particularly in large 3-D problems, where the storage capacity required for the system equations could be enormous.

Another method that has been developed but has not yet reached its maturity is the Boundary Element Method (BEM). In the BEM approach, as the name implies, the boundary is discretized into elements and the rest of the domain is not touched. This is one of the main advantages of the BEM over FEM and FDM.

The BEM is recognised as a powerful engineering tool. It offers the ability to transform the field equations, which describe the behaviour of the unknown functions and its derivatives, inside and on the boundary of the domain, to an integral equation, relating the unknown to the given value on the boundary. From a numerical analysis point of view, the advantage of the BEM is that, by transforming the problem to the boundary, the dimension of the problem is reduced by one. Instead of discretizing the whole domain, only the boundary is to be dealt with. A 3-D surface can be modelled by using two-dimensional elements (patches) and line elements for 2-D problems. This significantly reduces the data preparation time, computation time and interpretation of the results. The system equations are formed in terms of the surface unknowns, (i.e. displacements and tractions in elasticity

problems), therefore they can be determined directly. Although the initial results will always be on the surface, it is very easy to obtain results inside the solution domain. Since there will not be any further approximations, the results at interior points will be very accurate. However, there is a problem with the BEM for the interior points which are too close to the boundary: this problem will be looked at in later chapters.

The simplicity of the mesh generation is also a bonus for the method and, moreover, the problem under consideration can be modified drastically, without drastic changes in the existing model. Complete remeshing is not necessary.

In problems where the boundary conditions may include infinite domains, the Finite Element Method would be very expensive to use. In the BEM formulation, such problems are easily dealt with. Even when dealing with nearly incompressible or compressible materials, such as epoxy resin, which has Poisson's ratio of $\nu = 0.5$, the BEM would not present any problems (Floyd, 1984).

It is now accepted that the BEM is not just a direct substitute for the FEM. Further developments are continuing and the BEM is slowly becoming more popular. There are also developments being made in the coupling of the two methods to obtain the maximum benefits of each formulation.

The BEM has been very slow to develop. As the computer technology gradually developed the solutions of the integral equations, derived many years ago, became possible to be solved numerically. Although the history of the BEM can be traced back to the early 1900's, it was not until 1963 that the numerical examples of direct BEM were first published by Jaswon (1963) and Symm (1963). Further details of the development of the BEM can be found in numerous publications (see, for example, Banerjee & Butterfield (1981), Cookson et. al. (1986), Massonnet (1987), etc.).

The BEM has come a long way since the 1960's, but there are some major problems that still need attention and some particular weaknesses in the method that require

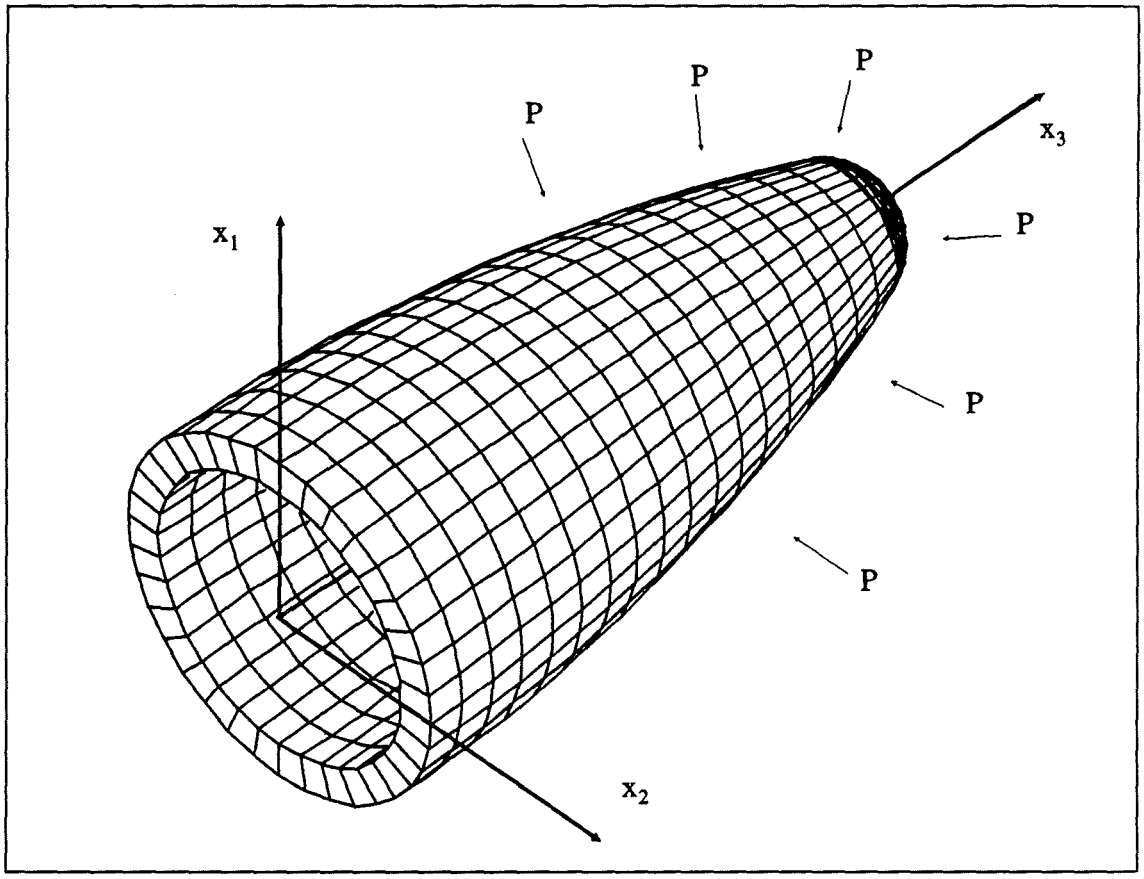

Figure 1.1: A typical nose cone, under external pressure, P, used for the analysis.

strengthening. The work presented in this thesis will concentrate on some of the weaknesses in the method discovered in this study, to determine the displacements and stresses in the wall of a nose cone under external pressure (see Figure 1.1).

As there were no analytical solutions available for the geometry in Figure 1.1, the following approach was taken. Firstly, the BEM was implemented on a solid sphere, where both linear and quadratic elements were used and compared. Then this was followed by slicing the sphere at the equator plane and looking to the corner problems associated with the BEM. Having made successful improvements to the formulation, the hemisphere was made hollow. As the analytical solutions for the solid sphere, the hemisphere and the hollow sphere are well known, the accuracy of the BEM method could thus be monitored. The hollow hemisphere model was used to look at the limitations of the BEM when dealing with long and slender sections. The next stage adopted was to modify the computer code

so that the original cone problem could then be solved. The hollow hemisphere model, which was already built, was so modified that the height of the model was made longer than the base: now, of course, the only checks on solution results possible are found by comparing the results with those of a FEM model.

Each chapter of this thesis begins with an introduction which includes the relevant previous work in that area followed by the appropriate formulation and numerical implementation. Numerical results concerning each section are also provided, with the analytical comparison where possible.

In chapter 2, the basic formulation of the BEM is illustrated for linear three-dimensional elastostatics. The intended problem could have been solved using a 2-D axisymmetric formulation, but for research and development purposes, it was decided to look at this as a general 3-D application where some form of axisymmetry may not be present. The BEM implementation to a solid sphere is dealt with in Chapter 3. Linear and quadratic elements are both used and particular attention is given to the integration method to deal with the singularities present in the fundamental solution. The application of a finite part integration was also employed to reduce the integration time used on the evaluation of the coefficients in elements where singularities are present.

Chapter 4 looks at the problems associated with the conflicting boundary conditions at corners by modelling a hemisphere. Application of the multiple node concept as well as a semi-continuous element are discussed. In Chapter 5 optimization of the collocation point for the semi-continuous corner element is illustrated. The limitation of the long and slender sections are discussed with the aid of a hollow hemisphere, where tests are conducted to establish some sort of limit to the element size to be used in relation to the wall thickness. The use of the subregioning technique is deliberately avoided in order to look at this problem in detail. Chapter 6 deals with the modification of the code developed so far and the testing of the variations in the nose cone geometry. Various shapes of nose cones were tested in order to see the effect of the geometry on the stress developed at the critical points.

A comparison of the FEM results with the BEM ones is also made and discussed. Chapter 7 then looks at some of the possible improvements to the BEM. This includes the use of Dual Boundary Element Method (DBEM) in connection with the serious limitation on the aspect ratio of the elements used in long and slender sections and some of the latest improvements in the evalution of strongly singular and hypersingular integrals.

Chapter

2

Boundary Element Method Formulation

"When I think of the many cases of men who have studied one subject for years, and have persuaded themselves of the truth of the foolishest doctrines, I feel sometimes a little frightened, whether I may not be one of these monomaniacs."

Charles Robert Darwin

1859

2.1 - INTRODUCTION

This chapter starts with the illustration of the basic theory of elasticity and then moves onto the fundamental BEM equation of elasticity upon which this work is based. Although some of this section appears in other publications, (see, for example, Cruse, 1977, Banerjee et al. 1981, and Brebbia 1980 & 1984), it is briefly reproduced here for the benefit of the reader and continuity.

The fundamental solutions of the governing differential equations for the displacements and the tractions are given for three-dimensional elasticity. These will be the basis for the further equations to be developed in the later chapters. The work described in this thesis

is based on the linear elasticity theory for a solid body and the following assumptions are made:

i - The material is to have linear stress-strain relations, i.e. linear material behaviour.

ii - The change in orientation of a body due to displacements is negligible.

2.2 - LINEAR THEORY OF ELASTICITY

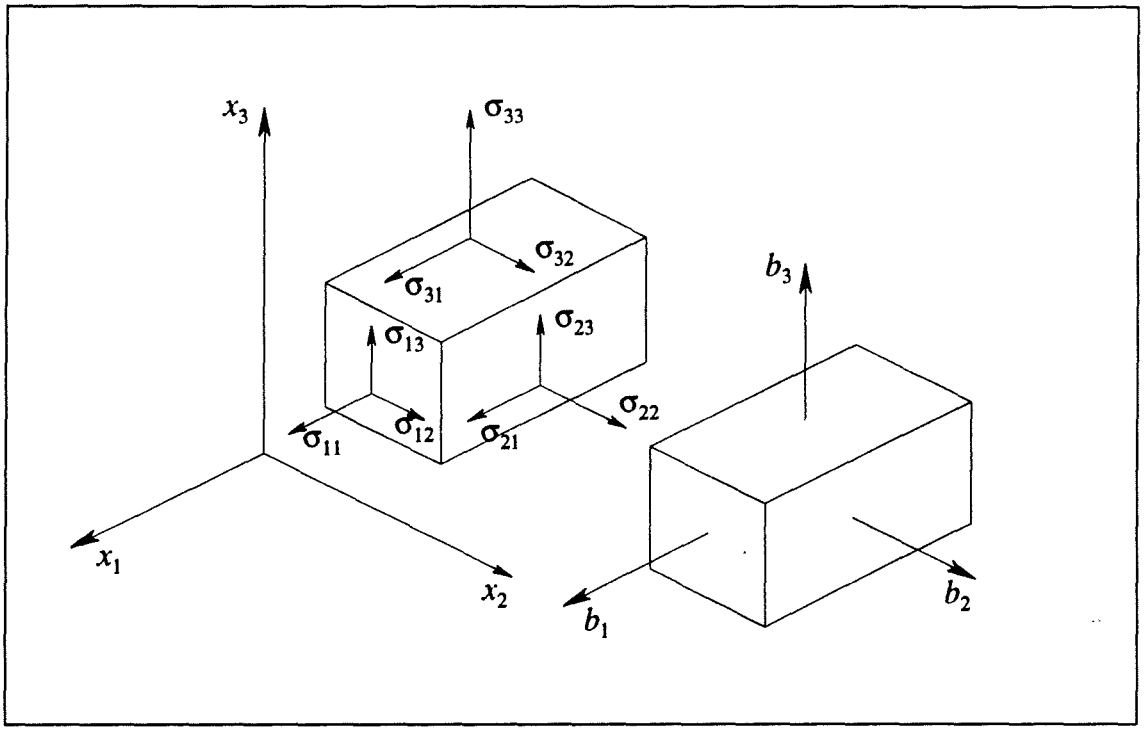

Figure 2.1: Stresses and body forces acting an a three-dimensional element.

Consider an isotropic elastic body as shown in Figure 2.1. The governing differential equation of equilibrium can be written in terms of the stress field components. In tensor form this would be,

$$\frac{\partial \sigma_{ij}}{\partial x_j} + b_i = 0 \qquad i = 1,2,3 \qquad j = 1,2,3 \tag{2.1}$$

Equation (2.1) is to be solved subject to certain boundary conditions given by the following equation:

$$p_i = \sigma_{ij} n_j \qquad i = 1,2,3 \qquad j = 1,2,3 \tag{2.2}$$

where p_i are the surface or boundary tractions and n_j are the direction cosines of the unit normal, $\boldsymbol{n}$, with respect to the cartesian axes, i.e.

$$n_j = \cos(\boldsymbol{n}\ , x_j) \tag{2.3}$$

The strains at any point are defined by the ε_{ij} components of the strain tensor, which in indicial form are,

$$\varepsilon_{ij} = \tfrac{1}{2}\left(\frac{\partial u_i}{\partial x_j} + \frac{\partial u_j}{\partial x_i}\right) \qquad i = 1,2,3 \qquad j = 1,2,3 \tag{2.4}$$

Hooke's law relating the stress and strain components in an isotropic elastic solid can be written as,

$$\sigma_{ij} = \frac{2\mu\nu}{1-2\nu}\,\delta_{ij}\,\varepsilon_{kk} + 2\mu\varepsilon_{ij} \qquad k = 1,2,3 \tag{2.5}$$

where δ_{ij} is the Kronecker's delta, ν is the Poisson's ratio and μ is the shear modulus, sometimes written as G.

2.3 - BASIC BEM EQUATIONS

The integral equations formulated in this thesis are based on the direct BEM approach where the integral equations provide values of solution variables at any internal field point in terms of the complete set of all the boundary data. The starting point for the work presented in this thesis will be to consider a three-dimensional, bounded elastic body under the action of predefined forces and with the volume Ω and the surface area, S, which is

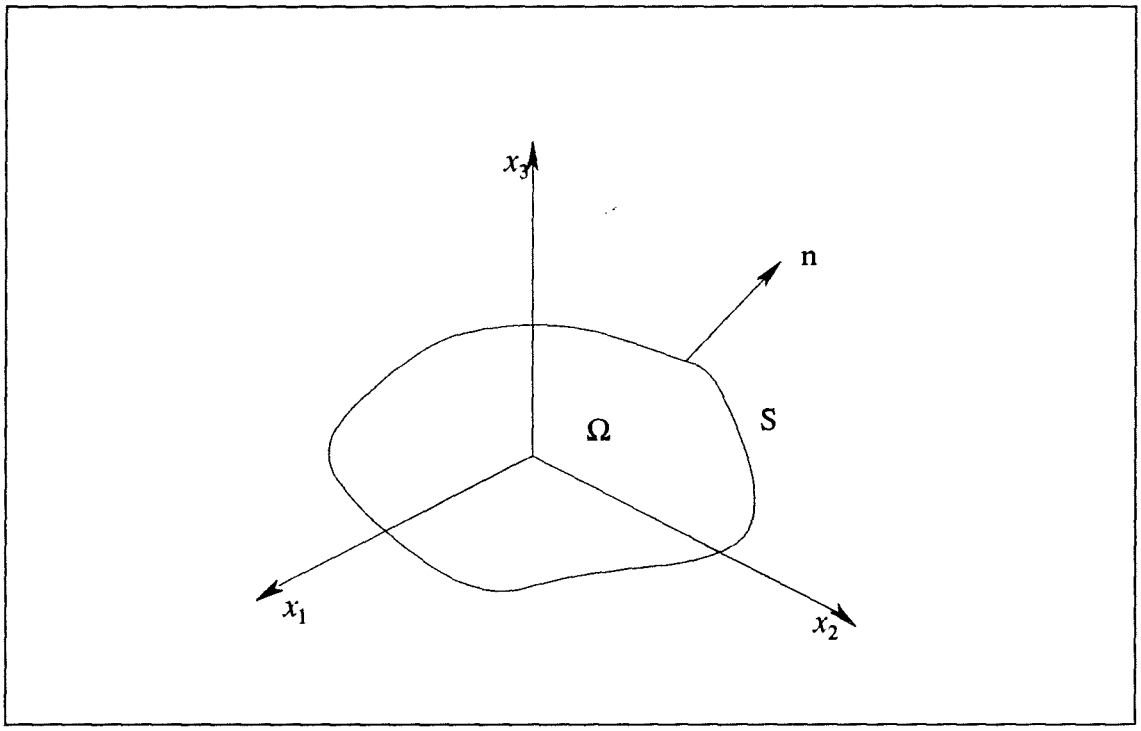

Figure 2.2: A three dimensional elastic body of volume Ω, surface area S and a unit normal vector $\boldsymbol{n}$.

assumed to be smooth, i.e. unit normal vector, $\boldsymbol{n}$, exists at each point of S, as shown in Figure 2.2. The starting point here is to consider the equilibrium equation (2.1) over the domain and to use the Divergence (Green's) Theorem, which states:

$$\int_{\Omega} \frac{\partial \phi}{\partial x_j} (x_1, x_2, x_3)\, d\Omega = \int_S \phi\, (x_1, x_2, x_3) \cos\, (\boldsymbol{n}, x_j)\, dS \tag{2.6}$$

If,

$$\phi(x_1, x_2, x_3) = \xi(x_1, x_2, x_3)\, \eta(x_1, x_2, x_3) \tag{2.7}$$

then differentiating ϕ with respect to x_j would give,

$$\frac{\partial \phi}{\partial x_j} = \xi \frac{\partial \eta}{\partial x_j} + \eta \frac{\partial \xi}{\partial x_j} \tag{2.8}$$

Using the relationship given in Equation (2.7) and Equation (2.6), Equation (2.8) can be arranged as follows:

$$\int_{\Omega} \xi \frac{\partial \eta}{\partial x_j} d\Omega = \int_S \xi \eta n_j \, dS - \int_{\Omega} \eta \frac{\partial \xi}{\partial x_j} d\Omega \tag{2.9}$$

where n_j is given by Equation (2.3). By letting $\eta = \sigma_{jk}$ and $\xi = w_k^*$, the following can be written:

$$\int_{\Omega} \frac{\partial \sigma_{jk}}{\partial x_j} w_k^* \, d\Omega = \int_S \sigma_{jk} w_k^* n_j \, dS - \int_{\Omega} \sigma_{jk} \frac{\partial w_k^*}{\partial x_j} d\Omega \tag{2.10}$$

where w_k^* is the displacement, which will be associated with a known displacement pattern that conforms to the following:

1 - Equilibrium equations

$$\sigma_{ij}^* = 0 \tag{2.11}$$

2 - Linear strain displacement relation

$$\varepsilon_{ij}^* = \tfrac{1}{2} \left(\frac{\partial w_i^*}{\partial x_j} + \frac{\partial w_j^*}{\partial x_i} \right) \tag{2.12}$$

3 - Hooke's Law

$$\sigma_{jk}^* = c_{lm}^{jk} \varepsilon_{lm}^* \qquad \text{where} \qquad c_{lm}^{jk} = c_{jk}^{lm} \tag{2.13}$$

2.3.1 - Internal Points:

The starting point to develop the BEM formulation will be to consider the governing equations of elasticity given in Equation (2.1), the boundary conditions given in Equation (2.2), and the displacement type functions w_k^*. We therefore start with:

$$\int_{\Omega} (\sigma_{jk,j} + b_k) \, w_k^* \, d\Omega \tag{2.14}$$

Applying Green's theorem, as given in Equation (2.6), and ignoring the body forces for the time being, Equation (2.14) can be written as:

$$\int_{\Omega} w_k^* \sigma_{jk,j} \, d\Omega = \int_S w_k^* \sigma_{jk} n_j \, dS - \int_{\Omega} \sigma_{jk} w_{k,j}^* \, d\Omega \tag{2.15}$$

From the Equations (2.2) and (2.12), Equation (2.15) is written as:

$$\int_{\Omega} w_k^* \sigma_{jk,j} \, d\Omega = \int_S p_k \sigma_{jk} n_j \, dS - \int_{\Omega} \sigma_{jk}^* \varepsilon_{j,k} \, d\Omega \tag{2.16}$$

The next step is to eliminate the domain integral in the second integral. First, this integral is written in terms of the displacement derivatives by using the relationship given in Equation (2.4). Hence:

$$\int_{\Omega} \sigma_{jk}^* \varepsilon_{jk} \, d\Omega = \tfrac{1}{2} \int_{\Omega} \sigma_{jk}^* (u_{k,j} + u_{j,k}) \, d\Omega \tag{2.17}$$

Applying Green's theorem to each of these terms, results in the following equation:

$$\int_{\Omega} \sigma_{jk}^* \varepsilon_{jk} \, d\Omega = \tfrac{1}{2} \int_S (\sigma_{jk}^* n_j u_k + \sigma_{jk}^* n_k u_j) \, dS - \tfrac{1}{2} \int_{\Omega} (\sigma_{jk,j}^* u_k + \sigma_{jk,j}^* u_j) \, d\Omega \tag{2.18}$$

As $p_k^* = \sigma_{kj}^* n_j$ and from $\sigma_{jk}^* = \sigma_{kj}^*$ Equation (2.18) becomes:

$$\int_{\Omega} \sigma_{jk}^* \varepsilon_{jk} \, d\Omega = \int_S p_k^* u_k \, dS - \int_{\Omega} \sigma_{kj,j} u_k \, d\Omega \tag{2.19}$$

Using the results from Equations (2.15), (2.16) and (2.19), the Equation (2.6) can be rewritten as:

$$\int_{\Omega} (\sigma_{jk,j} + b_k) w_k^* \, d\Omega = \int_S p_k w_k^* \, dS - \int_S p_k^* u_k \, dS + \int_{\Omega} \sigma_{kj,j}^* u_k \, d\Omega + \int_{\Omega} b_k w_k^* \, d\Omega \tag{2.20}$$

The relationship given in Equation (2.20) is the fundamental identity for the Boundary Element Method, where $\sigma_{jk,j} + b_k$ are the equilibrium results for the given problem with surface tractions p_k and displacements u_k, whereas w_k^* is a displacement pattern with surface tractions p_k^*, stresses σ_{jk}^* and strains ε_{jk}^*. The fundamental solution for w^* and p^* such that,

$$\sigma_{kjj} = 0 \qquad ; \qquad k=1,2,3 \tag{2.21}$$

is derived from the Kelvin's problem of a concentrated force acting at a point in the infinite elastic space. For a 3-D isotropic body the fundamental solutions given by Cruse (1977) are:

$$w_{lk}^* = \frac{1}{16\pi G(1-\nu)r}\left[(3-4\nu)\,\delta_{lk} + 3\frac{\partial r}{\partial x_l}\frac{\partial r}{\partial x_k}\right] \tag{2.22}$$

$$p_{lk}^* = \frac{1}{8\pi(1-\nu)r^2}\left[\frac{\partial r}{\partial n}\left\{(1-2\nu)\,\delta_{lk} + 3\frac{\partial r}{\partial x_l}\frac{\partial r}{\partial x_k}\right\} - (1-2\nu)\left\{\frac{\partial r}{\partial x_l}n_k - \frac{\partial r}{\partial x_l}n_l\right\}\right] \tag{2.23}$$

where n is the outward unit normal to the surface of the body, δ_{lk} is the Kronecker delta, r is the distance from the source point i to the field point k under consideration (Figure 2.3). n_k and n_l are the direction cosines as shown in Equation (2.3). Also,

$$\frac{\partial r}{\partial x_l} = \frac{x_l^i - x_l^k}{r} \qquad ; \qquad \frac{\partial r}{\partial n} = \frac{\partial r}{\partial x_l}n_l \tag{2.24}$$

where x_l^i represents the l coordinate of the internal point i, and x_l^k represents the l coordinate of the surface point k.

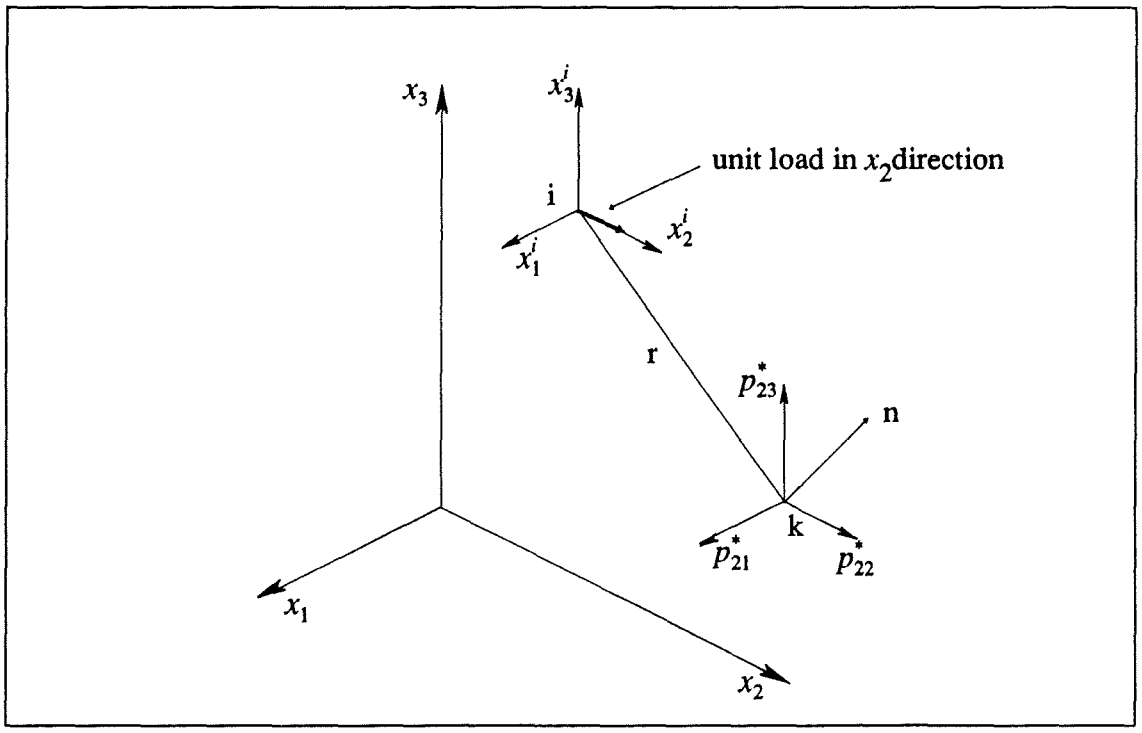

Figure 2.3: Coordinate system for the fundamental solutions.

Substituting w_{lk}^* and p_{lk}^* into relationship (2.20) poses a problem since the stresses σ_{kj}^* and $w_{lk}^* \rightarrow \infty$ as $r \rightarrow 0$. This problem is solved by enclosing the point i by a spherical ball of radius ε and denote it by $B(\varepsilon)$ with boundary ∂B as shown in Figure 2.4.

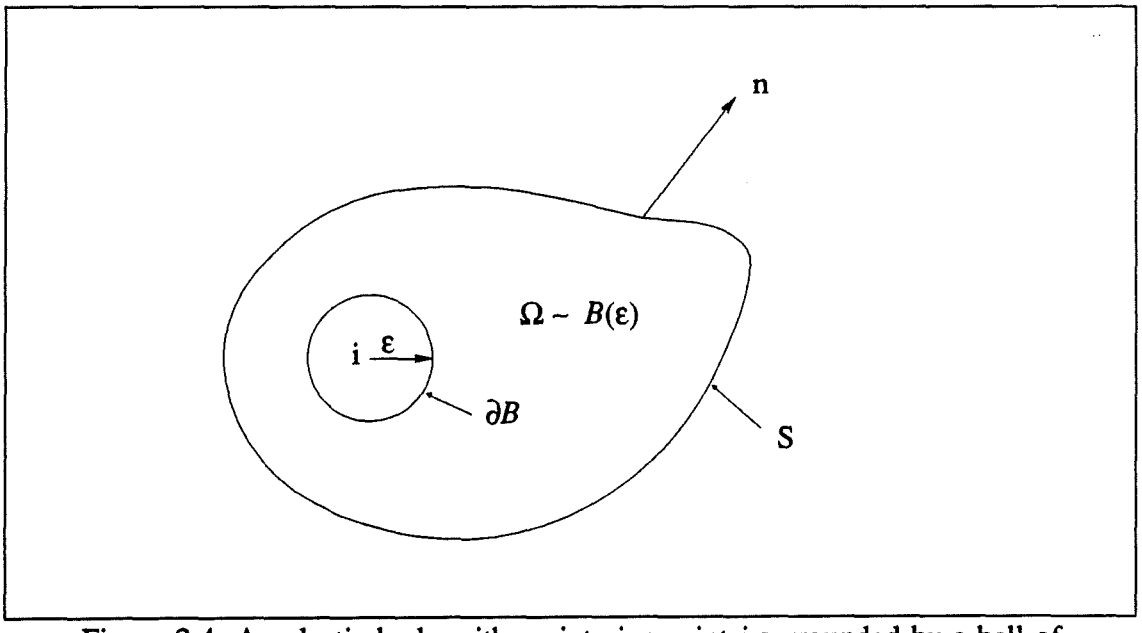

Figure 2.4: An elastic body with an interior point i surrounded by a ball of radius ε.

In the region $\bar{\Omega}$, which is defined by $\Omega \sim B(\varepsilon)$, the following conditions are assumed:

$$\sigma_{kj,j} + b_k = 0 \qquad \forall(x_1,x_2,x_3) \in \bar{\Omega} \qquad ;$$

$$\sigma^*_{kj,j} = 0 \qquad \forall(x_1,x_2,x_3) \in \bar{\Omega} \qquad ;$$

$$w^*_{lk} < \infty \qquad \forall(x_1,x_2,x_3) \in \bar{\Omega} \tag{2.25}$$

For the point i, three equations can be written by using the results given in Equations (2.20), (2.22) and (2.23). Typically, for the case of $l=1$:

$$\begin{aligned}\int_{\Omega}(\sigma_{jk,j} + b_k)\, w^*_{1k}\, d\Omega = &\int_S p_k\, w^*_{1k}\, dS + \int_{\partial B} p_k\, w^*_{1k}\, dS \\ &- \int_S p^*_{1k}\, u_k\, dS - \int_{\partial B} p^*_{1k}\, u_k\, dS \\ &+ \int_{\Omega}\left[\sigma^*_{jk,j}\right]^1 u_k\, d\Omega + \int_{\Omega} p_k\, w^*_{1k}\, d\Omega\end{aligned} \tag{2.26}$$

In the usual manner for *Improper Integrals*, the following applies:

$$\int_{\Omega}(\sigma_{jk,j} + b_k)\, w^*_{lk}\, d\Omega = \lim_{\varepsilon\to 0}\int_{\Omega}(\sigma_{jk,j} + b_k)\, w^*_{lk}\, d\Omega = 0 \tag{2.27}$$

$$\int_{\Omega}\sigma^*_{jk,j}\, u_k\, d\Omega = \lim_{\varepsilon\to 0}\int_{\Omega}\sigma^*_{jk,j} u_k\, d\Omega = 0 \tag{2.28}$$

Substituting these results into Equation (2.26) gives:

$$\begin{aligned}0 = &\int_S p_{1k}\, w^*_{1k}\, dS + \lim_{\varepsilon\to 0}\int_{\partial B} p_{1k}\, w^*_{1k}\, dS - \int_S p^*_{1k}\, u_k\, dS \\ &- \lim_{\varepsilon\to 0}\int_{\partial B} p^*_{1k}\, u_k\, dS + \int_{\Omega} b_{1k}\, w^*_{1k}\, d\Omega\end{aligned} \tag{2.29}$$

The integrals with limits in Equation (2.29) are determined as follows. Consider the geometry definitions given in Figure 2.5. For $l=1$ and $k=1,2,3$:

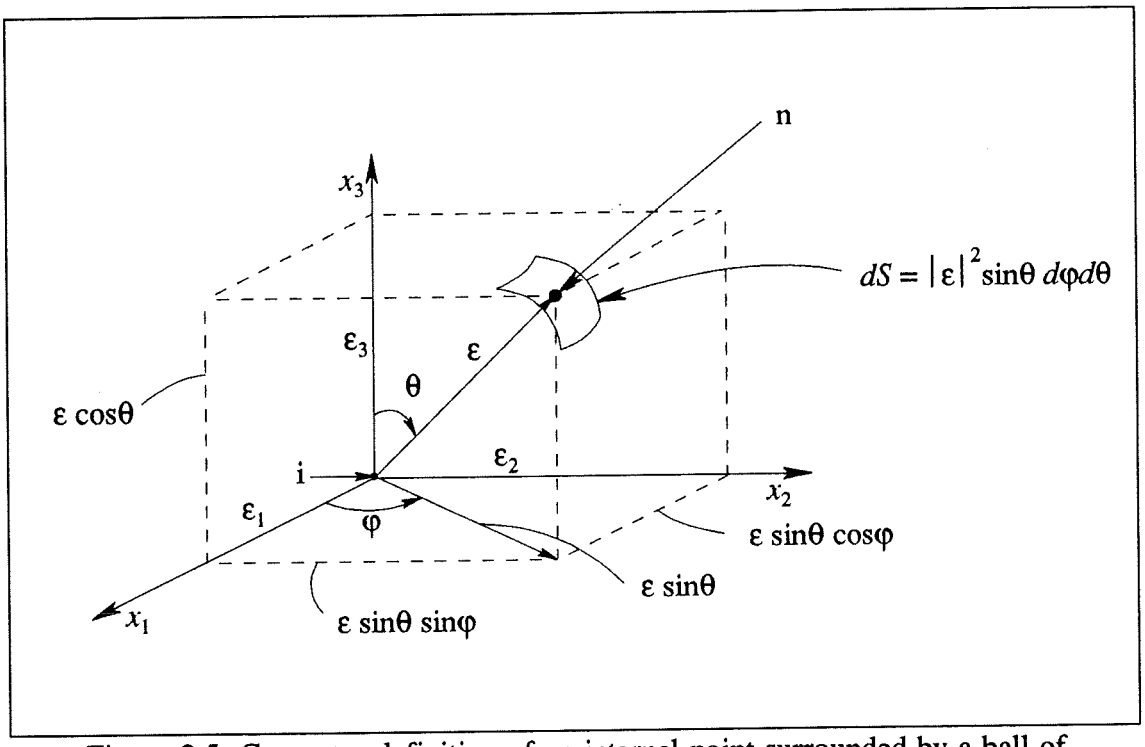

Figure 2.5: Geometry definition of an internal point surrounded by a ball of radius ε.

$$\lim_{\varepsilon \to 0} \int_{\partial B} (p^*_{11} u_1 + p^*_{12} u_2 + p^*_{13} u_3) \, dS \tag{2.30}$$

Since the unit normal vector is taken as +ve when directed outward, then:

$$\boldsymbol{n} = n_1 \varepsilon_1 + n_2 \varepsilon_2 + n_3 \varepsilon_3 \tag{2.31}$$

where

$$n_1 = \cos(\boldsymbol{n}, \varepsilon_1) = -\sin\theta \cos\varphi$$

$$n_2 = \cos(\boldsymbol{n}, \varepsilon_2) = -\sin\theta \sin\varphi$$

$$n_3 = \cos(\boldsymbol{n}, \varepsilon_3) = -\cos\theta \tag{2.32}$$

Using the identities given in (2.24):

$$\frac{\partial r}{\partial x_1} = \frac{x_1 - x_1^i}{|\varepsilon|} = \frac{|\varepsilon| \sin\theta \cos\varphi - 0}{|\varepsilon|} = \sin\theta \cos\varphi \tag{2.33}$$

Similarly,

$$\frac{\partial r}{\partial x_2} = \sin\theta \, \sin\varphi \tag{2.34}$$

$$\frac{\partial r}{\partial x_3} = \cos\theta \tag{2.35}$$

Hence,

$$\frac{\partial r}{\partial n} = \frac{\partial r}{\partial x_1} n_1 + \frac{\partial r}{\partial x_2} n_2 + \frac{\partial r}{\partial x_3} n_3 = -1 \tag{2.36}$$

From the results obtained in Equations (2.31) - (2.36) and using (2.23),

$$p^*_{11} = \frac{1}{8\pi\,(1-\nu)\varepsilon^2}\left[\,(1-2\nu) + 3\,\sin^2\theta\,\cos^2\varphi)\,\right] \tag{2.37}$$

$$p^*_{12} = \frac{1}{8\pi\,(1-\nu)\varepsilon^2}\left[\,3\,\sin^2\theta\,\cos^2\varphi\,\sin\varphi)\,\right] \tag{2.38}$$

$$p^*_{13} = \frac{1}{8\pi\,(1-\nu)\varepsilon^2}\left[\,3\,\sin\theta\,\cos\varphi\,\cos\theta)\,\right] \tag{2.39}$$

also,

$$dS = |\varepsilon|^2 \sin\theta \, d\varphi d\theta \tag{2.40}$$

Hence,

$$\int_{\partial B} p^*_{1k}\, u_k \, dS = \int_0^{\pi}\int_0^{2\pi} p^*_{1k}\, u_k \, |\varepsilon|^2 \sin\theta \, d\varphi d\theta \tag{2.41}$$

The mean value theorem gives:

$$\frac{u_k(\varepsilon,\theta,\varphi) - u^i_k}{|\varepsilon|} = \frac{\partial u}{\partial r}(\xi,\theta,\varphi) \qquad \text{where } 0 < \xi < \varepsilon \tag{2.42}$$

$$\therefore \quad u_k(\varepsilon,\theta,\varphi) = u_k^i + \frac{\partial u}{\partial r}(\xi,\theta,\varphi)\,|\varepsilon| \tag{2.43}$$

Substituting the result of Equation (2.43) into Equation (2.41)leads to :

$$\int_0^{\pi}\int_0^{2\pi} p_{1k}^{*}\, u_k \sin\theta d\varphi d\theta = u_k^i \int_0^{\pi}\int_0^{2\pi} p_{1k}^{*} \sin\theta d\varphi d\theta + |\varepsilon| \int_0^{\pi}\int_0^{2\pi} p_{1k}^{*} \frac{\partial u}{\partial r} \sin\theta d\varphi d\theta \tag{2.44}$$

Hence, as $\varepsilon \rightarrow 0$:

$$\iint p_{1k}^{*}\, u_k \sin\theta d\varphi d\theta \;\rightarrow\; u_k^i \iint p_{1k}^{*} \sin\theta d\varphi d\theta \tag{2.45}$$

and using the Equations (2.37) - (2.39),

$$u_k^i \int_0^{\pi}\int_0^{2\pi} (p_{11}^{*} + p_{12}^{*} + p_{13}^{*}) \sin\theta d\varphi d\theta = u_k^i\,[\,1+0+0\,] \tag{2.46}$$

Using the result from (2.46), Equation (2.30) can be rewritten as:

$$\lim_{\varepsilon\rightarrow 0} \int_{\partial B} p_{1k}^{*}\, u_k\, dS \;=\; u_1^i \tag{2.47}$$

Similar analysis shows that:

$$\lim_{\varepsilon\rightarrow 0} \int_{\partial B} p_{2k}^{*}\, u_k\, dS \;=\; u_2^i \tag{2.48}$$

$$\lim_{\varepsilon\rightarrow 0} \int_{\partial B} p_{3k}^{*}\, u_k\, dS \;=\; u_3^i \tag{2.49}$$

$$\lim_{\varepsilon\rightarrow 0} \int_{\partial B} p_{1k}\, w_k^{*}\, dS \;=\; 0 \tag{2.50}$$

$$\lim_{\varepsilon\rightarrow 0} \int_{\partial B} p_{2k}\, w_k^{*}\, dS \;=\; 0 \tag{2.51}$$

$$\lim_{\varepsilon\rightarrow 0} \int_{\partial B} p_{3k}\, w_k^{*}\, dS \;=\; 0 \tag{2.52}$$

Substituting Equations (2.47) - (2.52) into Equation (2.29) results in the Somigliana's displacements identity, in tensor form:

$$u_l^i = \int_S p_k w_{lk}^* \, dS - \int_S u_k p_{lk}^* \, dS + \int_\Omega b_k w_{lk}^* \, d\Omega \tag{2.53}$$

where S is the surface of the elastic body, u_k and p_k are the displacements and tractions of the boundary point k and the kernels p_{lk}^* and w_{lk}^* represent tractions and displacements in the k direction due to a unit force acting in the l direction (Figure 2.3).

The stresses at these internal points can be calculated by substituting Equation (2.53) and (2.4) into Equation (2.5). The resulting equation, also given by Cruse (1977), in tensor form is shown below:

$$\sigma_{ij} = \int_S D_{kij} p_k \, dS - \int_S S_{kij} u_k \, dS + \int_\Omega D_{kij} b_k \, d\Omega \tag{2.54}$$

where the third order tensor D_{kij} and S_{kij} can be calculated by making use of the relationships given in Equation (2.24). The resulting tensor definitions are:

$$D_{kij} = \frac{1}{8\pi(1-\nu)\, r^2} \left\{ (1-2\nu)\left(\delta_{ki}\frac{\partial r}{\partial x_j} + \delta_{kj}\frac{\partial r}{\partial x_i} - \delta_{ij}\frac{\partial r}{\partial x_k}\right) + 3\frac{\partial r}{\partial x_i}\frac{\partial r}{\partial x_j}\frac{\partial r}{\partial x_k} \right\} \tag{2.55}$$

$$\begin{aligned} S_{kij} = \frac{\mu}{4\pi(1-\nu)r^3} \Bigg\{ & 3\frac{\partial r}{\partial n}\left[(1-2\nu)\,\delta_{ij}\frac{\partial r}{\partial x_k} + \nu\left(\delta_{ik}\frac{\partial r}{\partial x_j} + \delta_{jk}\frac{\partial r}{\partial x_i}\right) \right. \\ & \left. - 5\frac{\partial r}{\partial x_i}\frac{\partial r}{\partial x_j}\frac{\partial r}{\partial x_k} \right] + 5\nu\left(n_i \frac{\partial r}{\partial x_j}\frac{\partial r}{\partial x_k} + n_j \frac{\partial r}{\partial x_i}\frac{\partial r}{\partial x_k} \right) \\ & + (1-2\nu)\left(5n_k \frac{\partial r}{\partial x_i}\frac{\partial r}{\partial x_j} + n_j\,\delta_{jk,} + n_i\,\delta_{jk} \right) - (1-4\nu)\, n_k\,\delta_{ij} \Bigg\} \end{aligned} \tag{2.56}$$

2.3.2 - Boundary Points:

Equation (2.53) can be used to find the displacements at any interior point of Ω if the R.H.S. is known. In general, not all the displacements and tractions are known on the boundary. An approximation to these can be found by taking the point i to the boundary.

This is done in the following way, which is similar to the method for an interior point. The point i is thus again surrounded with a ball $B(\varepsilon)$ of a radius ε (Figure 2.6).

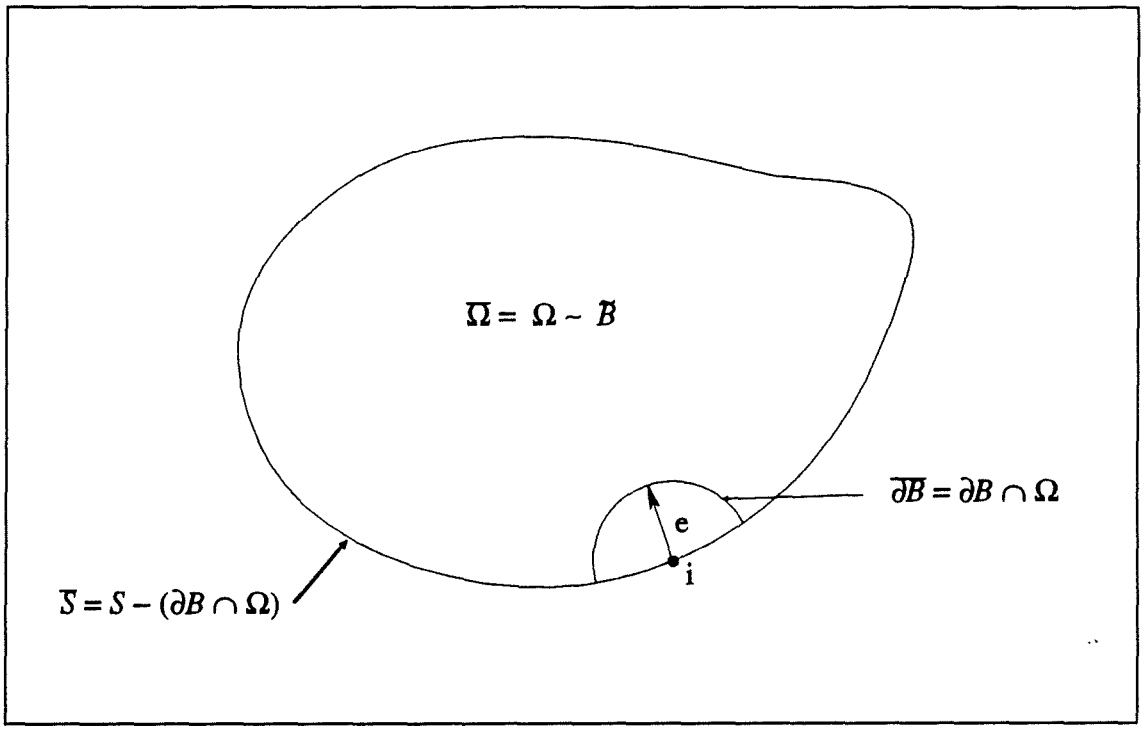

Figure 2.6: Geometry definitions of an elastic body with a surface point, i.

Set,

$$\bar{B} = B(\varepsilon) \cap \Omega$$

$$\bar{\Omega} = \Omega \sim \bar{B}$$

$$\bar{S} = S - (\partial B \cap \Omega)$$

$$\bar{\partial B} = \partial B \cap \Omega \qquad (2.57)$$

As before, making use of Equations (2.26) and (2.28), and applying boundary conditions, similar to those given in Equation (2.25), the following can be written:

$$0 = \lim_{\varepsilon \to 0} \int_S p_{lk} w^*_{lk} \, dS + \lim_{\varepsilon \to 0} \int_{\partial B} p_{lk} w^*_{lk} \, dS - \lim_{\varepsilon \to 0} \int_S p^*_{lk} u_k \, dS$$
$$- \lim_{\varepsilon \to 0} \int_{\partial B} p^*_{lk} u_{lk} \, dS + \lim_{\varepsilon \to 0} \int_\Omega b_{lk} w^*_{lk} \, d\Omega + \lim_{\varepsilon \to 0} \int_\Omega \sigma^*_{jk_j} u_k \, d\Omega \qquad (2.58)$$

For simplicity of the integration purposes, a smooth boundary will be assumed and as $\varepsilon \to 0$, the intersecting boundary $\overline{\partial B}$ can be assumed to become a hemisphere.

$$\therefore \quad \lim_{\varepsilon \to 0} \int_{\overline{\partial B}} p^*_{lk} u_k \, dS = \int_0^{\frac{\pi}{2}} \int_0^{2\pi} p^*_{lk} u_k \sin\theta d\varphi d\theta \qquad (2.59)$$

This is identical with the form of an interior point except that the integral for θ now run from $0 \to \frac{\pi}{2}$ whereas for the interior point θ run from $0 \to \pi$.

In general, the BEM displacement equation for a point, *i*, on a smooth boundary can be calculated from the following equation:

$$\frac{1}{2} u^i_l + \int_S u_k p^*_{lk} \, dS = \int_S \mathrm{P}_k w^*_{lk} \, dS + \int_\Omega b_k w^*_{lk} \, d\Omega \qquad (2.60)$$

In practice, at every boundary point, either displacements or tractions are known and it will be possible to solve the integral Equation (2.60) by an approximation procedure, which will be shown in Chapter 3. Having found an approximation to the displacement pattern over the boundary, the internal displacements and stresses for any point, *i*, can be approximated from Equation (2.53).

The work presented in the later chapters is based on the Equation (2.60) and the analysis will be carried out in the absence of the body forces. Therefore these equations arereduced to:

$$\frac{1}{2} u_1^i + \int_S u_k p_{1k}^* \, dS = \int_S p_k w_{1k}^* \, dS \tag{2.61}$$

$$\frac{1}{2} u_2^i + \int_S u_k p_{2k}^* \, dS = \int_S p_k w_{2k}^* \, dS \tag{2.62}$$

$$\frac{1}{2} u_3^i + \int_S u_k p_{3k}^* \, dS = \int_S p_k w_{3k}^* \, dS \tag{2.63}$$

Chapter

3

BEM For A Solid Sphere

"One of the symptoms of approaching a nervous breakdown is the belief that one's work is terribly important. If I were a medical man, I should prescribe a holiday to any patient who considered his work important."

Bertrand Russell

1930

3.1 - INTRODUCTION

The boundary of the domain is divided into a number of small segments. For two-dimensional problems, these segments take the form of a line, and in three-dimensional cases, rectangular or triangular patches. The variation of the displacements and the tractions over each element can be formulated to be constant, linear, quadratic, etc., by using an appropriate interpolation formula.

In this chapter, linear and quadratic variations of the displacements and tractions are demonstrated. Constant variation of these surface variables are not considered, as they will not have such variations in the final geometry.

The selected geometrical shape to be used in this chapter is a solid sphere, where an external pressure of 1MPa is exerted on the surface. Initially, linear variation is applied and the surface unknowns, in this case the surface displacements, are to be determined. The linear variation of the surface displacements are then used to determine the internal displacements and stresses. This is then repeated with a quadratic variation. In all cases, the numerical results are compared with the theoretical values.

Attention is also paid to the integration of the singular integrals and the problems associated with the discretization of the boundary, where there is a large variation of size in the adjacent elements used.

3.2 - LINEAR ELEMENTS

To derive the formulation for this section, the Equations (2.61), (2.62) and (2.63) are considered. However, due to the symmetrical geometry and the applied uniform pressure the BEM is only implemented on Equations (2.61) and (2.63).

3.2.1 - Surface Displacements

Rewriting Equation (2.61) in expanded form:

$$\frac{1}{2}u_1' + \int_0^{\pi}\int_0^{2\pi}(u_1p_{11}^* + u_2p_{12}^* + u_3p_{13}^*)\,R^2\sin\theta\,d\varphi d\theta$$

$$= \int_0^{\pi}\int_0^{2\pi}(p_1w_{11}^* + p_2w_{12}^* + p_3w_{13}^*)\,R^2\sin\theta\,d\varphi d\theta \qquad (3.1)$$

Consider only the L.H.S. of Equation (3.1) and substitute the transformation given in Equation (3.2) into the Equation (3.1).

$$u_1 = v_1 \cos\varphi$$

$$u_2 = v_1 \sin\varphi$$

$$u_3 = v_3 \tag{3.2}$$

$$\frac{1}{2} v_1^i + \int_0^{\pi} \int_0^{2\pi} (v_1 \cos\varphi p_{11}^* + v_1 \sin\varphi p_{12}^* + v_3 p_{13}^*) R^2 \sin\theta \, d\varphi d\theta \tag{3.3}$$

The boundary is to be discretized into several elements and summed up to form the total boundary. The integrals given in Equation (3.3) are divided into M segments in θ direction and N segments in φ direction (Figure 3.1). Due to the axisymmetry, the source points where the unknown displacements are required are distributed on a path where $0 \leq \theta \leq \pi$ and $\varphi = 0$. Each segment on this path is called an element and the source points, called *nodes*, are placed at the corners of each element. The displacements and tractions are assumed to vary linearly between these end points. Substitution into Equation (3.3) is

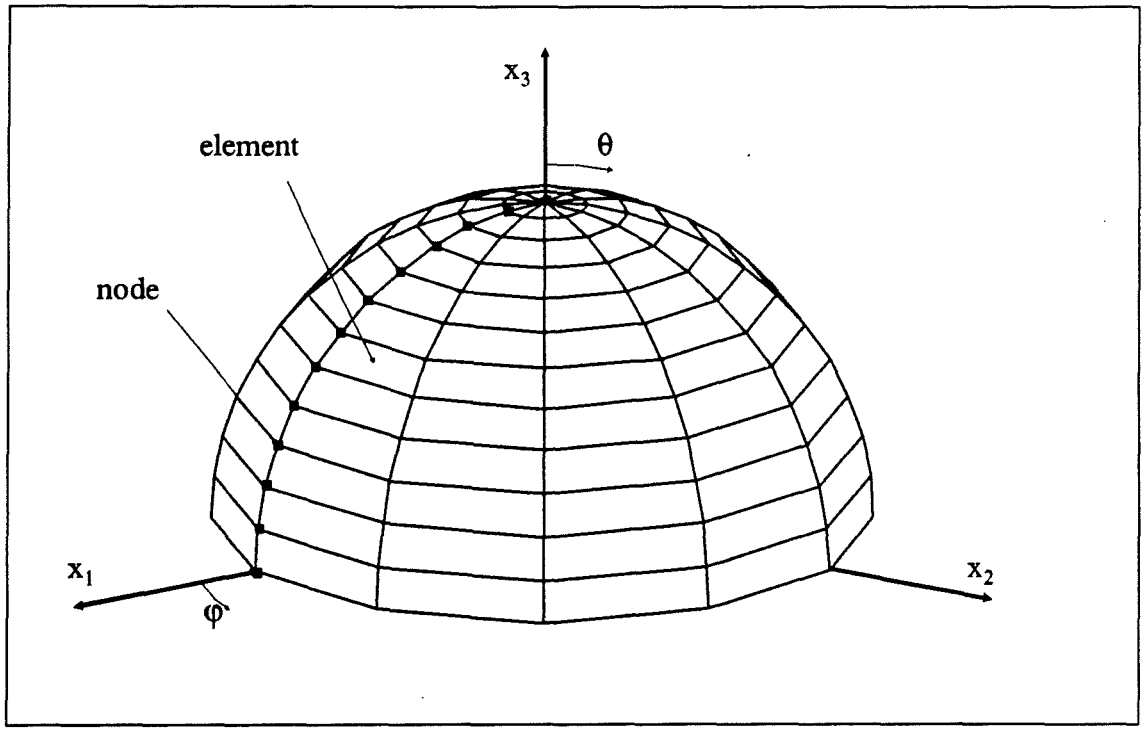

Figure 3.1: The top half of a solid sphere, divided into M × N segments. Marked nodes show the path selected for the unknown displacements (i.e. $\varphi = 0$).

achieved by making use of an interpolation formula, derived from a straight line fit (see Appendix A). The interpolation formula used is given below, where θ_j and θ_{j+1} are the coordinates of the end point of the element:

$$v = v^{j+1} \frac{(\theta - \theta_j)}{(\theta_{j+1} - \theta_j)} + v^j \frac{(\theta_{j+1} - \theta)}{(\theta_{j+1} - \theta_j)} \tag{3.4}$$

Equation (3.3) in discretized form is given as:

$$\frac{1}{2} v_1^i + \sum_{j=1}^{M} \int_{\theta_j}^{\theta_{j+1}} \sum_{k=1}^{N} \int_{\varphi_k}^{\varphi_{k+1}} (v_1 \cos\varphi p_{11}^* + v_1 \sin\varphi p_{12}^* + v_3 p_{13}^*) R^2 \sin\theta \, d\varphi d\theta \tag{3.5}$$

Substituting Equation (3.4) into Equation (3.5) and, after some mathematical manipulation, Equation (3.5) can be written in simple terms as:

$$\frac{1}{2} v_1^i + v_1^j A_1 + v_1^{j+1} B_1 + v_3^j C_1 + v_3^{j+1} D_1 \tag{3.6}$$

The integrals and other parameters are embedded in A_1, B_1, C_1 and D_1. The next step is to consider the R.H.S. of the Equation (3.1). The variables p_1, p_2, and p_3 are the surface tractions and they correspond to the components of the surface pressure (Figure 3.2).

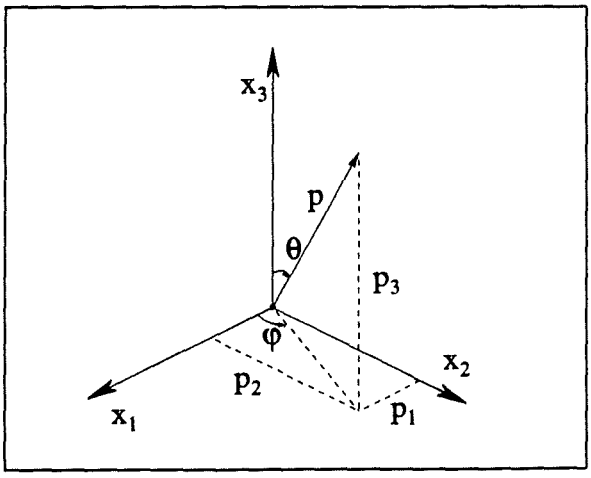

Figure 3.2: Components of the surface pressure p.

$$p^2 = p_1^2 + p_2^2 + p_3^3$$

$$p_1 = p \sin\theta \cos\varphi$$

$$p_2 = p \sin\theta \sin\varphi$$

$$p_3 = p \cos\theta \tag{3.7}$$

By using the relationships given in Equation (3.7), the R.H.S. of Equation (3.1) can be written in terms of the surface pressure, p, and it can be taken outside the integral as shown below.

$$p \int_0^{\pi} \int_0^{2\pi} (w_{11}^* \sin\theta\cos\varphi + w_{12}^* \sin\theta\sin\varphi + w_{13}^* \cos\theta)\, R^2 \sin\theta \, d\varphi d\theta \tag{3.8}$$

Putting the Equations (3.6) and (3.8) together, a set of equations can be written for each i point. The similar equations can also be written for the u_3 displacements as given in Equation (2.63). The complete set of these equations can easily be written in a matrix form as:

$$\begin{bmatrix} a_{11} & a_{12} & \cdots & a_{1n} \\ a_{21} & a_{22} & \cdots & a_{2n} \\ \vdots & \vdots & \cdots & \vdots \\ a_{n1} & a_{n2} & \cdots & a_{nn} \end{bmatrix} \begin{Bmatrix} x_1 \\ x_2 \\ \vdots \\ x_n \end{Bmatrix} = \begin{Bmatrix} b_1 \\ b_2 \\ \vdots \\ b_n \end{Bmatrix} \tag{3.9}$$

Since there are no mixed boundary conditions present, the Equation (3.9) can be written as,

$$\mathrm{A}\,\mathrm{x} = \mathbf{b} \tag{3.10}$$

When the source point and the field point coincide, i.e. when $i = j$, the free term of Equation (3.6) has a contribution of $\frac{1}{2}$ which is included in the diagonal terms of the A matrix. By using a suitable solver, the unknowns in the x vector can easily be calculated. The solver used in this work is a NAG routine called F04ATF which uses Crout's factorisation method.

The diagonal terms of the A matrix are calculated explicitly throughout this work. It is also possible to determine these terms by applying a rigid body displacement in the direction of one of the cartesian coordinates (Brebbia et. al., 1989). It is the intention of the author to evaluate these diagonal terms explicitly, in order to look at the possible improvements to the integration schemes used by previous researchers (i.e. Lachat 1975, Lera et. al. 1982, Jun et. al. 1985a, Labeyrie et. al. 1985 , Higashimachi et. al. 1986).

3.2.2 - Numerical Integration

In this section, the numerical integration scheme which is employed is shown. To determine all the coefficients of the A matrix, the Gauss integration scheme (Stroud et. al. 1966) is implemented. The transformation used that takes the integrals from (θ,φ) space to (ξ,η) with N× M quadrature rule is:

$$\int_{\theta_1}^{\theta_2}\int_{\varphi_1}^{\varphi_2} f(\theta,\varphi)\, d\varphi d\theta \approx m_1 m_2 \sum_{j=1}^{N} w_j \sum_{i=1}^{M} w_i f(m_1\xi_j + c_1\,,\, m_2\eta_i + c_2) \tag{3.11}$$

where ξ and η are the abscissas and w_i and w_j are the corresponding weights. Symbols m and c are used to change the limits of the integral, where,

$$m_1 = \frac{\varphi_2 - \varphi_1}{2} \qquad c_1 = \frac{\varphi_1 + \varphi_2}{2}$$

$$m_2 = \frac{\theta_2 - \theta_1}{2} \qquad c_2 = \frac{\theta_2 + \theta_1}{2} \tag{3.12}$$

The discretization of the surface is done in such a way that the singularities always occur between two adjacent elements and not on the corners of the elements. In the presence of a singularity, Gauss integration cannot be used in the normal way. When integrating over a singular element, the *Convergence Method* is used. This method isolates the singular point by subdividing the element into smaller areas. Normal Gauss integration is performed over these areas except for the singular sub-elements. The results of the individual integrations are then added together. The whole process is repeated until the cumulative result converges within a pre-defined percentage (1% in most cases). Similar methods were used by Lachat (1975), and Jun et. al. (1985a). Lachat used equally divided regions, whereas Jun et. al. tried unequally divided elements to approach the source point more rapidly by halving the size of the elements each time. The intention of these researchers was to distribute a larger number of integration points around the singularity and overcome the difficulty of dealing with singular integrals.

The method used here is closer to the one suggested by Jun with two exceptions:

i - The division ratio is set to be 10 rather than 2, so that the convergence is accelerated.

ii - Only one half of the singular element is integrated and the result is then doubled. This could only be used where the two adjacent singular elements are of the same size and symmetry of geometry and loading is obtained.

In cases where there are differences in the size of the neighbouring elements, the longer element is made the same size as the other element by partitioning it. Ordinary integration is performed over the excess area and the *Convergence Method* is used for the remainder (Figure 3.3). It is important to note that when the *Convergence Method* is used, the integration of the two adjacent elements must be done together. This is because the integrals present in the formulation are in the Cauchy Principal Value (CPV) sense.

To see the effect of the *Convergence Method*, the subdivisions were set at equal lengths, i.e. the division factor was set to 50%. This was then changed to 33% and then to 10%.

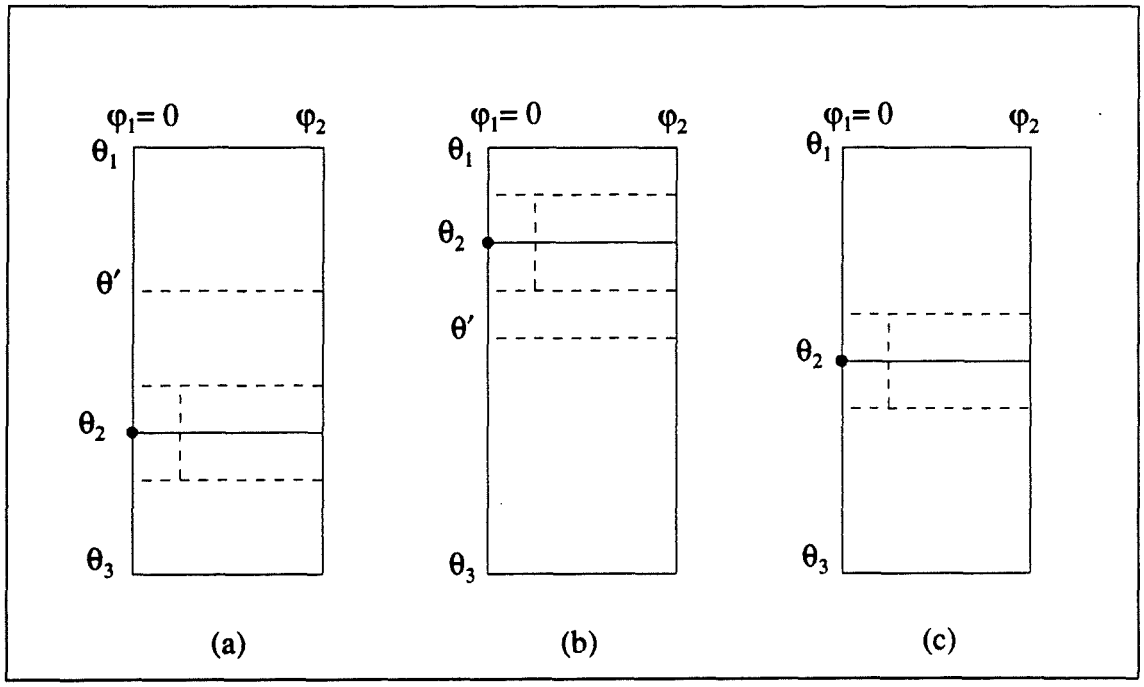

Figure 3.3: Possible cases of R.H.S. of singular elements: a) The top element is longer than the lower element; b) The lower element is longer than the top element; c) The elements are equal .

With the division factor set to 2, 7 iterations were needed to bring the convergence of the integral within 1%. When a division factor of 3 was used, this dropped to 4, and with 10, 2-3 iterations were found to be necessary for such accuracy.

The results obtained from the programmed formulation presented so far shown in Table 3.1, are those obtained for a solid sphere under a uniform external pressure of 1MPa, with an equally spaced mesh and a division factor set to 10. Good agreement was found with the analytical result.

Table 3.1: Accelerated convergence results for external displacements (analytical solution gives 0.2×10^{-5} m).

Node No.	Angle θ	Resultant Displacements
1	9.0	0.200123E-05
2	18.0	0.199666E-05
3	36.0	0.200242E-05
4	54.0	0.200279E-05
5	72.0	0.200282E-05
6	90.0	0.200282E-05
7	108.0	0.200282E-05
8	126.0	0.200279E-05
9	144.0	0.200242E-05
10	162.0	0.199666E-05
11	171.0	0.200123E-05

3.2.3 - Internal Displacements

Once the boundary displacements have been determined, the internal displacements are calculated from Equation (2.53) without the body forces. As in the surface displacement formulation, the transformations in Equations (3.2) and (3.7) and the interpolation formula given in Equation (3.4) is substituted into Equation (2.53). The resulting formulation is shown in the following equation for a horizontal displacement at point *i*:

$$u_1^i = P_1 - \left[v_1^j A_1 + v_1^{j+1} B_1 + v_3^j C_1 + v_3^{j+1} D_1 \right] \tag{3.13}$$

The first term, P_1, represents the first integral in Equation (2.53) which is given by Equation (3.8) and the second term represents the second integral in Equation (2.53) which is shown in the previous section (see Equation (3.6)). The values of P_1 , A_1 , B_1 , C_1 and D_1 can easily be calculated, as shown in section 3.2.2. Since the displacements on the surface are now known, any internal displacement can be determined from Equation (3.13).The internal displacements are obtained using the surface displacements determined in section

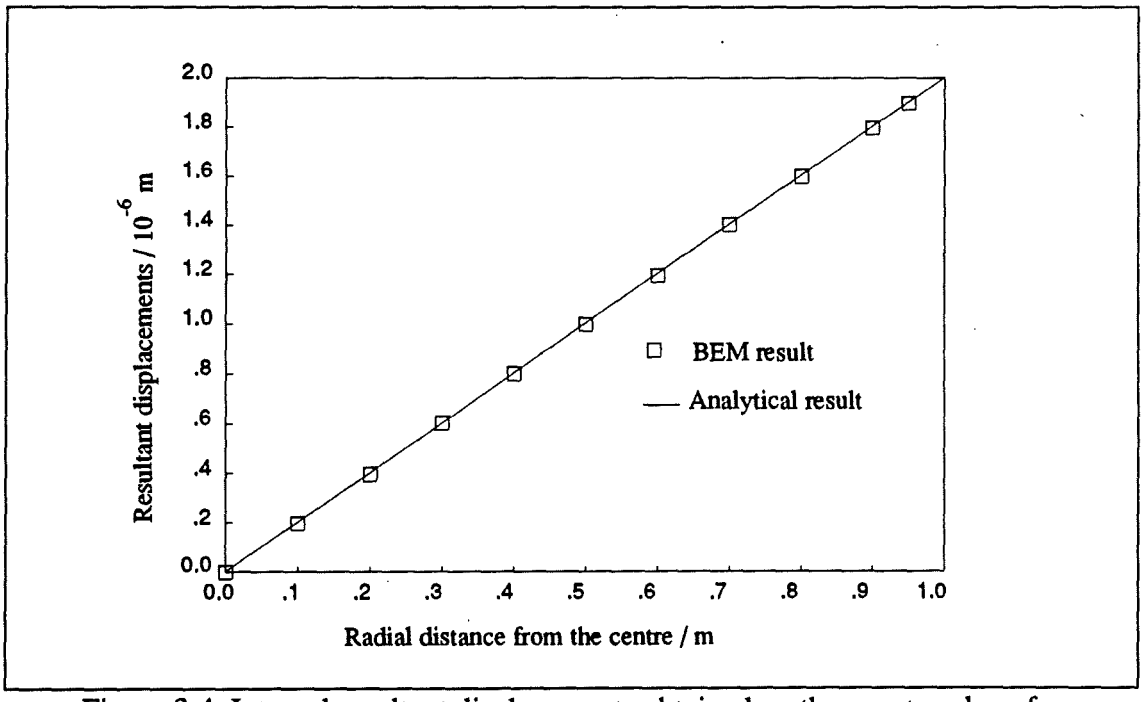

Figure 3.4: Internal resultant displacements obtained on the equator plane for a solid sphere.

3.2.2 and are presented in Figure 3.4. The results shown are determined along the equator of the sphere (θ= 90° ; φ= 0°), at regular increments in the radial direction measured from the origin.

In general, Equation (3.13) is well behaved. But, as the internal point approaches the surface, some inaccuracies in the results begin to appear. This is caused by the presence of the singularities in the displacement and traction kernels. The effect of this will be highlighted in section 3.4.3.

3.2.4 - Internal Stresses

The stresses at the internal points are calculated from Equation (2.54). The expanded form of this equation, without the body forces term for σ_{ij} is written as follows:

$$\sigma_{ij} = \int_S \left(D_{1ij} p_1 + D_{2ij} p_2 + D_{3ij} p_3 \right) dS - \int_S \left(S_{1ij} u_1 + S_{2ij} u_2 + S_{3ij} u_3 \right) dS \qquad (3.14)$$

The D_{kij} and S_{kij} terms are calculated from Equations (2.55) and (2.56). As before, Equations (3.2), (3.4) and (3.7) are used to reduce Equation (3.15) to:

$$\sigma_{ij} = P_{ij} - \left[v_1^j A_{ij} + v_1^{j+1} B_{ij} + v_3^j C_{ij} + v_3^{j+1} D_{ij} \right] \qquad (3.15)$$

where P_{ij} represents the first integral term of Equation (3.14) and the other terms are written in terms of the surface displacements as shown in the second integral of Equation (3.14). Again, there is a limitation on how close the internal point can approach the boundary. With stresses, this is more severe as the S_{kij} term involves a $1/r^3$ term rather than a $1/r^2$ term as it was in p^*_{lk} for the internal displacements. The effect of this will be shown in section 3.4.4.

Using the surface displacements determined in section 3.2.3, three direct and three shear stresses were calculated. The shear stresses, σ_{12}, σ_{13} and σ_{23} were found to be less than

10^{-10} N/m^2. This was expected as due to symmetrical loading, there was no shear on the sphere. The direct stresses σ_{11}, σ_{22} and σ_{33} were expected to be equal to the applied pressure (1 MN/m^2), and are given in Table 3.2 below:

Table 3.2: Direct stresses on the equator plane of a solid sphere using linear elements.

Radial distance / m	Internal Stresses / MN/m^2		
	σ_{11}	σ_{22}	σ_{33}
0	0.997205	0.997205	0.996983
0.1	0.997208	0.997206	0.996982
0.2	0.997216	0.997211	0.996980
0.3	0.997231	0.997218	0.996977
0.4	0.997254	0.997231	0.997973
0.5	0.997292	0.997250	0.996969
0.6	0.997359	0.997280	0.996958
0.7	0.997556	0.997341	0.996877
0.8	0.998487	0.997547	0.996358
0.9	1.002868	0.998741	0.994858
0.95	1.009510	1.001284	0.995306

The results shown in Table 3.2 confirm the formulation used in this section. However, the method explained in this section cannot be used to determine the stresses on the boundary. One alternative to the solution of this problem is to use the derivatives of the displacements on the surface to obtain the strains, and then using the Hooke's Law to evaluate the stresses on the boundary. This approach will be used in Chapter 6 to determine the surface stresses for the nose cone.

3.3 - EVALUATION OF SINGULAR INTEGRALS

3.3.1 - Previous Formulation

Evaluation of the singular integrals present in the BEM formulation by the *Convergence Method* is expensive in terms of the CPU time, due to its iterative nature. Therefore, a method is required for these singular integrals, of order $O(1/r^{\alpha})$ with $\alpha = 1, 2$, which could be evaluated efficiently and at a low CPU cost.

Nearly all of the known methods for dealing with singular integrals involve element subdivisioning. The aim of these methods is to increase the accuracy of the integration. To achieve this, the integration points are gathered close to the singular point by either using a process of element subdivisioning or of nonlinear mapping, or both.

Jun et. al. (1985b) and Higashimachi et. al. (1986) used a double-exponential formula which is based on the trapezoidal rule for two-dimensional elastic problems. However, this method requires a high number of sampling points for sufficient accuracy, (see Cerroloza et. al. (1989a & 1989b), Beswick (1992a)) and does not provide any significant advantage over the *Convergence Method.* Telles (1987) used a non-linear coordinate transformation to gather the sampling point nearby the source point. In this paper, the author also discusses the use of the numerical quadrature formula developed by Kutt (1975). Kutt quadrature is for the evaluation of finite-part integrals. This formulation can be used for the evaluation of the singular kernels that exist in the Cauchy Principal Value (CPV) sense. Kernels with singularities of order $O(\log r)$ cannot be evaluated with this method. Another way of dealing with singular integrals is to use the direct computation of CPV integrals developed by Guiggiani et.al. (1987) but this is limited to $O(1/r)$. In this method, the CPV integrals with first order singularity is reduced to two regular integrals plus two logarithmic terms. Later Cerroloza et. al. (1989) extended the works of Telles (1987) and Guiggiani (1987) by introducing a bi-cubic transformation that ensures total symmetry about the singular point when it is placed on the corner of an element. The importance of maintaining total

symmetry is lacking in Telles's work and this was confirmed by Guiggiani (1988). This was also discovered in the early stages of this study when dealing with adjacent elements of different size (see Karamanoglu et. al. 1991).

3.3.2 - Finite-part Integral Formulation

The aim of this section is to show the development of an integration method in the current work for accurate and efficient evaluation of the strongly singular kernels. The double integrals present in this 3-D analysis are evaluated by combining the Gauss (see Stroud et.al., 1966) and Kutt (1975) formulations. Both these formulae are given in terms of one dimension only, but using one formula for the inner integral and another for the outer integral, the double integrals can thus be evaluated. Consider two linear elements with a source point shared between them (see Figure 3.5). Notice that these elements are divided into two equal parts about $\varphi = 0$ and then doubled after the integration of the right hand side. These elements are divided into triangles in order to use local polar coordinates. The new method, named as *Composite Mapping*, is applied to each of the triangular areas

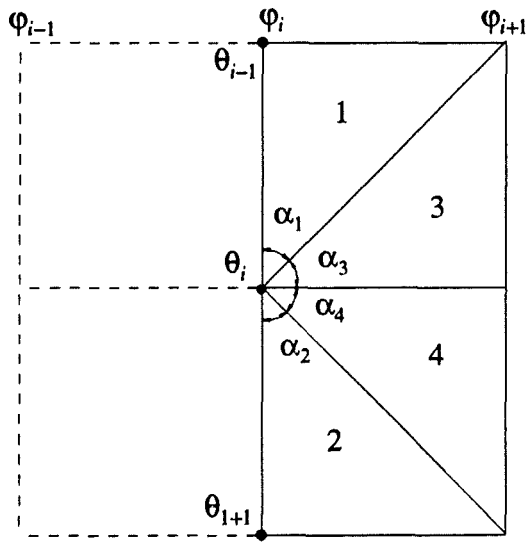

Figure 3.5: Element division for the Composite Mapping formulation.

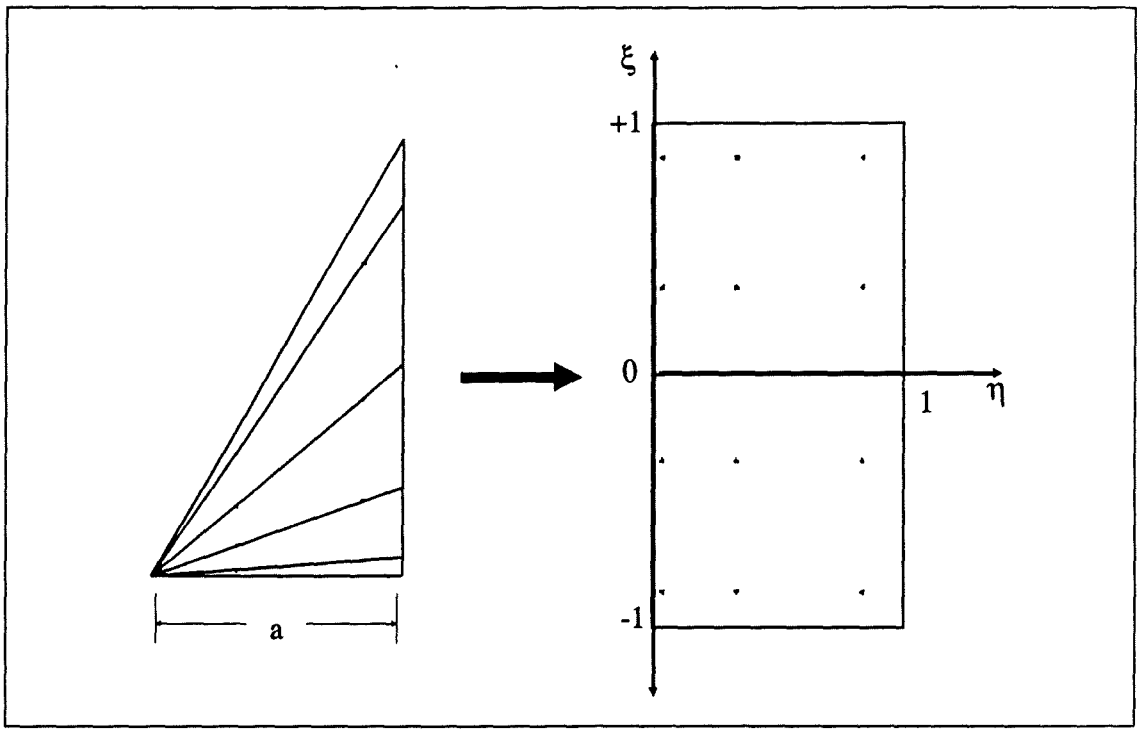

Figure 3.6: Composite Mapping transformation using 4 (Gauss) by 3 (Kutt) quadrature with $\alpha = 60°$ and a= 10.

(Figure 3.6). The aim is to use this formulation to cancel the singularity present in the integration and to pack more sampling points near the singular point. The formulation given by Kutt (1975) is:

$$\int_s^r \frac{f(x)}{(x-s)^\lambda} \approx (r-s)^{1-\lambda} \sum_{i=1}^{N} w_i f\,[(r-s)\,\xi_i + s] + \frac{f^{(\lambda-1)}(s) \ln|r-s|}{(\lambda-1)!} \tag{3.16}$$

where ξ_i is the co-ordinate of the ith integration point, w_i is the associated weighting factor, λ is used to control the order of the singularity, and N is the total number of points. The above relationship is subject to the following condition: $f(x)$ is a real function of the real variable x. It is also required that $f(x) \in C$ in an interval containing $[s,r]$ and $f(x) \in C^{[\lambda]}$ in the neighbourhood of s. For the case where the integration interval is $[0\,,\,b\,]$ and $\lambda = 1$, then the above formula simplifies to:

$$\int_0^b \frac{f(x)}{x} \approx \sum_{i=1}^{N} w_i f\,(b\,\xi_i) + f(0) \ln|b| \tag{3.17}$$

Take an example of a triangular area (Figure 3.5) for which the BEM integral is to be evaluated. The integral is:

$$\iint_{\Delta} f(\theta,\varphi)\, d\theta d\varphi = \int_0^{\alpha}\int_0^{b} f(\rho,\psi)\, \rho d\rho d\psi \tag{3.18}$$

Notice that b is dependant on ρ and it should be treated accordingly. The outer integral is to be evaluated using Gauss quadrature and the inner integral using Kutt quadrature. However, the integral given in Equation (3.18) is not in the right form for a Kutt type formulation. Therefore, Equation (3.18) is multiplied and divided by ρ so that it is turned into an acceptable form.

$$= \int_0^{\alpha}\int_0^{b} \frac{f(\rho,\psi)}{\rho}\, \rho^2\, d\rho d\psi \tag{3.19}$$

The ρ^2 term in Equation (3.19) will cancel out with the $1/r^2$ term inside the function f, since as $\rho \rightarrow 0$ then $\rho \rightarrow r$, provided that the local polar coordinates are used. Hence the strong singularity present in the integrals when dealing with singular elements, will not cause any problems, and the integrals can now be evaluated without any further element division.

As the BEM formulation is in a spherical coordinate system, then some transformations are necessary. Furthermore, the integral limits in Equation (3.19) need to be transformed to (-1 , +1) and (0 , 1) spaces for the quadrature formulae. The outer integral limit (0 , α) is to be mapped to (-1 , +1) space:

$$\psi = m\,\xi + c \tag{3.20}$$

$$\xi = -1 \quad ; \quad \psi = 0 \tag{3.21}$$

$$\xi = +1 \quad ; \quad \psi = \alpha \tag{3.22}$$

This leads to $m = \frac{\alpha}{2}$ and $c = \frac{\alpha}{2}$.

$$\therefore \qquad \psi = \frac{\alpha}{2}(\xi+1) \tag{3.23}$$

The inner integral limit (0 , b) is mapped to (0 , 1) space:

$$\rho = m\,\eta + c \tag{3.24}$$

$$\eta = 0 \quad ; \quad \rho = 0 \quad \Rightarrow \quad c = 0 \tag{3.25}$$

$$\eta = 1 \quad ; \quad \rho = b \quad \Rightarrow \quad m = b \tag{3.26}$$

$$\therefore \qquad \rho = b\,\eta \tag{3.27}$$

The upper limit b has to be computed for each value of ψ (see Figure 3.7) by using the relationship give in Equation (3.28);

$$b = \frac{a}{\cos\psi} \tag{3.28}$$

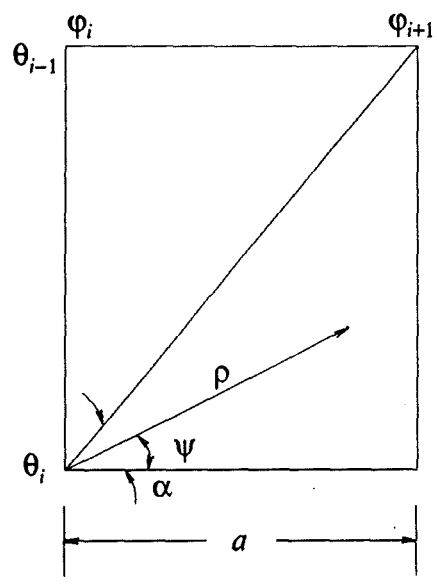

$$a = \varphi_{i+1} - \varphi_i$$

$$\alpha = \tan^{-1}\left(\frac{\theta_i - \theta_{i-1}}{a}\right)$$

$$\psi = \frac{\alpha}{2}(\xi+1)$$

$$\rho = \frac{a}{\cos\psi}\eta$$

$$\theta = \theta_i - \rho\sin\psi$$

Figure 3.7: Parameters and transformations used in *Composite Mapping*.

The formulation developed so far is used for the evaluation of the L.H.S. and the R.H.S. of the BEM equations. Although Kutt type quadrature is not needed for the R.H.S. integrals, these integrals were evaluated along with the others to save computing time in calculating the many common variables. The *Composite Mapping* was implemented to the existing code with little change and the formulation was tested using the surface displacements formulation; the results are given in Table 3.3.

The $f(0)$ ln (b) term in Equation (3.17), named as the log term, was disregarded during the implementation as it was discovered that the contribution coming from the upper element cancelled the contribution from the lower element. This was due to the equally spaced elements used in the mesh. This will be discussed in more detail in section 3.4.2.

Table 3.3: External displacements using *Composite Mapping* and linear elements. (Analytical result is 0.2×10^{-5}m)

Node Number	Angle θ	Resultant Displacements / 10-5 m
1	9.00	0.200846
2	18.00	0.199172
3	36.00	0.199204
4	54.00	0.198847
5	72.00	0.198625
6	90.00	0.198552
7	108.00	0.198625
8	126.00	0.198847
9	144.00	0.199204
10	162.00	0.199172
11	171.00	0.200846

3.4 - QUADRATIC ELEMENTS

In this section, a solid sphere is discretized by using quadratic elements. By making use of these elements, the geometry can be modelled more accurately and a higher order of variation of the surface variables can be used to improve the accuracy of the solution.

The solution is only provided for the top half of the solid sphere because of the symmetry about the equator plane. However, as the axisymmetric formulation is not used in the present work, again, the whole sphere has to be discretized so that contributions to the system matrix coefficients are collected from the whole sphere. By placing source points only on the top half of the sphere, the number of unknowns is halved and the size of the system matrices is greatly reduced, leading to a more economical use of computer resources. Again, the singular integrals are evaluated using the *Composite Mapping* method and the rest are computed using the ordinary Gauss integration.

3.4.1 - Surface Displacements - equal elements

The basic BEM formulation for the surface displacements is the same as the one used in Equation (3.3). However, when the boundary is discretized using quadratic elements, the interpolation formula is based on the Lagrange's Interpolation method. For a quadratic variation of displacement v:

$$v = N_1 v_i + N_2 v_{i+1} + N_3 v_{i+2} \tag{3.29}$$

where N_1, N_2, and N_3, called the shape functions, are given by:

$$N_1 = \frac{(\theta - \theta_{i+1})\,(\theta - \theta_{i+2})}{(\theta_i - \theta_{i+1})\,(\theta_i - \theta_{i+2})} \tag{3.30}$$

$$N_2 = \frac{(\theta - \theta_i)\,(\theta - \theta_{i+2})}{(\theta_{i+1} - \theta_i)\,(\theta_{i+1} - \theta_{i+2})} \tag{3.31}$$

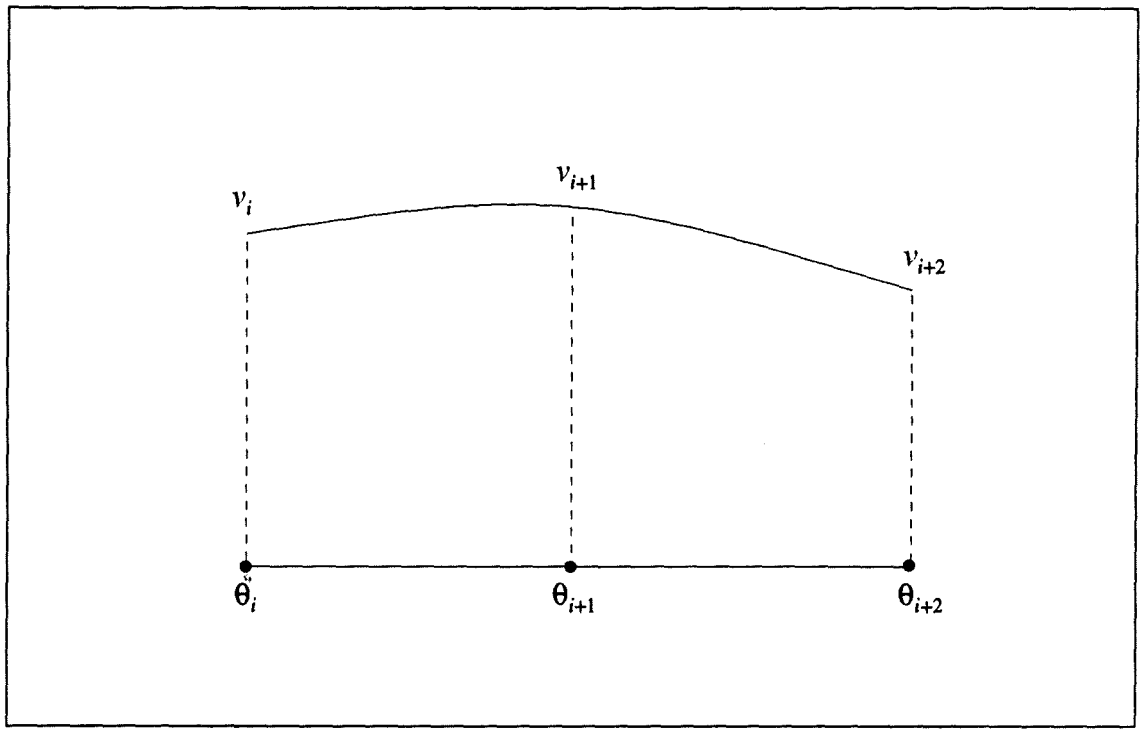

Figure 3.8: Parameters used in the quadratic element interpolation using Lagrange's interpolation formula and its shape functions.

$$N_3 = \frac{(\theta - \theta_i)\,(\theta - \theta_{i+1})}{(\theta_{i+2} - \theta_i)\,(\theta_{i+2} - \theta_{i+1})} \tag{3.32}$$

Equation (3.29) is substituted into Equation (3.5) and then simplified into a form similar to Equation (3.6), giving:

$$\frac{1}{2} v_1^i + v_1^j A_1 + v_1^{j+1} B_1 + v_1^{j+2} C_1 + v_3^j D_1 + v_3^{j+1} E_1 + v_3^{j+2} F_1 \tag{3.33}$$

As before, the integrals and other parameters are embedded in A_1, B_1, C_1, D_1, E_1 and F_1. The R.H.S. of the BEM equation (see Equation 3.1) is not affected by the change in the interpolation formula.

The outer nodes of the first element are both now placed on the ends of the element. i.e. the first node is placed on the north pole and is shared by all the pole elements around the x_3-axis; the same applies to the last element on the south pole of the sphere. It is worth noting here that the horizontal displacement component at the north pole node and the

vertical displacement component of the node placed on the equator plane are both zero. This is due to the symmetry.

System matrices are formed as given in Equation (3.9). The unknowns are then solved using the NAG routine F04ATF. The results were not as accurate as the previous formulation at the north pole. When coefficients of the A matrix were examined the a_{21} coefficient of the A matrix was found larger than the rest of the coefficients. Normally all the coefficients were found to be much less than 0.5, except the diagonal terms which have 0.5 added to them from the free term of the BEM equations. A value greater than 0.7 for a non-diagonal coefficient would therefore seem too high, and the first element was analysed for convergence. The integrations involving the Kutt quadrature give a single result at the end without any other information about the accuracy of this answer. So it was decided to check the integration result over the first element with the *Convergence Method*. The result of this analysis showed that the a_{21} coefficient, linking the horizontal and vertical displacements at the north pole node, was not converging to a finite value. However, as the horizontal displacement of the north pole node was zero, it was decided to exclude this from the system matrices. This meant that the first row and the first column of the A matrix were eliminated. This helped to overcome the problem of determining the a_{21} coefficient.

$$\begin{bmatrix} a_{1,1} & a_{1,2} & \cdots & a_{1,n-1} & a_{1,n} \\ a_{2,1} & a_{2,2} & \cdots & a_{2,n-1} & a_{2,n} \\ \vdots & \vdots & \cdots & \vdots & \vdots \\ a_{n-1,1} & a_{n-1,2} & \cdots & a_{n-1,n-1} & a_{n-1,n} \\ a_{n,1} & a_{n,2} & \cdots & a_{n,n-1} & a_{n,n} \end{bmatrix} \begin{Bmatrix} x_1 \\ x_2 \\ \vdots \\ x_{n-1} \\ x_n \end{Bmatrix} = \begin{Bmatrix} b_1 \\ b_2 \\ \vdots \\ b_{n-1} \\ b_n \end{Bmatrix} \tag{3.34}$$

Although it was not needed, the same procedure was applied to the vertical displacement of the node on the equator plane which eliminated the n-1 rows and the n-1 columns as shown below.

$$\begin{bmatrix} a_{1,1} & a_{1,2} & \cdots & a_{1,n-1} & a_{1,n} \\ a_{2,1} & a_{2,2} & \cdots & a_{2,n-1} & a_{2,n} \\ \vdots & \vdots & \cdots & \vdots & \vdots \\ a_{n-1,1} & a_{n-1,2} & \cdots & a_{n-1,n-1} & a_{n-1,n} \\ a_{n,1} & a_{n,2} & \cdots & a_{n,n-1} & a_{n,n} \end{bmatrix} \begin{Bmatrix} x_1 \\ x_2 \\ \vdots \\ x_{n-1} \\ x_n \end{Bmatrix} = \begin{Bmatrix} b_1 \\ b_2 \\ \vdots \\ b_{n-1} \\ b_n \end{Bmatrix} \tag{3.35}$$

The solution of the Equation (3.35) gave successful results and these are shown in Table 3.4 below. They were obtained using eight element divisions in the θ direction of the top half of the sphere and 15 segments in the φ direction.

Table 3.4: Surface displacements determined using quadratic elements (Theoretical value is 0.2×10^{-5}m).

Node Number	Angle θ	Resultant Displacements $/10^{-5}$m
1	0.00	0.200488
2	5.62	0.200127
3	11.25	0.199773
4	16.87	0.199732
5	22.50	0.199384
6	28.12	0.199506
7	33.75	0.199108
8	39.37	0.199350
9	45.00	0.198907
10	50.62	0.199239
11	56.25	0.198763
12	61.87	0.199162
13	67.50	0.198665
14	73.12	0.199113
15	78.75	0.198608
16	84.37	0.199089
17	90.00	0.198589

3.4.2 - Surface Displacements - unequal elements

Upto this stage, all the elements used in the mesh for the solid sphere have been of equal size. When elements of different sizes are to be used in the surface discretization, some fluctuations in the surface displacements are detected (see Karamanoglu et. al. 1991), whereas in the case of equally spaced elements, such inaccuracies do not occur.

This effect is examined in this section by considering a solid sphere, discretized using quadratic elements in two ways. The aim is to determine the surface displacements. In the first case, the mesh is made up of only equally spaced elements and in the second case, elements of various sizes are used to form the mesh. The results of the first case are listed in Table 3.4 on page 43 and are also illustrated in Figure 3.9. Figure 3.10 shows the integration scheme used for the singular element and the elements around it.

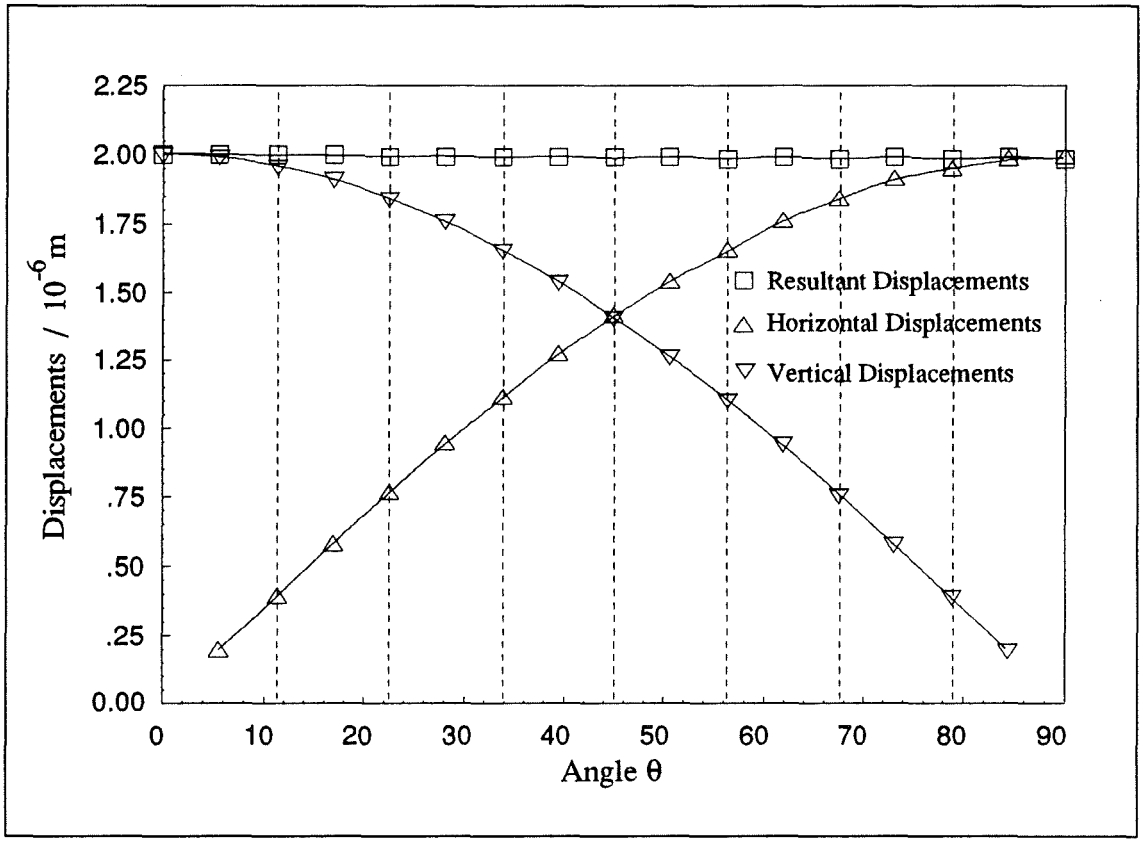

Figure 3.9: Surface displacements of equally spaced quadratic elements.

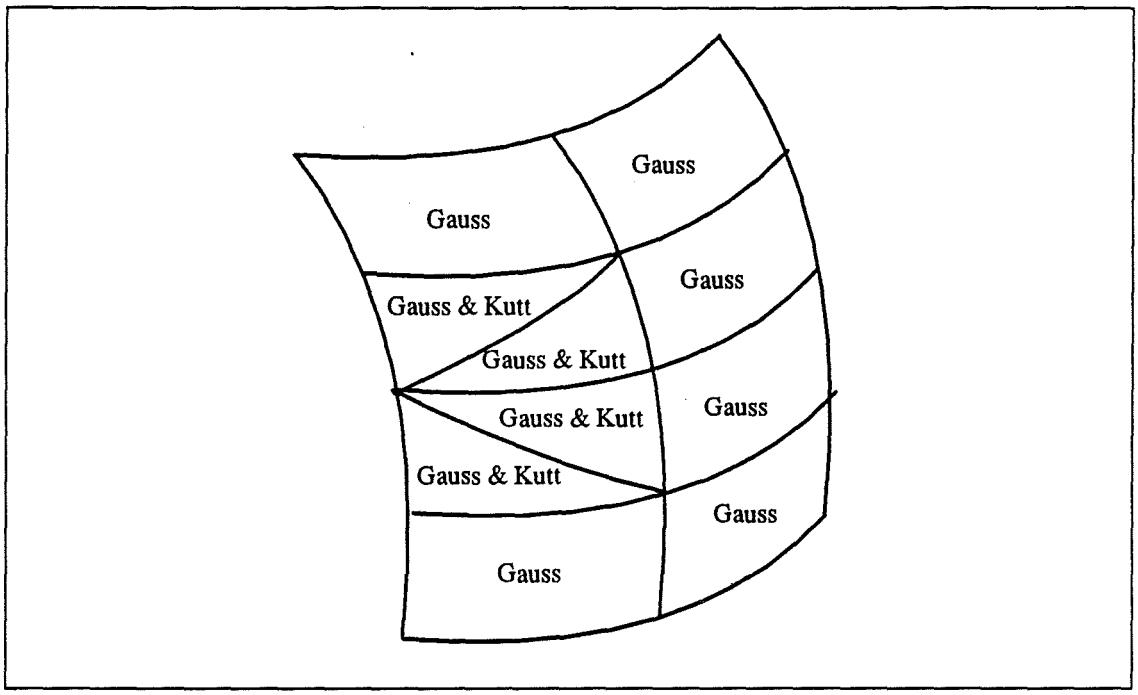

Figure 3.10: Integration scheme for equally spaced elements. No distortion in the results are observed.

Figure 3.11 shows the integration scheme used with different sizes of elements without having any special treatment. The inaccuracies in the displacements, caused by changing the element spacing, are given in Figure 3.12. This problem is solved by subdividing the

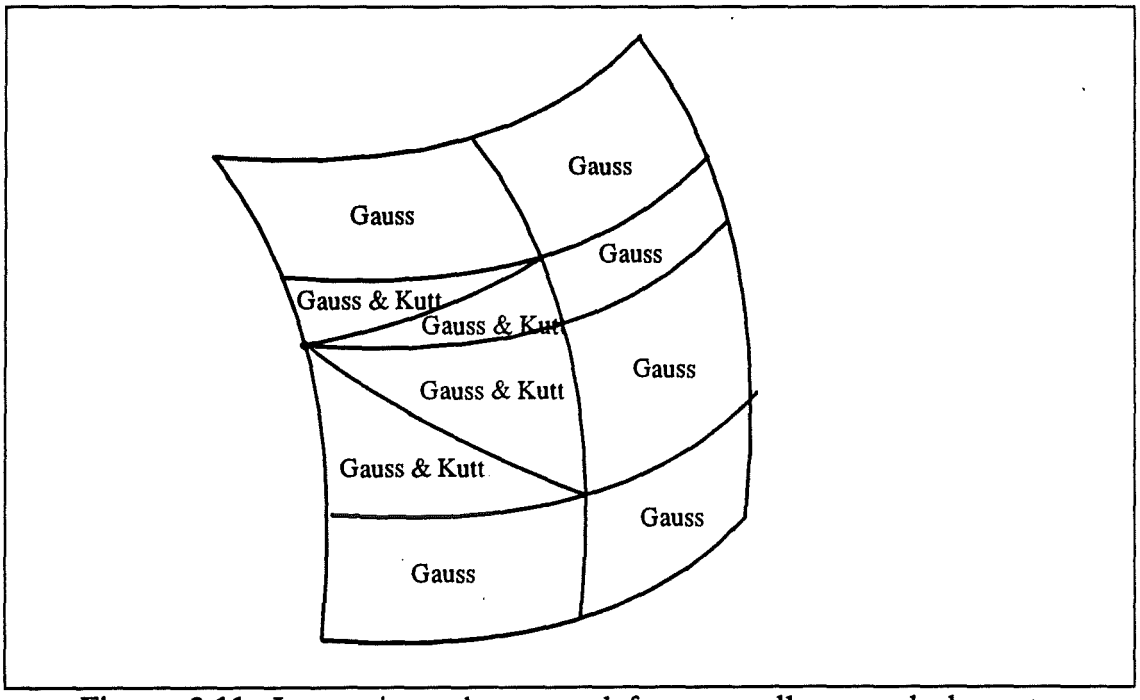

Figure 3.11: Integration scheme used for unequally spaced elements. Significant distortion in the results.

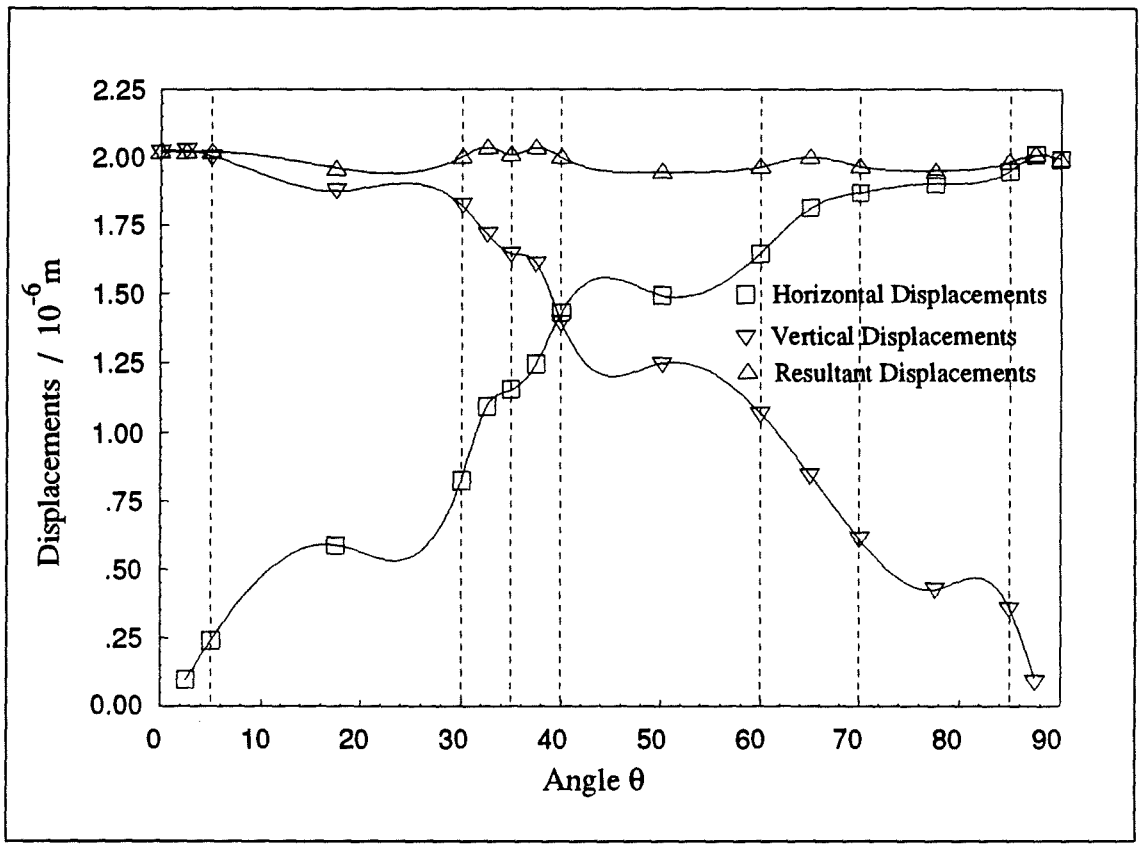

Figure 3.12: Surface displacements of unevenly distributed quadratic elements without element subdivisioning.

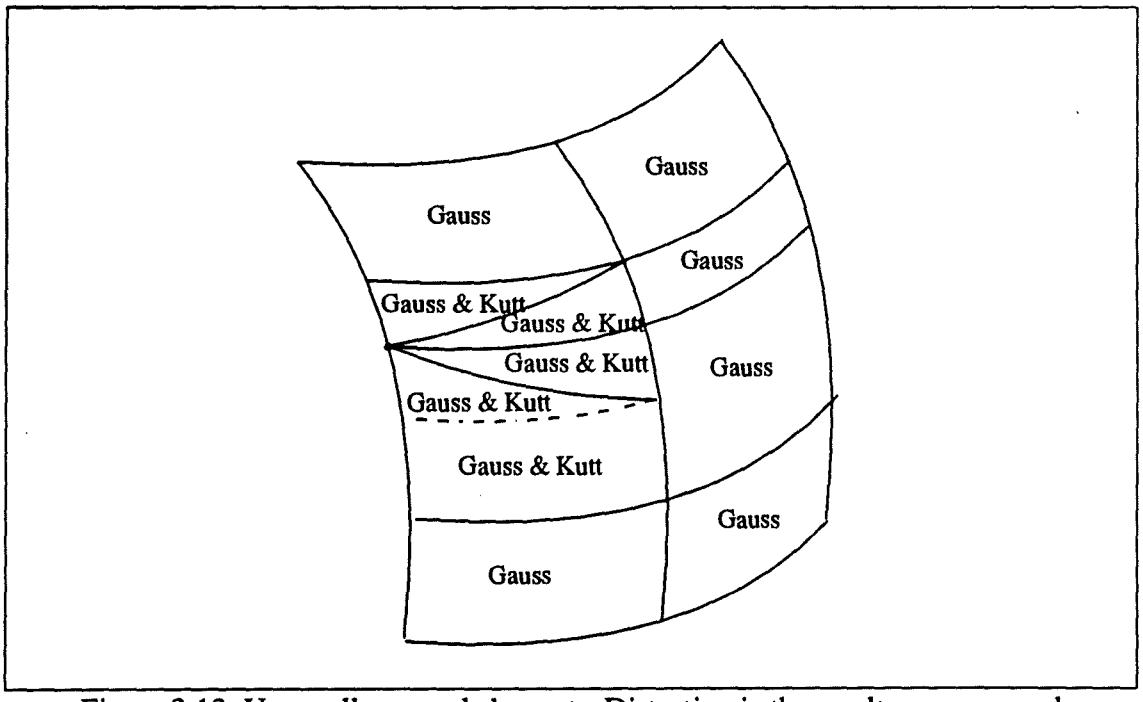

Figure 3.13: Unequally spaced elements. Distortion in the results are removed by the use of element subdivisioning.

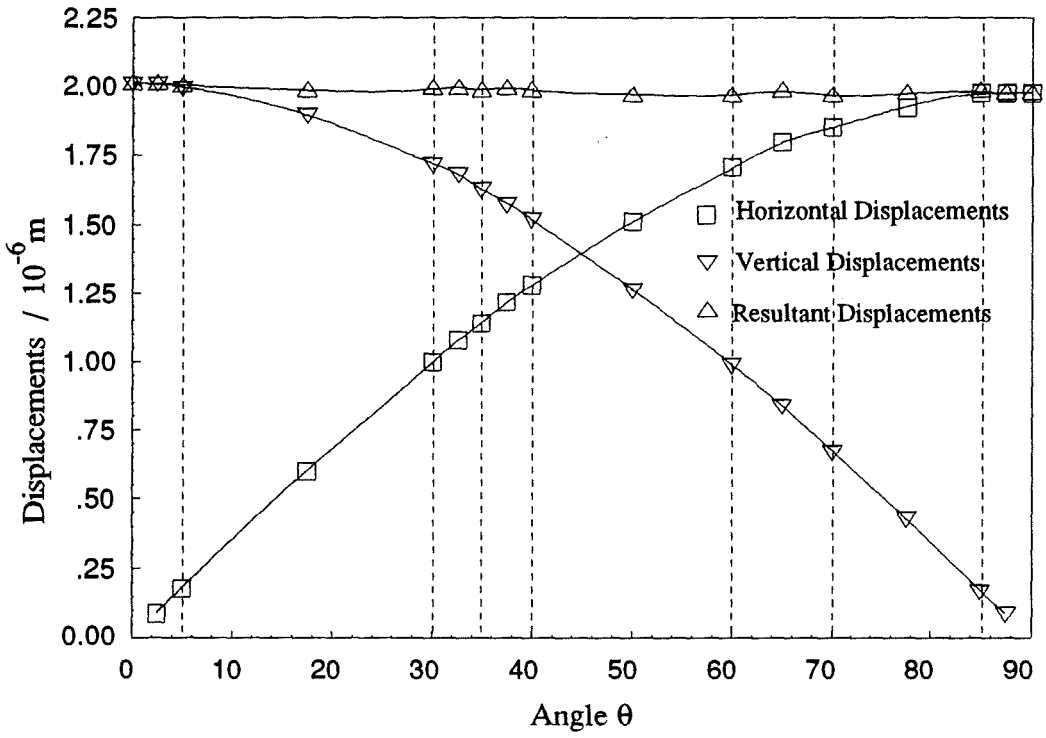

Figure 3.14: Surface displacements of unequally spaced quadratic elements with element subdivisioning. Fluctuations in the results are removed.

singular elements when the integration is performed. Before the integration of a singular element is carried out, the two adjacent elements are compared in size and if necessary they are made to be of equal size by dividing the longer element into two parts. The excess area is integrated using the ordinary Gauss quadrature and the integration over the singular area is evaluated by using the Composite Mapping method (see Figure 3.13). The results are improved considerably and are shown in Figure 3.14.

3.4.3 - Internal Displacements

The internal displacements using quadratic elements are calculated in a similar way to the linear element formulation. The only difference being the order of the interpolation formula used for the surface displacements. Again, Equation (2.53) is considered without any body forces and the transformations given in Equations (3.3) and (3.7) with the interpolation formula from Equation (3.29) are substituted into this equation. The final formula obtained for a horizontal displacement at point *i* is:

$$u_1^i = P_1 - \left[v_1^j A_1 + v_1^{j+1} B_1 + v_1^{j+2} C_1 + v_3^j D_1 + v_3^{j+1} E_1 + v_3^{j+2} F_1 \right] \tag{3.36}$$

When the above formulation is implemented, the results of internal displacements of the solid sphere is given in Table 3.5 (see Figure 3.15 for the plot of these results).

Table 3.5: Internal displacements using quadratic elements along $\theta = 45°$.

Node Number	Radius / m	Resultant / 10^{-5} m	Theoretical / 10^{-5} m	% Error
1	0.00	0.00000	0.00	0.00
2	0.10	0.01993	0.02	0.35
3	0.20	0.03989	0.04	0.27
4	0.30	0.05991	0.06	0.15
5	0.40	0.07993	0.08	0.09
6	0.50	0.09989	0.10	0.11
7	0.60	0.11979	0.12	0.18
8	0.70	0.13983	0.14	0.12
9	0.80	0.15976	0.16	0.15
10	0.90	0.17972	0.18	0.16
11	0.95	0.18968	0.19	0.17
12	0.96	0.19166	0.192	0.18
13	0.97	0.19365	0.194	0.18
14	0.98	0.19563	0.196	0.19
15	0.99	0.19761	0.198	0.20
16	0.992	0.19802	0.1984	0.19
17	0.994	0.19838	0.1988	0.21
18	0.996	0.19824	0.1992	0.48
19	0.997	0.19855	0.1994	0.43
20	0.998	0.20361	0.1996	2.01
21	0.999	0.21301	0.1998	6.61
22	0.9995	0.16804	0.1999	15.94
23	0.9999	0.10841	0.19998	45.79

As the internal point approaches the surface, the results begin to deteriorate until finally the computer code fails if continued. The reason for this is that as the internal point, being the source point, approaches the surface, the distance between the source point and the field point (i.e. the integration point over the surface element) becomes minimal: this distance is the r term referred to in the BEM formulation. Figure 3.15 shows the effects of this limitation. The main contributors of the inaccuracies in these results are the strongly singular traction kernels, p^*_{lk}, given by Equation (2.23). Higher orders of quadrature will improve these results but with corresponding increase of CPU time.

In practical situations, the results for the internal points can be determined at a reasonably close distance to the surface and, since the surface results are already known, the limitation presented here should only be a major concern in the presence of large variations of the displacements. The determination of results very close to the surface are more important for the stresses than for the displacements; this will be discussed in section 3.4.4.

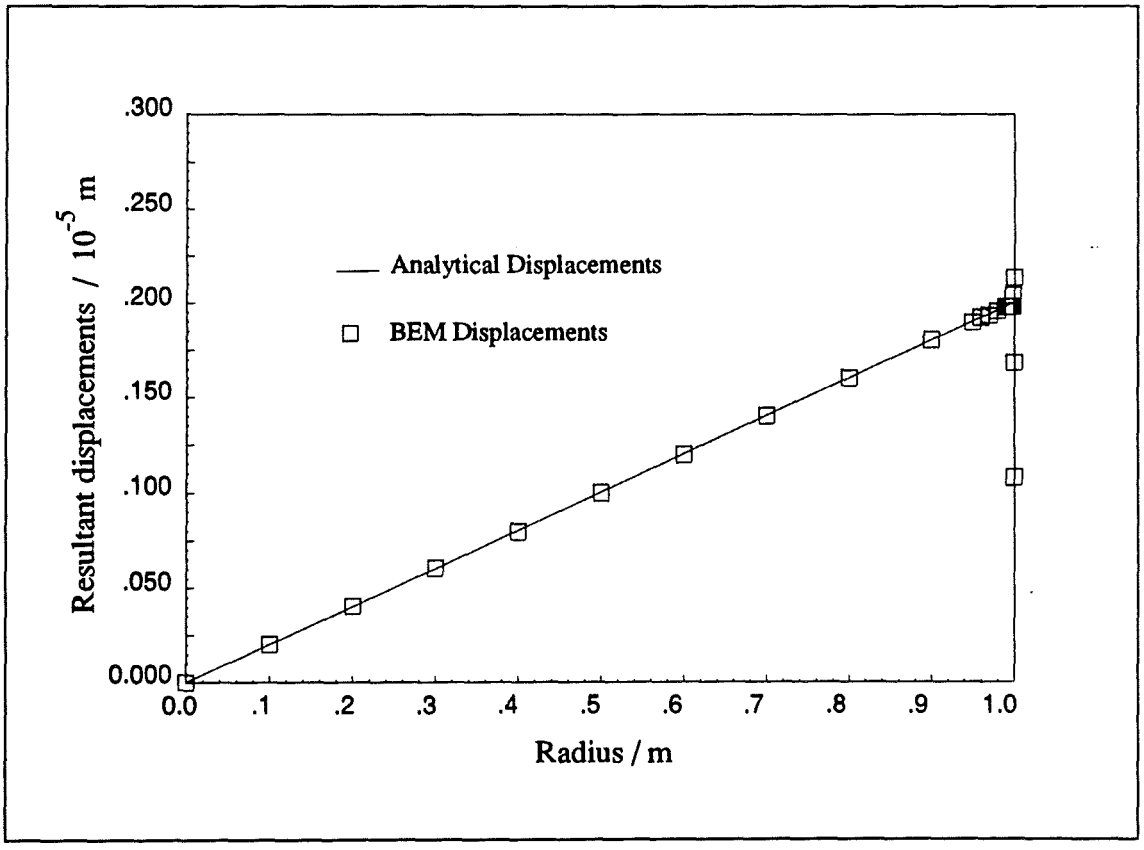

Figure 3.15: Internal displacements of a solid sphere along the path $\theta = 45°$.

3.4.4 - Internal Stresses

The evaluation of the internal stresses using quadratic elements for the discretization is very similar to the analysis shown in section 3.2.4. The only difference is the use of a quadratic variation for the surface displacements. If Equation (3.14) is considered for the analysis, substitution of the transformations given in Equations (3.2), (3.7) and the interpolation formula given in Equation (3.29), results in the following:

$$\sigma_{ij} = P_{ij} - \left[v_1^j A_{ij} + v_1^{j+1} B_{ij} + v_1^{j+2} C_{ij} + v_3^j D_{ij} + v_3^{j+1} E_{ij} + v_3^{j+2} F_{ij} \right] \tag{3.29}$$

Table 3.6: Internal stresses along θ= 0° for a solid sphere using quadratic elements.

Node Number	Radius m	Internal Stresses /MN/m^2		
		σ_{11}	σ_{22}	σ_{33}
1	0.00	0.9957250	0.9957250	0.9977682
2	0.10	0.9957318	0.9957318	0.9978293
3	0.20	0.9957674	0.9957674	0.9979945
4	0.30	0.9958719	0.9958719	0.9982162
5	0.40	0.9960909	0.9960909	0.9984458
6	0.50	0.9964418	0.9964418	0.9986991
7	0.60	0.9968814	0.9968814	0.9991720
8	0.70	0.9973623	0.9973623	1.0000363
9	0.80	0.9982047	0.9982047	1.0031072
10	0.90	1.0015550	1.0055501	1.0086613
11	0.95	1.0073561	1.0073561	1.0133601
12	0.96	1.0095420	1.0095422	1.0145341
13	0.97	1.012795	1.012795	1.0147891
14	0.98	1.002526	1.002526	1.0541050
15	0.99	1.420579	1.420579	-0.1613575
16	0.999	0.3409153	0.3409153	-186.10520

The values obtained from Equation (3.37) are given in Table 3.6. Notice that the values obtained for distances over 0.98m gave unacceptable results. With the internal displacements, it was found to be possible to get accurate results with less than 1% error at 0.997m, whereas for the internal stresses this value is much less. This shows the significance of the order of the singularity present in the BEM formulation.

At this stage, minimising the CPU time was not the main concern and the results given in Table 3.6 were obtained using equally spaced elements and Gauss quadrature of order 8. Initially a fixed order of integration was used to compare the values obtained along $\theta = 0°$, 45°, and 90°. Surprisingly, even though double precision arithmetic is used throughout the computer code, the three tests produced results with different accuracies. The most accurate results were obtained along $\theta = 0°$. This could be due to the cumulative numerical errors that may be produced in the evaluation of the large number of trigonometric functions.

The use of BEM in this way for stresses very close to the surface does not seem practical as large quadrature orders are required and the results may not be of acceptable accuracy. The surface stresses may not be calculated using the formulation given in this section due to the singular nature of the BEM equations. However, it is still possible to calculate the surface stresses using the surface displacements: this will be shown in chapter 6.

Chapter

4

BEM For A Hemisphere

"Reading after a certain age diverts the mind too much from its creative pursuits. Any man who reads too much and uses his own brain too little falls into lazy habits of thinking."

Albert Einstein

1931

4.1 - INTRODUCTION

In this chapter, the BEM analysis is implemented on a hemisphere to investigate the problems associated with solids with multiple surfaces and sharp corners and/or edges. A hemisphere is well suited for this work for the following reasons:

- It follows all the work presented in the previous chapters.
- Geometry is one step closer to the selected cone shape for the final analysis.
- The geometry has a sharp edge so that the problems associated with this can be identified, which also will affect the analysis of the cone.
- The analytical results are already known from Chapter 3.

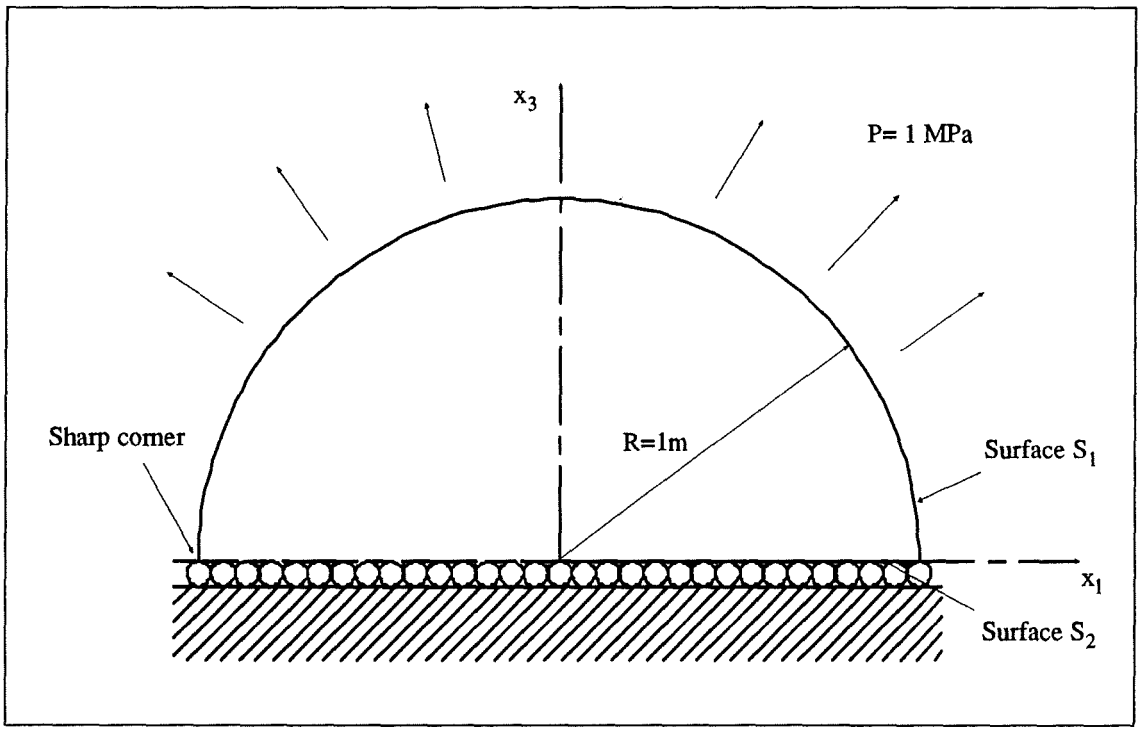

Figure 4.1: Boundary conditions for the hemisphere used for the analysis.

The hemisphere selected has a radius of 1 metre and is subjected to an external uniform outwards pressure of 1 MPa. The base is restrained in the x_3 direction and is free to move in the x_1 and x_2 directions as shown in Figure 4.1.

4.2 - BEM IMPLEMENTATION

The BEM formulation to be developed in this section takes into account the two surfaces, S_1 and S_2. The basic formulation is the same as before, but integral equations are written for both surfaces. The BEM equation for the horizontal component of the external displacements on the hemisphere is:

$$\frac{1}{2}u_1^i + \int_{S_1}(u_1p_{11}^* + u_2p_{12}^* + u_3p_{13}^*)\,R_j^2\sin\theta d\theta d\varphi + \int_{S_2}(u_1p_{11}^* + u_2p_{12}^* + u_3p_{13}^*)\,\rho d\rho d\varphi$$

$$= \int_{S_1}(w_{11}p_1 + w_{12}p_2 + w_{13}p_3)R_j^2\sin\theta d\theta d\varphi + \int_{S_2}(w_{11}\hat{p}_1 + w_{12}\hat{p}_2 + w_{13}\hat{p}_3)\,\rho d\rho d\varphi \quad (4.1)$$

However, the base of the hemisphere is restrained in x_3 direction and therefore the u_3 displacements on S_2 are zero. There are no tractions acting in the horizontal directions on the base. The only traction on S_2 is $\hat{p}_3$ and is distinguished from the p_3 on S_1 by the ^ symbol. By taking these conditions into account, the fact that the tractions on S_2 are unknown, it is best to rewrite Equation (4.1) as follows:

$$\begin{aligned}
&\frac{1}{2}u_1^i + \int_{S_1} (u_1 p_{11}^* + u_2 p_{12}^* + u_3 p_{13}^*)\, R_j^2 \sin\theta d\theta d\varphi \\
&\quad + \int_{S_2} (u_1 p_{11}^* + u_2 p_{12}^*)\, \rho d\rho d\varphi - \int_{S_2} w_{13}\hat{p}_3\, \rho d\rho d\varphi \\
&\quad = \int_{S_1} (w_{11}p_1 + w_{12}p_2 + w_{13}p_3) R_j^2 \sin\theta d\theta d\varphi
\end{aligned} \tag{4.2}$$

On surface S_2, the integration is done with respect to the radius ρ and the angle φ since the angle θ is constant at $\frac{\pi}{2}$. The transformation given in Equation (3.2) is substituted into Equation (4.2). The boundary is discretized using quadratic elements and therefore, the interpolation formula given in Equation (3.29) is used. The shape functions N_1, N_2 and N_3 are the same as given in Equations (3.30), (3.31) and (3.32) for the S_1 integrals, but for the S_2 integrals they are:

$$N_1 = \frac{(\rho - \rho_{i+1})(\rho - \rho_{i+2})}{(\rho_i - \rho_{i+1})(\rho_i - \rho_{i+2})} \tag{4.3}$$

$$N_2 = \frac{(\rho - \rho_i)(\rho - \rho_{i+2})}{(\rho_{i+1} - \rho_i)(\rho_{i+1} - \rho_{i+2})} \tag{4.4}$$

$$N_3 = \frac{(\rho - \rho_i)(\rho - \rho_{i+1})}{(\rho_{i+2} - \rho_i)(\rho_{i+2} - \rho_{i+1})} \tag{4.5}$$

The R.H.S. of Equation (4.2) is identical to the one used for the solid sphere and again the surface tractions on S_1 are written in terms of the surface pressure by using the relationships given in Equation (3.7). The final equation is written in a matrix form as before and since all the unknowns are on the L.H.S. and all the knowns are on the R.H.S. of Equation (4.2), the form $\mathbf{A}\,\mathbf{x} = \mathbf{b}$ is obtained. Only this time the unknown vector $\mathbf{x}$ holds the surface displacements u_1 and u_3 for the S_1 surface and u_1 displacements and $\hat{p}_3$ tractions for the S_2 surface. The A matrix is partitioned to hold the coefficients from the integration of both surfaces. Since the vertical displacements on the surface S_2 are zero, the $\frac{1}{2}$ term of the BEM equation is excluded from the diagonal coefficients of the A matrix for the rows that are used for the u_3 component of the displacement.

4.3 - PROBLEMS WITH CORNERS

One of the weaknesses in the BEM is the difficulty in dealing with geometries with sharp corners and edges. This is caused by the discontinuities in the geometry and the boundary conditions. For an elasticity problem, the displacements are uniquely defined but the surface tractions are multivalued at a corner node. This means that there are more unknowns than the number of equations available and the solution is not possible. This requires other approaches for the solutions involving corners and/or edges, and is normally referred to as *the corner problems* in the BEM.

4.3.1 - Previous Work

One obvious way to solve *the corner problems* is to round off the edges and corners (Banerjee et. al., 1981). This approach inevitably produces reasonable results away from the edges and the corners but introduces local errors. This method cannot be considered a satisfactory solution to the problem since in some cases the results at the edges and the corners can be a vital part of the solution.

Ricardella (1973), introduced the multiple independent node concept. For a two-dimensional problem, an extra node is introduced to avoid the ambiguities in the definition of the surface normal and the boundary conditions. In three-dimensional problems, two additional nodes are introduced. This also provided the extra equations needed for the solution of the system matrix. The problem with this method is that, unless a "sufficient" gap is left between the corner nodes, the system matrix will be singular due to the very similar rows of coefficients obtained for the corner nodes.

Another way to circumvent this problem when a displacement is specified at a corner is to assume that the corresponding multivalued tractions are equal. This approach was adopted by Lachat (1975) who found that the accuracy of results at points some distance away from the corner are not significantly affected.

The multiple node concept was further studied by Chaudonneret (1978) who let the multiple nodes at the corner share the same location. To avoid the singular solution of the system matrix, two auxiliary equations are derived for each of the corner nodes using the symmetry of the stress tensor and the invariance of the trace of the strain tensor. For a two-dimensional case, there would be two equations and four unknowns. Of the two additional equations, one of them can be obtained using the symmetry of the stress tensor and the other, using the invariance of the trace of the strain tensor. Using the auxiliary equations derived, it would be possible to eliminate one set of the tractions and convert the problem into a well-posed one. Similar analysis is applied to three-dimensional problems by using a triple point at the corner to represent the traction discontinuities.

4.3.2 - Use of the Double Node Concept

The problem associated with the corners for the hemisphere is tackled with a concept similar to the one introduced by Ricardella. The boundary is discretized with conforming quadratic elements. Due to the symmetry, the surface displacements in the x_2 direction are not calculated. Like the solid sphere in Chapter 3, the source points are distributed along

a path where angle $\varphi = 0°$. This path is made of two surfaces, S_1 and S_2. Both these surfaces are divided equally into 5 elements with quadratic variation (Figure 4.2). The whole boundary is also discretized in φ direction by 20 equally spaced segments around the x_3 axis. The two elements forming the sharp corner have their outer node on the corner. The element belonging to the S_1 surface has u_1 and u_3 displacements as unknowns on its corner node, whereas the corner node of the element belonging to S_2 has the unknowns u_1 and $\hat{p}_3$. If the system matrix A is formed using this discretization as it is, two similar rows will be obtained for the u_1 displacements at the corner nodes, and this will result in a singular matrix. To avoid this, the row associated with the u_3 displacement on node 11, and the row associated with the u_1 displacement on node 12 are removed from the A matrix. In practice, this does not produce any problems as the u_3 displacement at the corner node 11 is zero and the u_1 displacement must be the same at nodes 11 and 12.

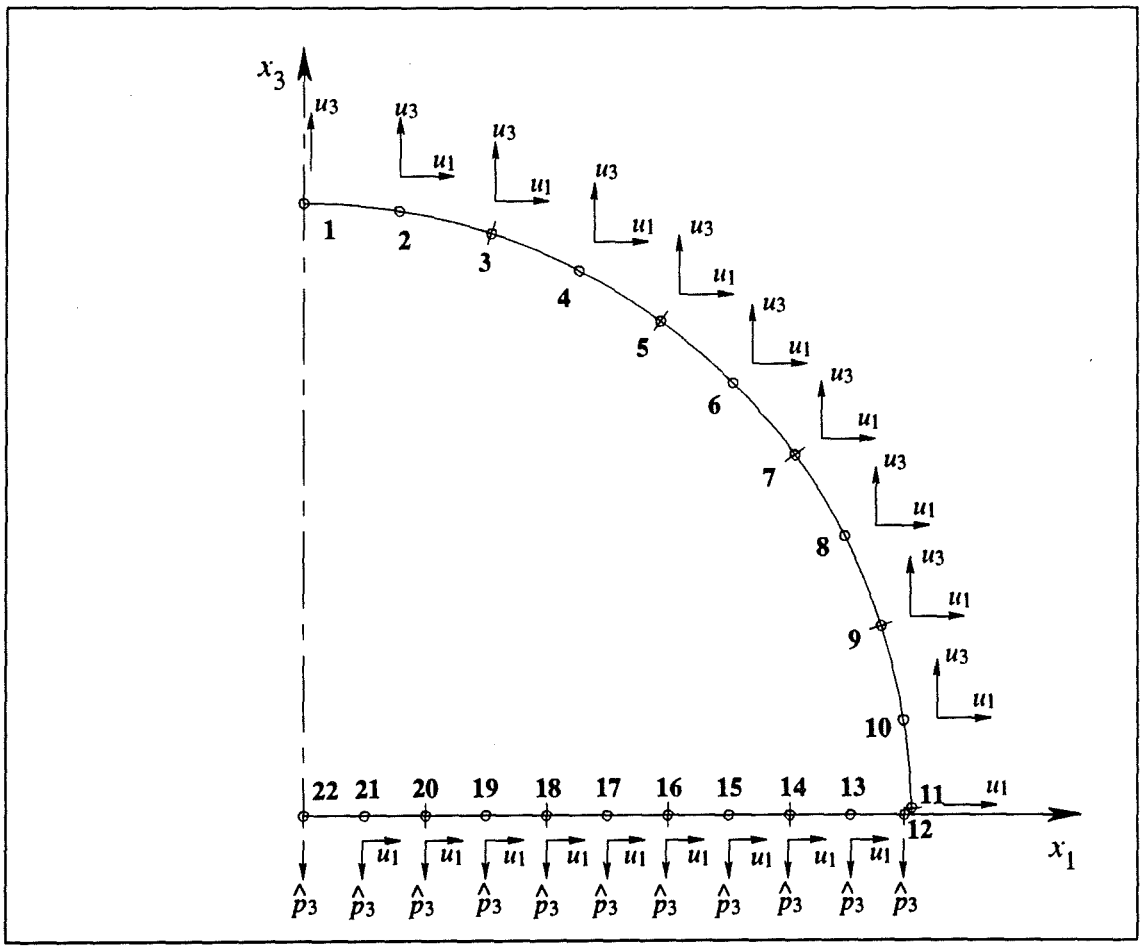

Figure 4.2: Descretization used for the hemisphere.

4.4 - PROBLEMS WITH INTEGRATION

The procedures for the numerical integration developed so far are not sufficient to evaluate all the integrals over the hemisphere. The additional problems that were come across are detailed in the next two sections.

4.4.1 - Integration of the Corner Elements

In Chapter 3, it is shown that maintaining the size of two adjacent elements equal in the presence of a singularity is essential for the integration purposes. For this reason, care should be taken when dealing with the two elements on the corner. For the integrals involving these corner elements, a special routine is developed for the case when the source point is on one of the two corner nodes. The difficulty is the dissimilar shape of the two corner elements for the element length comparison. Ideally, the two elements should be integrated and their contributions added together. Because of the geometry limitation, a Kutt type of integration cannot be applied to the flat corner element which is on the base surface, S_2.

An alternative is to use the *Convergence Method.* As shown in Chapter 3, this method can be used to deal with unequally spaced elements by comparing the angle θ if the elements concerned are on the S_1 surface. However, as one of the elements is on S_2 surface, comparison of the element size cannot be made by using just this angle. So, for the element on S_2, the base radius has to be used to determine the element length and to compare this with the arc length of the adjacent element which is on S_1 surface. The element with the longer side is divided so that two elements with identical lengths are obtained. The excess area is integrated using the ordinary Gauss quadrature and the other areas are integrated using the *Convergence Method.*

However, as the u_3 displacement on the corner node and on the S_2 surface is zero, some of the coefficients become zero. This helps to simplify the convergence procedure as there

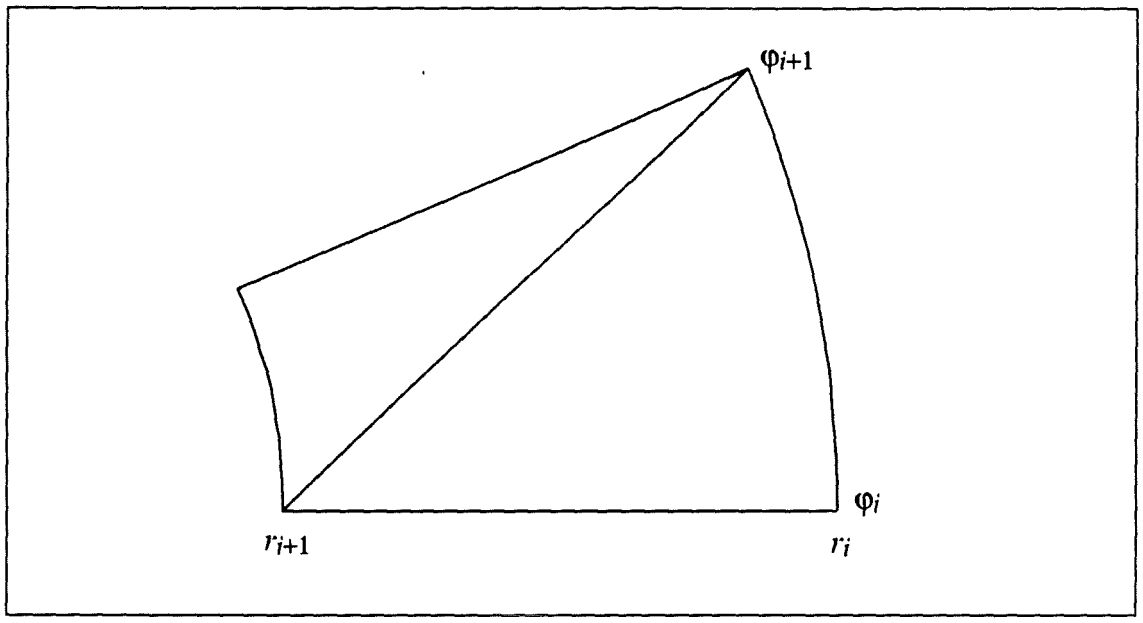

Figure 4.3: Limitation on the Kutt integration for the S_2 elements.

would be fewer terms to check for convergence. Because of these diminishing and somewhat redundant coefficients, it was possible to use the ordinary Gauss integration method to evaluate the integrals over the corner elements. To check the validity of this assumption, comparison with the *Convergence Method* is made for both of the corner elements. As expected, very similar results are obtained from both methods. The testing was then extended to see the effect of using these two different integration procedures for the corner elements on the surface displacements and tractions. The results are given in section 4.5.

4.4.2 - Integration Over the Base Elements

The integrals over the singular elements on the S_2 surface could not be evaluated using the *Composite Mapping* method. The restriction is that when the rectangular elements are divided across their diagonal into two triangular elements, one of the sides of the triangular area is always curvilinear (see Figure 4.3) and this is not suitable for the Kutt integration. Therefore, a convergence type integration procedure is developed for these elements. When

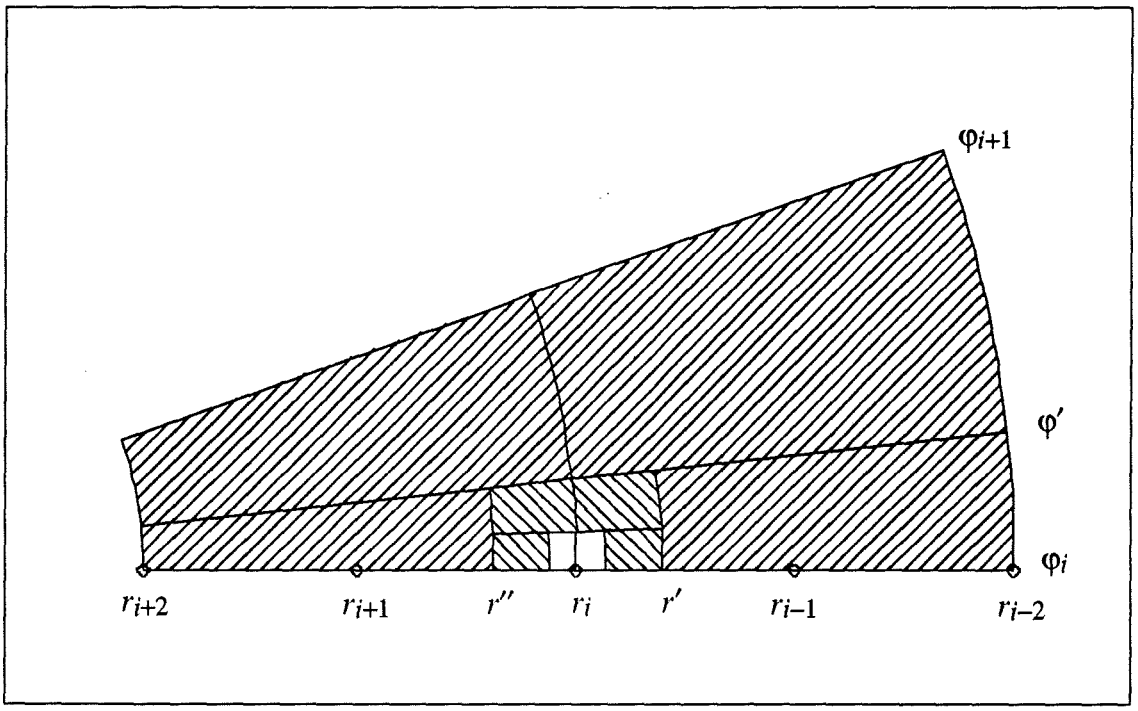

Figure 4.4: Convergence Method used for the elements on the S_2 surface.

the source point is shared by two adjacent elements which are both on the S_2 surface, the size of the radial lengths of these elements are checked and if necessary, the longer element is made the same size as the neighbouring element by partitioning it and then the integration is performed over the small areas and added together. Further division is continued until the cumulative sum of all the coefficients are converged within a predetermined tolerance of $\leq 1\%$. The mesh used for the base surface is made of only equally spaced elements and therefore, element length comparison was not necessary. As a result, element subdivisioning, such as the one shown in Figure 4.4, is used. The same procedure is also used for the case when the source point is on the midside node.

As in the S_1 surface, all the integrations that involved singularities on surface S_2 have been evaluated using one half of the singular element and then the result doubled to give the total result over the whole element.

One exception where the previously described convergence type integration method is not suitable is the central element of the S_2 surface. In this case a modified convergence method is used where the division of the surface element is only done in the radial direction. The

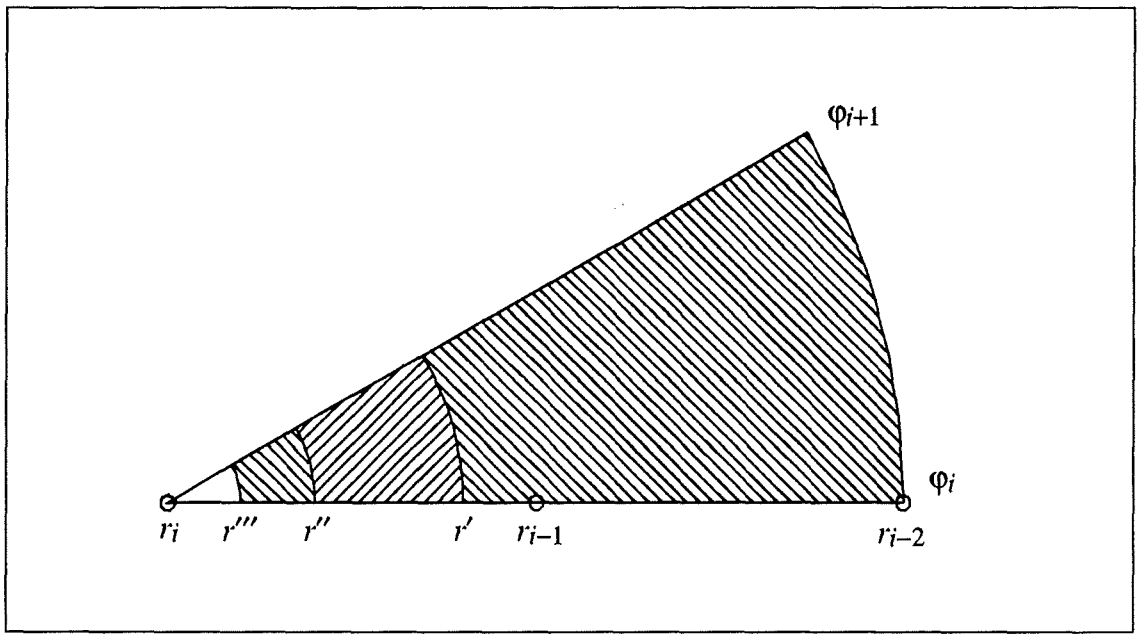

Figure 4.5: Integration scheme used for the central element of the S_2 surface (Drawing not to scale).

The integrated area rapidly converges towards the central origin of the base surface as the divisioning factor is set to 10 (see Figure 4.5).

4.5 - RESULTS

The following results are obtained using 5 element divisions on the S_1 path and 4 element divisions on the S_2 path. The number of segments created around the x_3 axis is 20. Although the expectancy of local errors has been reported by other researchers previously, it is intended to see which integration method for the corner elements would result in a more accurate solution. These results are also used to see the effect of using the double node concept on the corner elements and how much local error this will introduce.

The comparisons are made for the resultant displacements on surfaces S_1 and S_2 and also the tractions on the S_2 surface. Two methods of integration are used for the corner elements:

- Gauss integration without any element subdivision
- Gauss integration with element subdivision (Convergence Method)

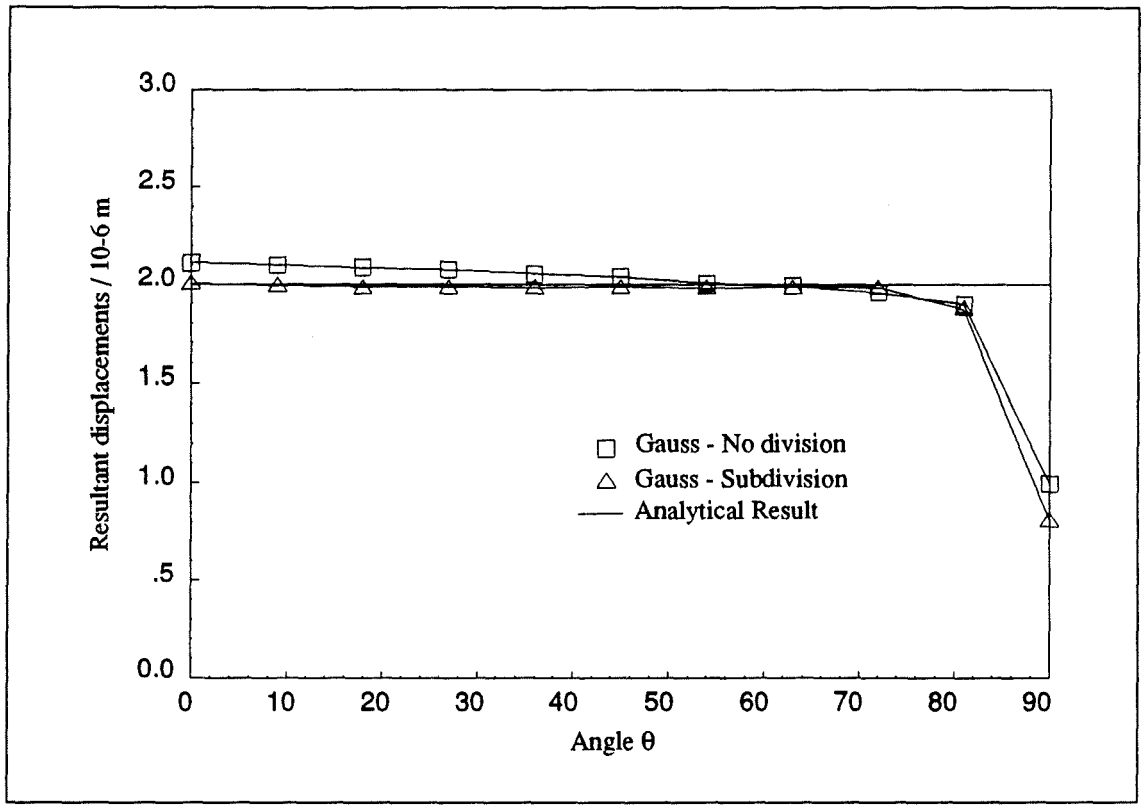

Figure 4.6: Comparison of the resultant displacements on surface S_1.

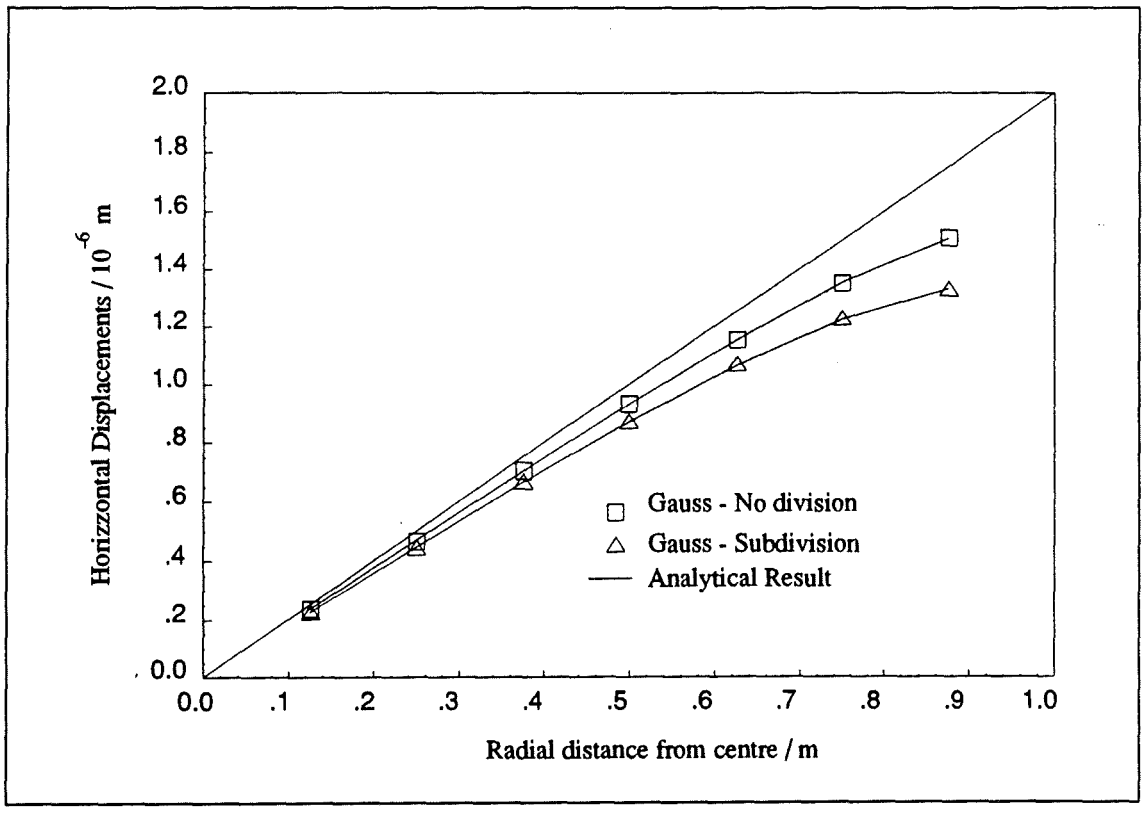

Figure 4.7: Comparison of the horizontal displacements on surface S_2.

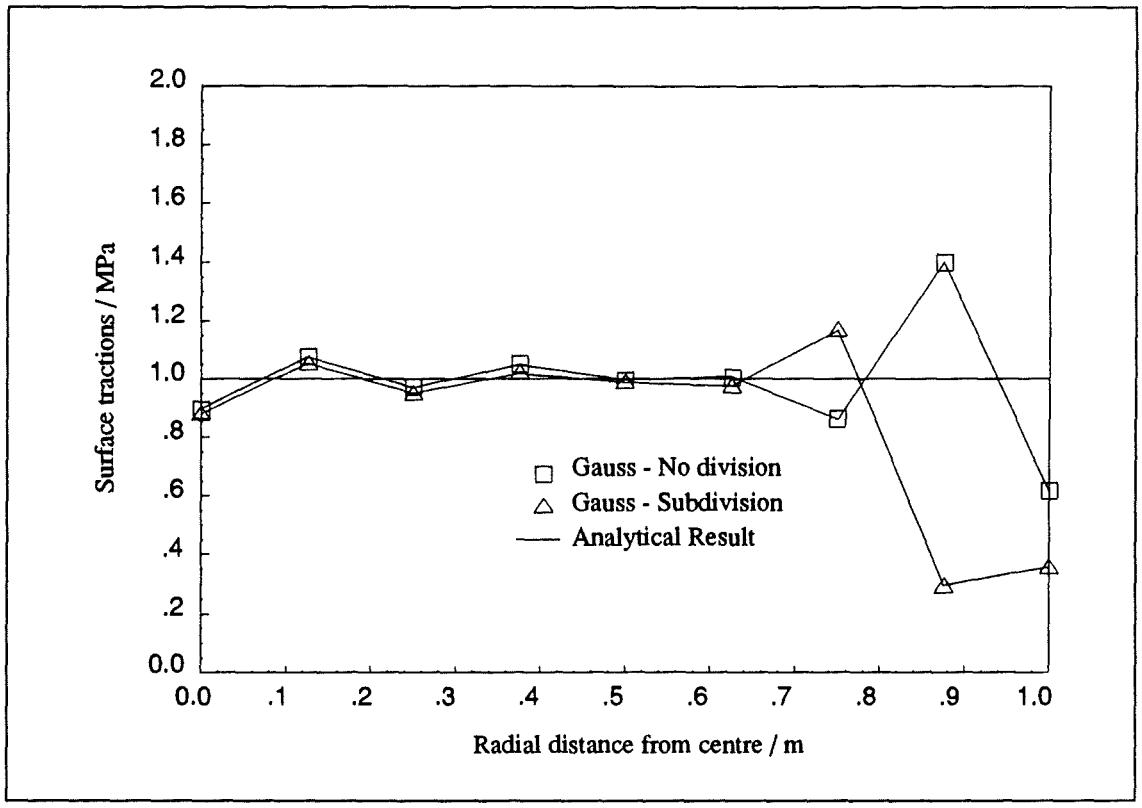

Figure 4.8: Comparison of surface tractions on S_2 using a different integration scheme and double node concept for the corner elements.

In Figures 4.6, 4.7 and 4.8, comparison of surface unknowns are made. The results obtained using the two different integration methods for the corner elements (Gauss integration with element subdivisioning and Gauss integration without any element subdivisioning) are compared against the analytical result. Both integration methods gave very poor results at the corner element nodes. However, the errors around the corner are not so pronounced at the other elements.

If the results other than the ones on the corner elements are considered, the two different integration methods do not have any significant variations in the other results. Therefore, the use of normal Gauss integration on the corner elements produces just as good results as the case where a convergence type of integration is employed. Having said that, it should be remembered that this is only due to the convenient type of boundary conditions present on the S_2 surface. Otherwise, a convergence method should be used to avoid any possible singularity problems.

The results produced for the corner elements are not at all suitable for the purpose of the work presented in this thesis. Therefore, alternative ways of getting around the problem of local errors introduced at the corners are required. This problem will be further discussed in Chapter 5 using a hollow sphere where the path defining the source points will have two corners; inner and outer.

Chapter

5

BEM For A Hollow Sphere

"When a distinguished elderly scientist says something is possible, he is probably right; when he says something is impossible he is probably wrong"

Arthur C. Clarke

1969

5.1 INTRODUCTION

This chapter concentrates on finding an alternative method to those suggested in Chapter 4, concerning the problems associated with the corners and edges and to look at the limitations of having long and slender geometries in BEM analysis.

Initially, a thick walled hollow sphere is considered to look at the corner problems. The selection of a thick wall is to avoid any problems that may be caused by having a thin and long structure.

Having completed the appropriate treatment of corners and edges, attention is paid to long and slender structures. Previous research suggests that serious problems arise when dealing with structures of such geometry (Bakr 1983, Brebbia & Dominguez 1989, Brebbia &

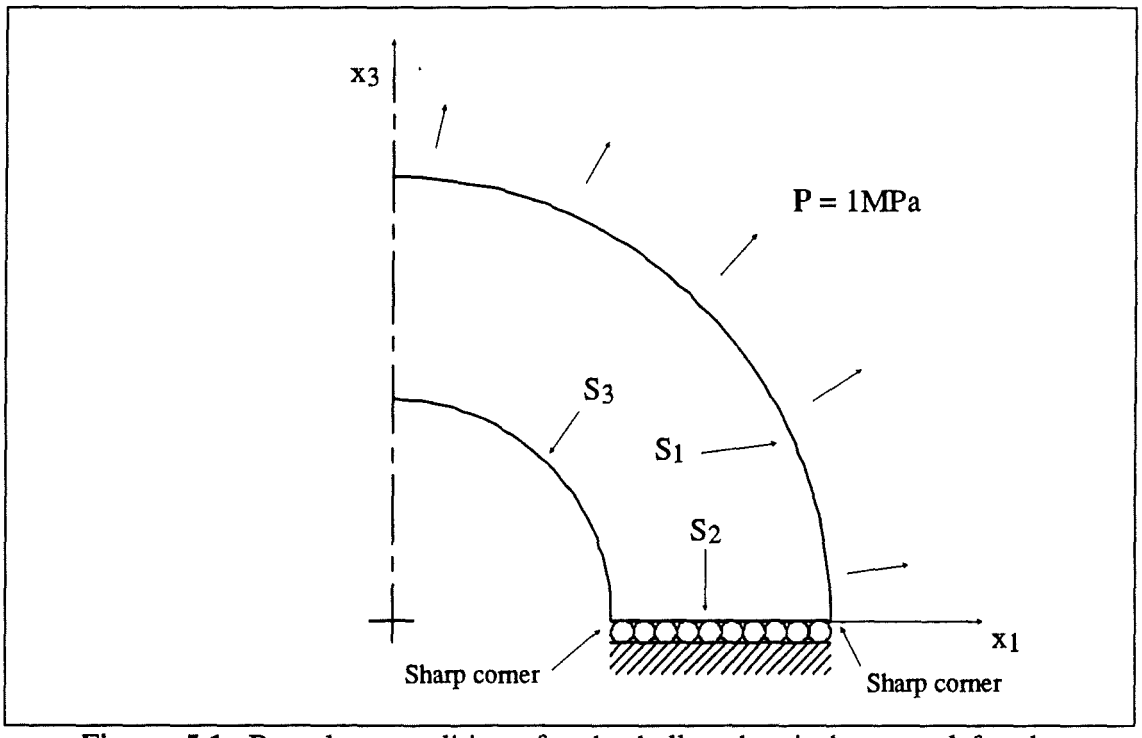

Figure 5.1: Boundary conditions for the hollow hemisphere used for the analysis.

Walker 1980). Problems of this kind are not unique to BEM and they also appear in FEM applications where the structure under consideration involves elements with a large aspect ratio (Cook et. al. 1989). The selected thick hollow sphere has an internal radius of 0.5m and an outer radius of 1.0m. The applied boundary conditions are shown in Figure 5.1.

5.2 BEM IMPLEMENTATION OF A HOLLOW SPHERE

The BEM formulation for the hollow sphere is similar to the one used for the hemisphere in Chapter 4. In this case, there is one more surface to consider in order to take into account the inner surface, S_3. Note that the axis of symmetry is not discretized. As in Chapter 4, the BEM equation for the horizontal component of the surface displacements can be written by considering the formulation derived in Chapter 2. The formulation is very similar to the one used in Equation (4.2), but extra terms are required to cover the inner surface. These are the integrals concerning the surface displacement fields and the surface tractions. On the inner surface the surface tractions are zero as there is no applied pressure, so this term

is absent from the formulation. Once these terms are added on, the BEM equation for the hollow sphere is ready and is given in Equation (5.1).

$$\begin{aligned}
&\frac{1}{2}u_1^i + \int_{S_1} (u_1 p_{11}^* + u_2 p_{12}^* + u_3 p_{13}^*)\, R_j^2 \sin\theta d\theta d\varphi \\
&+ \int_{S_2} (u_1 p_{11}^* + u_2 p_{12}^*)\, \rho d\rho d\varphi - \int_{S_2} w_{13} \hat{p}_3\, \rho d\rho d\varphi \\
&+ \int_{S_3} (u_1 p_{11}^* + u_2 p_{12}^* + u_3 p_{13}^*)\, R_j^2 \sin\theta d\theta d\varphi \\
&= \int_{S_1} (w_{11} p_1 + w_{12} p_2 + w_{13} p_3) R_j^2 \sin\theta d\theta d\varphi
\end{aligned} \tag{5.1}$$

The implementation of the Equation (5.1) is almost identical to the case of hemisphere with the exception of considering two corners. Again all the unknown terms are on the L.H.S. and all the known terms are on the R.H.S. The same transformations and interpolation functions are used as given in Equations (3.2), (3.29 - 3.32) and (4.3 - 4.5) and are substituted into Equation (5.1). This leads to a system of equations that are easily written in the form of **A x = b** . As before, the vector **x** holds mixed surface unknowns.

5.3 RESULTS OF A THICK WALLED SPHERE

5.3.1 - Analytical Formulation

Theoretical analysis of a thick walled sphere can be found in a book by Prescot (1961). The general formulae for a thick sphere with an inner and outer radii a and b, and the pressures on the inner and outer surfaces p and q is given as:

$$\sigma_r = \frac{1}{b^3 - a^3} \left\{ -b^3 q + a^3 p + \frac{a^3 b^3}{r^3} (q - p) \right\} \tag{5.2}$$

$$\sigma_\theta = \frac{1}{b^3 - a^3} \left\{ -b^3 q + a^3 p + \frac{a^3 b^3}{2r^3} (q - p) \right\} \tag{5.3}$$

$$u = \frac{r}{E}\left\{(1-\nu)\sigma_\theta - \nu\sigma_r\right\} \tag{5.4}$$

where σ_r and σ_θ represents the radial and hoop stresses and u represents the radial displacements. Distance r is measured from the centre of the sphere. The thick sphere used in this chapter is subjected to external pressure only and, therefore, Equations (5.2) and (5.3) simplify to:

$$\sigma_r = \frac{b^3 q}{b^3 - a^3}\left\{\frac{a}{r^3} - 1\right\} \tag{5.5}$$

$$\sigma_\theta = \frac{b^3 q}{b^3 - a^3}\left\{\frac{a}{2r^3} - 1\right\} \tag{5.6}$$

5.3.2 - BEM Results For A Thick Sphere

When the formulation explained in section 5.2 was implemented for the hollow sphere, initial testing was done using the double node concept on the inner and outer corners. Ordinary Gauss integration was used for the corner elements. On surfaces S_1 and S_3 the *Composite Mapping* was used to evaluate the singular integrals and the *Convergence Method* method was used on surface S_2. All the non-singular integrals were evaluated using ordinary Gauss quadrature. The surface divisions for S_1, S_2 and S_3 were 7,4 and 5 respectfully. Twenty segments were generated around the φ direction. The elements on the first three and the last three segments had a fixed number of quadrature order of 15×16 and all the other elements had a quadrature order of 12×12. These results are given in Figures 5.1, 5.2, 5.3 and 5.4.

The CPU time for this analysis took 18 minutes on an IBM 4381 mainframe to form the system matrices. The reduction of this large amount of CPU time is discussed in section 5.6. As for the hemisphere example in Chapter 4, there were severe local errors on the corners. However, for the displacements on surfaces S_1 and S_3, more accurate surface

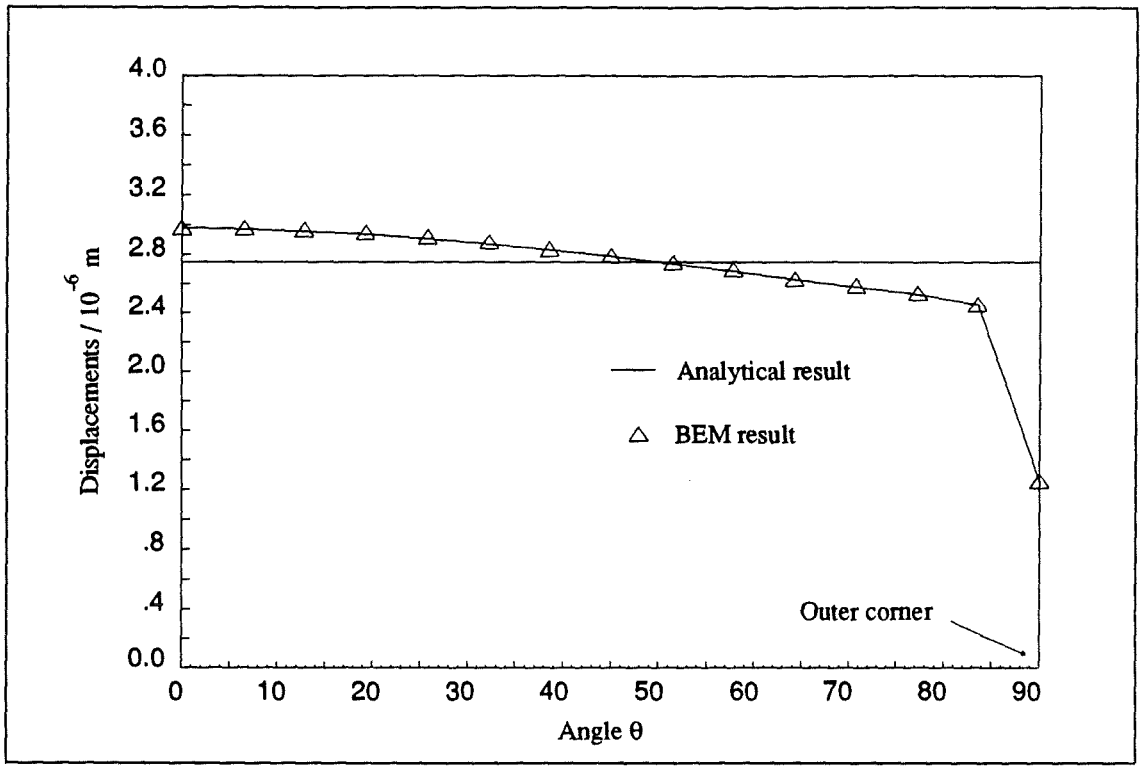

Figure 5.2: Comparison of resultant displacements on surface S_1.

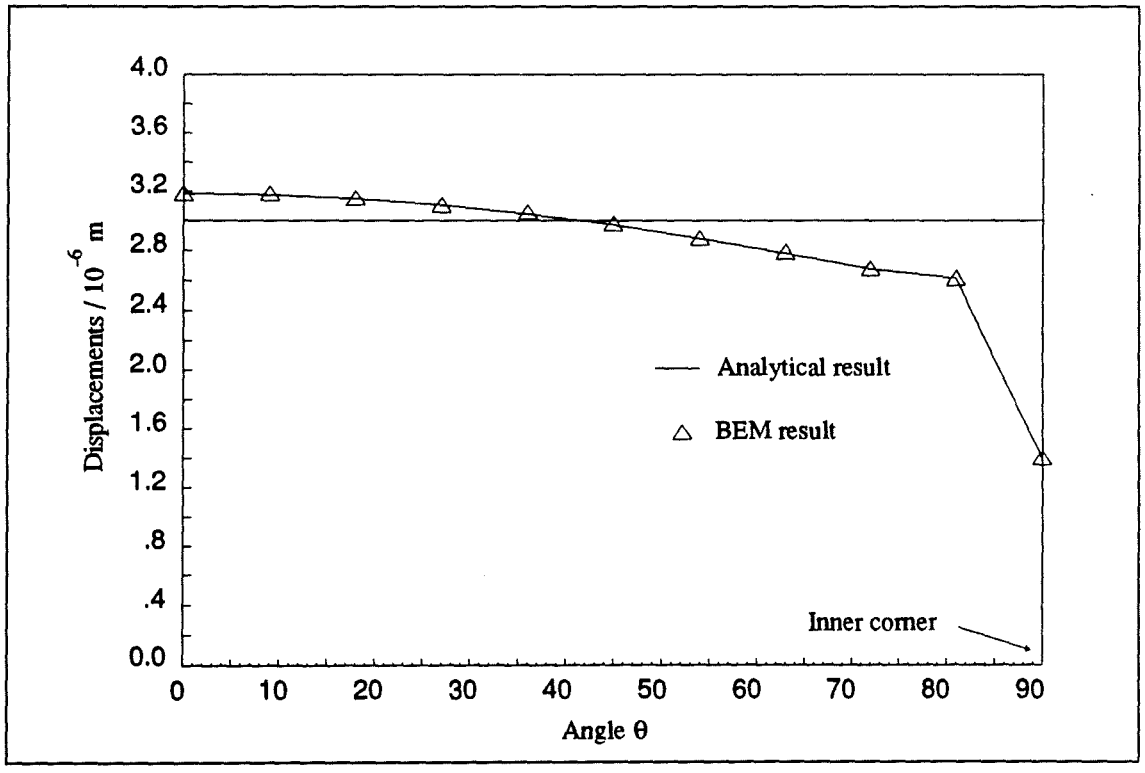

Figure 5.3: Comparison of resultant displacements on surface S_3.

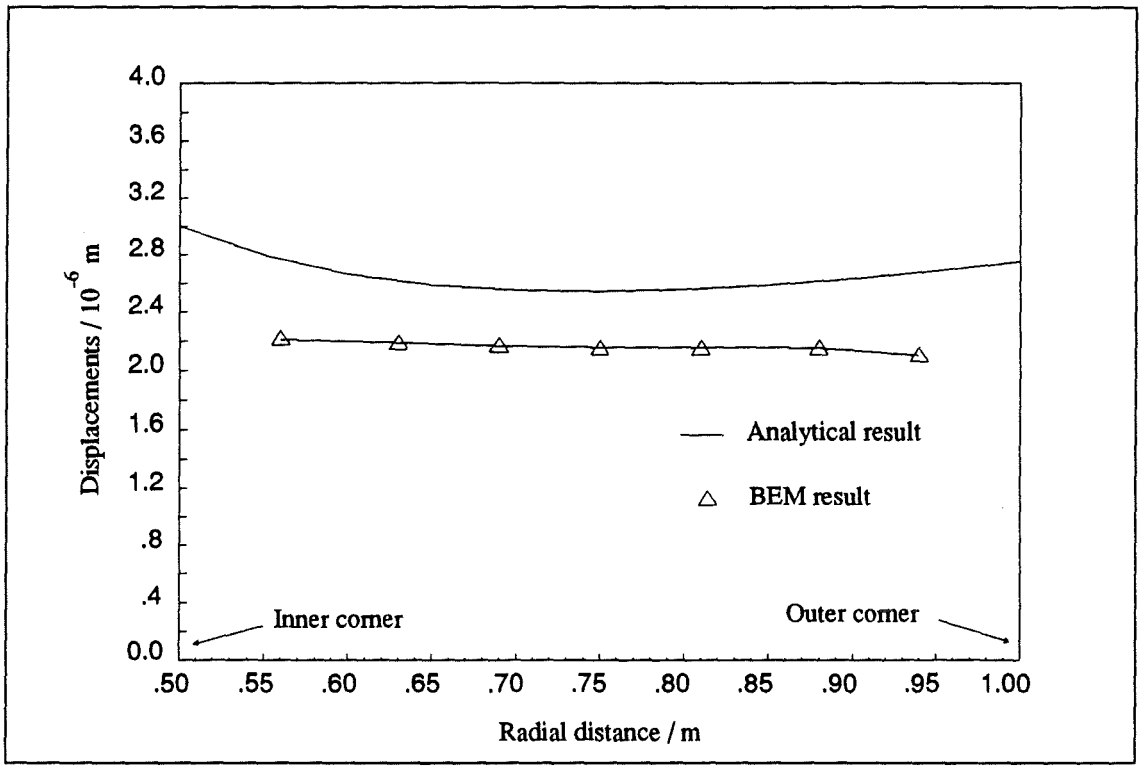

Figure 5.4: Comparison of horizontal displacements on surface S_2.

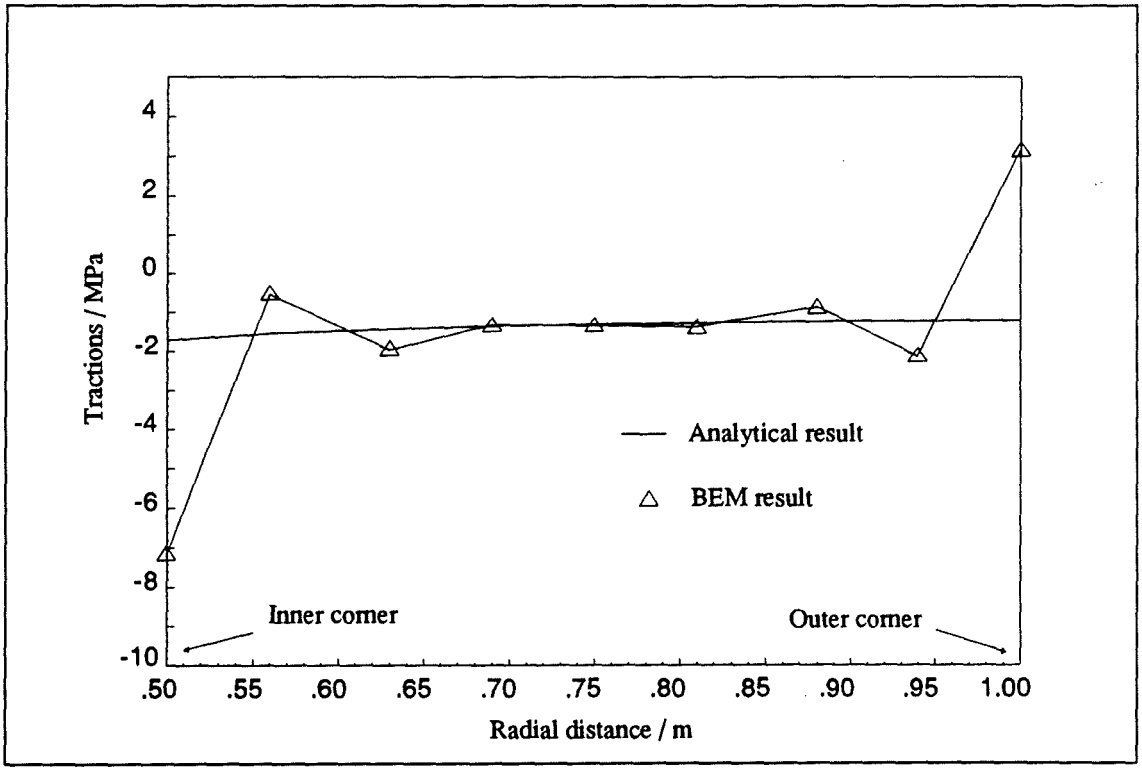

Figure 5.5: Comparison of tractions on surface S_2.

displacement values can be obtained by taking an average of the results on each surface, especially when the corner node result is not included (see Figures 5.2 & 5.3).

5.4 SEMI-CONTINUOUS ELEMENTS

5.4.1 - Position of the End Node

Use of the double node approach in section 5.3 showed severe errors on the nodes belonging to the corner elements. In this section, the nodes on the corners will be moved away from the corners, towards the inside of the corner elements. The nodes at the other end of these elements are to remain in their previous positions, making these elements semi-continuous. The new position of the midside nodes will then be adjusted to suit the existing interpolation formulae.

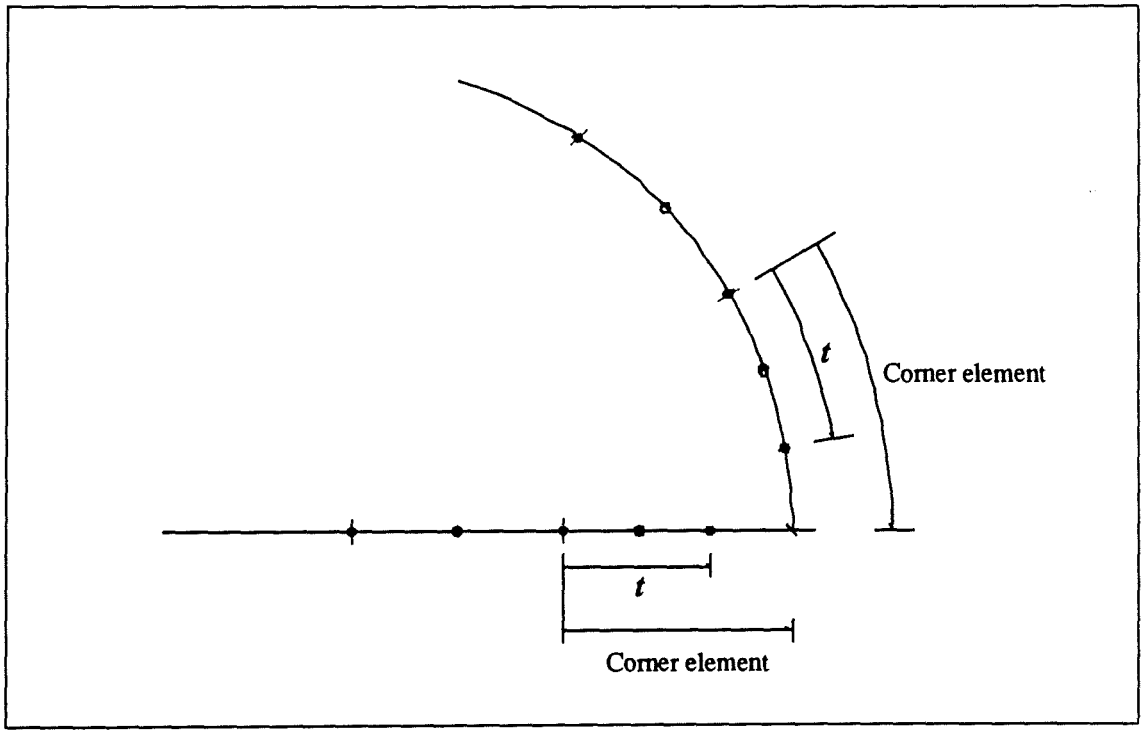

Figure 5.6: Use of semi-continuous elements to prevent the corner problems.

Table 5.1: Comparison of the extrapolated results for the semi-continuous elements.

Description of Extrapolated Results	% Error on Extrapolated Results		
	$t = 0.5$	$t = 0.6$	$t = 0.7$
S_1 Resultant Displacement - outer corner	2.23	1.05	0.58
S_2 Horizontal Displacement - inner corner	1.14	0.86	0.66
S_2 Horizontal Displacement - outer corner	1.16	0.58	0.89
S_2 Traction - inner corner	1.04	1.20	1.11
S_2 Traction - outer corner	1.92	0.73	0.91
S_3 Resultant Displacement - inner corner	0.25	0.23	0.22

The optimum position of the shifted node was not known. To determine this, a series of tests were conducted using the same sphere and the mesh throughout the tests. The distance between the outer and the inner nodes, t, was taken as a percentage of the actual element size (see Figure 5.6). The values of t were taken between 30% and 90% with increments of 10 %. A further value of 99% was also tried to see the effect of numerical instability of the system matrix A.

The results of surface displacements for S_1, S_2, S_3 and surface tractions for surface S_2 are given in Figures 5.7-5.10 respectively. The most accurate results appear to be obtained for t values of 50%, 60% and 70%. To get the most accurate position for the offset nodes, the results for the 50%, 60% and 70% offset positions are plotted together with the offset nodes extrapolated to the corners and compared in Figures 5.11-5.14 as before. The summary of the findings are given in Table 5.1 above. By looking at the results given in Table 5.1, the accuracy of the extrapolated results seem to get better as the fraction t approaches 70%. However, when t=80% the results get worse. There is also evidence that a unique value for the optimum position for the outer node, which will provide the most accurate solution for the displacements and the tractions for all the corner nodes, is not available.

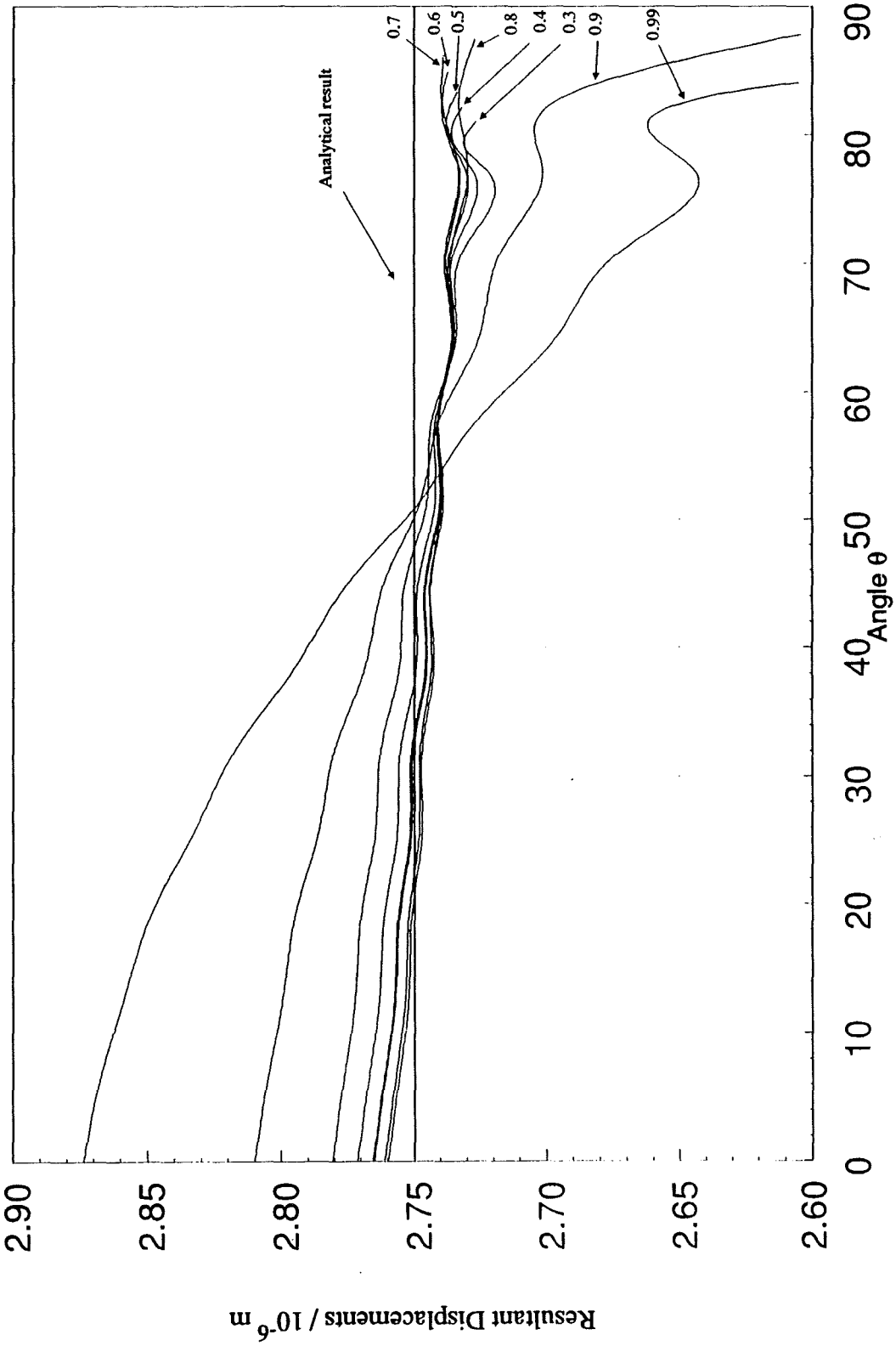

Figure 5.7: Resultant displacements on surface S_1 obtained with different values of fraction t for the semi-continuous corner elements. (Hollow hemisphere inner radius 0.5m, outer radius 1.0m)

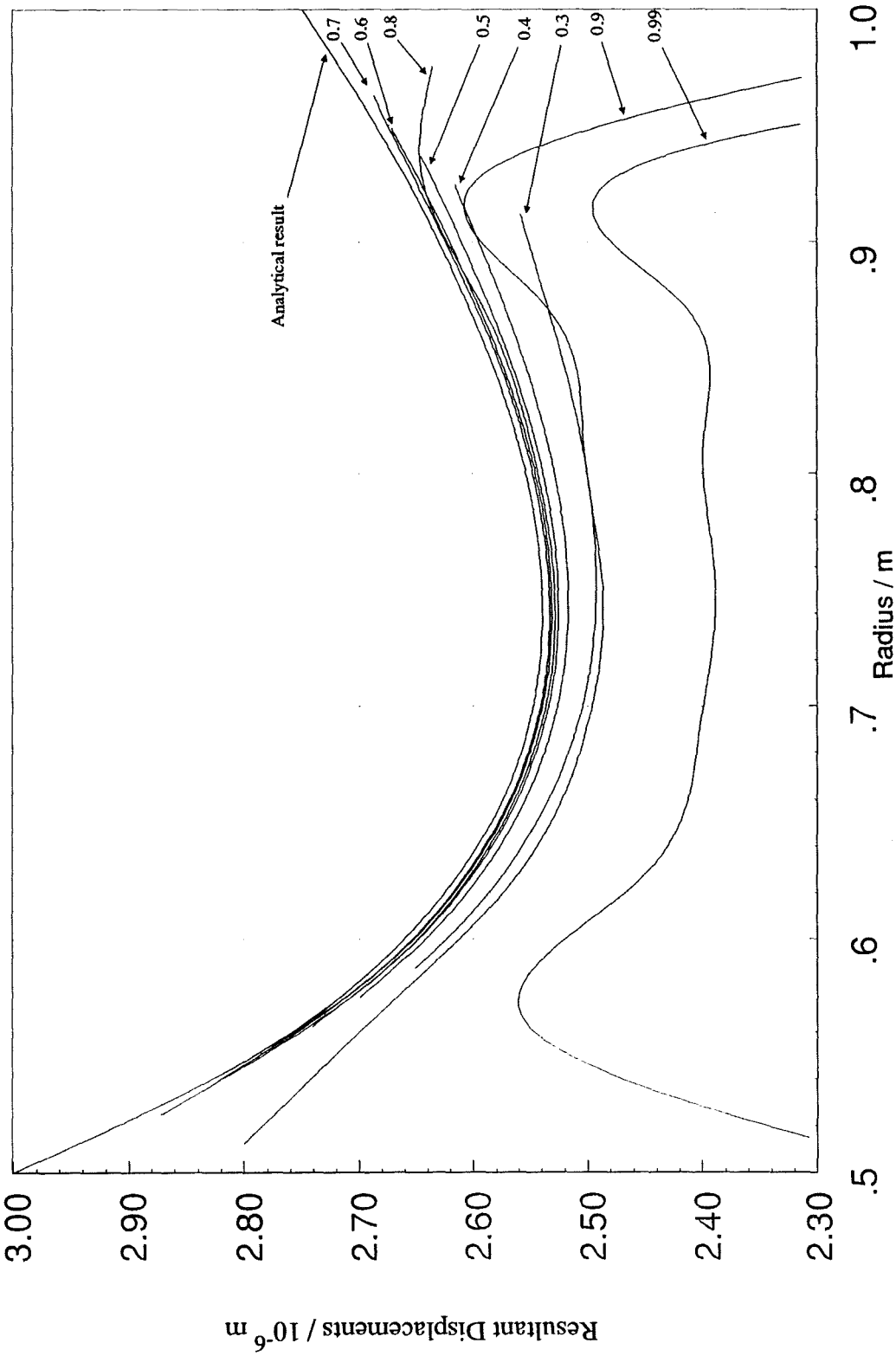

Figure 5.8: Horizontal displacements on surface S_2 obtained with different values of fraction t for the semi-continuous corner elements. (Hollow hemisphere inner radius 0.5m, outer radius 1.0m)

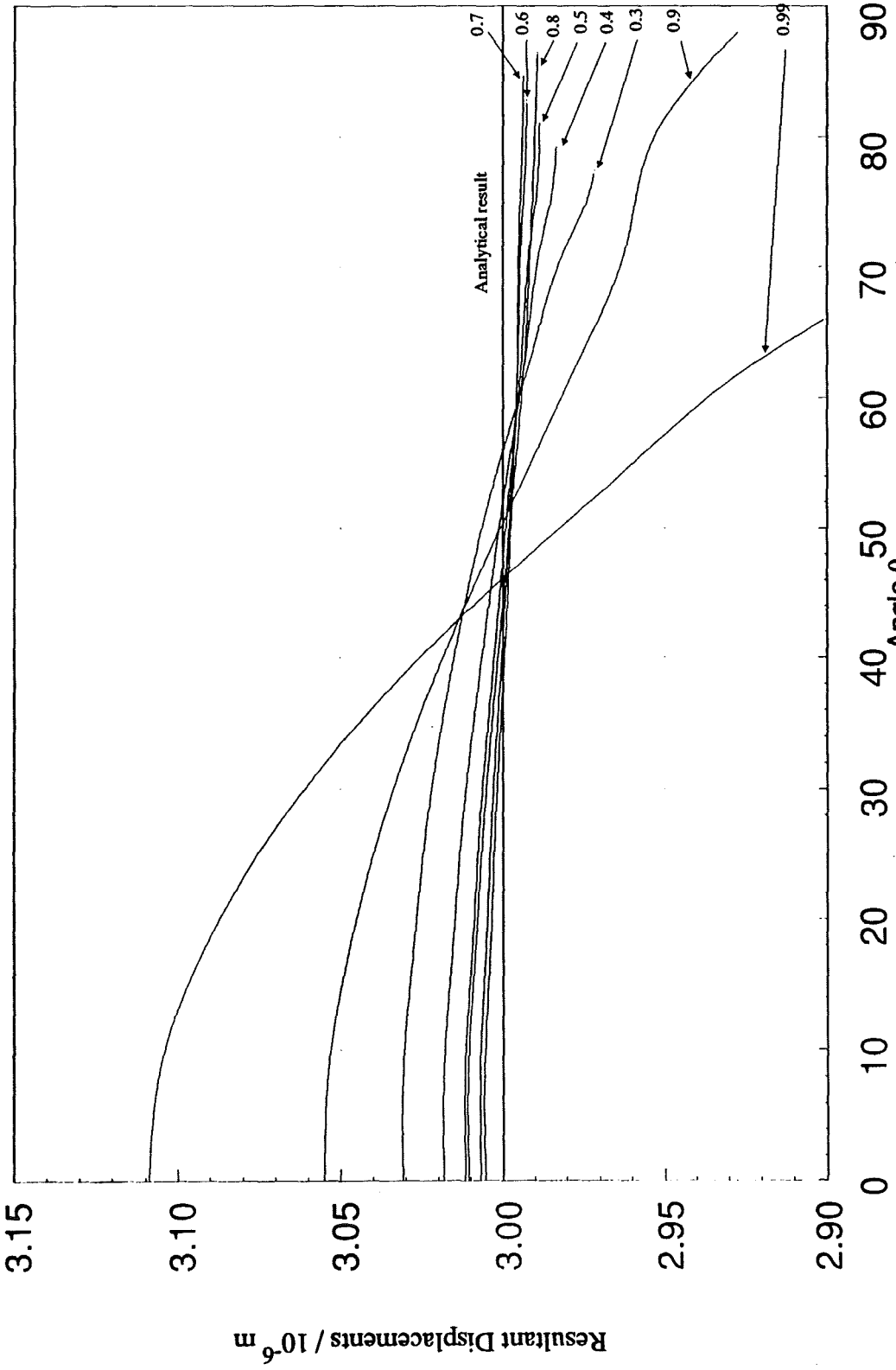

Figure 5.9: Resultant displacements on surface S_3 obtained with different values of fraction t for the semi-continuous corner elements. (Hollow hemisphere inner radius 0.5m, outer radius 1.0m)

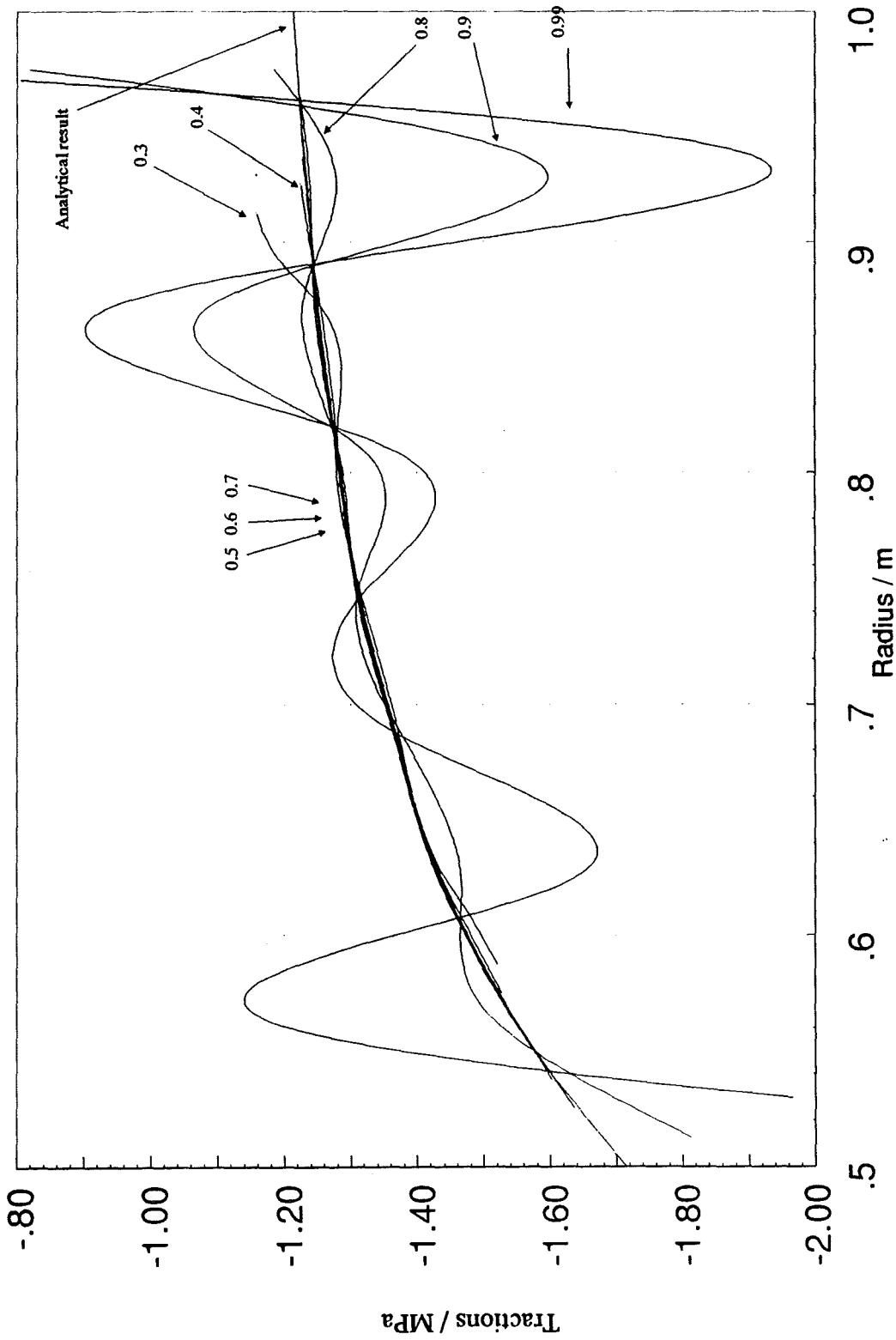

Figure 5.10: Tractions on surface S_2 obtained with different values of fraction t for the semi-continuous corner elements. (Hollow hemisphere inner radius 0.5m, outer radius 1.0m)

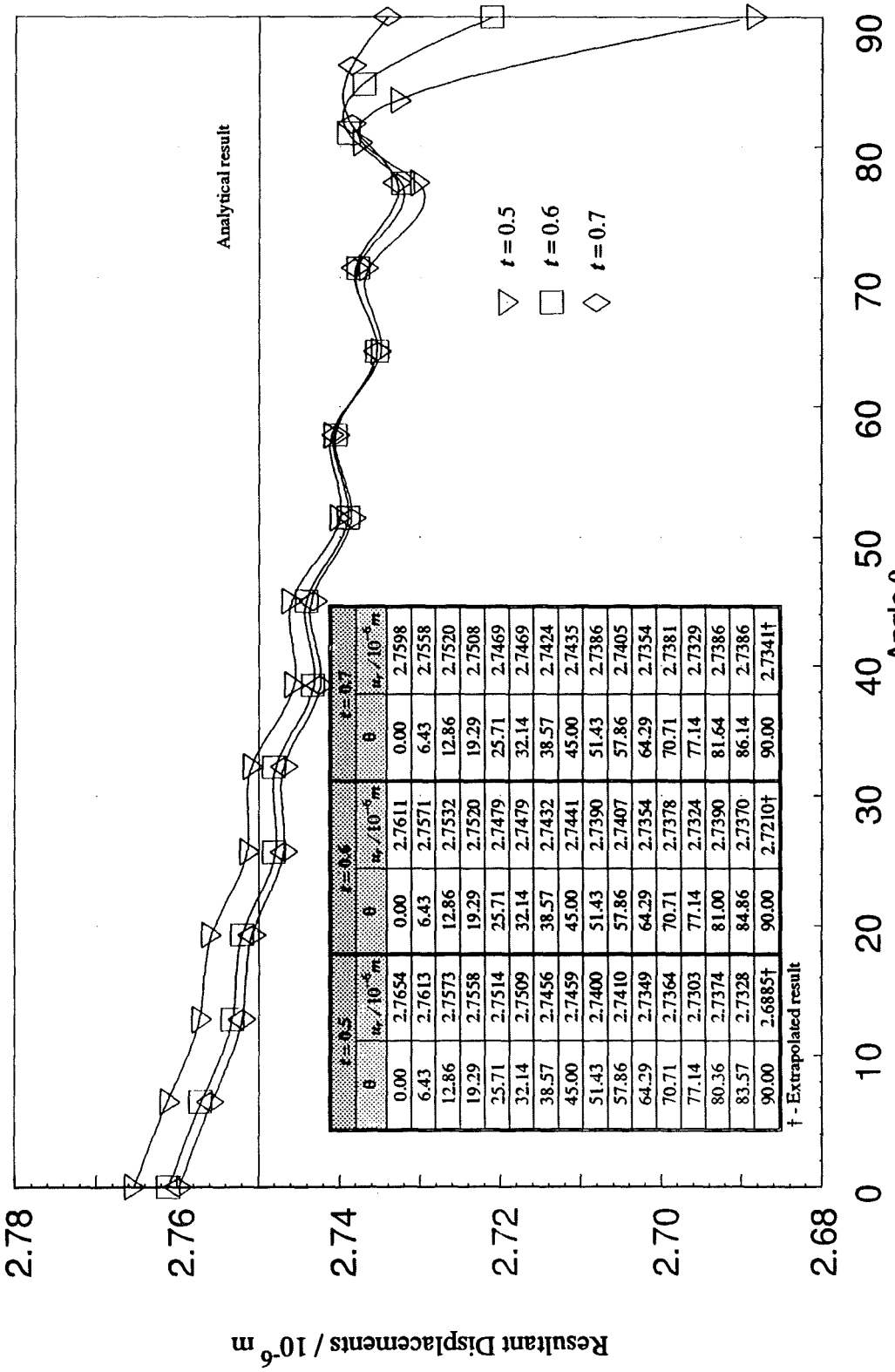

t = 0.5		t = 0.6		t = 0.7	
θ	u_r / 10^{-6} m	θ	u_r / 10^{-6} m	θ	u_r / 10^{-6} m
0.00	2.7654	0.00	2.7611	0.00	2.7598
6.43	2.7613	6.43	2.7571	6.43	2.7558
12.86	2.7573	12.86	2.7532	12.86	2.7520
19.29	2.7558	19.29	2.7520	19.29	2.7508
25.71	2.7514	25.71	2.7479	25.71	2.7469
32.14	2.7509	32.14	2.7479	32.14	2.7469
38.57	2.7456	38.57	2.7432	38.57	2.7424
45.00	2.7459	45.00	2.7441	45.00	2.7435
51.43	2.7400	51.43	2.7390	51.43	2.7386
57.86	2.7410	57.86	2.7407	57.86	2.7405
64.29	2.7349	64.29	2.7354	64.29	2.7354
70.71	2.7364	70.71	2.7378	70.71	2.7381
77.14	2.7303	77.14	2.7324	77.14	2.7329
80.36	2.7374	81.00	2.7390	81.64	2.7386
83.57	2.7328	84.86	2.7370	86.14	2.7386
90.00	2.6885†	90.00	2.7210†	90.00	2.7341†

† - Extrapolated result

Figure 5.11: Resultant displacements on surface S_1 obtained with the t values of 0.5, 0.6 and 0.7. The results are extrapolated to the inner and outer corners. (Hollow hemisphere inner radius 0.5m, outer radius 1.0m)

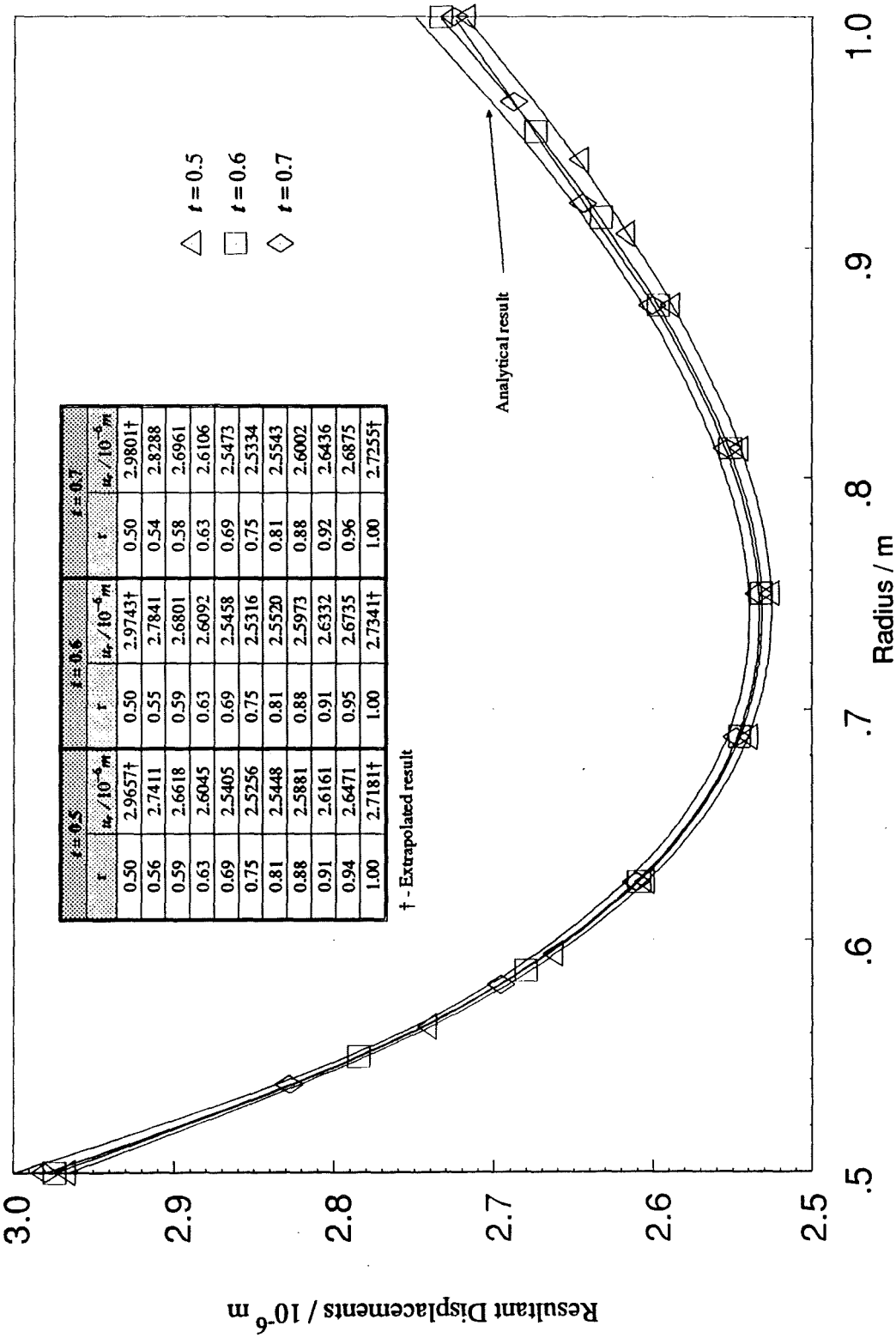

$t = 0.5$		$t = 0.6$		$t = 0.7$	
r	$u_r / 10^{-6} m$	r	$u_r / 10^{-6} m$	r	$u_r / 10^{-6} m$
0.50	2.9657†	0.50	2.9743†	0.50	2.9801†
0.56	2.7411	0.55	2.7841	0.54	2.8288
0.59	2.6618	0.59	2.6801	0.58	2.6961
0.63	2.6045	0.63	2.6092	0.63	2.6106
0.69	2.5405	0.69	2.5458	0.69	2.5473
0.75	2.5256	0.75	2.5316	0.75	2.5334
0.81	2.5448	0.81	2.5520	0.81	2.5543
0.88	2.5881	0.88	2.5973	0.88	2.6002
0.91	2.6161	0.91	2.6332	0.92	2.6436
0.94	2.6471	0.95	2.6735	0.96	2.6875
1.00	2.7181†	1.00	2.7341†	1.00	2.7255†

† - Extrapolated result

Figure 5.12: Horizontal displacements on surface S_2 obtained with the t values of 0.5, 0.6 and 0.7. The results are extrapolated to the inner and outer corners. (Hollow hemisphere inner radius 0.5m, outer radius 1.0m)

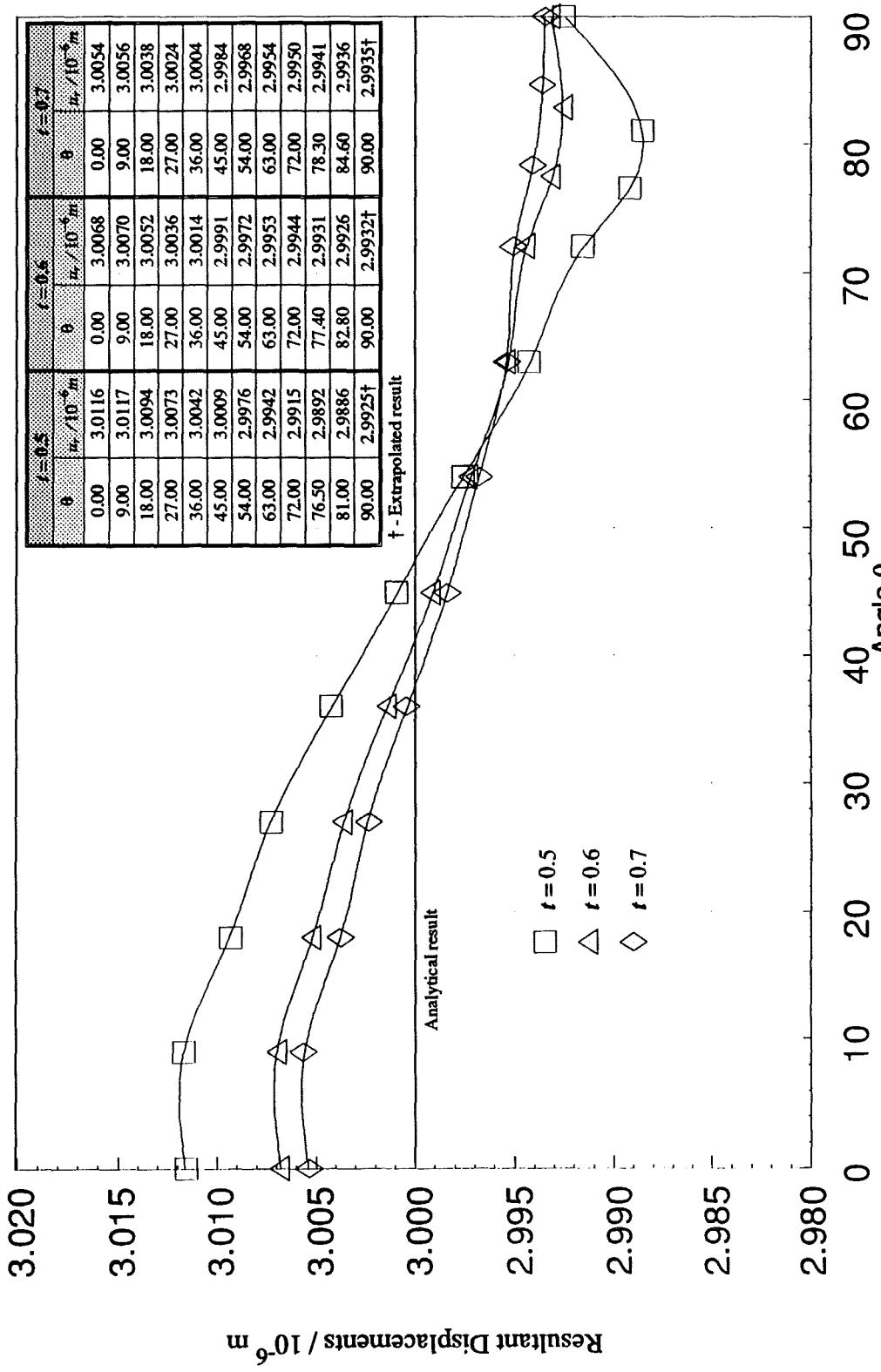

t = 0.5		t = 0.6		t = 0.7	
θ	u_r / 10^{-6}m	θ	u_r / 10^{-6}m	θ	u_r / 10^{-6}m
0.00	3.0116	0.00	3.0068	0.00	3.0054
9.00	3.0117	9.00	3.0070	9.00	3.0056
18.00	3.0094	18.00	3.0052	18.00	3.0038
27.00	3.0073	27.00	3.0036	27.00	3.0024
36.00	3.0042	36.00	3.0014	36.00	3.0004
45.00	3.0009	45.00	2.9991	45.00	2.9984
54.00	2.9976	54.00	2.9972	54.00	2.9968
63.00	2.9942	63.00	2.9953	63.00	2.9954
72.00	2.9915	72.00	2.9944	72.00	2.9950
76.50	2.9892	77.40	2.9931	78.30	2.9941
81.00	2.9886	82.80	2.9926	84.60	2.9936
90.00	2.9925†	90.00	2.9932†	90.00	2.9935†

† - Extrapolated result

Figure 5.13: Resultant displacements on surface S_3 obtained with the t values of 0.5, 0.6 and 0.7. The results are extrapolated to the inner and outer corners. (Hollow hemisphere inner radius 0.5m, outer radius 1.0m)

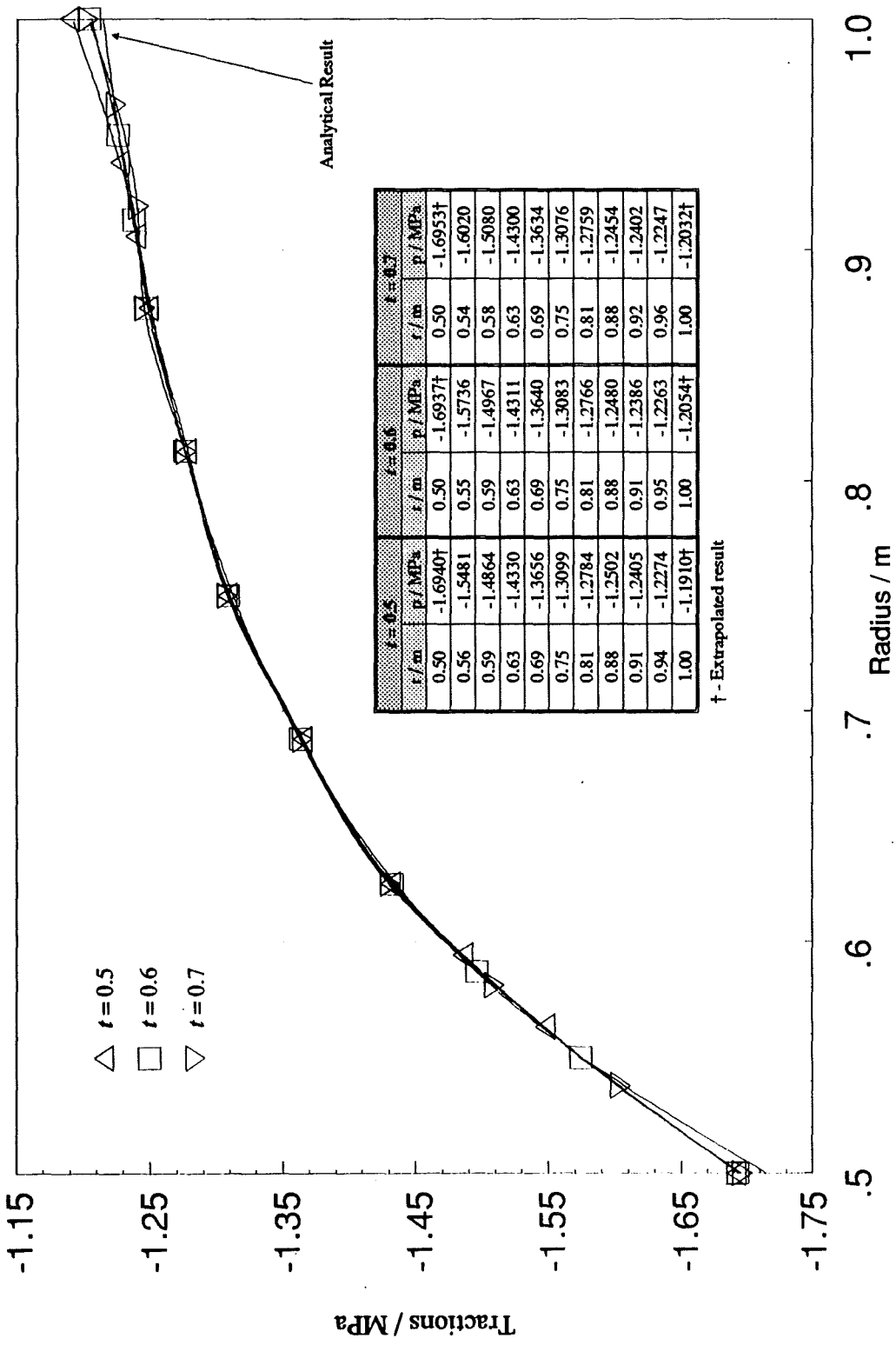

t = 0.5		t = 0.6		t = 0.7	
r / m	p / MPa	r / m	p / MPa	r / m	p / MPa
0.50	-1.6940†	0.50	-1.6937†	0.50	-1.6953†
0.56	-1.5481	0.55	-1.5736	0.54	-1.6020
0.59	-1.4864	0.59	-1.4967	0.58	-1.5080
0.63	-1.4330	0.63	-1.4311	0.63	-1.4300
0.69	-1.3656	0.69	-1.3640	0.69	-1.3634
0.75	-1.3099	0.75	-1.3083	0.75	-1.3076
0.81	-1.2784	0.81	-1.2766	0.81	-1.2759
0.88	-1.2502	0.88	-1.2480	0.88	-1.2454
0.91	-1.2405	0.91	-1.2386	0.92	-1.2402
0.94	-1.2274	0.95	-1.2263	0.96	-1.2247
1.00	-1.1910†	1.00	-1.2054†	1.00	-1.2032†

† - Extrapolated result

Figure 5.14: Tractions on surface S_2 obtained with the t values of 0.5, 0.6 and 0.7. The results are extrapolated to the inner and outer corners. (Hollow hemisphere inner radius 0.5m, outer radius 1.0m)

5.4.2 - Relationship Between Node Position and Gauss Points

In a paper, Xu and Brebbia (1986) suggest that there is a relationship between the optimum location of the nodes in a discontinuous element and the Gauss integration points. However, their investigation is based purely on numerical experimentation. They claim that for minimal error in results, the position of the node inside a discontinuous element should coincide with a Gauss integration point. In their tests, linear discontinuous elements were used throughout in their mesh. However the elements used in this work are quadratic, continuous everywhere except for the four elements forming the inner and the outer corners, which are semi-continuous.

From the numerical tests carried out in the previous section, values of t less than 0.5 and bigger than 0.7 did not produce satisfactory results. Better results are achieved within the region of 0.5 and 0.7. This shows that not all the Gauss points available can be used to produce results with minimal error. In the work carried out at present, the order of Gauss quadrature was set to 16 for the integration of the singular elements. The projection of the Gauss points onto the corner element on S_1 surface is given in Figure 5.15.

Gauss Abcisa ξ	Angle θ	Angle α	Ratio $\frac{\alpha}{\Delta\theta}$
0.9894	89.93	12.79	0.99
0.9446	89.64	12.50	0.97
0.8656	89.14	11.99	0.93
0.7554	88.43	11.28	0.88
0.6179	87.54	10.40	0.81
0.4580	86.52	9.37	0.73
0.2816	85.38	8.24	0.64
0.0950	84.18	7.04	0.54

$\Delta\theta = 90 - 77.1428 = 12.8572$

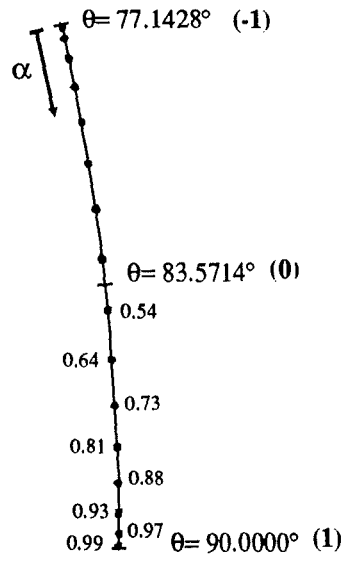

Figure 5.15: Mapping of Gauss points over the corner element on S_1.

To test the validity of the claim by Xu et. al., several Gauss points were selected as the location for the end node on the semi-continuous elements (see the table in Figure 5.15). Identical mesh and Gauss quadrature order were used for t= 0.54, 0.64, 0.73 and 0.81. The aim is to see if the errors in the displacements and the tractions would be minimized at one of these Gauss points. The results of the displacements and the tractions are plotted in Figures 5.18-21. A summary of these results and a comparison with other values of t are given in Table 5.2. These errors are given at the actual nodes instead of the mesh points. The intention was to avoid possible errors that may be caused by the extrapolation of the results to the mesh points. A graphical illustration of Table 5.2 is also given in Figure 5.16. A comparison of the results given in Table 5.2, when extrapolated to the mesh points are given in Table 5.3 and graphically illustrated in Figure 5.17.

It is interesting to see that not all the node positions corresponding to the Gauss point locations give the best accuarcy. However, it is clear that the best results are obtained when t is between 0.60 and 0.73 where errors of under 0.51% are seen. There is also a clear indication that in this range, the error in the results are minimised at the Gauss points; namely at 0.64 and 0.73. This is also valid when the extrapolated results are considered and errors around 1% are determined. Although the minimum errors were obtained at t = 0.64 and t = 0.73, other t locations corresponding to the Gauss points gave much worse results compared to locations that did not corresspond to the Gauss points. This shows that not all the locations corresponding to the Gauss points give the best results. It is also evident that the optimum node position determined in one Gauss order will not be the same location in another Gauss order since the location of the end node is a function of the Gauss abscissa. Until a mathematical relationship between the Gauss points and the optimum node location can be established, the optimum location for the nodes in a semi-continuous or discontinuous elements should be determined by experimental methods for each of the Gauss quadrature orders to be used in the actual analysis. For a Gauss order of 16, the best location could be taken as 0.64 but for a different Gauss order this value would not be appropriate. Optimum location for Gauss order of 12 is discussed in Chapter 6.

Table 5.2: Comparison of the results at the corner nodes to investigate the effect of end nodes coinciding with the Gauss points.

Description of Results	% Error							
	$t = 0.5$	$t = 0.54$	$t = 0.6$	$t = 0.64$	$t = 0.7$	$t = 0.73$	$t = 0.8$	$t = 0.81$
S_1 Resultant disps. - outer corner	0.63	0.52	0.44	0.40	0.41	0.35	0.84	0.60
S_2 Horizontal Disps.- outer corner	0.90	0.61	0.46	0.32	0.51	0.36	3.00	1.87
S_2 Horizontal disps. - inner corner	0.44	0.33	0.28	0.23	0.24	0.21	0.42	0.30
S_3 Resultant Disps. - inner corner	0.38	0.29	0.25	0.20	0.21	0.17	0.36	0.27
S_2 Traction - outer corner	0.17	0.07	0.01	0.07	0.14	0.15	2.93	1.78
S_2 Traction - inner corner	0.25	0.17	0.09	0.04	0.05	0.08	0.05	0.14

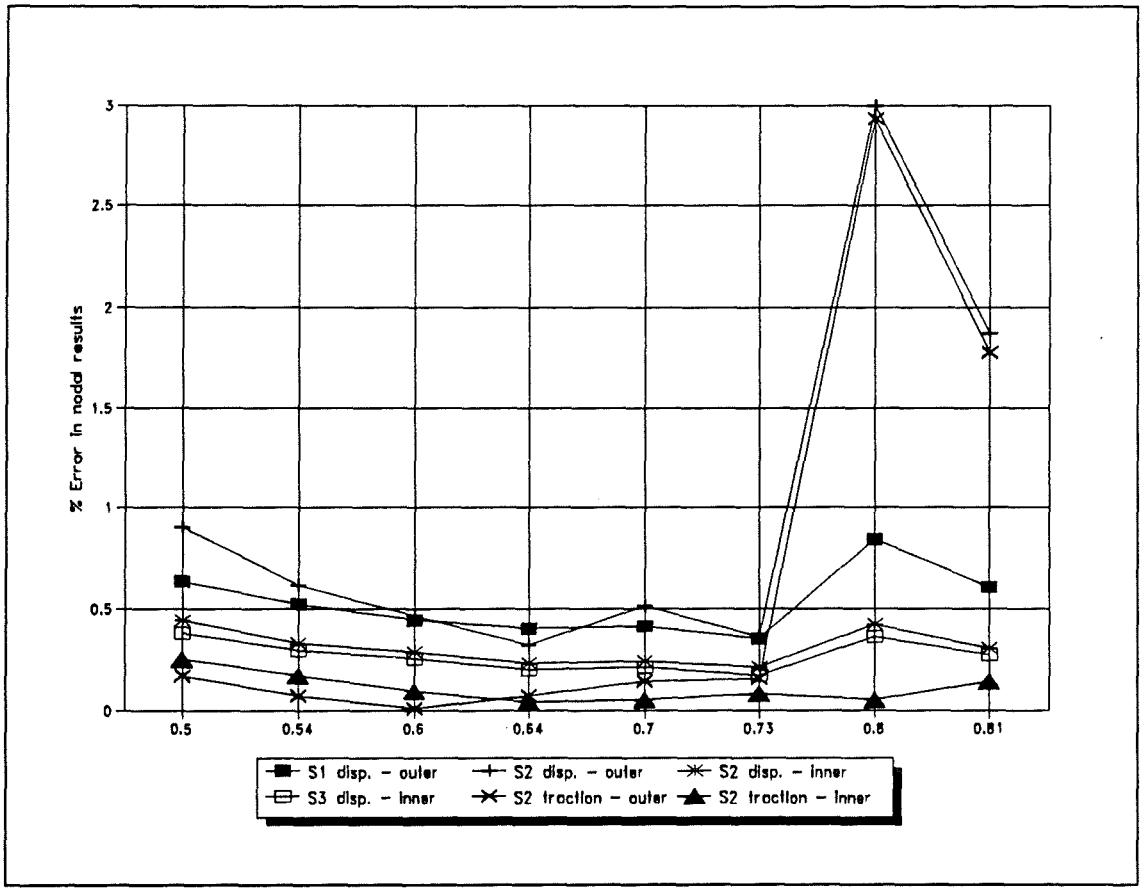

Figure 5.16: Plot of the errors in the nodal results shown in Table 5.2.

Table 5.3: Comparison of the *extrapolated* results at the corner nodes to investigate the effect of end nodes coinciding with the Gauss points.

Description of Results	% Error							
	$t = 0.5$	$t = 0.54$	$t = 0.6$	$t = 0.64$	$t = 0.7$	$t = 0.73$	$t = 0.8$	$t = 0.81$
S_1 Resultant disps. - outer corner	2.23	1.45	1.05	0.70	0.58	0.43	1.08	0.71
S_2 Horizontal Disps.- outer corner	1.16	0.73	0.86	0.36	0.89	0.57	5.11	3.08
S_2 Horizontal disps. - inner corner	1.14	0.99	0.58	0.76	0.66	1.32	0.72	0.56
S_3 Resultant Disps. - inner corner	0.25	0.23	0.23	0.20	0.22	0.12	0.23	0.29
S_2 Traction - outer corner	1.92	1.30	0.73	0.31	0.91	0.44	10.79	6.23
S_2 Traction - inner corner	1.04	1.00	1.20	1.16	1.11	1.09	0.74	0.79

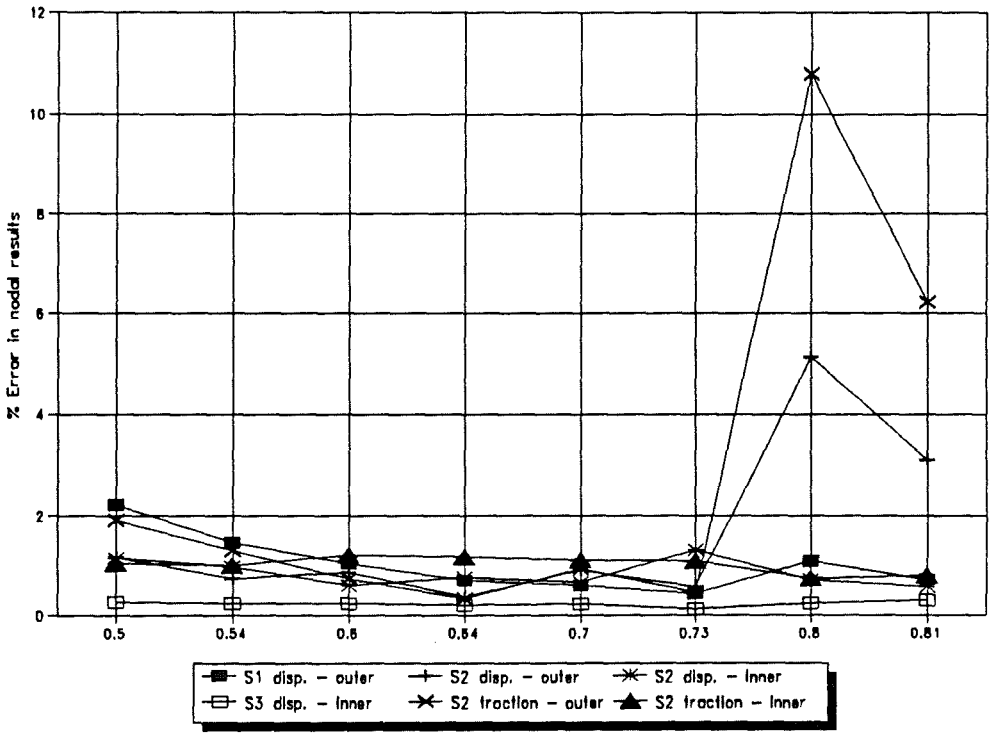

Figure 5.17: Plot of the errors in the *extrapolated* results for the corner nodes shown in Table 5.3.

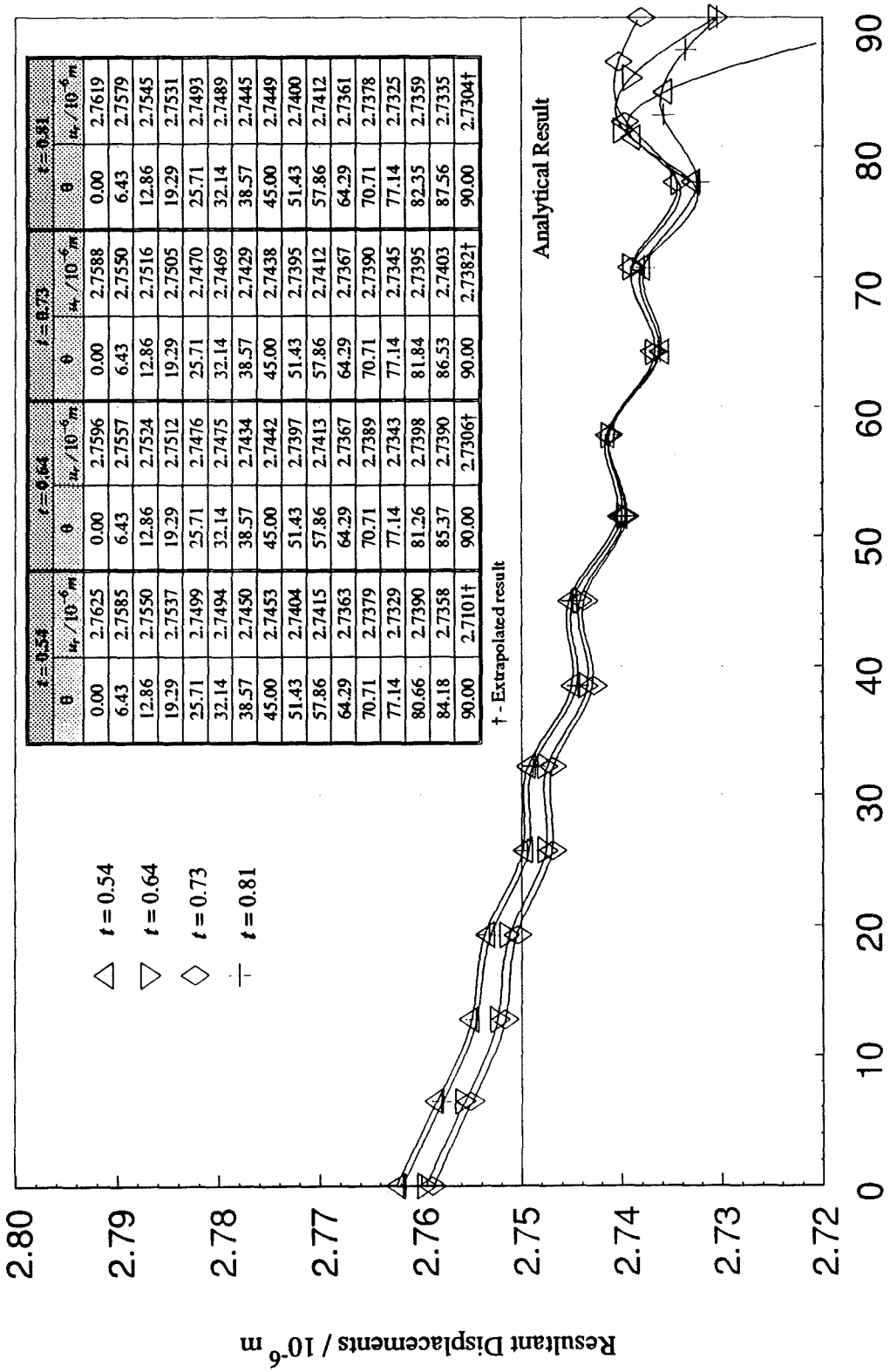

t = 0.54		t = 0.64		t = 0.73		t = 0.81	
θ	$u_r/10^{-6}m$	θ	$u_r/10^{-6}m$	θ	$u_r/10^{-6}m$	θ	$u_r/10^{-6}m$
0.00	2.7625	0.00	2.7596	0.00	2.7588	0.00	2.7619
6.43	2.7585	6.43	2.7557	6.43	2.7550	6.43	2.7579
12.86	2.7550	12.86	2.7524	12.86	2.7516	12.86	2.7545
19.29	2.7537	19.29	2.7512	19.29	2.7505	19.29	2.7531
25.71	2.7499	25.71	2.7476	25.71	2.7470	25.71	2.7493
32.14	2.7494	32.14	2.7475	32.14	2.7469	32.14	2.7489
38.57	2.7450	38.57	2.7434	38.57	2.7429	38.57	2.7445
45.00	2.7453	45.00	2.7442	45.00	2.7438	45.00	2.7449
51.43	2.7404	51.43	2.7397	51.43	2.7395	51.43	2.7400
57.86	2.7415	57.86	2.7413	57.86	2.7412	57.86	2.7412
64.29	2.7363	64.29	2.7367	64.29	2.7367	64.29	2.7361
70.71	2.7379	70.71	2.7389	70.71	2.7390	70.71	2.7378
77.14	2.7329	77.14	2.7343	77.14	2.7345	77.14	2.7325
80.66	2.7390	81.26	2.7398	81.84	2.7395	82.35	2.7359
84.18	2.7358	85.37	2.7390	86.53	2.7403	87.56	2.7335
90.00	2.7101†	90.00	2.7306†	90.00	2.7382†	90.00	2.7304†

† - Extrapolated result

Figure 5.18: Resultant displacements on surface S_1 obtained with t = 0.54, 0.64, 0.73 and 0.81 which corresponds to the Gauss points. (Hollow hemisphere inner radius 0.5m, outer radius 1.0m)

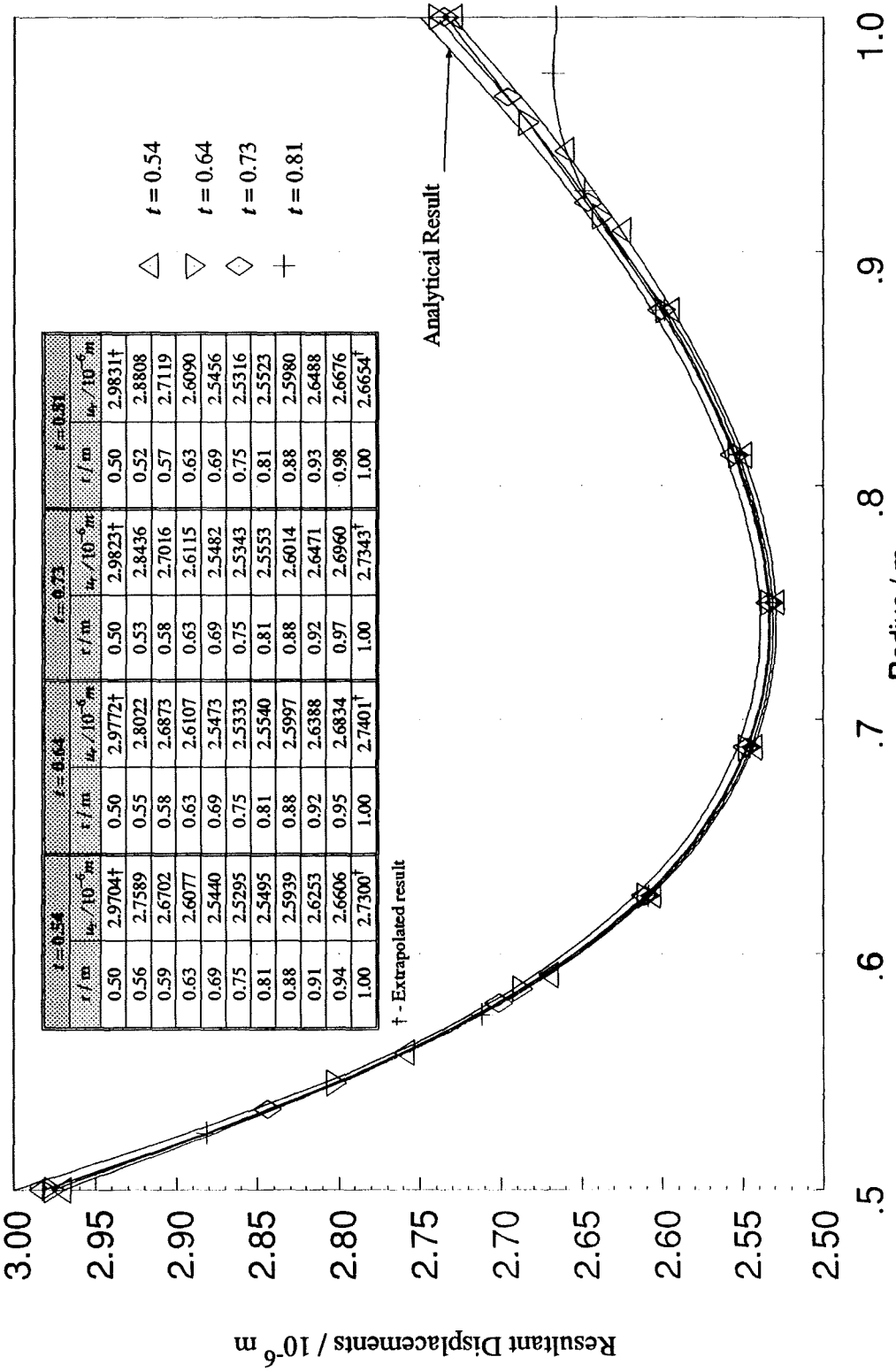

t = 0.54		t = 0.64		t = 0.73		t = 0.81	
r / m	u_r / 10^{-6} m	r / m	u_r / 10^{-6} m	r / m	u_r / 10^{-6} m	r / m	u_r / 10^{-6} m
0.50	2.9704†	0.50	2.9772†	0.50	2.9823†	0.50	2.9831†
0.56	2.7589	0.55	2.8022	0.53	2.8436	0.52	2.8808
0.59	2.6702	0.58	2.6873	0.58	2.7016	0.57	2.7119
0.63	2.6077	0.63	2.6107	0.63	2.6115	0.63	2.6090
0.69	2.5440	0.69	2.5473	0.69	2.5482	0.69	2.5456
0.75	2.5295	0.75	2.5333	0.75	2.5343	0.75	2.5316
0.81	2.5495	0.81	2.5540	0.81	2.5553	0.81	2.5523
0.88	2.5939	0.88	2.5997	0.88	2.6014	0.88	2.5980
0.91	2.6253	0.92	2.6388	0.92	2.6471	0.93	2.6488
0.94	2.6606	0.95	2.6834	0.97	2.6960	0.98	2.6676
1.00	2.7300†	1.00	2.7401†	1.00	2.7343†	1.00	2.6654†

† - Extrapolated result

Figure 5.19: Horizontal displacements on surface S_2 obtained with t = 0.54, 0.64, 0.73 and 0.81 which corresponds to the Gauss points. (Hollow hemisphere inner radius 0.5m, outer radius 1.0m)

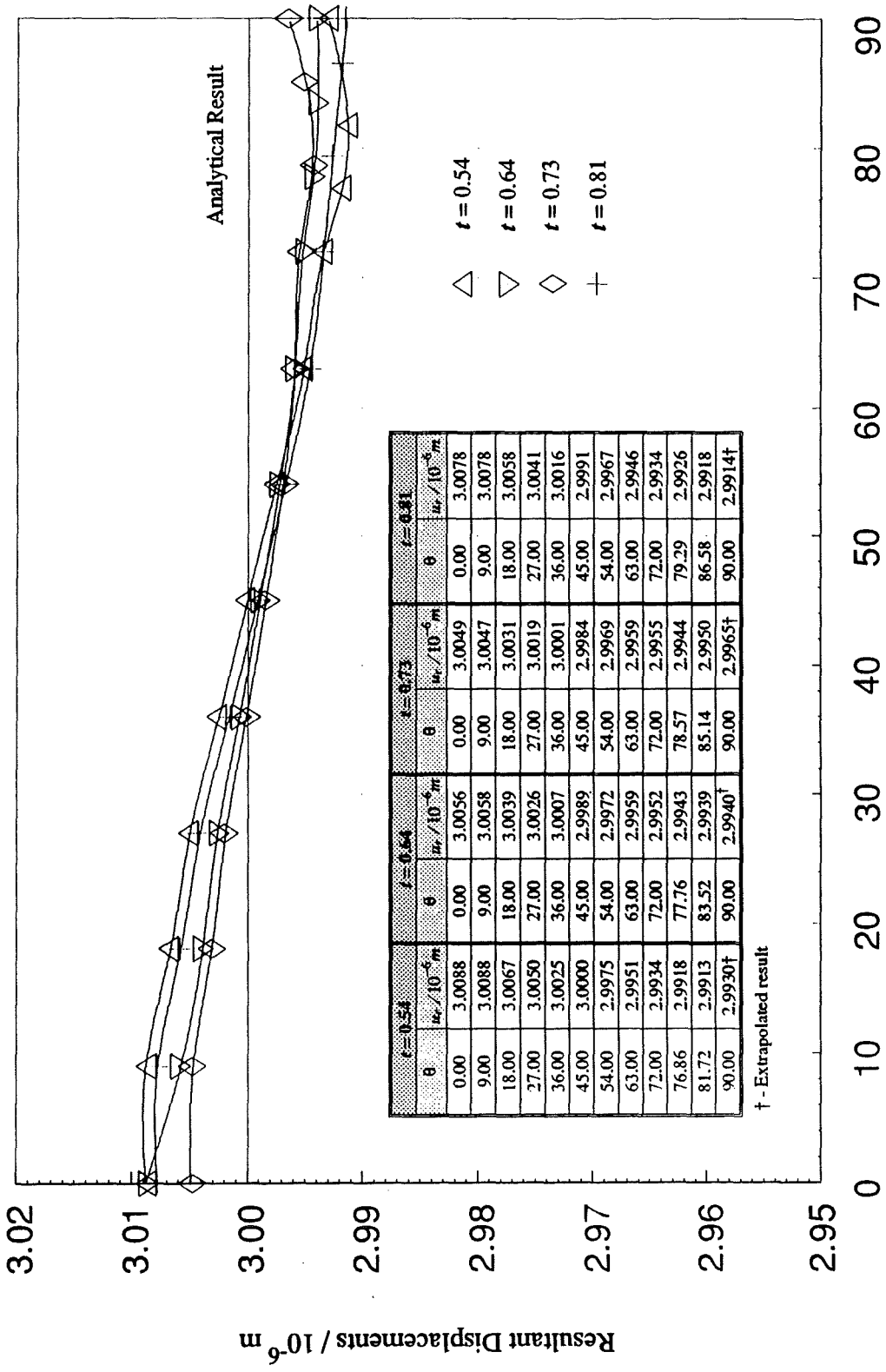

t = 0.54		t = 0.64		t = 0.73		t = 0.81	
θ	u_r / 10^{-6} m	θ	u_r / 10^{-6} m	θ	u_r / 10^{-6} m	θ	u_r / 10^{-6} m
0.00	3.0088	0.00	3.0056	0.00	3.0049	0.00	3.0078
9.00	3.0088	9.00	3.0058	9.00	3.0047	9.00	3.0078
18.00	3.0067	18.00	3.0039	18.00	3.0031	18.00	3.0058
27.00	3.0050	27.00	3.0026	27.00	3.0019	27.00	3.0041
36.00	3.0025	36.00	3.0007	36.00	3.0001	36.00	3.0016
45.00	3.0000	45.00	2.9989	45.00	2.9984	45.00	2.9991
54.00	2.9975	54.00	2.9972	54.00	2.9969	54.00	2.9967
63.00	2.9951	63.00	2.9959	63.00	2.9959	63.00	2.9946
72.00	2.9934	72.00	2.9952	72.00	2.9955	72.00	2.9934
76.86	2.9918	77.76	2.9943	78.57	2.9944	79.29	2.9926
81.72	2.9913	83.52	2.9939	85.14	2.9950	86.58	2.9918
90.00	2.9930†	90.00	2.9940†	90.00	2.9965†	90.00	2.9914†

† - Extrapolated result

Figure 5.20: Resultant displacements on surface S_3 obtained with t = 0.54, 0.64, 0.73 and 0.81 which corresponds to the Gauss points. (Hollow hemisphere inner radius 0.5m, outer radius 1.0m)

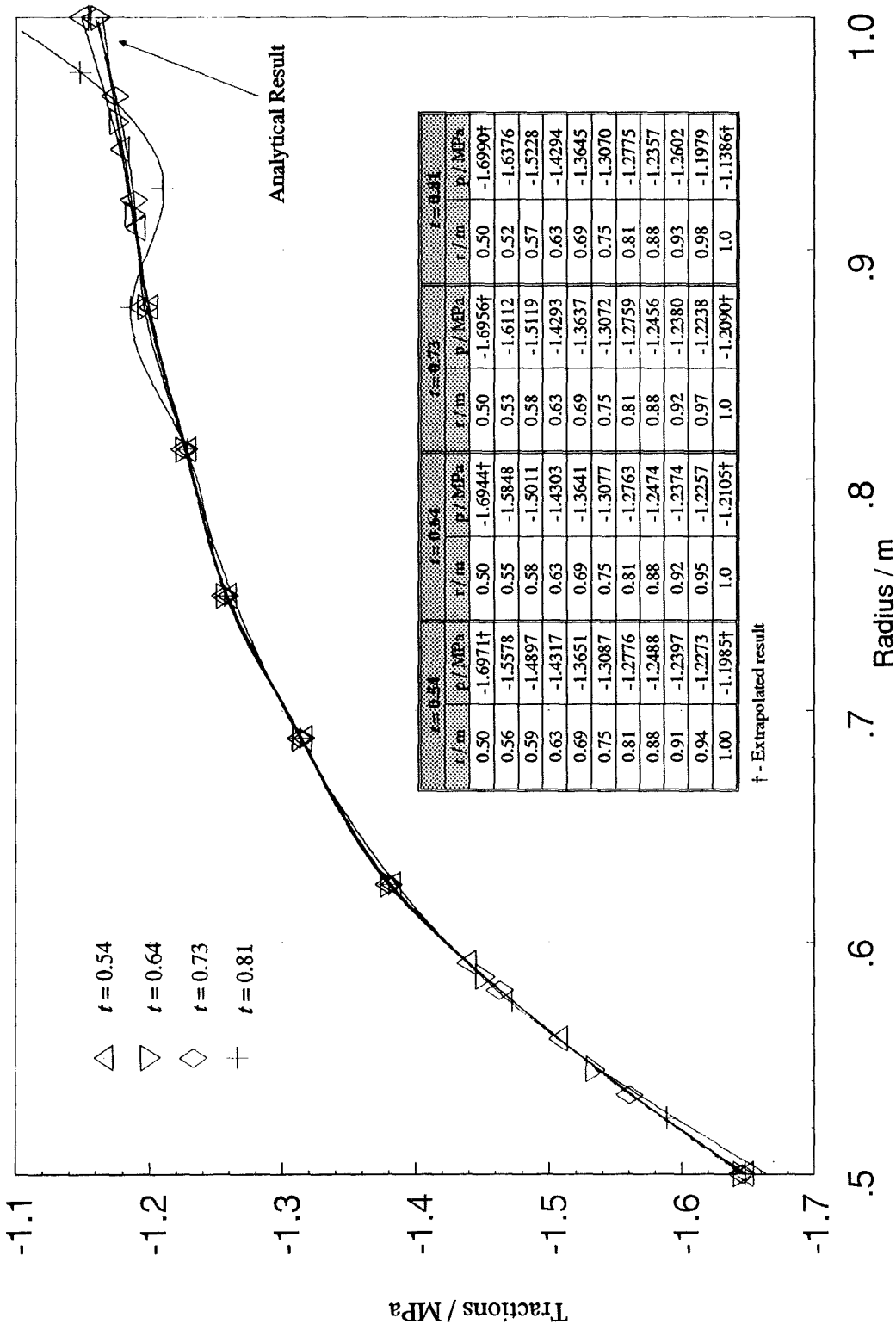

t = 0.54		t = 0.64		t = 0.73		t = 0.81	
r / m	p / MPa	r / m	p / MPa	r / m	p / MPa	r / m	p / MPa
0.50	-1.6971†	0.50	-1.6944†	0.50	-1.6956†	0.50	-1.6990†
0.56	-1.5578	0.55	-1.5848	0.53	-1.6112	0.52	-1.6376
0.59	-1.4897	0.58	-1.5011	0.58	-1.5119	0.57	-1.5228
0.63	-1.4317	0.63	-1.4303	0.63	-1.4293	0.63	-1.4294
0.69	-1.3651	0.69	-1.3641	0.69	-1.3637	0.69	-1.3645
0.75	-1.3087	0.75	-1.3077	0.75	-1.3072	0.75	-1.3070
0.81	-1.2776	0.81	-1.2763	0.81	-1.2759	0.81	-1.2775
0.88	-1.2488	0.88	-1.2474	0.88	-1.2456	0.88	-1.2357
0.91	-1.2397	0.92	-1.2374	0.92	-1.2380	0.93	-1.2602
0.94	-1.2273	0.95	-1.2257	0.97	-1.2238	0.98	-1.1979
1.00	-1.1985†	1.0	-1.2105†	1.0	-1.2090†	1.0	-1.1386†

† - Extrapolated result

Figure 5.21: Tractions on surface S_2 obtained with t = 0.54, 0.64, 0.73 and 0.81 which corresponds to the Gauss points. (Hollow hemisphere inner radius 0.5m, outer radius 1.0m)

5.5 INCREASING THE EFFICIENCY

In all of the previous calculations the mesh around the x_3-axis was generated using a constant segment length. i.e. the surface was divided into equally spaced segments in φ direction. Normally the number of segments were predefined and a typical value used was 20. The quadrature order used for all the elements except the ones with singularities was constant and it was set to be 8 by 8 or 10 by 10. Such high quadrature orders for elements away from the singularities are not necessary to maintain an acceptable level of accuracy.

Since the bulk of the CPU time is taken by the amount of integration, a scheme was devised to minimize the number of elements in φ direction and also allow the quadrature order of the elements to reduce as they get further away from the singular points. To avoid rapid changes to the element size in φ direction the following was adopted:

- Make all of the elements on $\varphi = 0$ have the same length in φ direction as their length in θ direction. This would make these elements square.
- The first segment is reflected to the opposite side.
- The rest of the surface between the first and the opposite segment is divided into segments which is incremented by 1.0, 1.5, 2.0, 2.5, 3.0 etc. multiplied by the first segment.
- The created mesh is mirror-imaged to the opposite side to form the complete mesh.

Once the number of elements on surface S_1 is set, then the size of each element in θ direction is calculated. By applying the algorithm described above the coordinates for the elements in φ direction are calculated. In this way the total number of elements are greately reduced. Another way that was implemented to reduce the CPU time was to allow variable quadrature orders during the execution of the program. Three levels of quadrature order were set before the execution. Again the mirror image mechanism was used to assign the quadrature orders. The order was reduced as the integration progressed in the

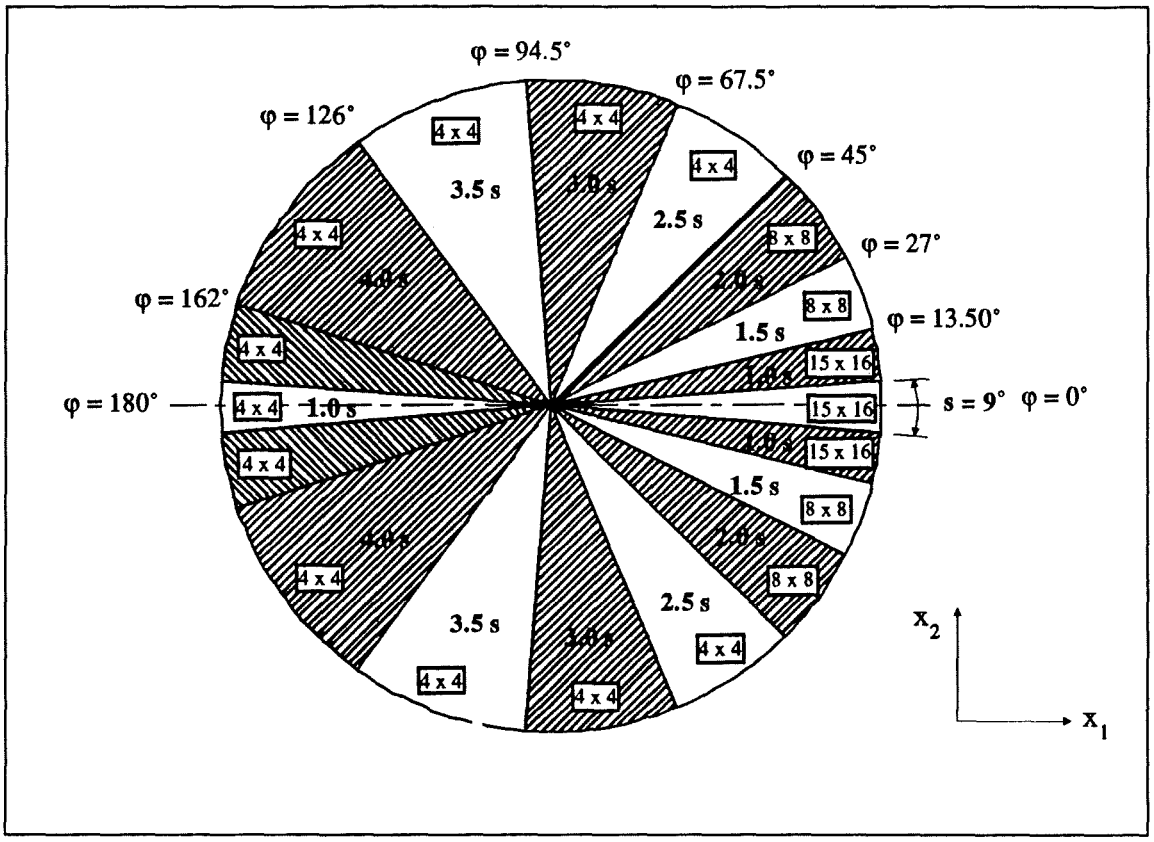

Figure 5.22: A typical allocation of segments in φ direction to reduce the CPU time by allowing incremental segment size based on the element length in θ direction and also variable quadrature order for integration.

counterclockwise direction. The first segment is the one with the singularity and the integration order was set to the highest. This was 16 by 15. The elements, belonging to the segments one before and one after the first segment was also set to this order. The quadrature order for the next two segments was set to 8 by 8 and also for the two segments on the other side. The elements in the rest of the segments were integrated using a 4 by 4 quadrature order. A diagram showing the implementation of the two methods described above is given in Figure 5.22 above.

5.6 THIN WALLED HOLLOW SPHERE

The hollow sphere geometry used in the previous sections had a wall thickness of 0.5 m. Such wall thickness was selected to avoid the problems that may be caused by having long and slender geometry. In this section, the limitation of BEM for dealing with long and slender geometries is investigated.

The cone to be used in Chapter 6 has a wall thickness of 5 mm and a height of 100 mm. This gives an aspect ratio of 20:1. In packages for FEM analysis such as PAFEC, there is a limit to the ratio of longest to the shortest side of an element and this is limited to 5:1. In BEM, there is a limitation for having elements too close to each other. In a short course in BEM applications, Mercy & Trevelyan (1986) gave some guidelines on the ratio of element length to the distance between them. These were based on their experience in FEM applications and they are:

Element Ratio	Advice
> 5 : 1	Avoid.
3 : 1 - 5 : 1	Check results.
< 3 : 1	Normally O.K.
< 2 : 1	O.K.

In the hollow sphere example, when the wall thickness is reduced to 5 mm, the limitation about the distance between the elements on the inner and outer surfaces becomes a major concern. The number of elements have to be increased to reduce the ratio. For convenience, this ratio will be referred to as SOT in this thesis (S over T ; S being the element length and T being the wall thickness).

5.6.1 - Element Size Limitation

To see the significance of the SOT ratio, two tests were conducted. The first was to maintain the hollow sphere dimensions constant and to change the SOT ratio by varying the number of elements on the inner and outer surfaces. The second was to keep the SOT ratio constant and reduce the wall thickness by increasing the inner radius. The aim of this test was to see the effect of having elements too close together.

Table 5.4 shows the summary of the results of the first test. The SOT ratio varied between 1.0 and 3.5. As the element size increased on surfaces S_1 and S_3, the error in the results also increased. The most sensitive results were the horizontal displacements on the surface S_2. Although the averaged displacement results on the surfaces S_1 and S_3 were not as bad as the S_2 displacements, the error in the nodal displacements was much bigger. For

Table 5.4: Summary of results of a hollow hemisphere with various SOT ratios. The dimensions were kept constant. (Inner radius = 0.045m; outer radius = 0.050m)

SOT ratio	No. of Elements on Surface			No. of φ Segments	% Error				System Matrix Size	CPU time (s)
	S_1	S_2	S_3		S_1 disp‡	S_2 disp†	S_3 disp‡	S_2 tractions†		
1.0	16	2	14	21	0.07	0.39	0.01	0.03	132 x 132	987
1.5	10	2	9	17	0.06	4.51	0.13	0.44	88 x 88	639
2.0	8	2	7	15	0.39	16.62	0.49	0.79	72 x 72	410
2.5	6	2	6	13	1.39	41.32	1.47	0.26	60 x 60	275
3.0	5	2	5	13	2.53	58.14	2.75	1.14	27 x 27	205
3.5	4	2	4	11	3.98	57.54	4.15	1.22	23 x 23	141

‡ - Results are averaged over the surface concerned.
† - Results are taken at the midside node along the surface S_2.

example, for the SOT=3.5, the S_1 displacement at $\theta = 0°$ resulted in +10.2% of error and at the other end -27.9% of error. However, when all the results were averaged, the errors were minimized and gave only an average error of 3.98%. This implies that averaging of the results cannot be used as a good measure of the reliability of the error estimates. Therefore, inspection of all the results are necessary and these can be seen in Figures 5.23-5.26. According to these figures, the best results are obtained at SOT=1.0 and the worst results at SOT=3.5. From Table 5.4, the surface tractions on S_2 show small errors for all the SOT ratios. This can be explained by inspecting Figure 5.26. The errors are almost symmetric about the midside node and of opposite sign. As the results are given at this midside node, such small errors are expected.

All the graphs shown in Figures 5.23-5.26, with the exception of Figure 5.24, show curves meeting at a certain point. On S_1 displacements, this is about 68°, for S_3 displacements this is at 22° and for the tractions on surface S_2 the cross-over point is at half-way along the thickness. This pattern is not present for the S_2 displacements. In this case, the whole curve is displaced away from the ideal curve and none of the curves cut the analytical curve.

In a similar investigation which involved a 2-D axisymmetric formulation, Bakr (1983) showed that for a hollow sphere, SOT ratio of 5.0 can be tolerated if 10 Gauss points are used. He also shows that in the absence of sharp edges or corners, averaged errors of less than 1% is possible. In the presence of a sharp corner, Bakr advises not to exceed the ratio of 2.0. In the hollow hemisphere example, shown in this chapter, where there are two sharp corners, it is shown that even with an SOT ratio of 2.0, nodal errors of upto 13% can be expected for the inner and outer surface displacements, whereas the average error for these are less than 0.5%.

Based on the findings shown in this section, the SOT ratio of 1.0 is recommended for thin sections with sharp corners and where the accuracy of the results across the wall thickness is important. Otherwise SOT ratio of 1.5 can be used if the errors of about 5% across the wall thickness can be allowed.

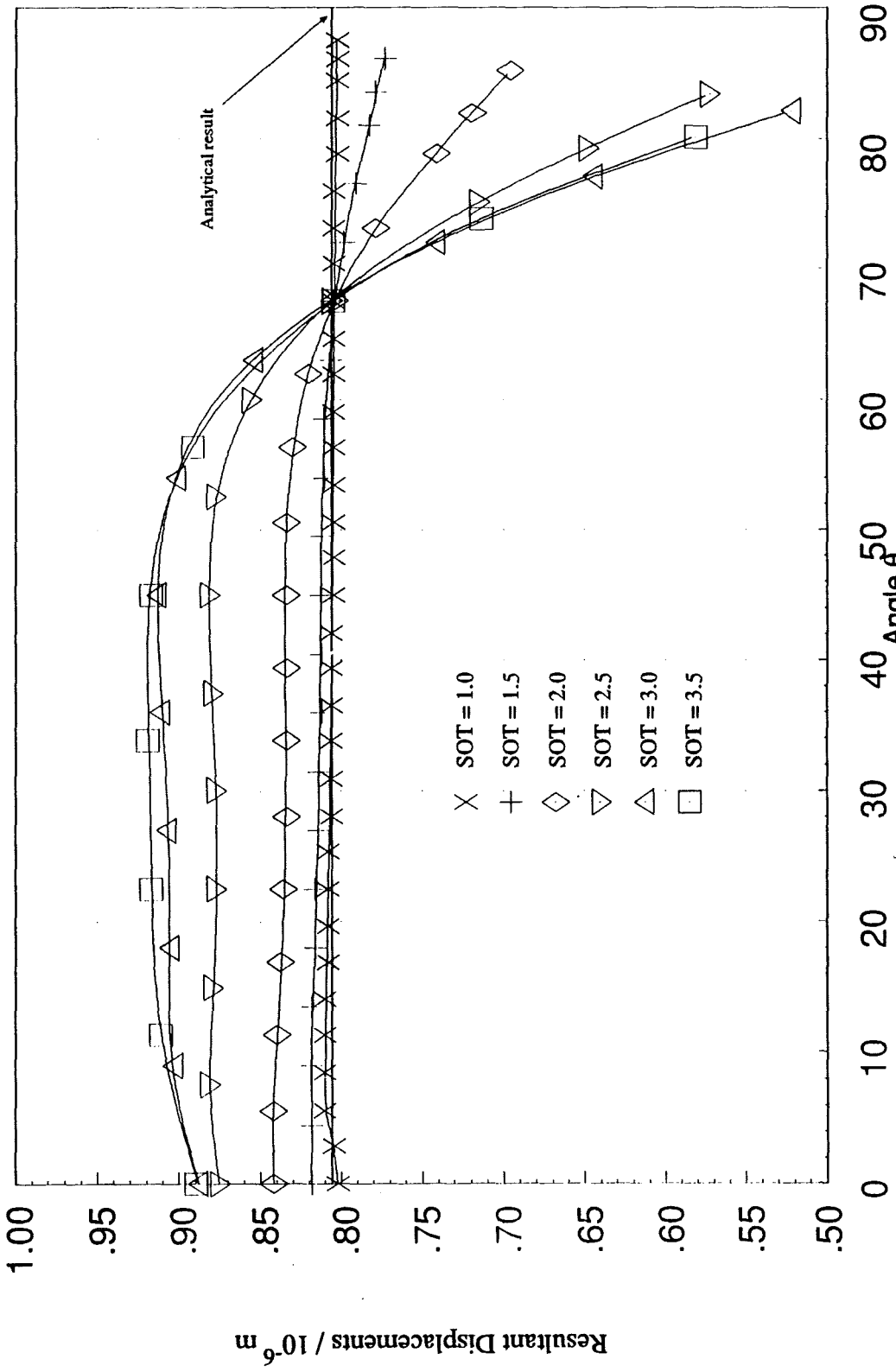

Figure 5.23: Resultant displacements on surface S_I obtained with different values of the ratio SOT for the hollow hemisphere. (Hollow hemisphere inner radius 0.045m, outer radius 0.05m)

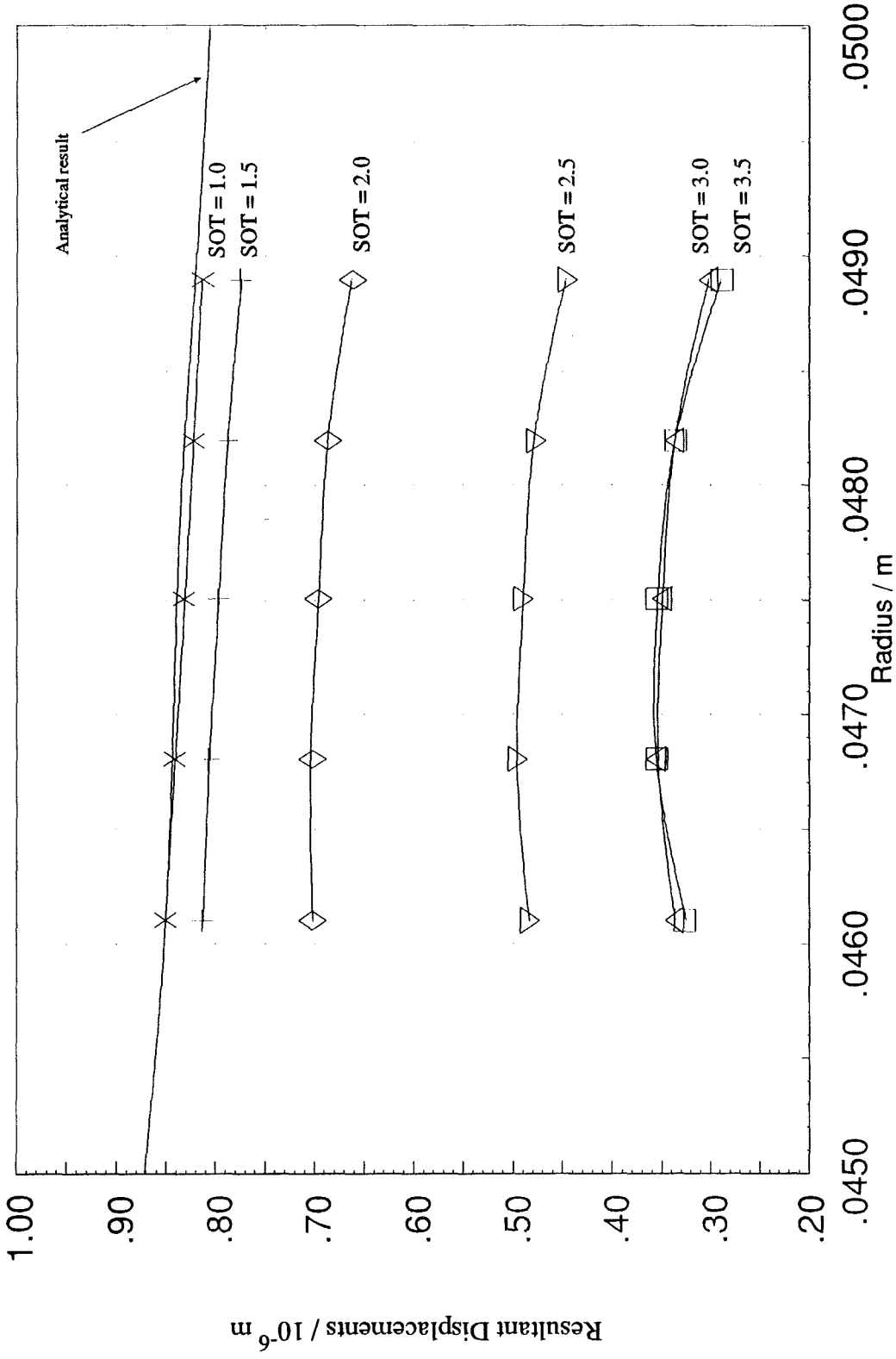

Figure 5.24: Horizontal displacements on surface S_2 obtained with different values of the ratio SOT for the hollow hemisphere. (Hollow hemisphere inner radius 0.045m, outer radius 0.05m)

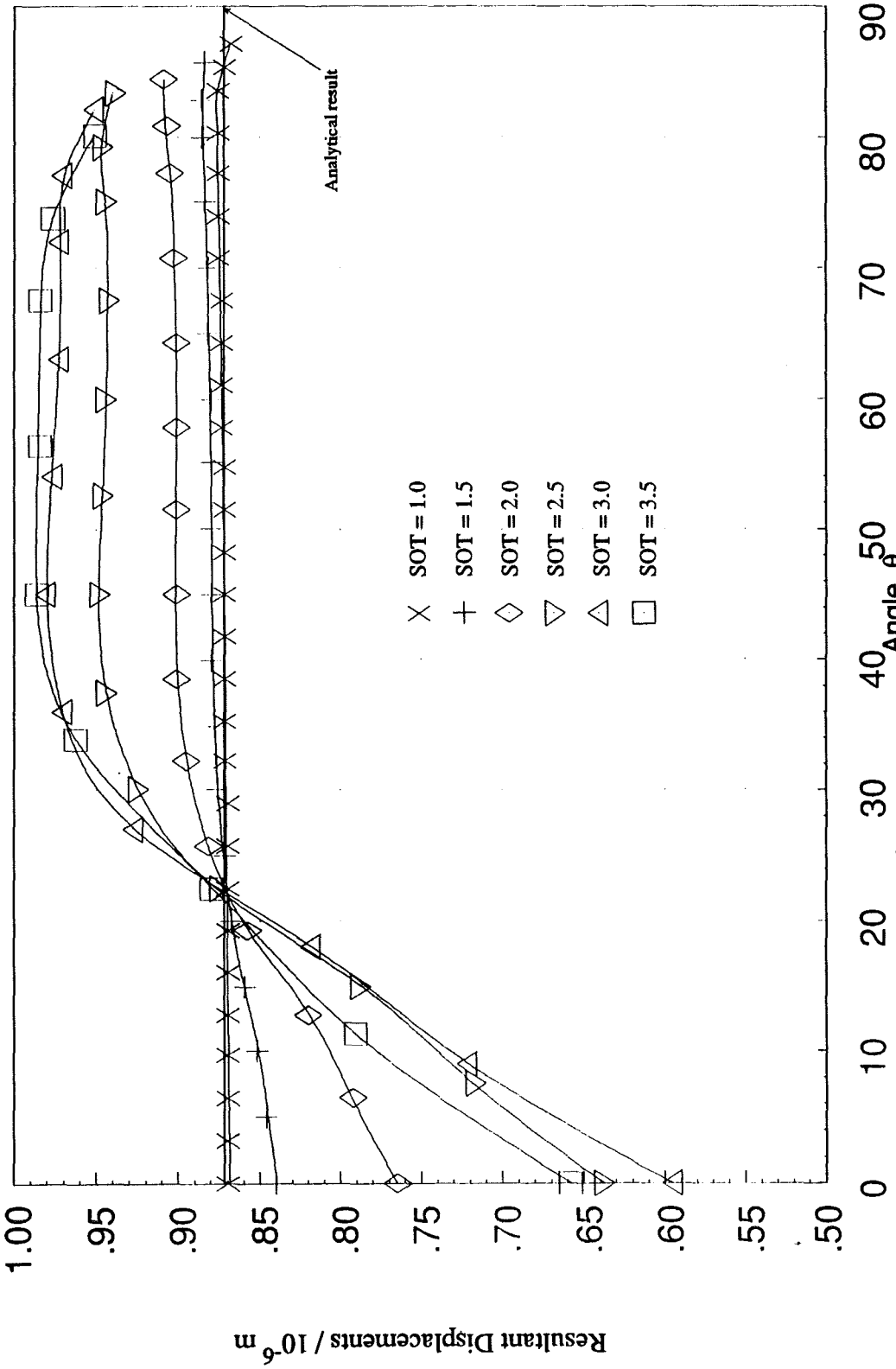

Figure 5.25: Resultant displacements on surface S_3 obtained with different values of the ratio SOT for the hollow hemisphere. (Hollow hemisphere inner radius 0.045m, outer radius 0.05m)

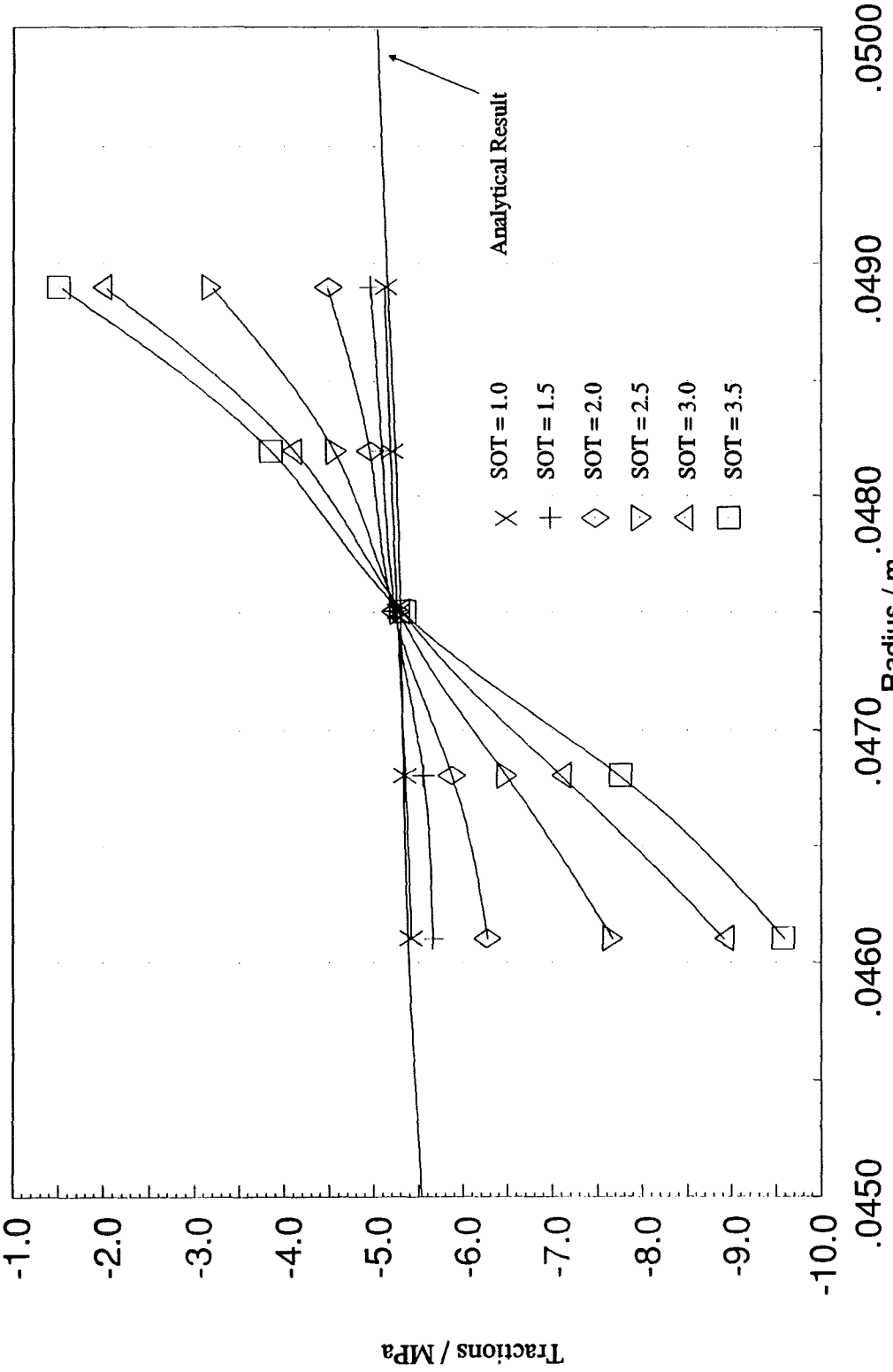

Figure 5.26: Tractions on surface S_2 obtained with different values of the ratio SOT for the hollow hemisphere. (Hollow hemisphere inner radius 0.045m, outer radius 0.05m)

Table 5.5: Summary of results of a hollow hemisphere with various inner radii. The outer radius dimension was kept constant at 0.050 m.

Inner radius m	SOT ratio	No. of Elements on Surface			No. of φ Segments	% Error				System Matrix Size	CPU time (s)
		S_1	S_2	S_3		S_1 disp‡	S_2 disp†	S_3 disp‡	S_2 tractions†		
0.030	0.8	5	2	3	11	0.35	1.24	0.08	0.10	44 x 44	141
0.035	0.8	7	2	5	13	0.20	0.82	0.04	0.12	60 x 60	275
0.040	0.8	10	2	8	17	0.09	0.53	0.03	0.09	84 x 84	590
0.045	0.8	20	2	18	23	0.08	0.23	0.03	0.08	164 x 164	2516
0.046	1.0	20	2	18	23	0.09	0.33	0.05	0.03	164 x 164	2513
0.047	1.0	26	2	25	27	0.11	0.32	0.08	0.05	216 x 216	4640
0.048	1.0	39	2	38	35	Singular matrix				320 x 320	8036
0.049	1.0	79	2	77	49	Data storage problems				636 x636	-

‡ - Results are averaged over the surface concerned.
† - Results are taken at the midside node along the surface S_2.

The findings of the second test, where the SOT ratio was kept constant and the wall thickness was reduced by increasing the inner radius, are given in Table 5.5. All of the results have a very low percentage of error in their averaged values. However, when the nodal values are examined in Figures 5.27-5.30, it is clear that such small percentage of errors are not just confined to the averaged values but to all of the nodal values too. Selection of the SOT ratio of 0.8 and 1.0 which were used for the second test proved that reliable and accurate results can be expected for small and large wall thicknesses.

Tests of wall thicknesses from 20mm down to 3mm showed very similar error values and this again reflects the importance of the role that SOT ratio plays when dealing with thin and long structures where elements are close together. It is also interesting to see that there was no sign of interference from the two sharp corners on all the results shown in Figures 5.27-5.30.

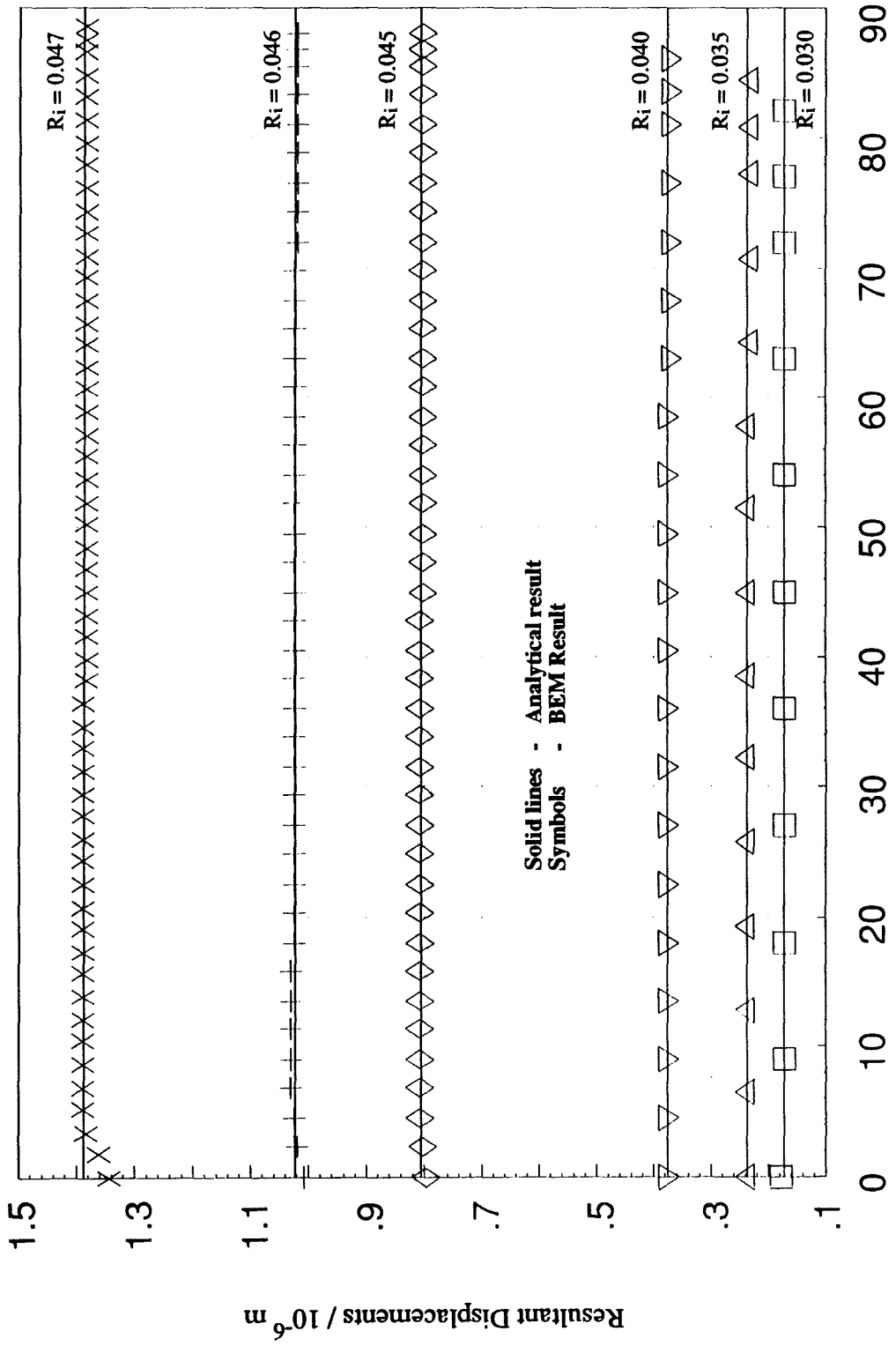

Figure 5.27: Resultant displacements on surface S_1 obtained with different wall thicknesses for the hollow hemisphere. (Hollow hemisphere outer radius was maintained at 0.05m. SOT ratio was maintained constant - see Table 5.5)

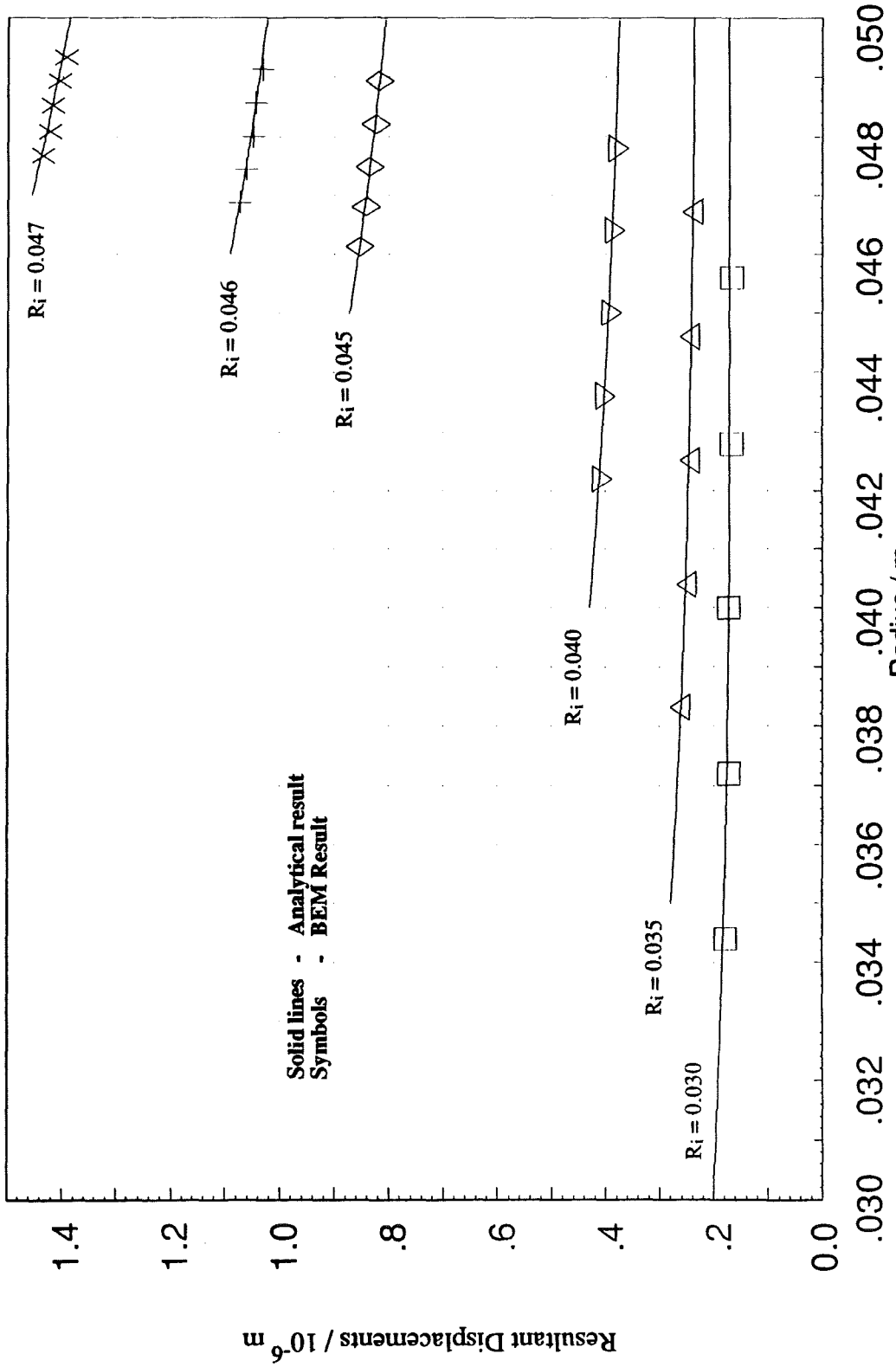

Figure 5.28: Horizontal displacements on surface S_2 obtained with different wall thicknesses for the hollow hemisphere. (Hollow hemisphere outer radius was maintained at 0.05m. SOT ratio was maintained constant - see Table 5.5)

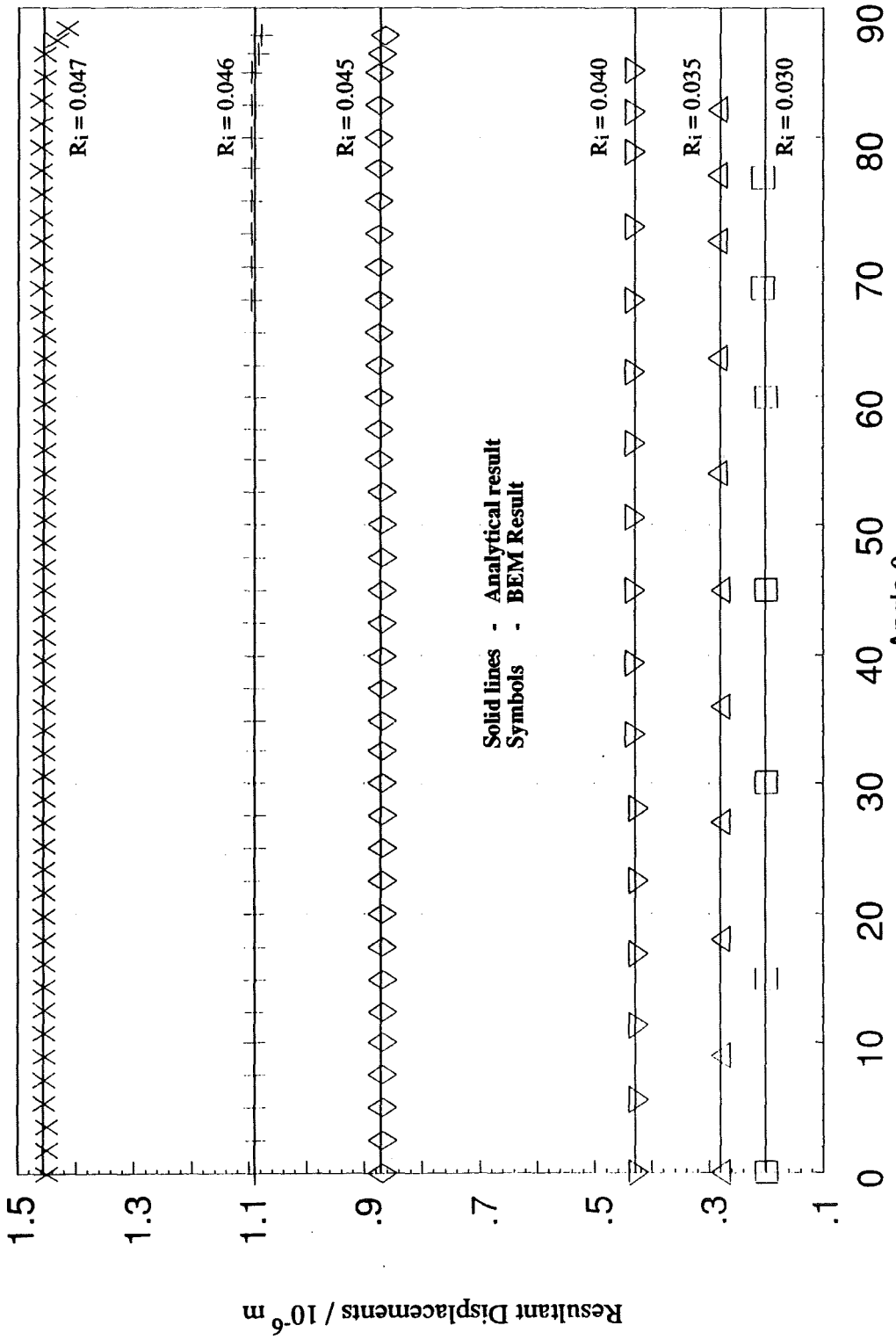

Figure 5.29: Resultant displacements on surface S_3 obtained with different wall thicknesses for the hollow hemisphere. (Hollow hemisphere outer radius was maintained at 0.05m. SOT ratio was maintained constant - see Table 5.5)

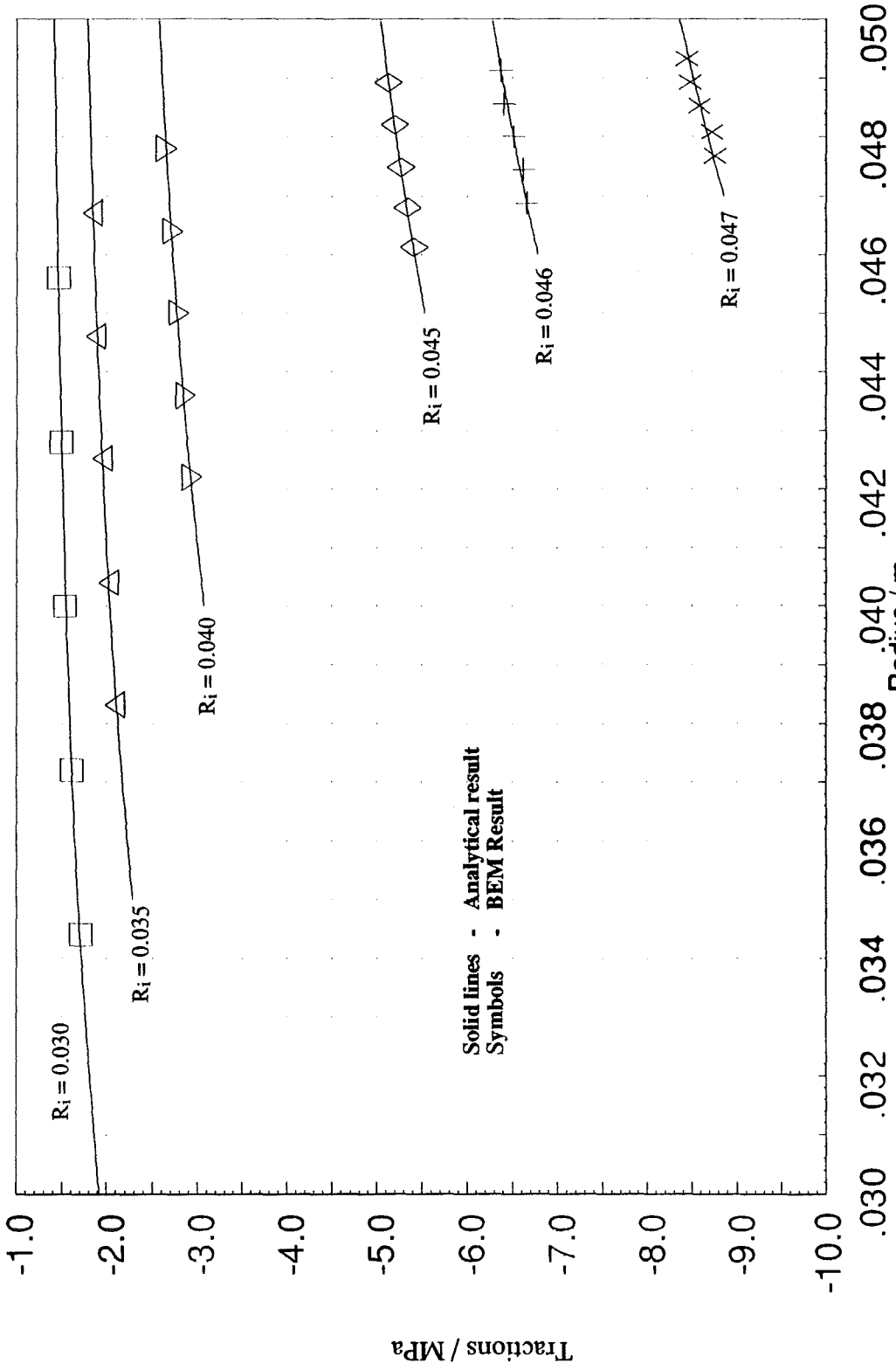

Figure 5.30: Tractions on surface S_2 obtained with different wall thicknesses for the hollow hemisphere. (Hollow hemisphere outer radius was maintained at 0.05m. SOT ratio was maintained constant - see Table 5.5)

5.6.2 - Limitation of the System Matrix

Selection of small SOT ratios, such as 1.0, forces a large number of elements to be generated and this is reflected in the CPU times (see Table 5.5). Storage of large files can also cause some problems and may result in the termination of the analysis.

Further reduction of the wall thickness was not possible for two reasons. The first cause was found when an attempt was made to run the analysis with a wall thickness of 2mm. Although the calculation of the system matrix was not a problem, the solution of this matrix was not possible because of many similar rows being generated and this caused the matrix to be singular.

The second cause that prevented testing the hollow hemisphere became apparent when the wall thickness was set to 1mm. Before running into problems of having similar rows in the system matrix, there was demand for an unrealistic amount of storage area needed for the system matrix. At the time of running out of disk storage, the CPU time required to determine the system matrix was so large that it was decided to abandon the testing at this stage. There was also every chance of obtaining another singular system matrix.

Chapter

6

BEM For A Cone

"Why does this magnificent applied science which saves work and makes life easier bring us so little happiness? The simple answer runs: Because we have not yet learned to make sensible use of it."

Albert Einstein

1931

6.1 - INTRODUCTION

Analysis of a nose cone has been the main concern in this thesis. The work presented in this chapter uses the findings described in the previous chapters, and these are applied to a nose cone. All of the work presented in the previous chapters are systematically implemented in this chapter.

As the analysis of the nose cone is the prime object of this thesis, the BEM formulation developed so far is fully implemented and a comprehensive set of results are obtained. This includes surface displacements, internal displacements, and internal and surface stresses. All of these results are calculated directly with the exception of the surface stresses. These are calculated from the surface displacements using natural cubic splines.

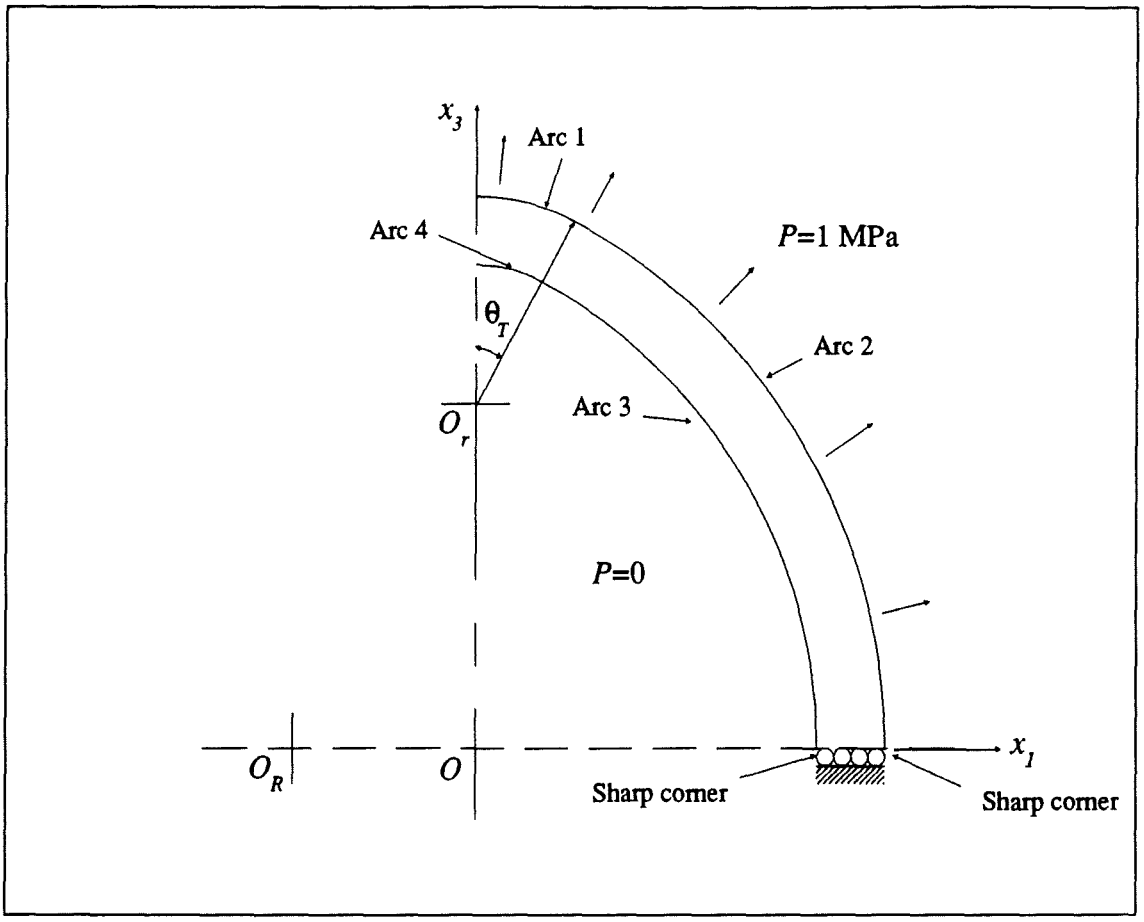

Figure 6.1: Profile and boundary conditions of a nose cone used for the analysis

The profile of the nose cone used in this chapter is made of two circular arcs for the outer surface and two circular arcs for the inner surface. Arc 1and arc 2 form the outer surface S_1 whereas arc 3 and arc 4 form the inner surface S_3. These surfaces are joined by surface S_2 (see Figure 6.1).

Again, a uniform external pressure of 1MPa is exerted in the outwards direction. The vertical displacements of the structure on surface S_2 are restrained in the x_3 direction and only the horizontal movement is allowed in x_1 and x_2 directions along the surface S_2.

Semi-continuous quadratic elements are used at the two sharp corners, and continuous quadratic elements for the rest of the structure. The number of segments are again determined by the method described in section 5.5 in order to maintain square elements around the path where the nodes are placed.

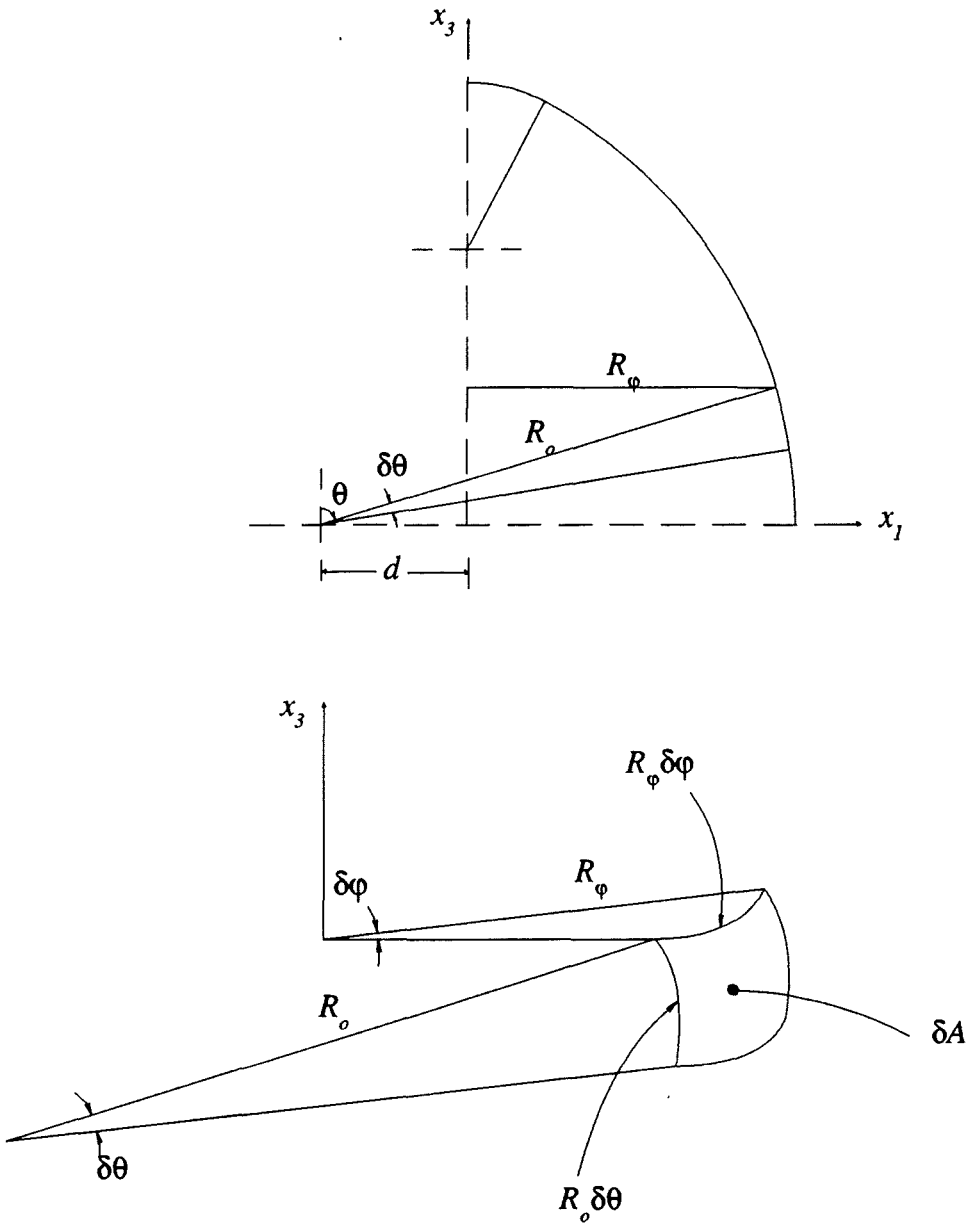

$$R_\varphi = R_o \sin\theta - d$$

$$\delta A = R_\varphi \delta\varphi R_o \delta\theta$$

$$\delta A = (R_o \sin\theta - d)\, R_o \delta\varphi\delta\theta$$

Figure 6.2: Diagram showing the parameters used in the calculation of the jacobian for the large arc of the cone.

6.2 - BEM IMPLEMENTATION OF A CONE

The implementation of the BEM to a nose cone is shown in this section. The formulation is very similar to the one used for the hollow sphere in Chapter 5. However, as there are two separate arcs for the inner and outer surfaces, slightly different equations are used, as each arc had a different origin. For arcs 1 and 4, the origin for the integration purpose is taken at O_r and for arcs 2 and 4 at O_R (see Figure 6.1).

The BEM equation for the cone is similar to Equation (5.1) with the following exceptions. The integrals involving the surface S_1 and the surface S_3 are broken down to two separate integrals to deal with the two separate arcs that form these surfaces. This of course required different jacobians for these integrals. The jacobians for the arcs 1 and 4 present no difficulty as their origin is on the axis of rotation, x_3, and these are $r_o^2 \sin^2\theta$ and $r_i^2 \sin^2\theta$ respectively, where r_i and r_o represent the radii for these arcs.

The origin of the large arcs 2 and 3 is a distance d away from the rotation axis. As the integration advances in the φ direction, the location of this origin varies with the angle φ. To take this effect into account, a new variable R_φ is defined which will enable the rotation of the origin of the large arcs (see Figure 6.2). For a given point on arc 2, the following can be written:

$$dA = (R_o \sin\theta - d)\, R_o d\varphi d\theta \tag{6.1}$$

Similarly for a point on arc 3 the jacobian becomes:

$$dA = (R_i \sin\theta - d)\, R_o d\varphi d\theta \tag{6.2}$$

The values of R_o, R_i, r_o, r_i and d are calculated before hand. Details of these are given in Appendix B and are further discussed in section 6.3.

The integration on the surface S_2 is unchanged. When the above equations are implemented for all the surfaces, the complete BEM equation for the horizontal component of the surface displacements and tractions can be written as follows:

$$
\begin{aligned}
&\frac{1}{2} u_1^i + \int_{Arc_1} (u_1 p_{11}^* + u_2 p_{12}^* + u_3 p_{13}^*)\, r_o^2 \sin\theta d\theta d\varphi \\
&\quad + \int_{Arc_2} (u_1 p_{11}^* + u_2 p_{12}^* + u_3 p_{13}^*)\, (R_o \sin\theta - d)\, R_o d\theta d\varphi \\
&\quad + \int_{S_2} (u_1 p_{11}^* + u_2 p_{12}^*)\, \rho d\rho d\varphi - \int_{S_2} w_{13} \hat{p}_3\, \rho d\rho d\varphi \\
&\quad + \int_{Arc_3} (u_1 p_{11}^* + u_2 p_{12}^* + u_3 p_{13}^*)\, (R_i \sin\theta - d)\, R_i d\theta d\varphi \\
&\quad + \int_{Arc_4} (u_1 p_{11}^* + u_2 p_{12}^* + u_3 p_{13}^*)\, r_i^2 \sin\theta d\theta d\varphi \\
&\quad = \int_{Arc_1} (w_{11} p_1 + w_{12} p_2 + w_{13} p_3) r_i^2 \sin\theta d\theta d\varphi \\
&\quad + \int_{Arc_2} (w_{11} p_1 + w_{12} p_2 + w_{13} p_3)\, (R_i \sin\theta - d)\, R_i d\theta d\varphi
\end{aligned}
\tag{6.3}
$$

Numerical implementation of the Equation (6.3) is identical with the hollow hemisphere in Chapter 5. Quadratic elements are used for the mesh and the system equations are determined as before. As all the knowns are on the R.H.S. and all the unknowns are arranged to be on the L.H.S. of the Equation (6.3), no real problem is encountered in forming the A x = b.

6.3 - COORDINATE GENERATION FOR THE CONE

The geometry of the nose cone used in this chapter is formed by taking two arcs of two different size circles and merging these two arcs at a common tangent to form the outer surface. The inner surface is also formed in a similar way by choosing smaller radii for the other two arcs. These two surfaces are rotated about the vertical axis, x_3 to form the cone.

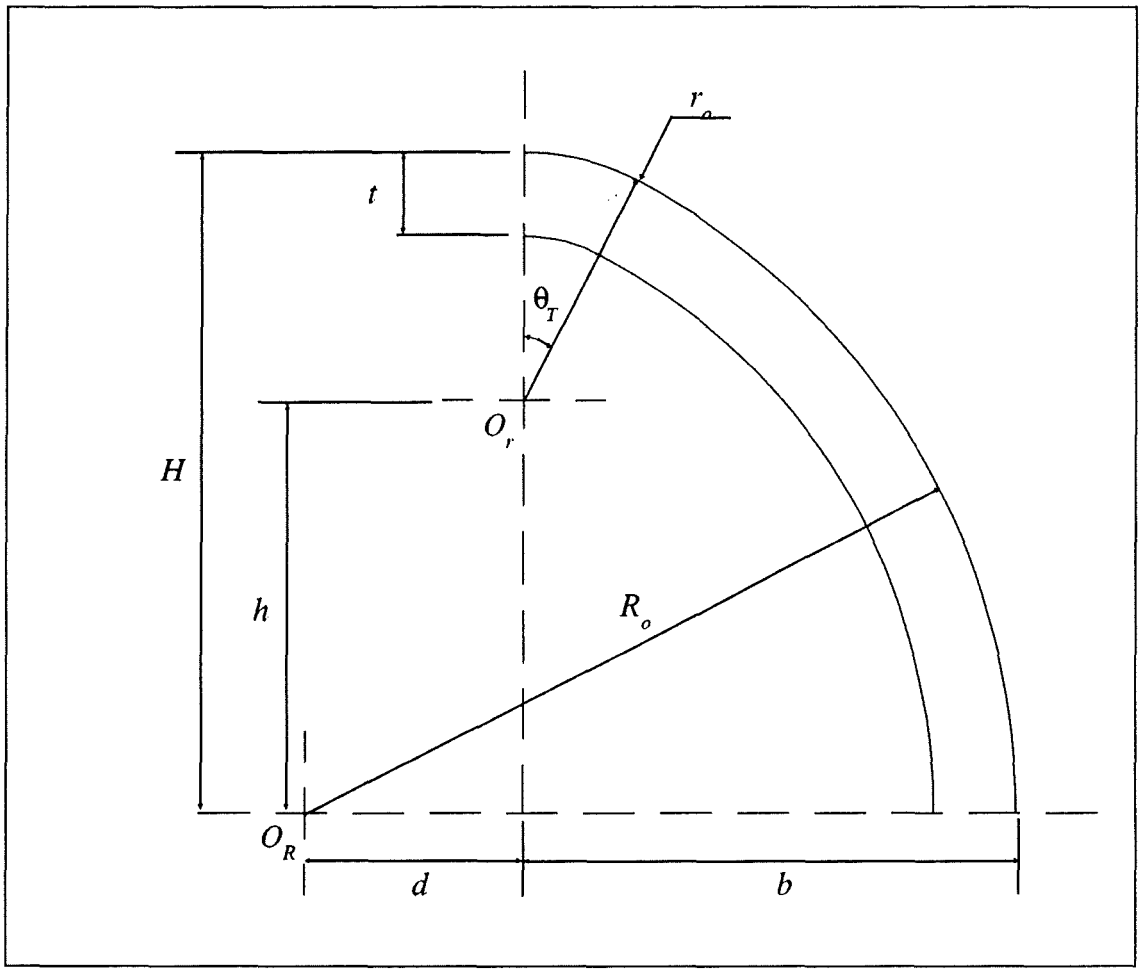

Figure 6.3: Parameters used in the determination of the cone geometry.

The height of the cone, H, the base radius b and the tip radius r_o are specified to form the outer surface. With these parameters known, Equation (6.4) is used to find a suitable large arc. Given the wall thickness, the inner surface can also be formed (see Figure 6.3) to generate the nose cone.

$$R_o = \frac{b^2 + h^2 - r_o^2}{2\,(b - r_o^2)} \tag{6.4}$$

$$d = R_o - b \tag{6.5}$$

$$\theta_T = \tan^{-1}\frac{d}{h} \tag{6.6}$$

Because of the different origins for different surfaces, new equations for the coordinates of the nodes are calculated as follows. For the outer large arc, arc 2:

$$x_1^i = R_o \sin\theta_i - d \tag{6.7}$$

$$x_2^i = 0 \tag{6.8}$$

$$x_3^i = R_o \cos\theta_i \tag{6.9}$$

$$x_1^j = (R_o \sin\theta_j - d)\cos\varphi_j \tag{6.10}$$

$$x_2^j = (R_o \sin\theta_j - d)\sin\varphi_j \tag{6.11}$$

$$x_3^j = R_o \cos\theta_j \tag{6.12}$$

For the small arc, arc 1, the coordinates are:

$$x_1^i = r_o \sin\theta_i \tag{6.13}$$

$$x_2^i = 0 \tag{6.14}$$

$$x_3^i = r_o \cos\theta_i + h \tag{6.15}$$

$$x_1^j = r_o \sin\theta_j \cos\varphi_j \tag{6.16}$$

$$x_2^j = r_o \sin\theta_j \sin\varphi_j \tag{6.17}$$

$$x_3^j = r_o \cos\theta_j + h \tag{6.18}$$

Similar equations are written for the nodes on the arcs 2 and 3 by replacing r_o with r_i and R_o with R_i. The equations for calculating the coordinates on surface S_2 is not changed.

6.4 - SURFACE DISPLACEMENTS

This section concentrates on the surface displacements and the tractions on the surface S_2. Results are given for cones of 10 and 5 mm wall thicknesses and a height of 80mm. Further tests with various cone heights were conducted and for all the cones tested, base radius was selected to be 60mm.

6.4.1 - BEM Model

Equation (6.2) was implemented using quadratic elements to determine the unknown surface displacements and the tractions. The same integration procedure described in Chapter 5 was used and also the SOT ratio of 1.0 was maintained when generating the mesh.

Initially, a 10mm wall thickness and a base radius of 60mm and a cone height of 80mm was tested. The mesh used for this structure involved 4 elements on arcs 1& 4 and 10 elements on arcs 2 & 3. On the flat surface, surface S_2, 2 elements were used. The number of segments generated around the φ direction was based on the element size on arc 2, which was around 20 segments (see Figure 6.4). A similar mesh was created for the 5mm wall thickness and this is shown in Figure 6.5 with 3 elements on arcs 1& 4 and 16 elements on arcs 2 & 3. Surface S_2 was divided into 2 elements.

There was no analytical solution or experimental result available for the geometry generated. The only way to check these results was to compare them against another method, even though some disagreements were expected. Therefore, the same problem was modelled using the same mesh in a finite element package, namely PAFEC®. The results were then compared. Once satisfied with the comparison, further analysis was performed on the cone, such as different wall thicknesses and aspect ratios of height and base radius. These are discussed in section 6.6.

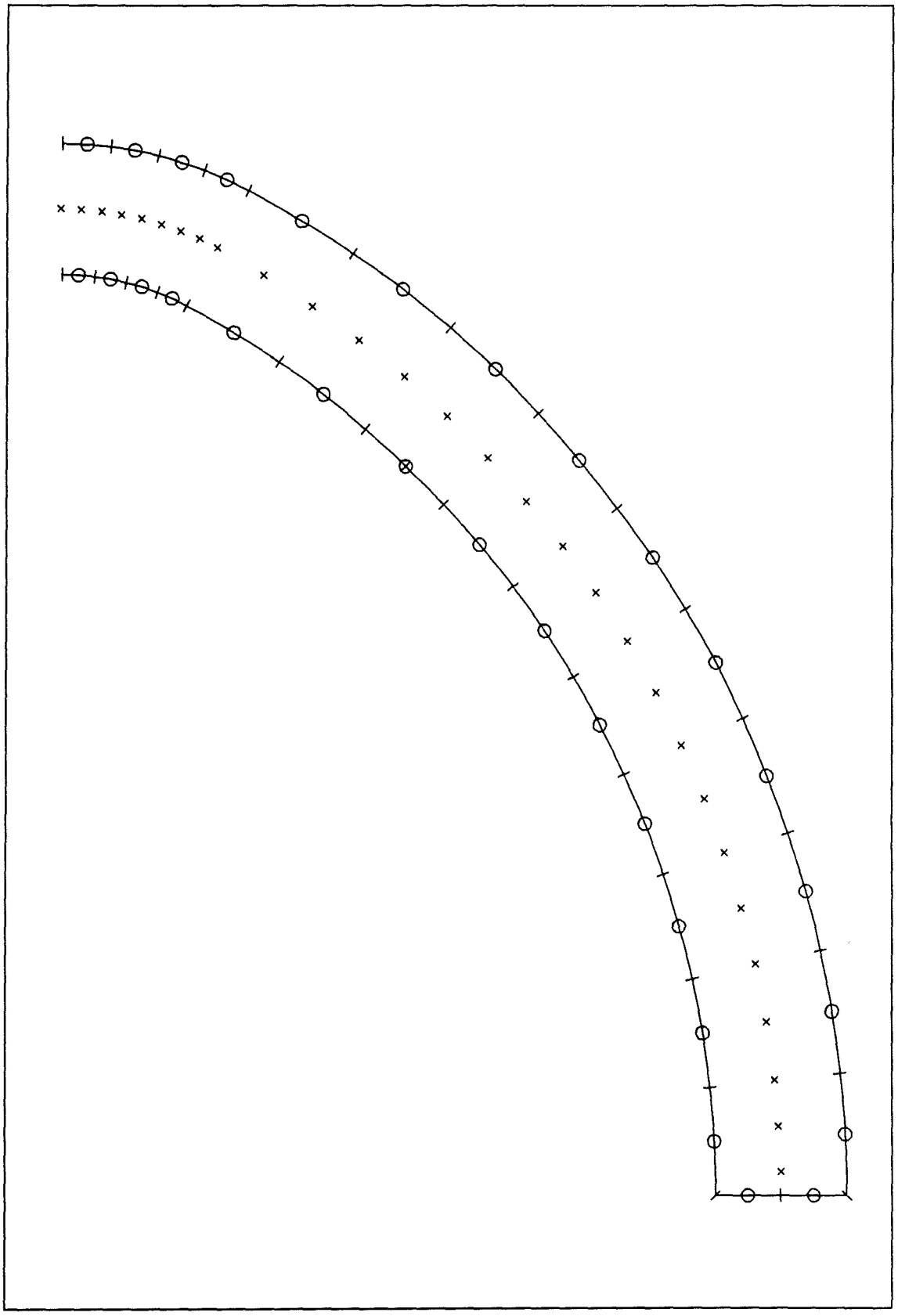

Figure 6.4: TheBEM mesh used for the cone with 10 mm wall thickness. Inner and outer surfaces were divided into 14 and the base surface was divided into 2 quadratic elements. Initially, the internal points were distributed along the mid-wall. Semi-continuous corner elements are not shown in this mesh.

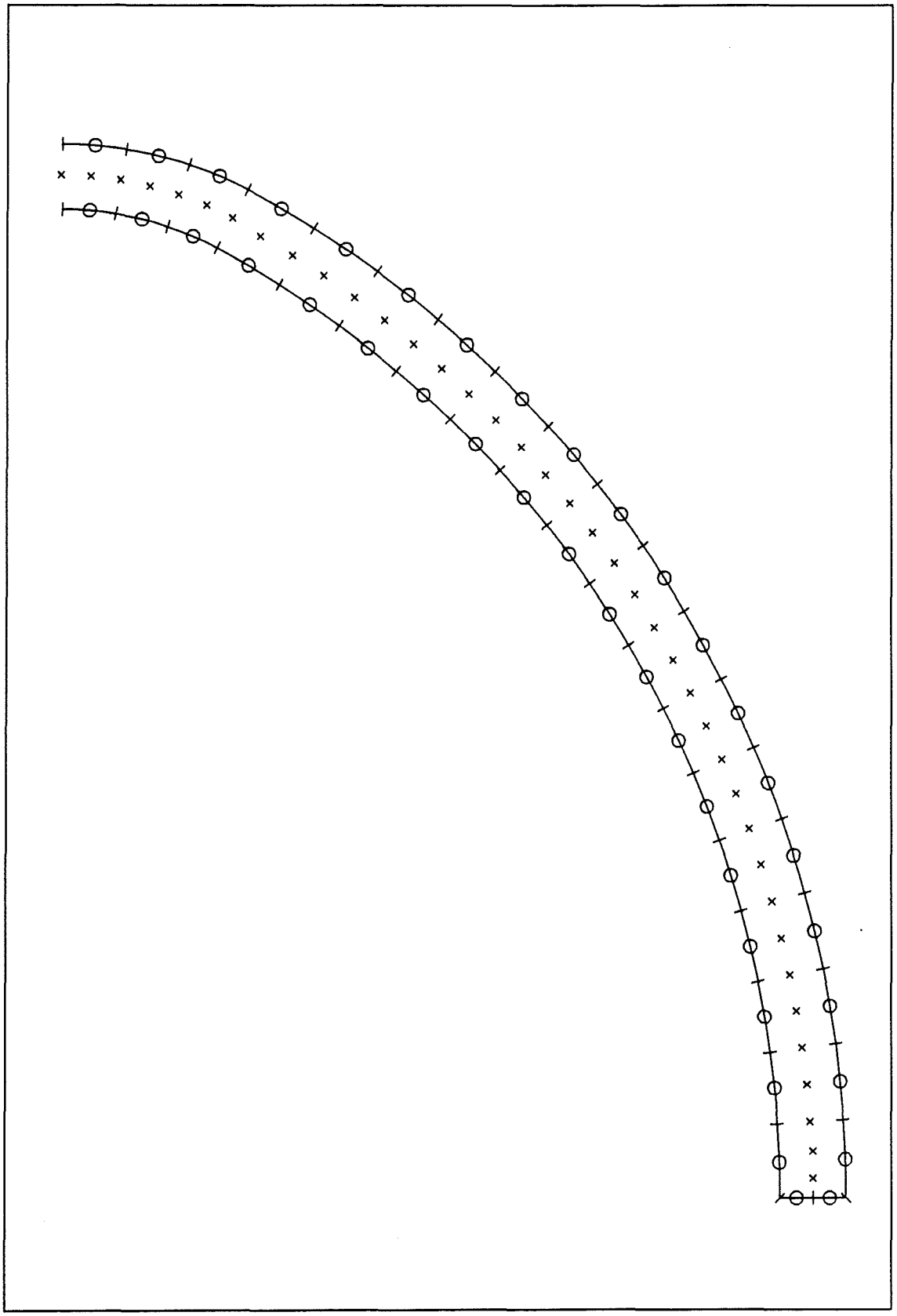

Figure 6.5: The BEM mesh used for the cone with 5 mm wall thickness. Inner and outer surfaces were divided into 19 and the base surface was divided into 2 quadratic elements. Initially, the internal points were distributed along the mid-wall. Semi-continuous corner elements are not shown in this mesh.

6.4.2 - FEM Model

The Pafec FEM model contained 28 8-noded isoparametric rectangular elements of type 36210. The analysis was done in 2-D axisymmetric mode so that the vast amount of data generated by the Pafec program was minimized. A typical mesh is shown in Figure 6.6.

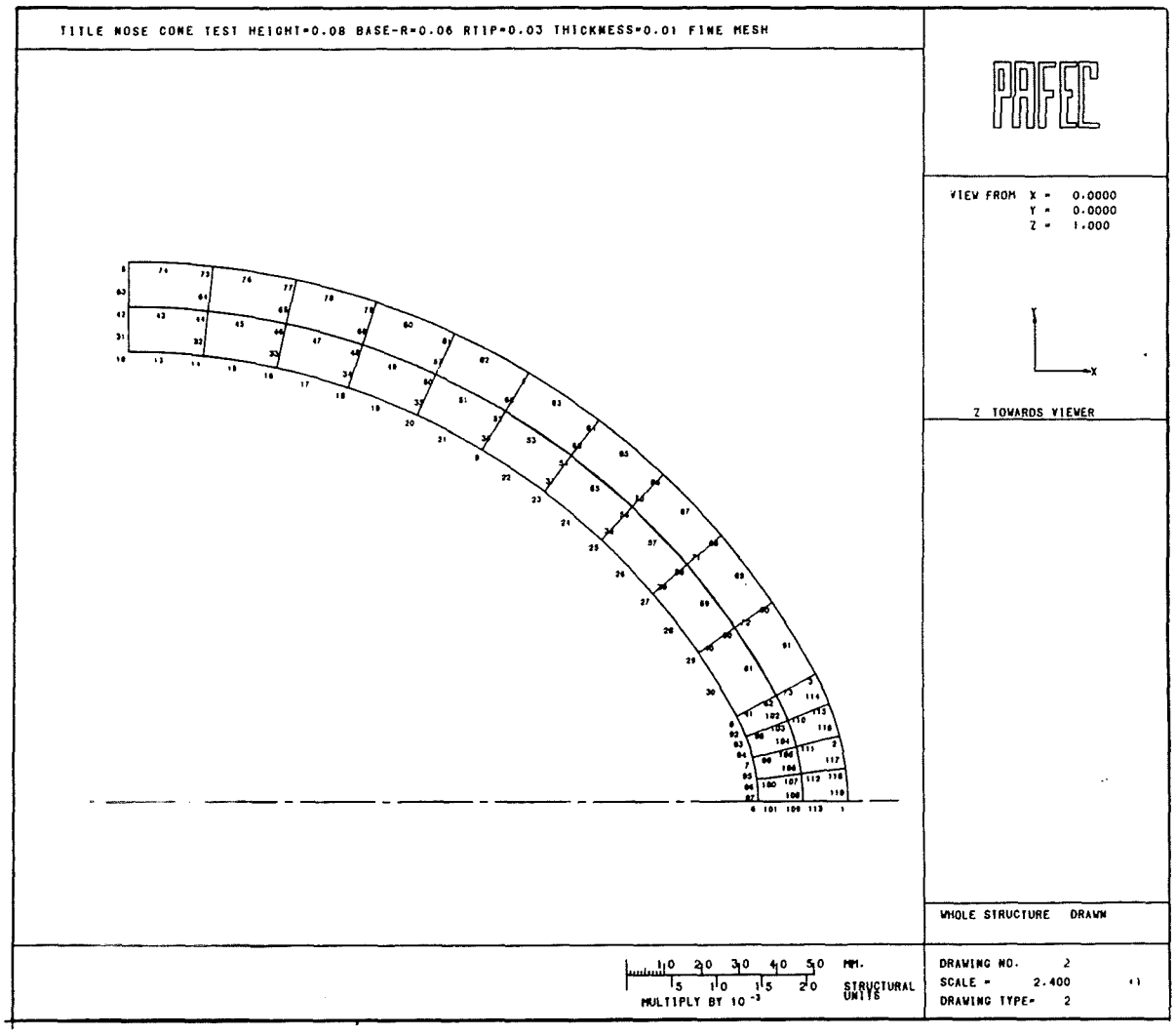

Figure 6.6: The FEM mesh used for comparing the BEM results. Care was taken to maintain the same nodal positions as the BEM mesh shown in Figure 6.4 for direct comparison.

6.5 - INTERNAL DISPLACEMENTS

The formula for the internal displacements is similar to Equation (2.53). However, this equation is written for one continuous surface and in the presence of body forces. Equation (2.53) can easily be modified for the cone used in this chapter to take into account of the different surfaces and arcs. In the absence of body forces, the equation giving the internal displacements in x_1 direction, at any point within the cone wall, is:

$$
\begin{aligned}
u_1^i = & \int_{Arc_1} (w_{11}p_1 + w_{12}p_2 + w_{13}p_3) r_i^2 \sin\theta d\theta d\varphi \\
& + \int_{Arc_2} (w_{11}p_1 + w_{12}p_2 + w_{13}p_3)\,(R_i \sin\theta - d)\, R_i d\theta d\varphi \\
& - \int_{Arc_1} (u_1 p_{11}^* + u_2 p_{12}^* + u_3 p_{13}^*)\, r_o^2 \sin\theta d\theta d\varphi \\
& - \int_{Arc_2} (u_1 p_{11}^* + u_2 p_{12}^* + u_3 p_{13}^*)\,(R_o \sin\theta - d)\, R_o d\theta d\varphi \\
& - \int_{S_2} (u_1 p_{11}^* + u_2 p_{12}^*)\, \rho d\rho d\varphi - \int_{S_2} w_{13}\hat{p}_3\, \rho d\rho d\varphi \\
& - \int_{Arc_3} (u_1 p_{11}^* + u_2 p_{12}^* + u_3 p_{13}^*)\,(R_i \sin\theta - d)\, R_i d\theta d\varphi \\
& - \int_{Arc_4} (u_1 p_{11}^* + u_2 p_{12}^* + u_3 p_{13}^*)\, r_i^2 \sin\theta d\theta d\varphi
\end{aligned}
\tag{6.19}
$$

A similar equation can also be written for the displacements in the x_3 direction (u_3^i). The variables p_1, p_2 and p_3 are the components of the external pressure. When Equation (6.19) is implemented, these can be written in terms of the resultant external pressure using Equation (3.7).

The numerical results of these displacements are given at various distances away from the inner wall surface for both the 10mm and 5mm wall thicknesses. Comparisons are also made with the FEM results for the internal displacements at mid-wall position and they are given in Section 6.6.

6.6 - COMPARISON OF BEM AND FEM DISPLACEMENTS

The following results are determined for a cone of height 80mm, base radius of 60mm, tip radius of 30mm and wall thicknesses of 10mm and 5mm. The results for the 10mm and 5mm wall thicknesses are given in sections 6.6.2 and 6.6.3 respectively.

The displacements are compared at various parts of the cone. These include the surfaces S_1, S_2 and S_3. Displacements along $\theta = 0°$ and $\theta = \theta_T$ are also compared. Tractions on surface S_2 are also shown. On all the graphs, centred symbols represent the point results obtained by the BEM and the cubic spline fitted solid lines represent the FEM results.

6.6.1 - Optimising Node Positions

In Chapter 5 it was shown that for a Gauss order of 16, the optimum position for the semi-continuous element node is to use t=0.64. However, in this chapter the highest Gauss order was 12. Therefore new t value was required for the optimum results. Tests similar to those in Chapter 5 were conducted to establish the optimum position of the end node of the semi-continuous element. In this case the actual cone geometry was used and the results were compared against the FEM ones. Test were conducted for the t values of 0.56, 0.68

Table 6.1: Comparison of the extrapolated results at the corner nodes with various t values.

Description	% Error			
	$t = 0.56^{\dagger}$	$t = 0.56^{\ddagger}$	$t = 0.68^{\ddagger}$	$t = 0.79^{\ddagger}$
S_1 disps. - outer corner	1.02	0.46	0.76	0.72
S_2 disps. - outer corner	1.95	0.43	0.60	1.35
S_2 disps. - inner corner	1.06	0.46	0.59	0.90
S_3 disps. - inner corner	0.65	0.34	0.44	0.61
S_2 tractions - outer corner	1.83	1.70	1.49	5.90
S_2 tractions - inner corner	2.42	1.24	2.47	2.69

† - 4 elements on surface S_2
‡ - 2 elements on surface S_2

and 0.79. The results are illustrated in Figures E.1-E.4 in Appendix E and a summary is also given in Table 6.1. For the Gauss order of 12, the optimum results were obtained with the t value of 0.56.

The effect of having too many elements on the S_2 surface was also investigated. For t=0.56, the S_2 surface was divided into 2 and 4 elements. Since the wall thickness was only 10 mm, having 4 elements caused some deficiencies in the corner areas. The results of S_2 surface having 4 elements are illustrated in the Figures E.5-E.7 in Appendix E, and also a comparison is given in Table 6.1.

6.6.2 - Wall thickness = 10mm

The following results shown in Figures 6.7, 6.8, 6.9 and 6.10 are for a cone with 10mm wall thickness and compare very well with the FEM results.

The problem of selecting internal points too close to the surface is shown well in Figure 6.10, particularly when nodes are placed 1mm away from both surfaces. The sign of oscillations developing in these results is very clear.

It is a general belief that the distance between the internal points and the surface should be greater than the size of the surface elements. However, it is shown in Figure 6.10 that with the correct selection of the element size and the number of Gauss points, an accurate analysis, involving internal points which are very close to the surface, can be made possible In the example discussed in this section, the element size on arc 2, which dominated surface S_1, was 9.4mm and the wall thickness was 10mm. A variable number of Gauss points were used and although the elements close to the internal point were integrated using 12 by 12 Gauss order, this was reduced to 4 by 4 for all other elements. However, excellent results were obtained even at points placed 3mm away from the boundary surfaces. This shows that results very close to the surface can be determined. It will be shown in Section 6.6.3 that internal points much closer to the surface can also be placed.

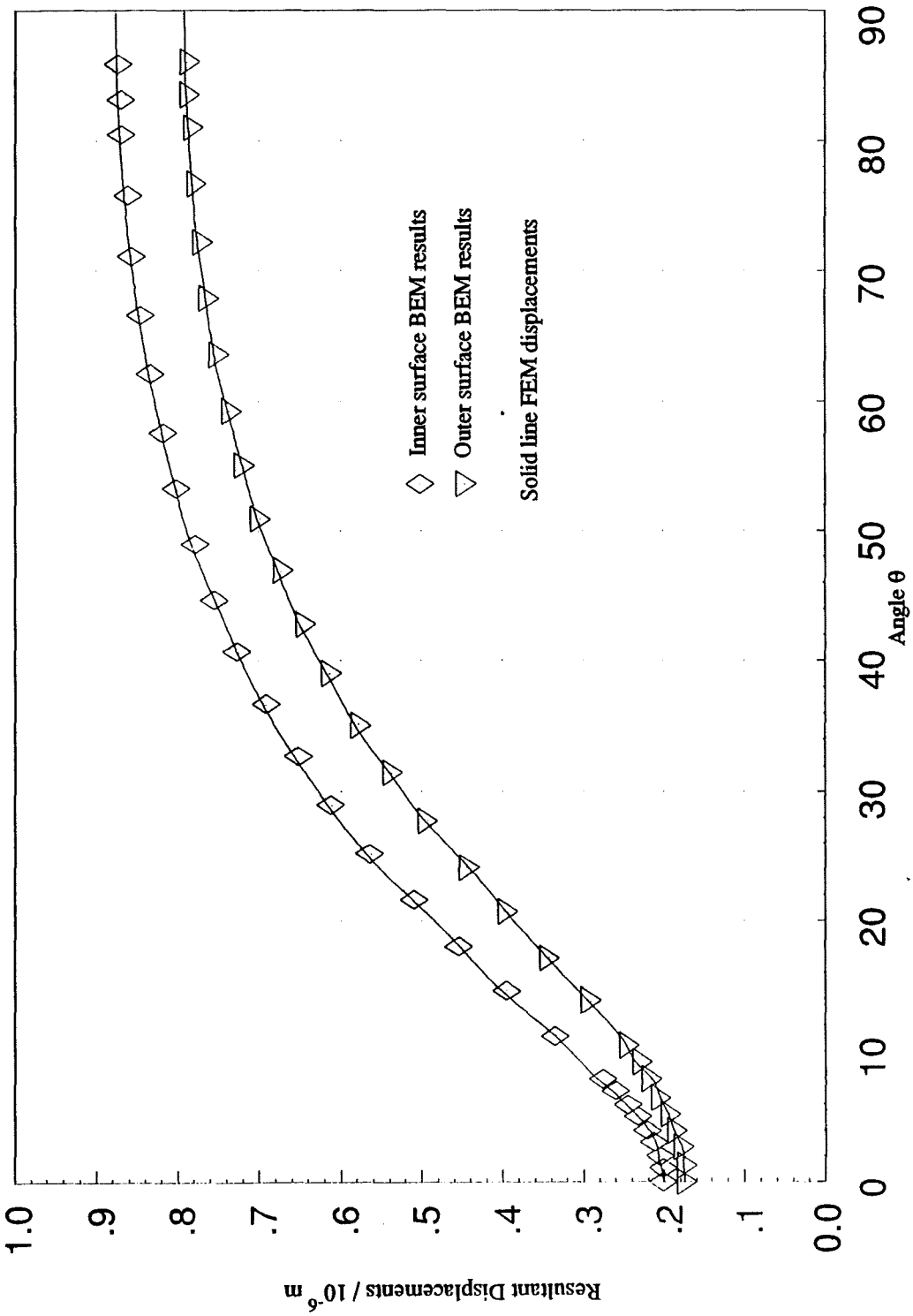

Figure 6.7: Resultant displacements on surfaces S_1 and S_3 of the cone with 10mm wall thickness.

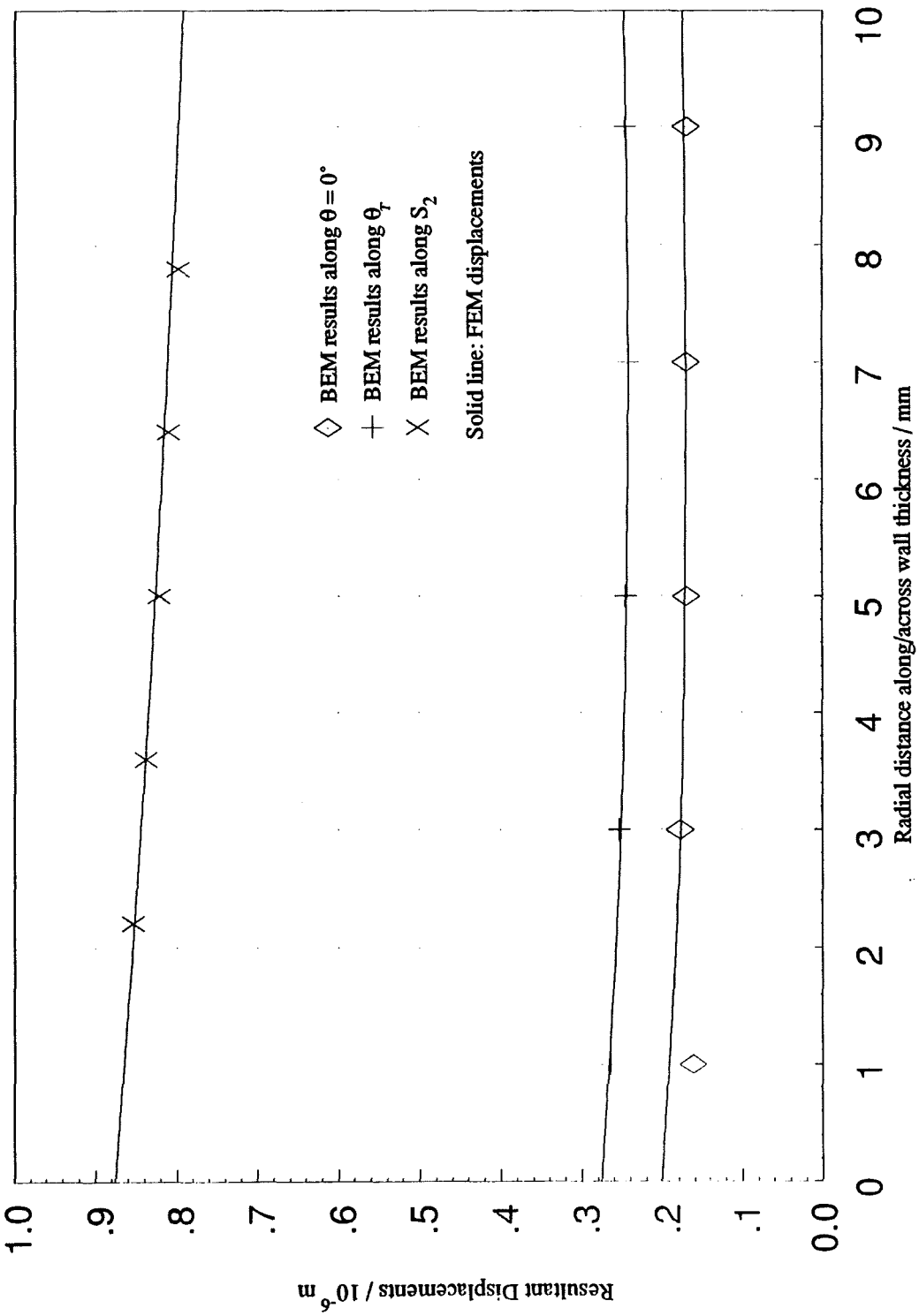

Figure 6.8: Comparison of BEM and FEM displacements along three radial directions. (Wall thickness = 10mm)

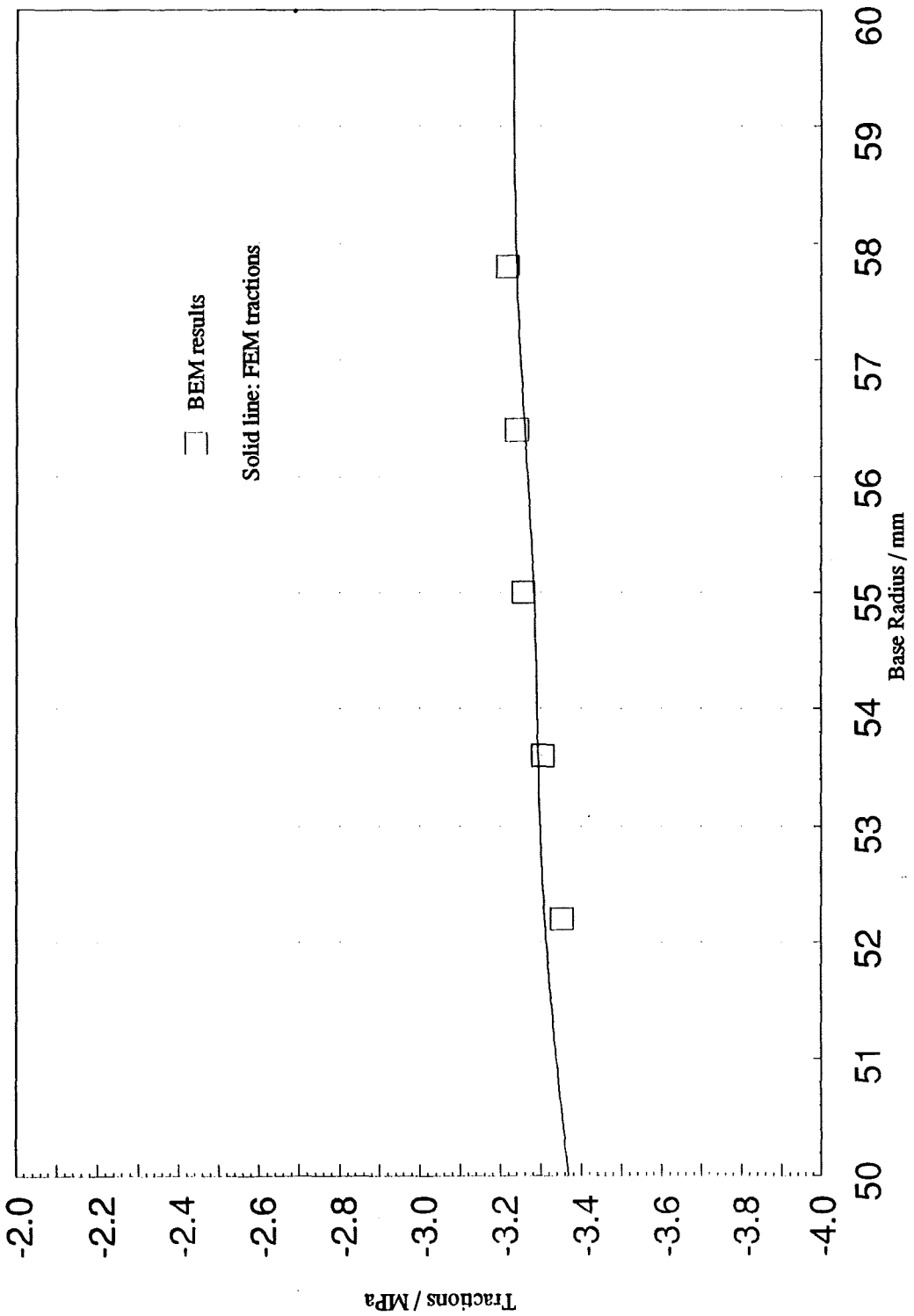

Figure 6.9: Comparison of BEM and FEM tractions along surface S_2. (Wall thickness = 10mm)

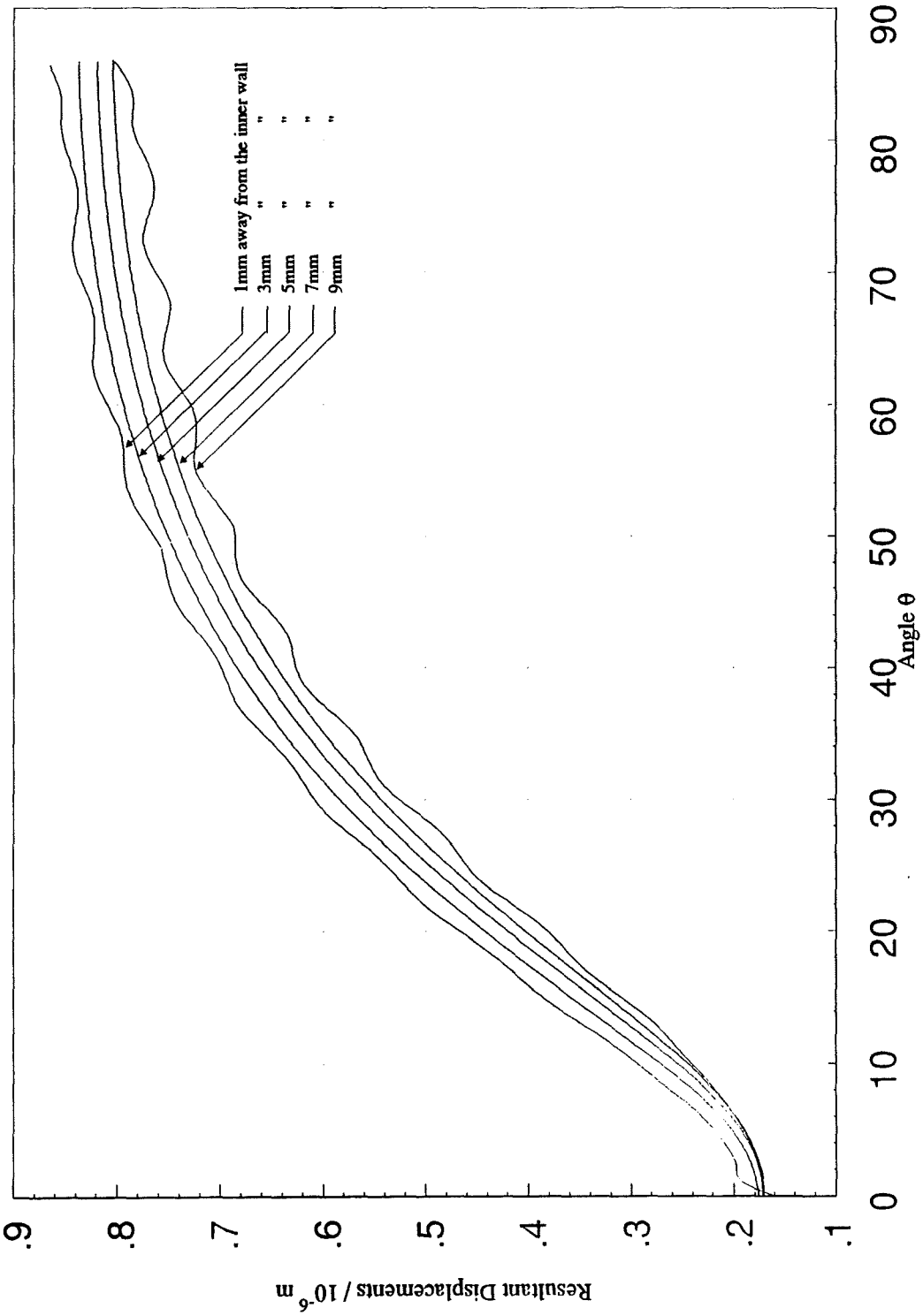

Figure 6.10: Internal displacements shown at various distances from the inner wall surface S_3. (Wall thickness = 10mm)

6.6.3 - Wall thickness = 5mm

Having completed a set of results with a 10mm wall, another cone of the same base radius, tip radius and height with 5mm wall thickness was tested. 5mm wall thickness is the main interest in this thesis as the investigation is concentrated on thin structures.

Results for the same parameters as in the previous section were obtained and they are illustrated in Figures 6.11, 6.12, 6.13 and 6.14. The selected mesh was more dense than the 10mm one as the SOT ratio was to be maintained at around 1.0 for all the surfaces. Therefore, 19 elements were used for both the inner and the outer surfaces, whereas two elements were used for the flat surface, S_2. For the small arc on the outer surface, 3 elements were used and the remaining 16 were distributed on the large arc. The same allocation of elements was also done on the inner surface. On surface S_2, 4 elements were too dense and resulted in a singular system matrix. The number of the elements on the S_2 surface was then reduced to 2 elements which solved the problem.

All the results given in Figures 6.11-6.14 have been compared with the results obtained using FEM. They all showed very close agreement with the FEM results with the exception of the tractions on surface S_2. This was due to having two small elements on surface S_2. However, a minimum of two elements were necessary so that semi-continuous element could be used. In Figure 6.14, the internal displacements showed remarkable accuracy even for points placed at 1mm away from the inner and outer surfaces.

6.6.4 - Various Cone Heights

Further investigation was conducted to see the effect on the surface displacements at various cone heights with the same base radius and wall thickness. In this test, the wall thickness was kept at 10mm and the outer base radius at 60mm. As the largest displacements occured on the inner surface, S_3, the comparison is done on these displacements and they are shown in Figure 6.15.

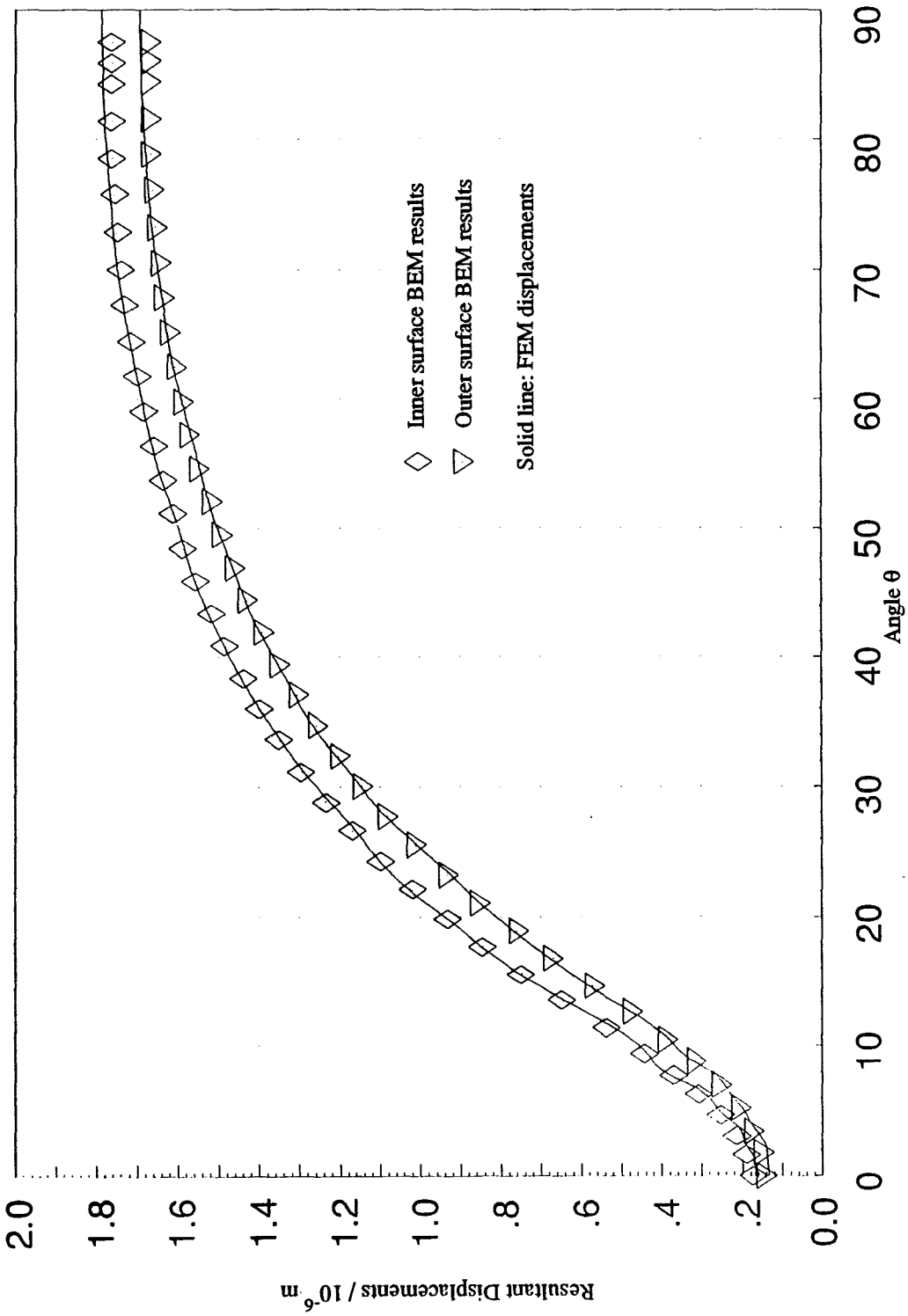

Figure 6.11: Resultant displacements on surfaces S_1 and S_3 of the cone with 5mm wall thickness.

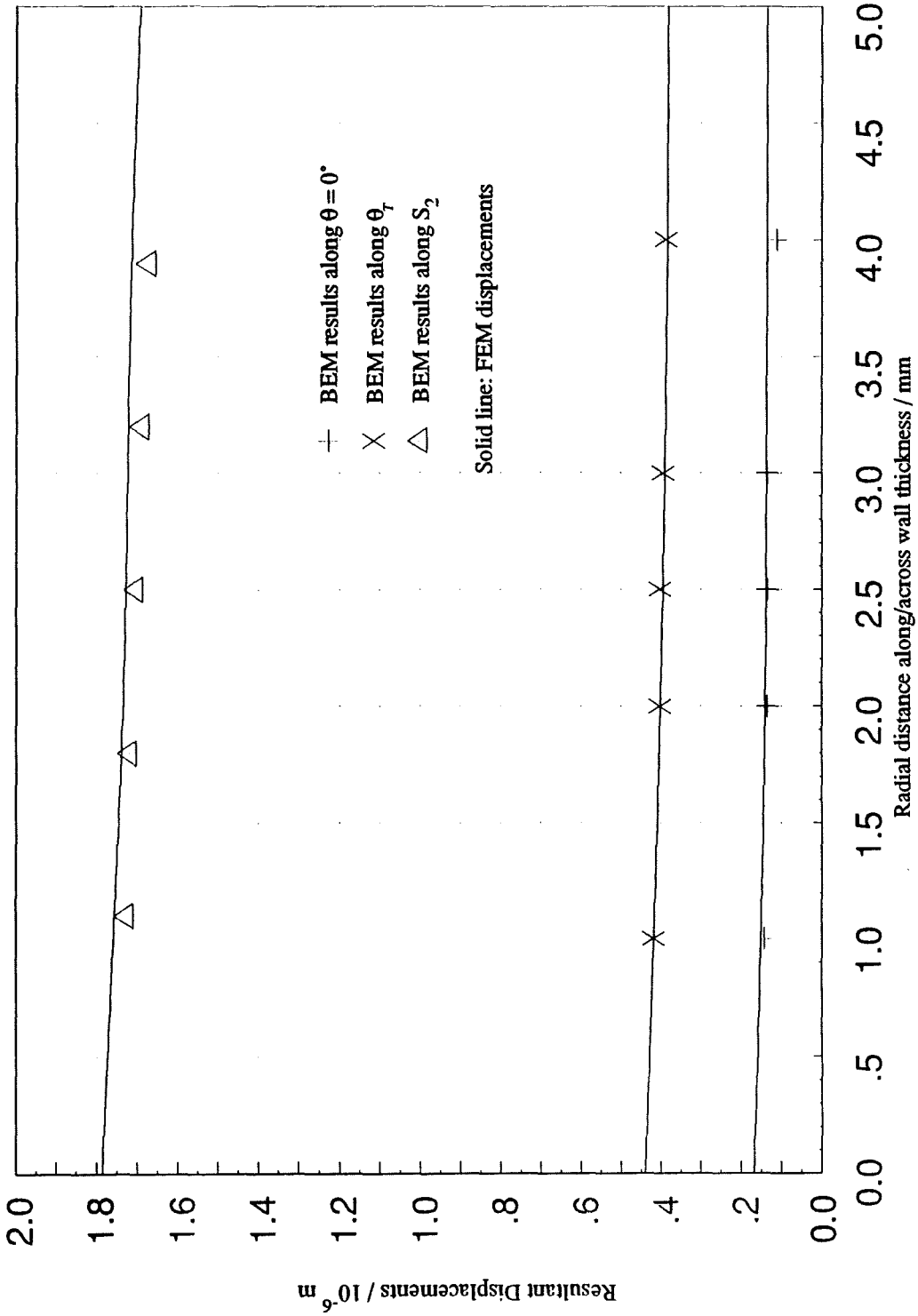

Figure 6.12: Comparison of BEM and FEM displacements along three radial directions. (Wall thickness = 5mm)

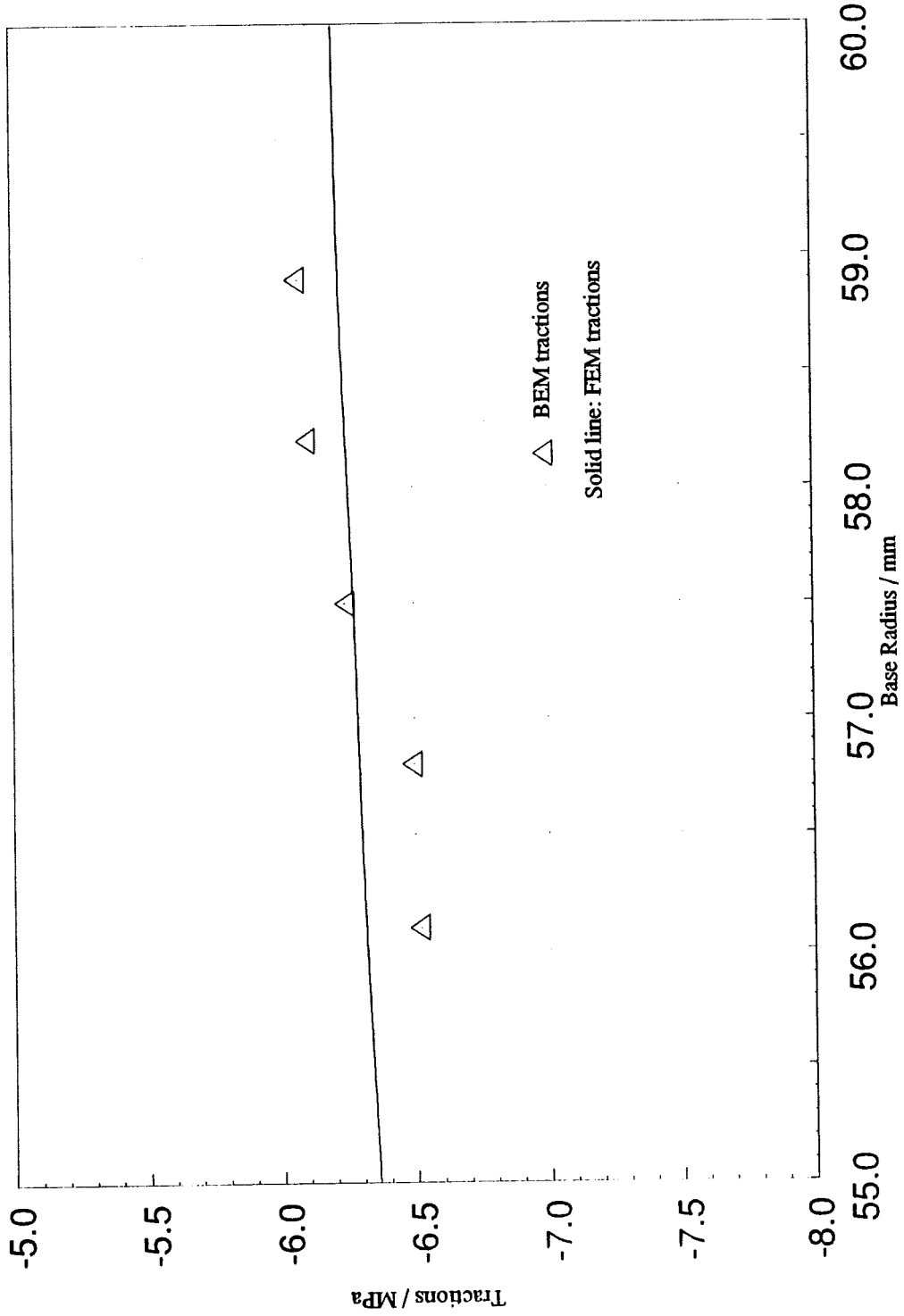

Figure 6.13: Comparison of BEM and FEM tractions along surface S_2. (Wall thickness = 5mm)

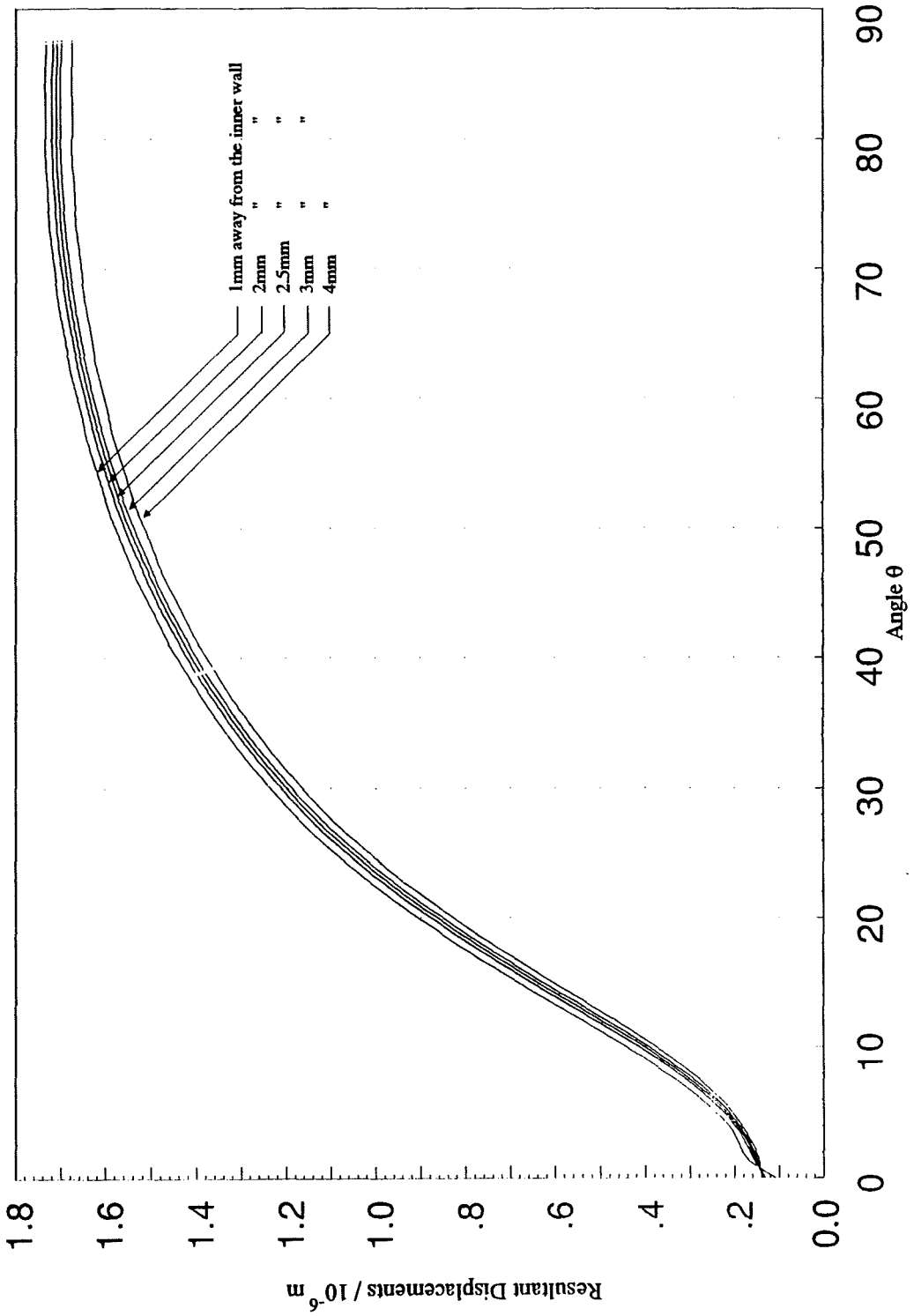

Figure 6.14: Internal displacements shown at various distances from the inner wall surface S_3. (Wall thickness = 5mm)

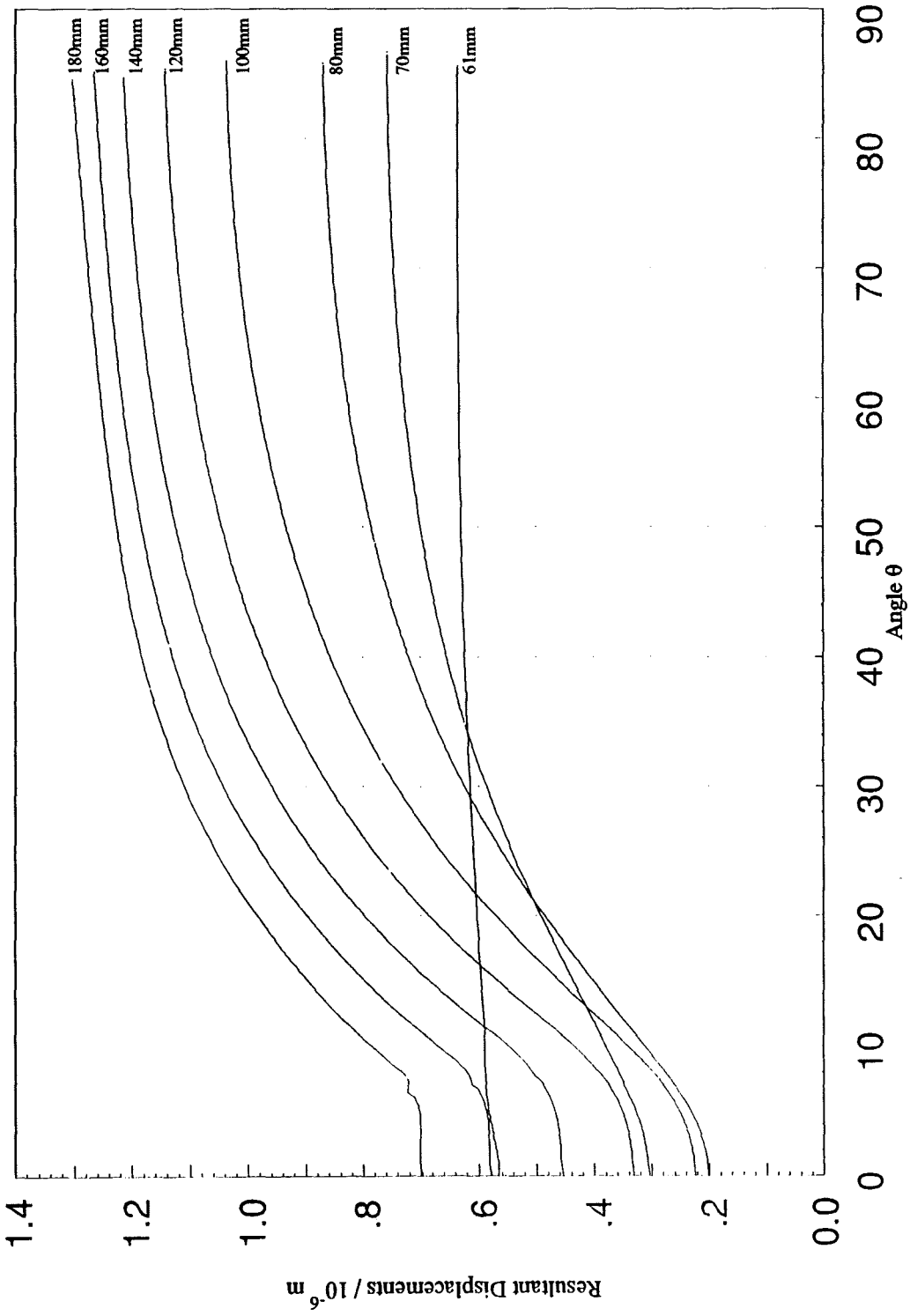

Figure 6.15: Comparison of the resultant displacements on the inner wall surface S_3 with various cone heights. (Wall thickness = 10mm , outer base radius=60mm))

6.7 - INTERNAL STRESSES

In this section the internal stresses are worked out using Equation (2.54) without the volume integral which represents the body forces. The calculated BEM stresses are then compared with the FEM results. By symmetry, the shear stresses σ_{12} and σ_{23} are zero and therefore, are not compared. The cone considered has outer surface dimensions of 60mm base radius, tip radius of 30mm, height of 80mm and wall thickness of 5mm.

Although the internal stresses are calculated at 1mm intervals across the wall, only the mid-wall stresses are compared. Nodal values are compared for the shear stress σ_{13}, hoop stress $\sigma_{\varphi\varphi}$ and the *Von Mises equivalent stress* σ_e. The equivalent stress, defined in terms of the global directional stresses, is given below (see, for example, Pafec, 1975):

$$\sigma_e = \sqrt{\frac{(\sigma_{11}-\sigma_{22})^2+(\sigma_{22}-\sigma_{33})^2+(\sigma_{11}-\sigma_{33})^2+6\,(\sigma_{12}^2+\sigma_{23}^2+\sigma_{13}^2)}{2}} \qquad (6.20)$$

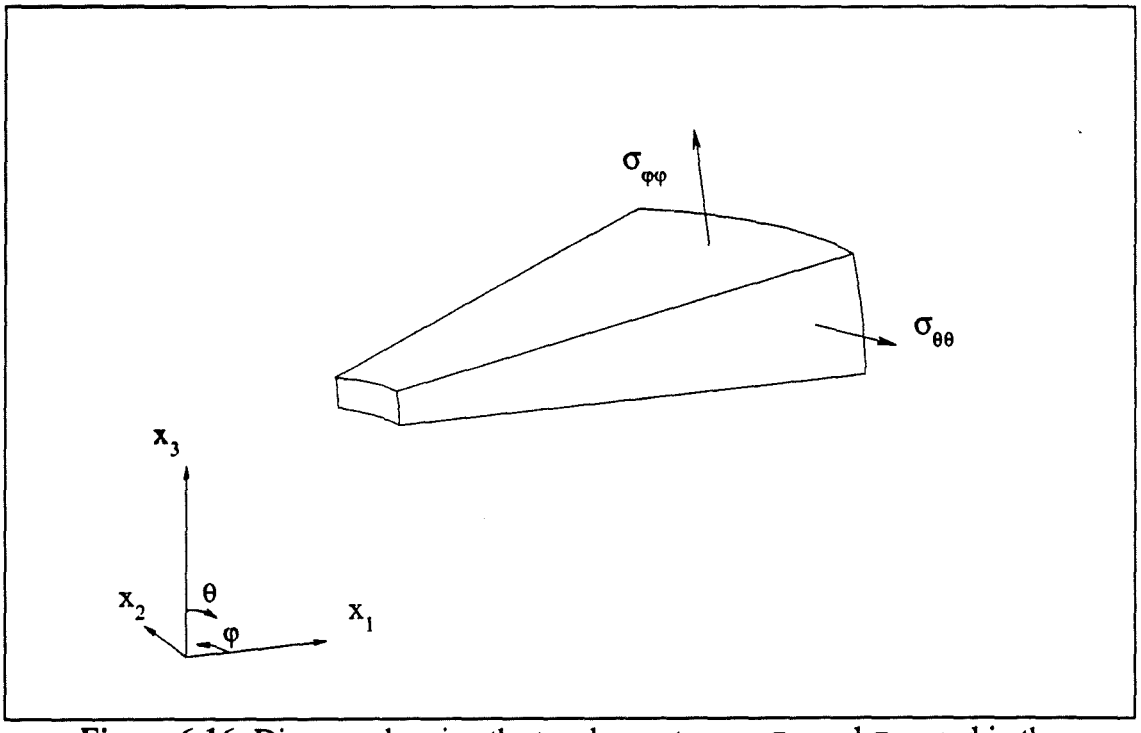

Figure 6.16: Diagram showing the two hoop stresses $\sigma_{\theta\theta}$ and $\sigma_{\varphi\varphi}$ used in the nodal stress comparison.

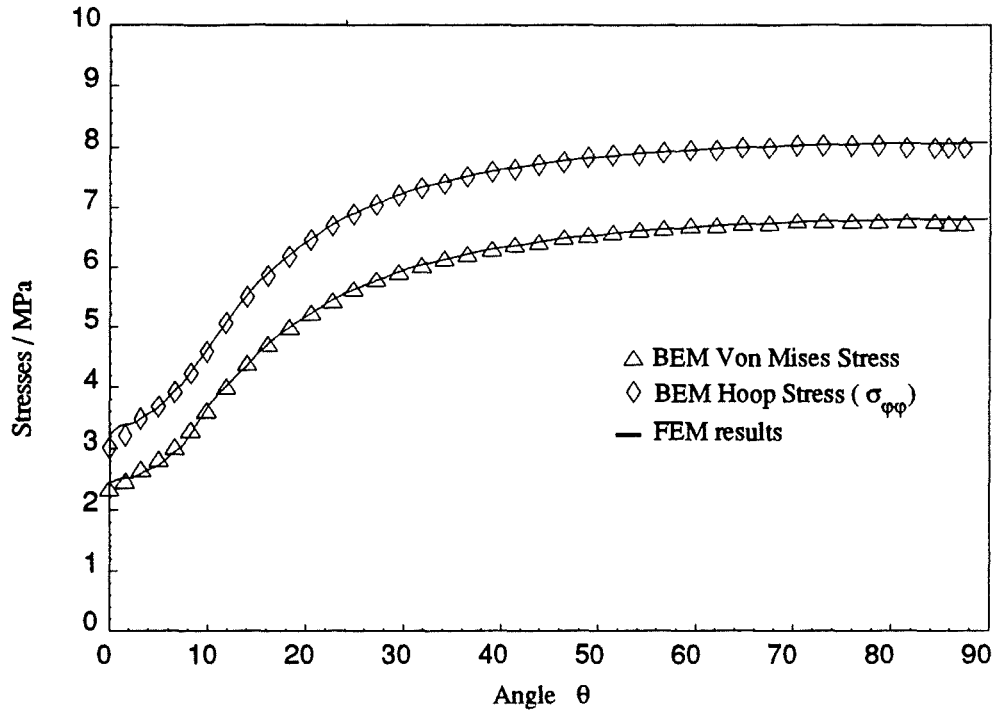

Figure 6.17: Comparison of BEM and FEM Von Mises and Hoop Stress ($\sigma_{\varphi\varphi}$) at mid-wall of the cone. (Wall thickness=5mm)

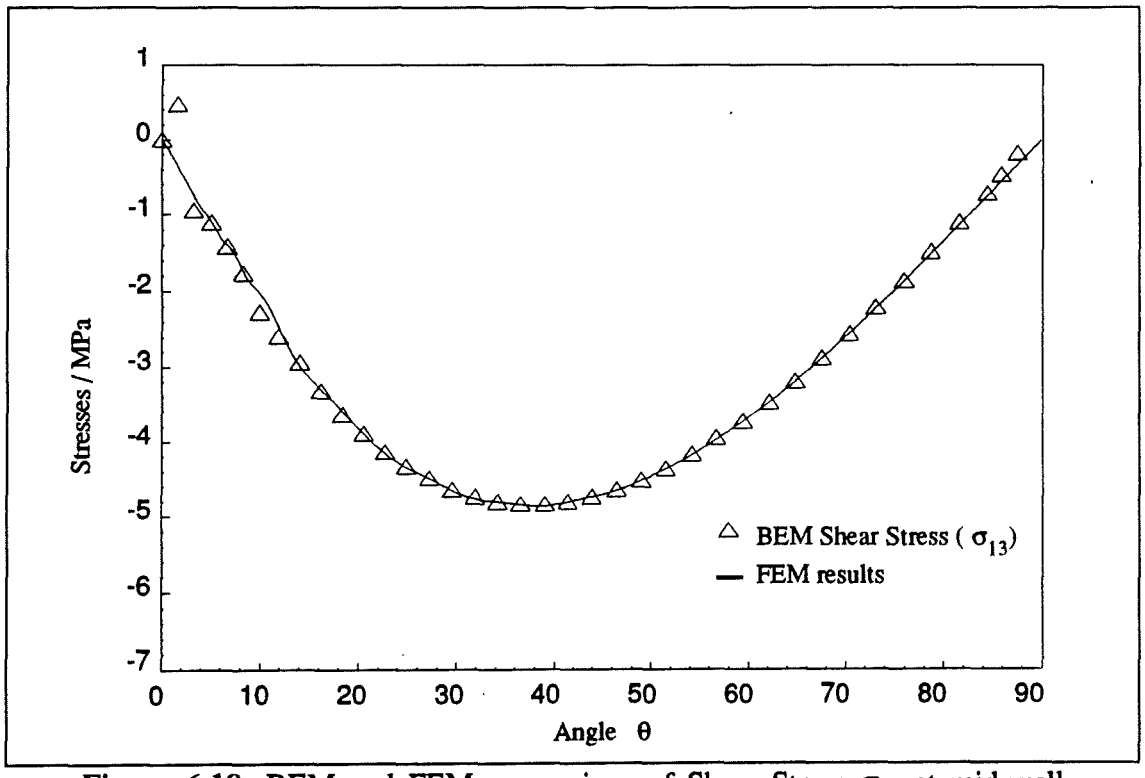

Figure 6.18: BEM and FEM comparison of Shear Stress σ_{13} at mid-wall thickness for the cone. (Wall thickness=5mm)

Figure 6.17 shows the hoop stress $\sigma_{\varphi\varphi}$ and the von Mises equivalent stress σ_e determined at the mid-wall for the cone with a 5mm wall thickness. A good agreement with the FEM results is obtained. This is also reflected in the shear stress results shown in Figure 6.18. The shear stress is maximum along $\theta = 40°$. The angle theta is measured clockwise from the x_3 axis to x_1 axis as shown in Figure 6.16.

6.7.1 - Stresses Close To Surface:

As discussed in Chapter 1, the stresses for the internal points very close to the boundary are expected to show substantial errors due to the singular nature of the BEM formulation. This effect is demonstrated here by showing the hoop stress $\sigma_{\varphi\varphi}$ and Von Mises equivalent stress σ_e at internal points across the wall thickness at small intervals. Results for both wall thicknesses, 5mm and 10mm, are shown in Figures 6.19-6.22. For both the wall thicknesses, the results calculated at 1mm from the inner and outer surfaces showed very large errors and these appeared as severe oscillations. However, at points placed 2mm or more away from the boundary surfaces, good results are obtained. Comparison of these results with the FEM analysis at the mid-wall support this claim (see Figures 6.18 and 6.19).

For the 10mm wall thickness, the internal point stresses results are shown at 1, 2, 4, 6, 8 and 9mm away from the inner surface. For the 5mm wall thickness, These are shown at 1, 2, 3 and 4mm away from the inner surface.

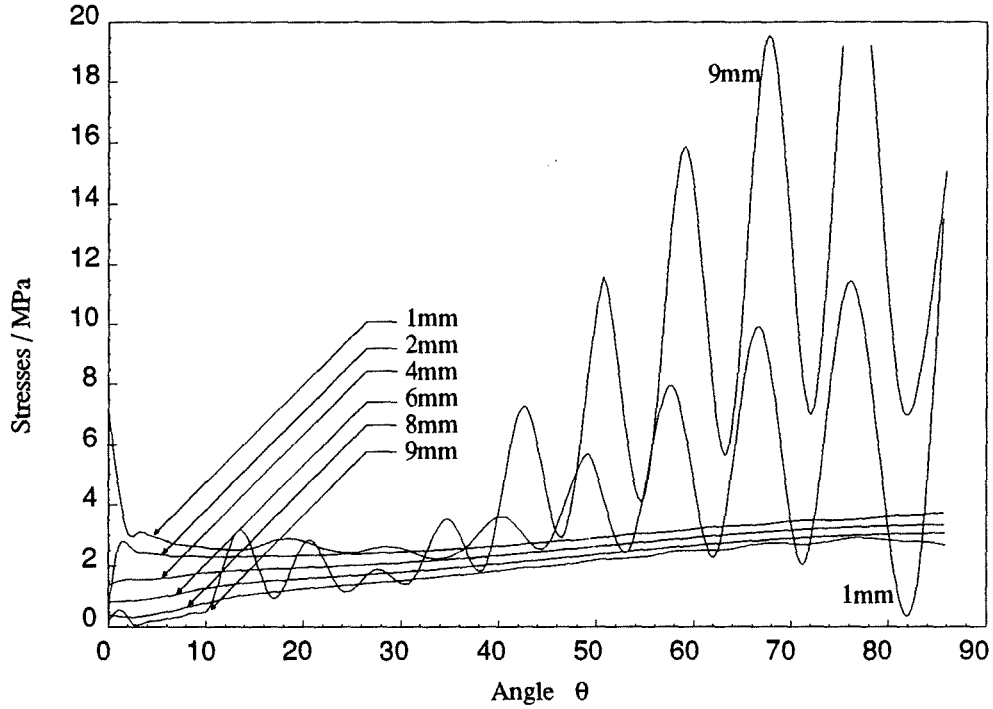

Figure 6.19: Von Mises stresses at various distances away from the inner wall. (Wall thickness=10mm)

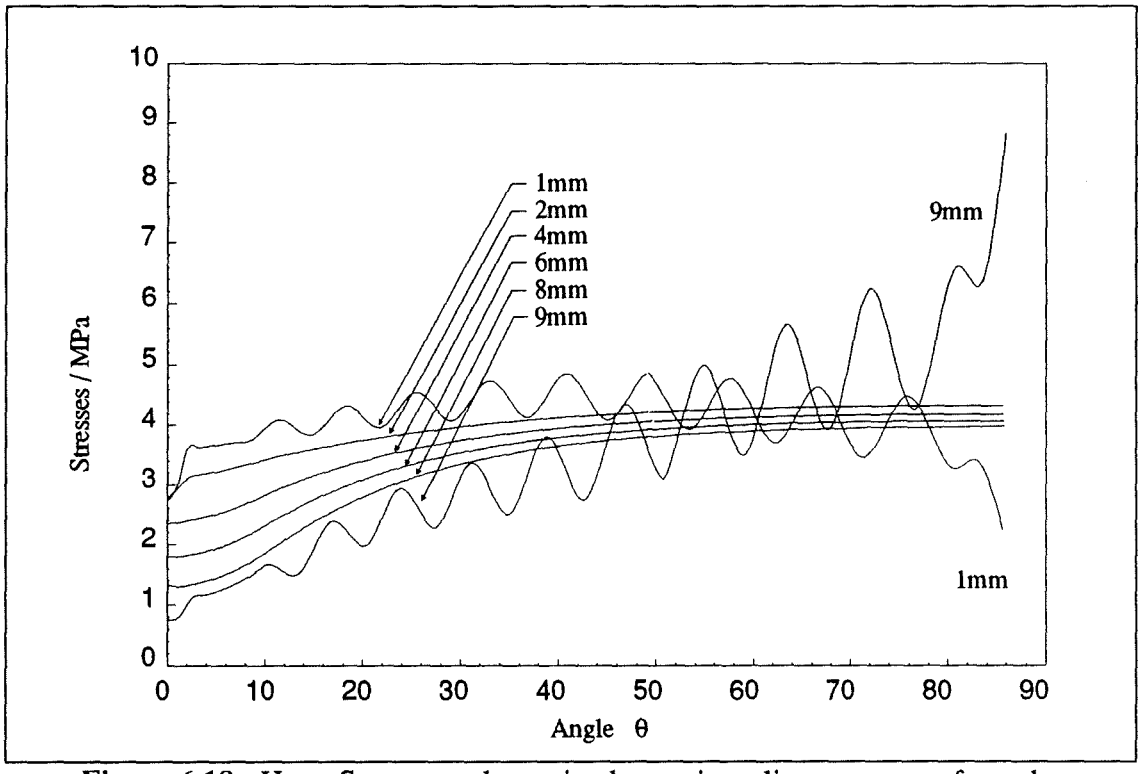

Figure 6.18: Hoop Stress $\sigma_{\varphi\varphi}$ determined at various distances away from the inner wall surface. (Wall thickness=10mm)

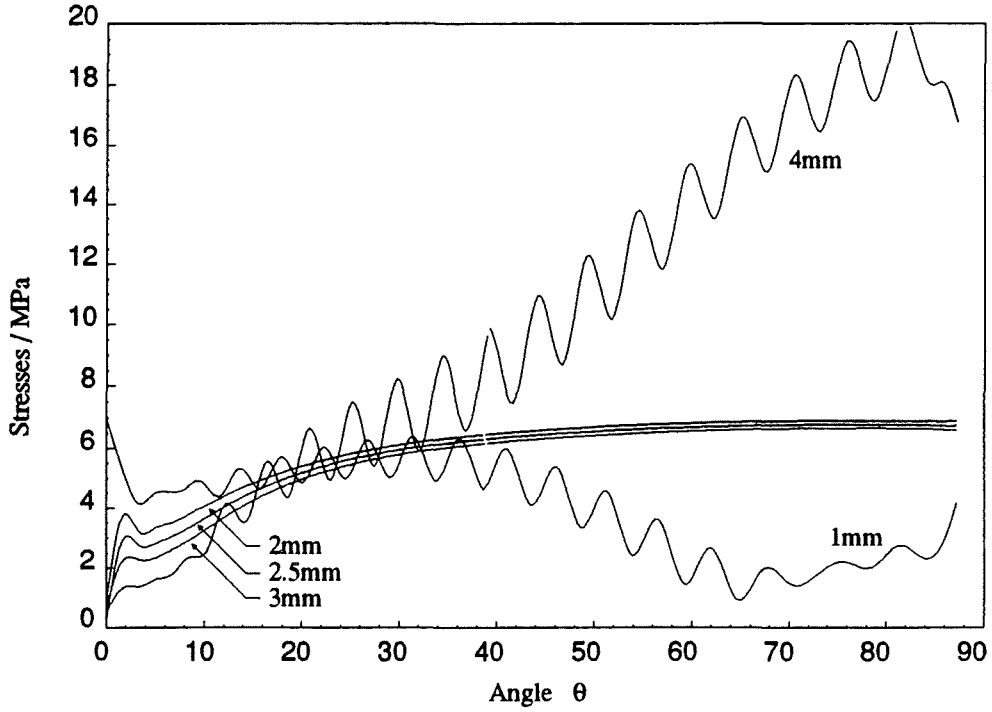

Figure 6.21: Von Mises stresses at various distances away from the inner wall. (Wall thickness=5mm)

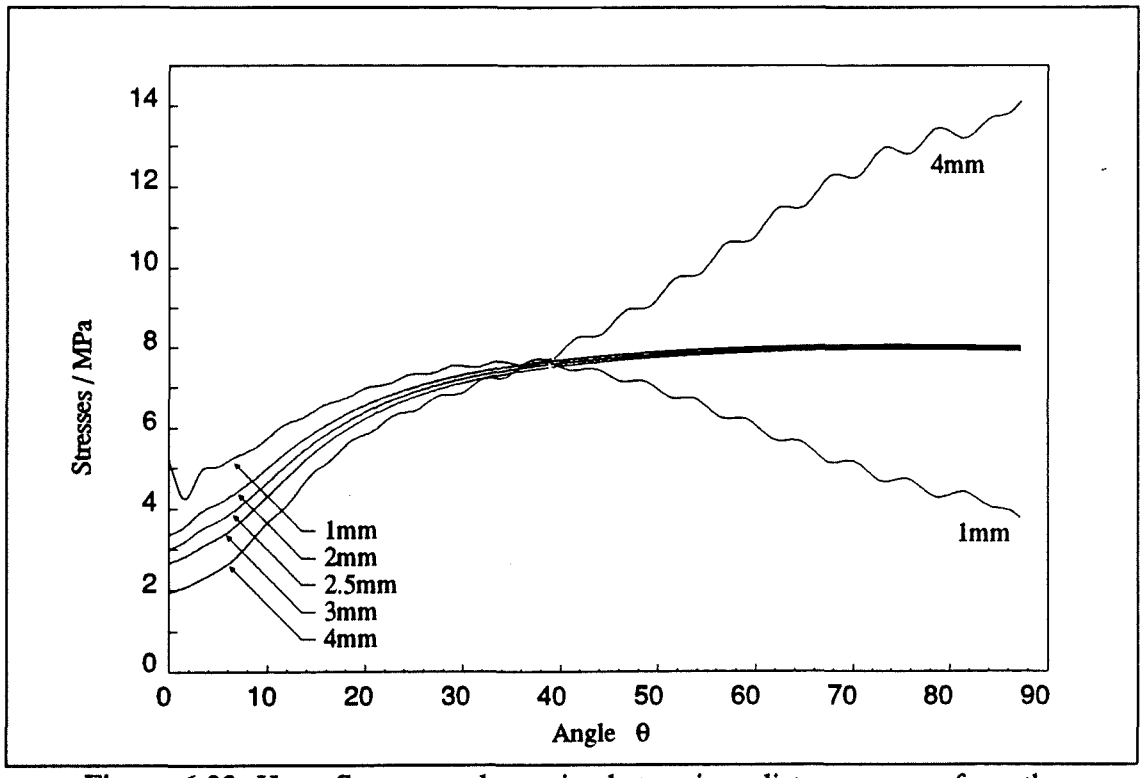

Figure 6.22: Hoop Stress $\sigma_{\varphi\varphi}$ determined at various distances away from the inner wall surface. (Wall thickness=5mm)

6.8 - SURFACE STRESSES

The stresses on the boundary cannot be determined by using the formulation derived for the stresses at internal points. This is due to the singular behaviour of the third order tensors S_{kij} and D_{kij} shown in Equations (2.55) and (2.56) when the point under consideration is placed on the boundary. For this reason, the surface stresses are determined by using the surface displacements. This section shows the details of this method.

6.8.1 - Stress - Strain Relationship

To determine the stresses, the strains must be determined first. The following equations show the stress - strain relationship:

$$\varepsilon_{rr} = \frac{1}{E}\left\{\sigma_{rr} - \nu\sigma_{\theta\theta} - \nu\sigma_{\varphi\varphi}\right\} \tag{6.21}$$

$$\varepsilon_{\theta\theta} = \frac{1}{E}\left\{\sigma_{\theta\theta} - \nu\sigma_{rr} - \nu\sigma_{\varphi\varphi}\right\} \tag{6.22}$$

$$\varepsilon_{\varphi\varphi} = \frac{1}{E}\left\{\sigma_{\varphi\varphi} - \nu\sigma_{rr} - \nu\sigma_{\theta\theta}\right\} \tag{6.23}$$

On the inner surface, the radial stress is equal to zero as there is no pressure acting on that surface. Therefore, only Equations (6.22) and (6.23) are required. The two hoop stresses can be rewritten in terms of the hoop strains as follows:

$$\sigma_{\theta\theta} = \frac{E}{1-\nu^2}\left\{\varepsilon_{\theta\theta} + \nu\sigma_{\varphi\varphi}\right\} \tag{6.24}$$

$$\sigma_{\varphi\varphi} = \frac{E}{1-\nu^2}\left\{\varepsilon_{\varphi\varphi} + \nu\sigma_{\theta\theta}\right\} \tag{6.25}$$

The next step is to determine the two hoop strains from the surface displacements, and this is shown in the next section.

6.8.2 - Strain - Displacement Relationship

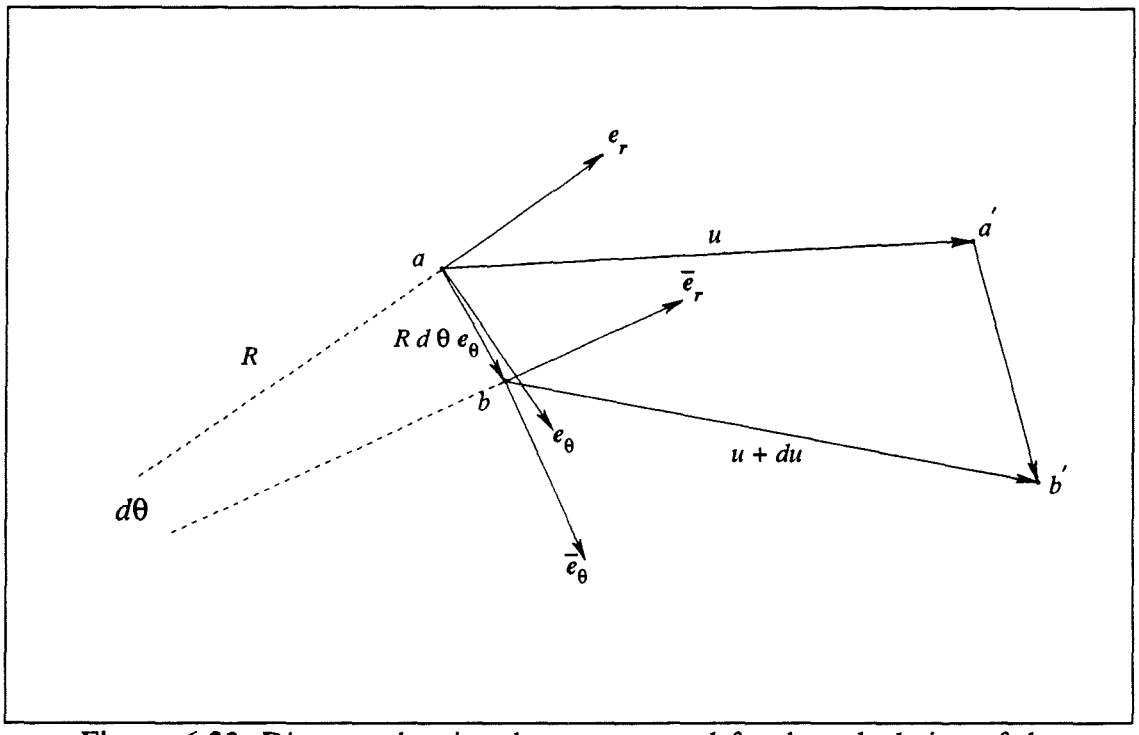

Figure 6.23: Diagram showing the vectors used for the calculation of the tangent strains.

The tangential strains (hoop strains) $\varepsilon_{\theta\theta}$ and $\varepsilon_{\varphi\varphi}$ are determined in this section. Figure 6.23 shows two surface points a and b, displaced to a' and b' respectively. It also shows the vectors associated with the displaced shape in the x_1 and x_3 plane. The vector $\boldsymbol{a'b'}$ can be written in terms of the other vectors forming the polygon, such that:

$$\boldsymbol{ab'} = \boldsymbol{u} + \boldsymbol{a'b'} \tag{6.26}$$

$$= \boldsymbol{ab} + (\boldsymbol{u} + \delta\boldsymbol{u}) \tag{6.27}$$

Therefore,

$$\boldsymbol{a'b'} = \boldsymbol{ab} + (\boldsymbol{u} + \delta\boldsymbol{u}) - \boldsymbol{u} \tag{6.28}$$

$$\boldsymbol{a'b'} = R\,\delta\theta\,\boldsymbol{e}_\theta + (\boldsymbol{u} + \delta\boldsymbol{u}) - \boldsymbol{u} \tag{6.29}$$

$$u = u_r(\theta)\, e_r(\theta) + u_\theta(\theta)\, e_\theta(\theta) \tag{6.30}$$

$$(u + \delta u) = u_r(\theta + \delta\theta)\, \bar{e}_r(\theta + \delta\theta) \;+\; u_\theta(\theta + \delta\theta)\, \bar{e}_\theta(\theta + \delta\theta) \tag{6.31}$$

However;

$$\bar{e}_r = e_r + \delta\theta e_\theta \tag{6.32}$$

$$\bar{e}_\theta = e_\theta - \delta\theta e_r \tag{6.33}$$

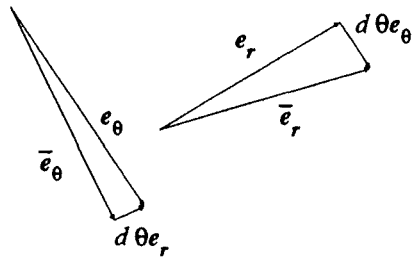

$$\begin{aligned}(u + \delta u) - u \;=\; & \left[u_r(\theta) + \frac{\partial u_\theta}{\partial\theta}\,\delta\theta\right]\left[e_r(\theta) + \delta\theta\, e_\theta(\theta)\right] \\ & + \left[u_\theta(\theta) + \frac{\partial u_\theta}{\partial\theta}\,\delta\theta\right]\left[e_\theta(\theta) - \delta\theta\, e_r(\theta)\right] \\ & - u_r(\theta)\, e_r(\theta) - u_\theta(\theta)\, e_\theta(\theta)\end{aligned} \tag{6.34}$$

$$\begin{aligned}(u + \delta u) - u \;=\; & u_r(\theta)\, e_r(\theta) + u_r(\theta)\,\delta\theta\, e_\theta(\theta) + \frac{\partial u_r}{\partial\theta}\,\delta\theta\, e_r(\theta) + \frac{\partial u_r}{\partial\theta}\,\delta^2\theta\, e_\theta(\theta) \\ & + u_\theta(\theta)\, e_\theta(\theta) - u_\theta(\theta)\,\delta\theta\, e_r(\theta) + \frac{\partial u_\theta}{\partial\theta}\,\delta\theta\, e_\theta(\theta) - \frac{\partial u_\theta}{\partial\theta}\delta^2\theta\, e_r(\theta) \\ & - u_r(\theta)\, e_r(\theta) - u_\theta(\theta)\, e_\theta(\theta)\end{aligned} \tag{6.35}$$

Ignoring the second order terms and collecting the similar terms together, Equation (6.35) simplifies to:

$$(u + \delta u) - u \;=\; \delta\theta\left\{\left[\frac{\partial u_r}{\partial\theta} - u_\theta(\theta)\right] e_r(\theta) \;+\; \left[\frac{\partial u_\theta}{\partial\theta} + u_r(\theta)\right] e_\theta(\theta)\right\} \tag{6.36}$$

Substituting Equation (6.36) into Equation (6.29);

$$a'b' \;=\; \delta\theta\left\{\left[\frac{\partial u_r}{\partial\theta} - u_\theta(\theta)\right] e_r(\theta) \;+\; \left[R + \frac{\partial u_\theta}{\partial\theta} + u_r(\theta)\right] e_\theta(\theta)\right\} \tag{6.37}$$

$$\varepsilon_{\theta\theta} = \frac{|\boldsymbol{a'b'}| - |\boldsymbol{a\,b}|}{|\boldsymbol{a\,b}|} \tag{6.38}$$

$$\left|\boldsymbol{a'b'}\right| = \sqrt{\boldsymbol{a'b'}\,.\,\boldsymbol{a'b'}} \tag{6.39}$$

Rewriting Equation (6.37),

$$\boldsymbol{a'b'} = R\,\delta\theta\left\{\left[\frac{1}{R}\frac{\partial u_r}{\partial\theta} - \frac{u_\theta(\theta)}{R}\right]\boldsymbol{e}_r(\theta) + \left[1 + \frac{1}{R}\frac{\partial u_\theta}{\partial\theta} + \frac{u_r(\theta)}{R}\right]\boldsymbol{e}_\theta(\theta)\right\} \tag{6.40}$$

Let,

$$t_\theta = \frac{1}{R}\frac{\partial u_\theta}{\partial\theta} + \frac{u_r}{R} \tag{6.41}$$

$$t_r = \frac{1}{R}\frac{\partial u_r}{\partial\theta} + \frac{u_\theta}{R} \tag{6.42}$$

Substituting Equations (6.41) and (6.42) into (6.40);

$$\boldsymbol{a'b'} = R\,\delta\theta\left[\,(1 + t_\theta)\,\boldsymbol{e}_\theta(\theta) + t_r\,\boldsymbol{e}_r(\theta)\,\right] \tag{6.43}$$

$$\boldsymbol{a'b'}\,.\,\boldsymbol{a'b'} = R\,\delta\theta\left[\,(1 + t_\theta)\,\boldsymbol{e}_\theta(\theta) + t_r\,\boldsymbol{e}_r(\theta)\,\right].\;R\,\delta\theta\left[\,(1 + t_\theta)\,\boldsymbol{e}_\theta(\theta) + t_r\,\boldsymbol{e}_r(\theta)\,\right] \tag{6.44}$$

$$= R^2\,\delta^2\theta\left[\,(1 + t_\theta)^2 + t_r^2\,\right] \tag{6.45}$$

$$= R^2\delta^2\theta\left[\,1 + 2\,t_\theta + t_\theta^2 + t_r^2\,\right] \tag{6.46}$$

Ignoring the high order terms;

$$\boldsymbol{a'b'}\,.\,\boldsymbol{a'b'} = R^2\,\delta^2\theta\left(1 + 2\,t_\theta\right) \tag{6.47}$$

$$\left| a'b' \right| = R\,\delta\theta \left(1 + 2\,t_\theta \right)^{\frac{1}{2}} \tag{6.48}$$

Using only the first two terms of binomial series;

$$(1 + x)^n = 1 + nx \tag{6.49}$$

gives;

$$\left| a'b' \right| = R\,\delta\theta\,(1 + t_\theta) \tag{6.50}$$

Substituting this result into Equation (6.38):

$$\varepsilon_{\theta\theta} = \frac{R\,\delta\theta\,(1 + t_\theta) - R\,\delta\theta}{R\,\delta\theta} \tag{6.51}$$

$$\varepsilon_{\theta\theta} = t_\theta = \frac{1}{R}\frac{\partial u_\theta}{\partial\theta} + \frac{u_r}{R} \tag{6.52}$$

By similar analysis the hoop strain in the φ direction is determined as;

$$\varepsilon_{\varphi\varphi} = \frac{u_1}{R_\varphi} + \frac{1}{R}\frac{\partial u_2}{\partial\varphi} \tag{6.53}$$

Because of the symmetry, $\frac{\partial u_2}{d\varphi} = 0$, and therefore;

$$\varepsilon_{\varphi\varphi} = \frac{u_1}{R_\varphi} \tag{6.54}$$

The definition of R_φ is given in Figure 6.2. The tangential strains can now be calculated using Equations (6.52) and (6.54). However, the $\varepsilon_{\theta\theta}$ is in terms of the displacement u_r and the derivative $\frac{\partial u_\theta}{\partial\theta}$. These terms should be expressed in terms of the known displacements

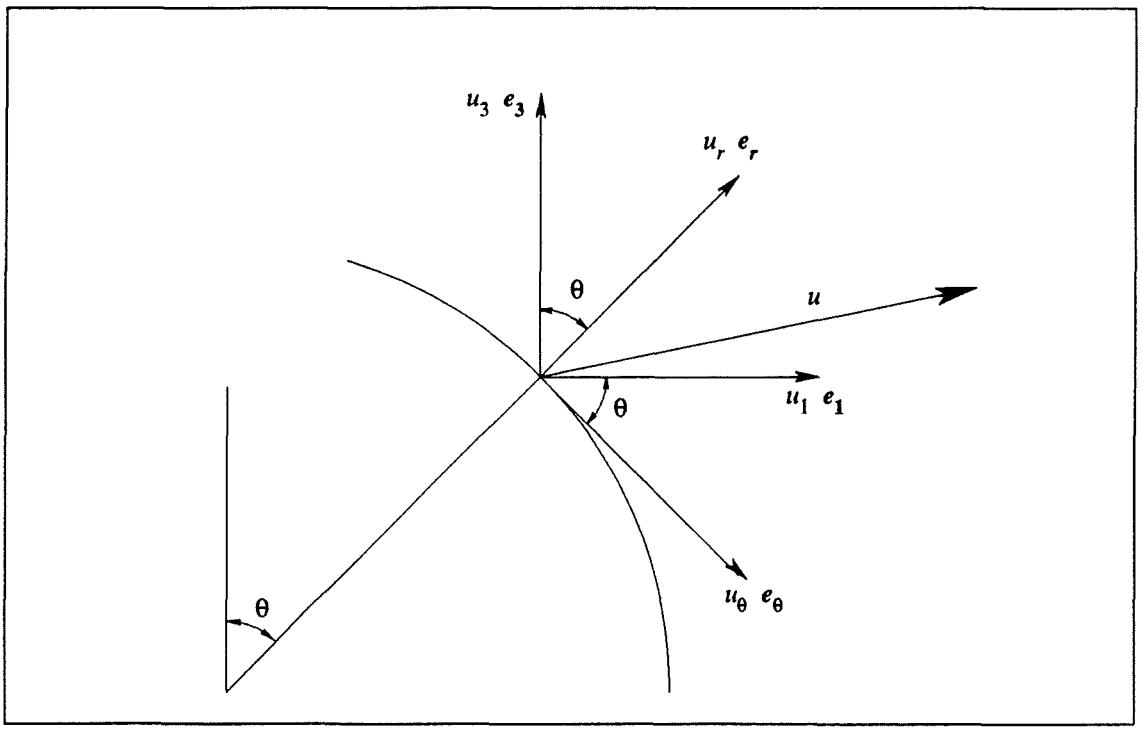

Figure 6.24: Diagram showing the vector components of a surface displacement.

u_1 and u_3 and they are worked out in the following way (see Figure 6.24). The displacement vector $\boldsymbol{u}$ can be written as follows:

$$\boldsymbol{u} = u_1 e_1 + u_3 e_3 = u_\theta e_\theta + u_r e_r \tag{6.55}$$

The tangential displacement u_θ can be written in terms of the known displacements u_1 and u_3 as follows:

$$u_\theta = u_1 e_1 \cdot e_\theta + u_3 e_3 \cdot e_\theta \tag{6.56}$$

The dot product of two vectors is defined as follows:

$$\boldsymbol{a}.\boldsymbol{b} = |a|\,|b| \cos\alpha \tag{6.57}$$

where α is the angle between these vectors $\boldsymbol{a}$ and $\boldsymbol{b}$. For vectors of unit magnitude, the dot product simply reduces to the cosine of the angle between the two vectors.

Hence from Figure (6.24);

$$e_1 \cdot e_\theta = \cos\theta \tag{6.58}$$

$$e_3 \cdot e_\theta = \cos\left(\frac{\pi}{2} + \theta\right) = -\sin\theta \tag{6.59}$$

Now, substituiting Equations (6.58) and (6.59) into Equation (6.56);

$$u_\theta = u_1\cos\theta - u_3\sin\theta \tag{6.60}$$

Similarly for the u_r displacement:

$$u_r = u_1 e_1 \cdot e_r + u_3 e_e \cdot e_r \tag{6.61}$$

$$u_r = u_1\cos\left(\frac{\pi}{2} - \theta\right) + u_3\cos\theta \tag{6.62}$$

$$u_r = u_1\sin\theta + u_3\cos\theta \tag{6.63}$$

To determine the derivative $\frac{\partial u_\theta}{\partial\theta}$, Equation (6.60) is differentiated with respect to angle θ using the product rule:

$$\frac{\partial u_\theta}{\partial\theta} = -u_1\sin\theta + \frac{\partial u_1}{\partial\theta}\cos\theta - u_3\cos\theta - \frac{\partial u_3}{\partial\theta}\sin\theta \tag{6.64}$$

$$\frac{\partial u_\theta}{\partial\theta} = \frac{\partial u_1}{\partial\theta}\cos\theta - \frac{\partial u_3}{\partial\theta}\sin\theta - u_r \tag{6.65}$$

It was decided at this stage to express $\frac{\partial u_\theta}{\partial\theta}$ in terms of the arc length as the preliminary investigation showed discontinuities in the slopes of u_1 and u_3 at the intersection of the two arcs forming the surfaces if θ was kept as a parameter.

Hence:

$$\frac{\partial u_1}{\partial \theta} = \frac{\partial u_1}{\partial s}\frac{\partial s}{\partial \theta} \tag{6.66}$$

$$\frac{\partial u_3}{\partial \theta} = \frac{\partial u_3}{\partial s}\frac{\partial s}{\partial \theta} \tag{6.67}$$

But,

$$s = R\, d\theta \tag{6.68}$$

$$\frac{\partial s}{\partial \theta} = R \tag{6.69}$$

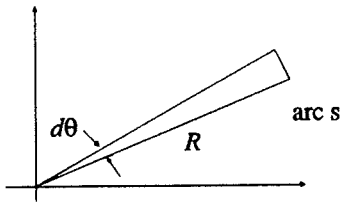

Therefore;

$$\frac{\partial u_1}{\partial \theta} = \frac{\partial u_1}{\partial s} R \tag{6.70}$$

$$\frac{\partial u_3}{\partial \theta} = \frac{\partial u_3}{\partial s} R \tag{6.71}$$

$$\frac{\partial u_\theta}{\partial \theta} = \frac{\partial u_1}{\partial s} R \cos\theta - \frac{\partial u_3}{\partial s} R \sin\theta - u_r \tag{6.72}$$

Substituting Equation (6.72) into Equation (6.52), simplifies to the following:

$$\varepsilon_{\theta\theta} = \frac{\partial u_1}{\partial s}\cos\theta - \frac{\partial u_3}{\partial s}\sin\theta \tag{6.73}$$

6.8.3 - Use of Cubic Spline

Having determined the necessary expressions to calculate the tangential strains, the next step is to calculate the displacement derivatives required by Equation (6.72). These derivatives can be calculated from the quadratic shape functions used for the BEM elements, but the first derivative would not be continuous, in general, at the ends of each element and this would show in the strains and, therefore, stresses.

This is best explained by considering a small number of the elements and comparing the first derivative of the displacements. For example, the derivatives of four elements on the inner surface that belong to the large arc were calculated using both the quadratic formulation and the cubic spline formulation. The results for quadratic formulation are given in Figure 6.25 and for the cubic spline they are plotted in Figure 6.26. A very noticable difference in the end nodes of the quadratic elements are seen and this is also reflected in the final stress values.

In a different study (see Beswick, 1992b), a circular ring section under a point load was tested to see the result of using quadratic elements for stresses across the thickness. The results were taken at the 45° line across the thickness. The two extreme points which were on this line, were also the end nodes of the quadratic elements. The results were both compared with BEM analysis using BEASY® and the analytical theory. All the internal points agreed with the theoretical results except the surfce points, where an error of 3.3% was seen. The same problem was again solved with BEASY®, but this time the mesh was modified so that the results were taken along a line that corresponded to the midside nodes. The previous errors seen on the surface nodes had now diminished. The detailes are given in Appendix C. Due to the apparent discontiniuties in the derivatives, as shown in Figure 6.25, a cubic spline was fitted through the displacement points available, and their derivatives determined accordingly. Since by definition, a cubic spline is C^2, the derivatives were of quadratic order and smooth results obtained as the continuity of the derivatives was maintained. The formulae used are given below (Stoer and Bulirsch, 1983). The

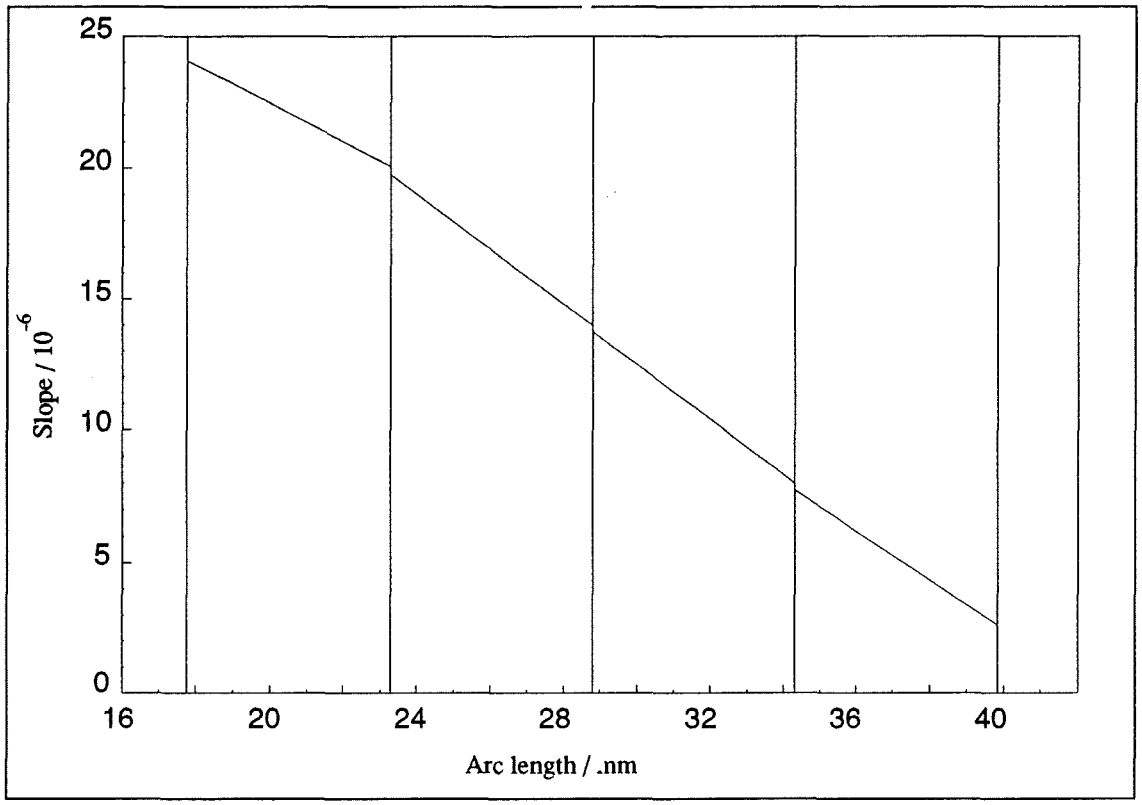

Figure 6.25: The derivative of the vertical displacements determined using quadratic variation. (Each interval shows an element)

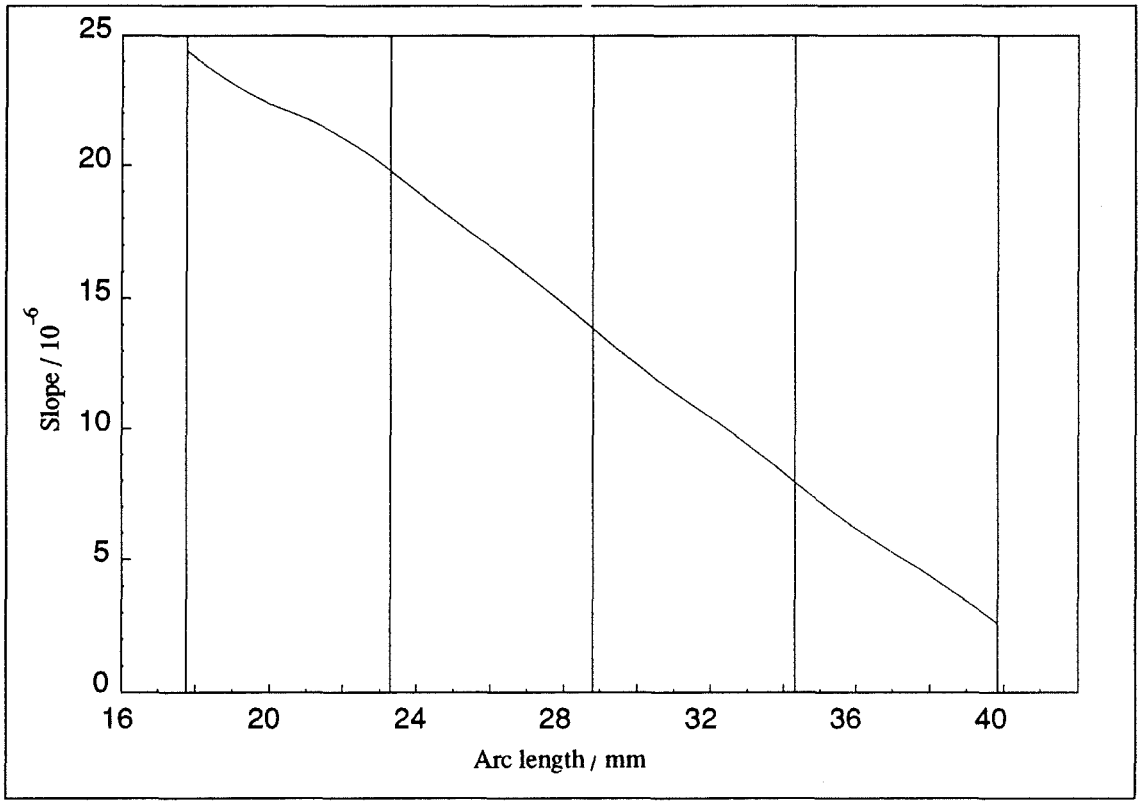

Figure 6.26: The derivative of the vertical displacements determined using cubic spline fit. (Each interval shows an element)

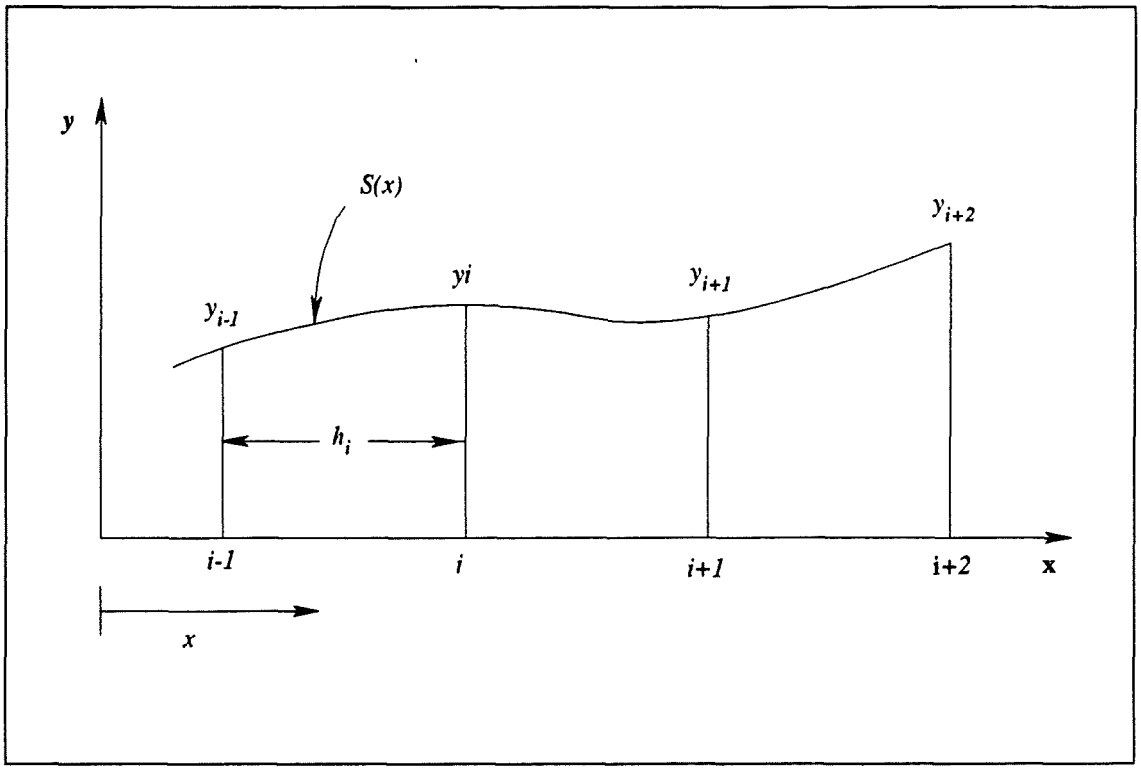

Figure 6.27: Parameters used for the spline fitting.

variable definitions are given in Figure (6.27). The second derivatives of the knots are referred as the *moments* and are defined as $M_i \equiv S''(x_i)$.

$$S(x) = M_{i-1}\frac{(x_i - x)^3}{6h_i} + M_i\frac{(x - x_{i-1})^3}{6h_i} + \frac{(x_i - x)}{h_i}\left\{y_{i-1} - \frac{h_i^2}{6}M_{i-1}\right\}$$

$$+\frac{(x - x_{i-1})}{h_i}\left\{y_i - \frac{h_i^2}{6}M_i\right\} \qquad \text{for } x \in [\,x_{i-1}\,,\,x_i\,]\,,\ i=1,2,\ldots,n \qquad (6.74)$$

$$S'(x) = -M_{i-1}\frac{(x_i - x)^2}{2h_i} + M_i\frac{(x - x_{i-1})^2}{2h_i} + \frac{1}{h_i}(y_i - y_{i-1}) - \frac{h_i}{6}(M_i - M_{i-1}) \qquad (6.75)$$

$$\text{for } x \in [\,x_{i-1}\,,\,x_i\,]\,,\ i=1,2,\ldots,n$$

$$S''(x) = M_{i-1}\frac{(x_i - x)}{h_i} + M_i\frac{(x - x_{i-1})}{h_i} \qquad \text{for } x \in [\,x_{i-1}\,,\,x_i\,]\,,\ i=1,2,\ldots,n \qquad (6.76)$$

From the information given so far, there are *n-1* equations and *n+1* unknown moments. Therefore, two further equations are required and these can be gained from the end conditions. This leads to a linear system of equations for the moment M_i. In matrix notation, it can be shown as follows:

$$\begin{bmatrix} 2 & 1 & & & & 0 \\ \alpha_1 & 2 & \beta_1 & & & \\ & \alpha_2 & 2 & \beta_2 & & \\ & & \cdot & \cdot & \cdot & \\ & & & \cdot & \cdot & \cdot \\ & & & \alpha_{n-1} & 2 & \beta_{n-1} \\ 0 & & & & 1 & 2 \end{bmatrix} \begin{bmatrix} M_0 \\ M_1 \\ M_2 \\ \cdot \\ \cdot \\ M_{n-1} \\ M_n \end{bmatrix} = \begin{bmatrix} \gamma_0 \\ \gamma_1 \\ \gamma_2 \\ \cdot \\ \cdot \\ \gamma_{n-1} \\ \gamma_n \end{bmatrix} \tag{6.77}$$

where,

$$\alpha_i = \frac{h_i}{h_i + h_{i+1}} \tag{6.78}$$

$$\beta_i = \frac{h_{i+1}}{h_i + h_{i+1}} = 1 - \alpha_i \tag{6.79}$$

$$\gamma_i = \frac{6}{h_i + h_{i+1}} \left\{ \frac{1}{h_{i+1}} (y_{i+1} - y_i) - \frac{1}{h_i} (y_i - y_{i-1}) \right\} \quad ; \quad \text{for } i=1, n-1 \tag{6.80}$$

If the first derivatives are specified at $x = x_o$ and $x = x_n$:

$$S'(x_0) = y'(x_0) \tag{6.81}$$

$$S'(x_n) = y'(x_n) \tag{6.82}$$

therefore,

$$\gamma_0 = \frac{6}{h_1}\left\{\frac{y_1 - y_o}{h_1} - y_0'\right\} \tag{6.83}$$

$$\gamma_n = \frac{6}{h_n}\left\{y_n' - \frac{y_n - y_{n-1}}{h_n}\right\} \tag{6.84}$$

For the cone used in this chapter, the slopes for the horizontal displacements u_1 (see Figure 6.28);

$$y_0' = \frac{y_1 - y_0}{h_1} \quad ; \quad y_n' = 0 \tag{6.85}$$

and for the vertical displacements u_3:

$$y_0' = 0 \quad ; \quad y_n' = \frac{y_1 - y_0}{h_1} \tag{6.86}$$

The formulation given in this chapter is implemented for the inner surface of the cone and the results are shown in Section 6.9.

6.9 - RESULTS

This section is divided into three sub-sections. First section, section 6.9.1, gives a set of sample results obtained by using the BEM displacements and the cubic spline fit. The next section, section 6.9.2, shows the effect of the change in height over the inner surface stresses. Section 6.9.3 compares a selection of cone height results of the inner surface, with the results obtained by using the FEM analysis.

6.9.1 - Results - BEM Spline Fit

In this section, the results of a cone of 80mm high, 60mm outer base radius and 5mm wall thickness are given. The bounadry conditions are those illustrated in Figure 6.1. Figure 6.28 shows the horizontal and vertical displacements on the inner surface of the cone. These results were determined using the spline formulation given in section 6.8.3. The derivatives of the displacements are given in Figure 6.29. It is these values that were used to calculate the strains which are given in Figure 6.30.

As pointed out in section 6.8.2, the displacement derivatives were calculated with respect to the inner surface arc length. To maintain consistency, all of the following results shown in Figures 6.28-6.31 were plotted against the arc length. The hoop stresses $\sigma_{\theta\theta}$ and $\sigma_{\varphi\varphi}$ are given in Figure 6.31. The direct stresses σ_{11}, σ_{22}, σ_{33} and the shear stress σ_{13} are also compared with the FEM results. These BEM stresses were determined from the calculated hoop stresses $\sigma_{\theta\theta}$ and $\sigma_{\varphi\varphi}$ by using the following relationships:

$$\sigma_{11} = \sigma_{\theta\theta} \cos^2\theta \tag{6.87}$$

$$\sigma_{22} = \sigma_{\varphi\varphi} \tag{6.88}$$

$$\sigma_{33} = \sigma_{\theta\theta} \sin^2\theta \tag{6.89}$$

$$\sigma_{13} = \frac{-\sigma_{11} \sin^2\theta - \sigma_{33}\cos^2\theta}{\sin 2\theta} \tag{6.90}$$

The details of these relationships are given in Appendix D. These stresses are also compared with the FEM results and they are given in Figures 6.32-6.34 where excellent agreement between theses results can be seen.

6.9.2 - Results - Various Cone Heights

In this section, three sets of results are provided for cones of 10mm wall thickness and outer base radius of 60mm. The cone heights tested are 80mm, 100mm, 120mm, 140mm, 160mm and 180mm. The compared stresses are hoop stress $\sigma_{\varphi\varphi}$, Von Mises stress σ_v and the shear stress σ_{13}. From the results, it is clearly shown that as the cone height increases, the hoop stress and the Von Mises stress at the base of the cone also increase and, decrease at the nose section of the cone. However, these stresses tend to pick up again at the tip. The shear stress is maximum at around the point where two arcs merge on the inner surface. The results are shown in Figures 6.35-6.37.

6.9.3 - Results - FEM-BEM Comparison

The results explained in section 6.9.2 are only the BEM results. In this section, a selection of these results are compared with the results obtained by using the FEM. The mesh used for the FEM model matches identically with the BEM mesh on the inner and outer surfaces with the exception that the FEM mesh elements across the wall thickness is divided into two so that several internal points were also obtained.

Again, the hoop stress $\sigma_{\varphi\varphi}$, the Von Mises stress σ_v and the shear stress σ_{13} are compared for the cone heigths of 80mm, 100mm,140mm and 180mm. The BEM results agree well with the FEM results except for the point very close to the tip of the cone. These are given in Figures 6.38 and 6.39.

The comparison of the shear stress σ_{13} is given in Figure 6.40. The results indicate that there is practically no change in the shear stress at the merging point of the two arcs irrespective of the change in the cone height.

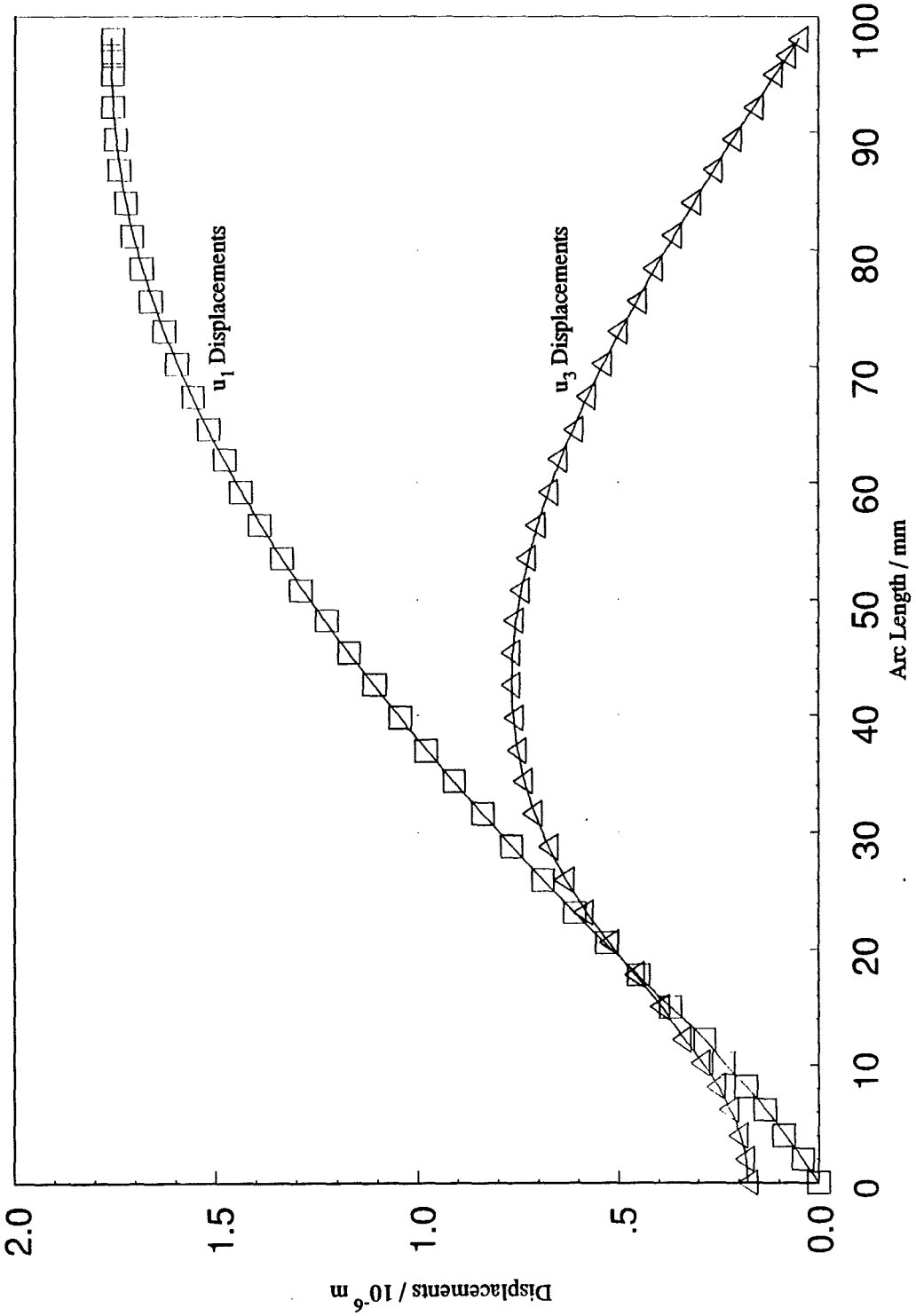

Figure 6.28: Spline fit of the displacements on the inner surface. (Wall thickness = 5mm)

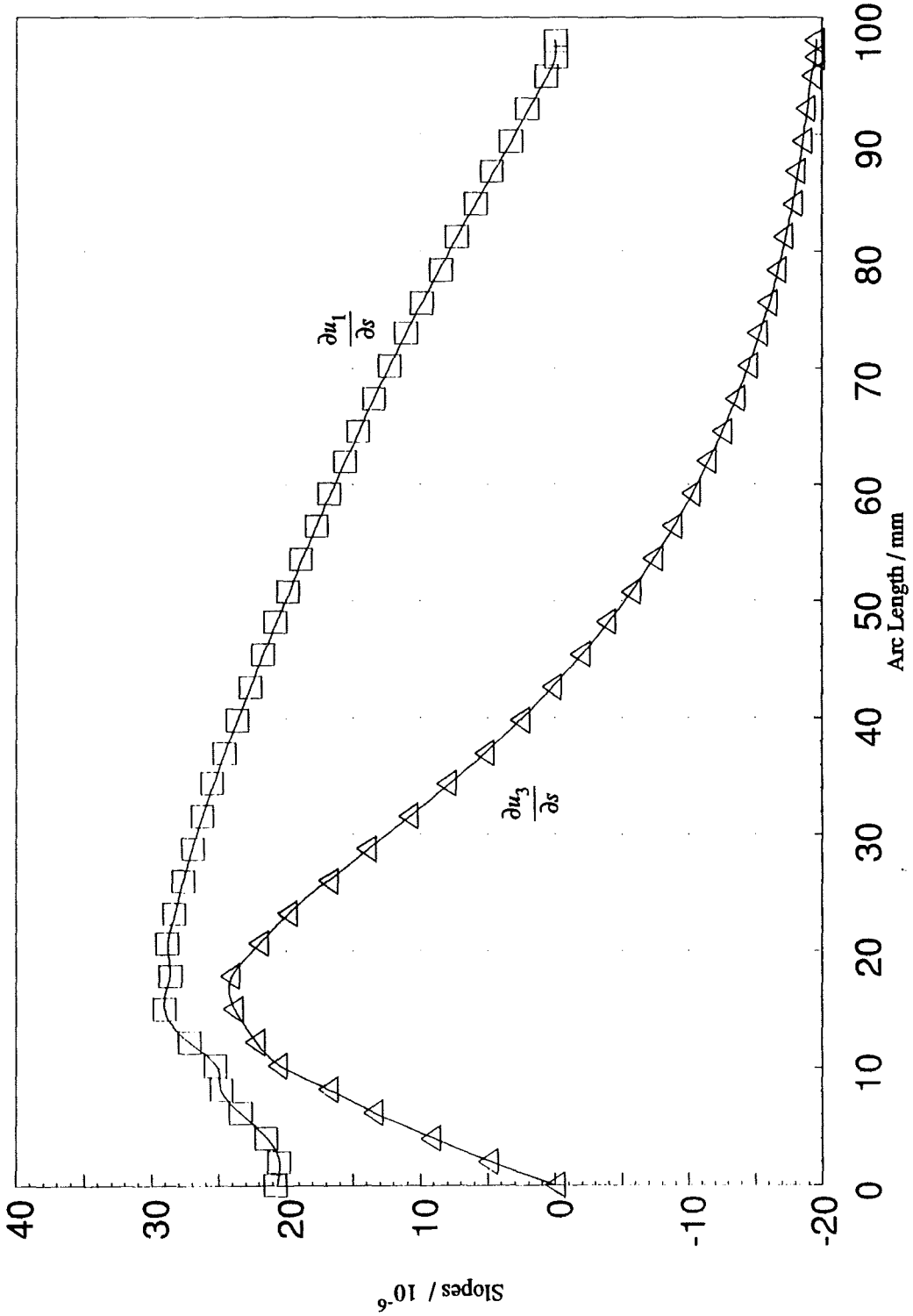

Figure 6.29: Derivatives of the displacments on the inner surface using spline. (Wall thickness = 5mm)

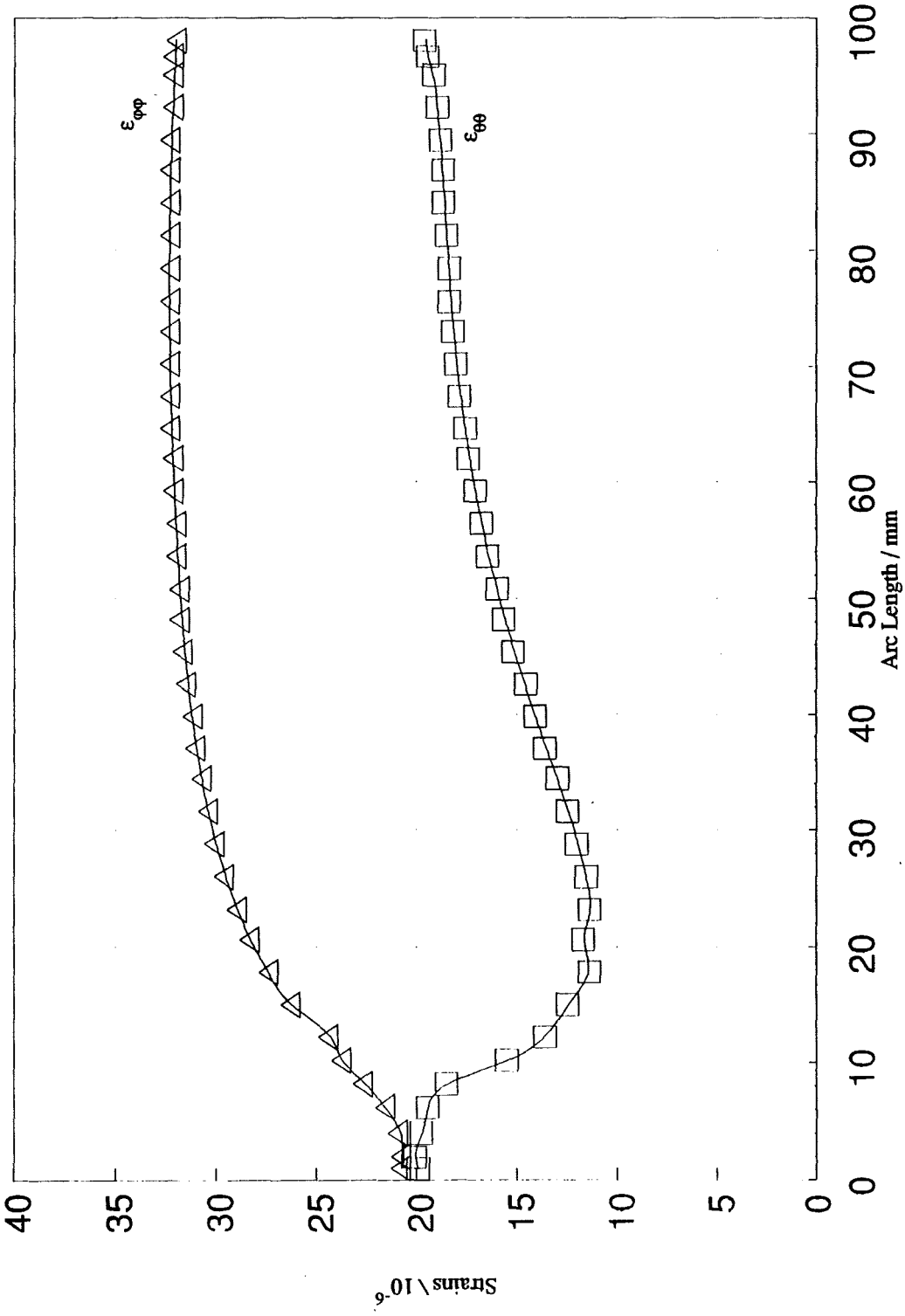

Figure 6.30: BEM hoop (tangential) strains along the inner surface S_3. (Wall thickness = 5mm)

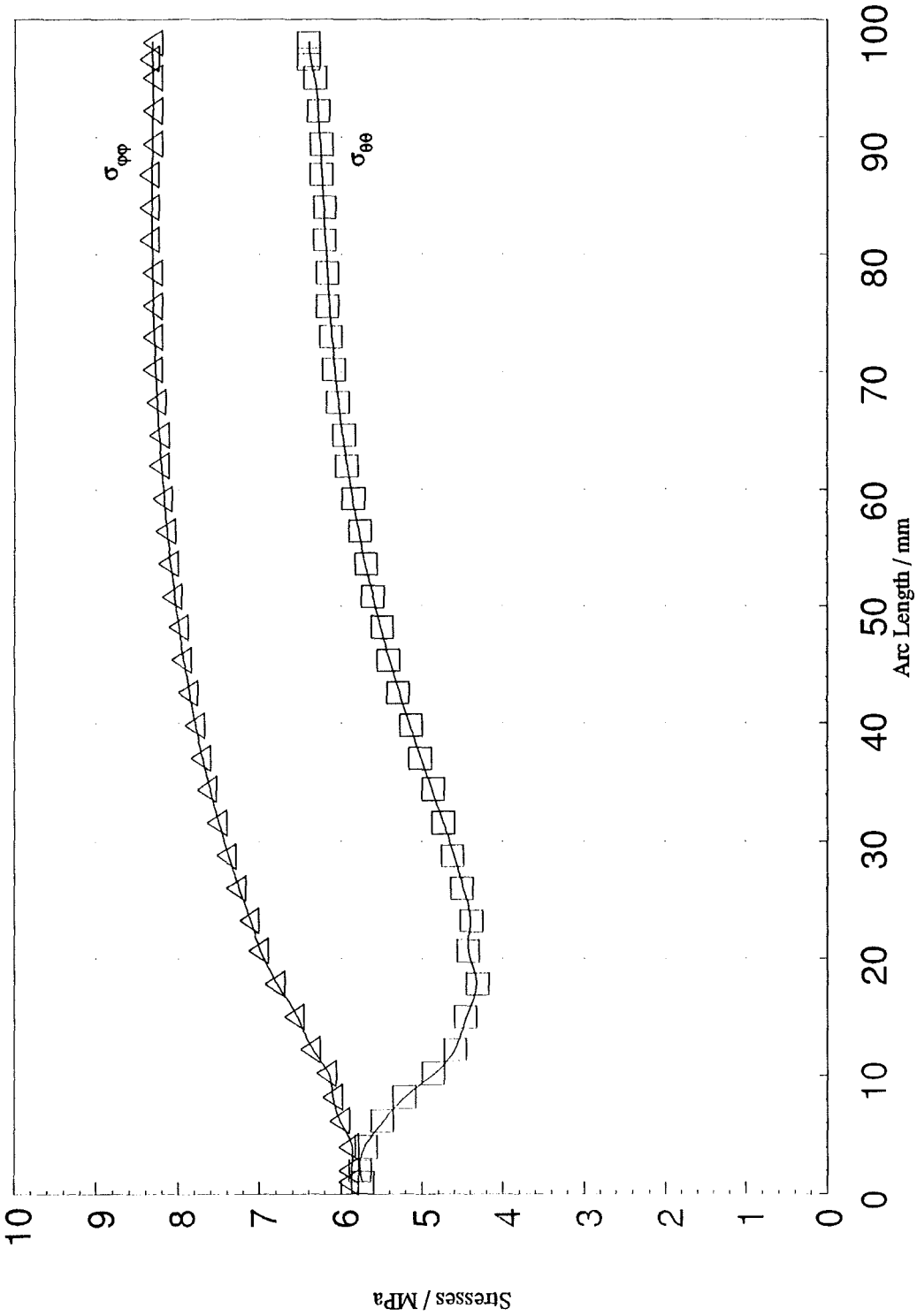

Figure 6.31: BEM hoop (tangential) stresses $\sigma_{\theta\theta}$ and $\sigma_{\varphi\varphi}$ on the inner surface. (Wall thickness = 5mm)

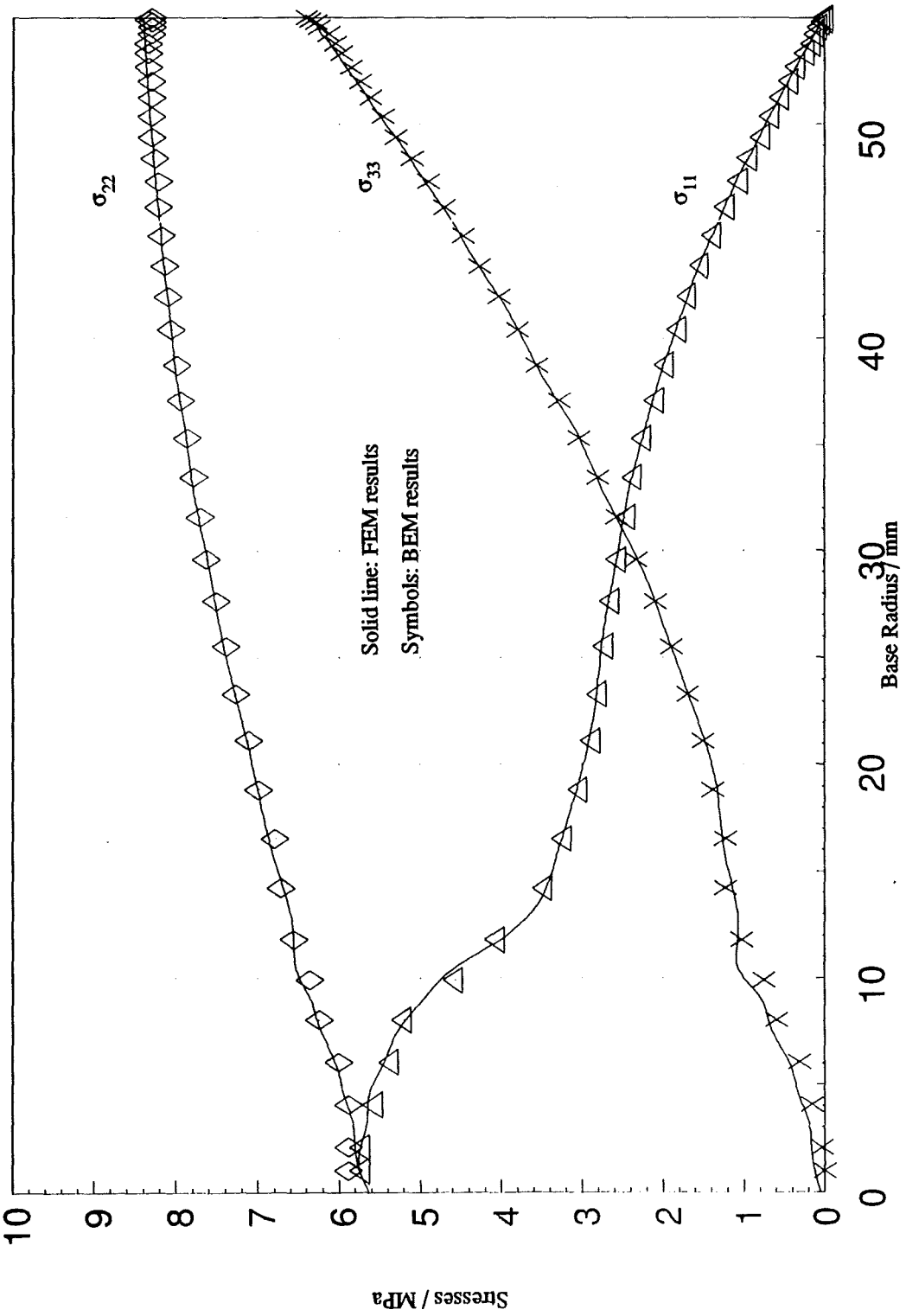

Figure 6.32: Comparison of BEM and FEM stresses along the inner surface. (Wall thickness = 5mm)

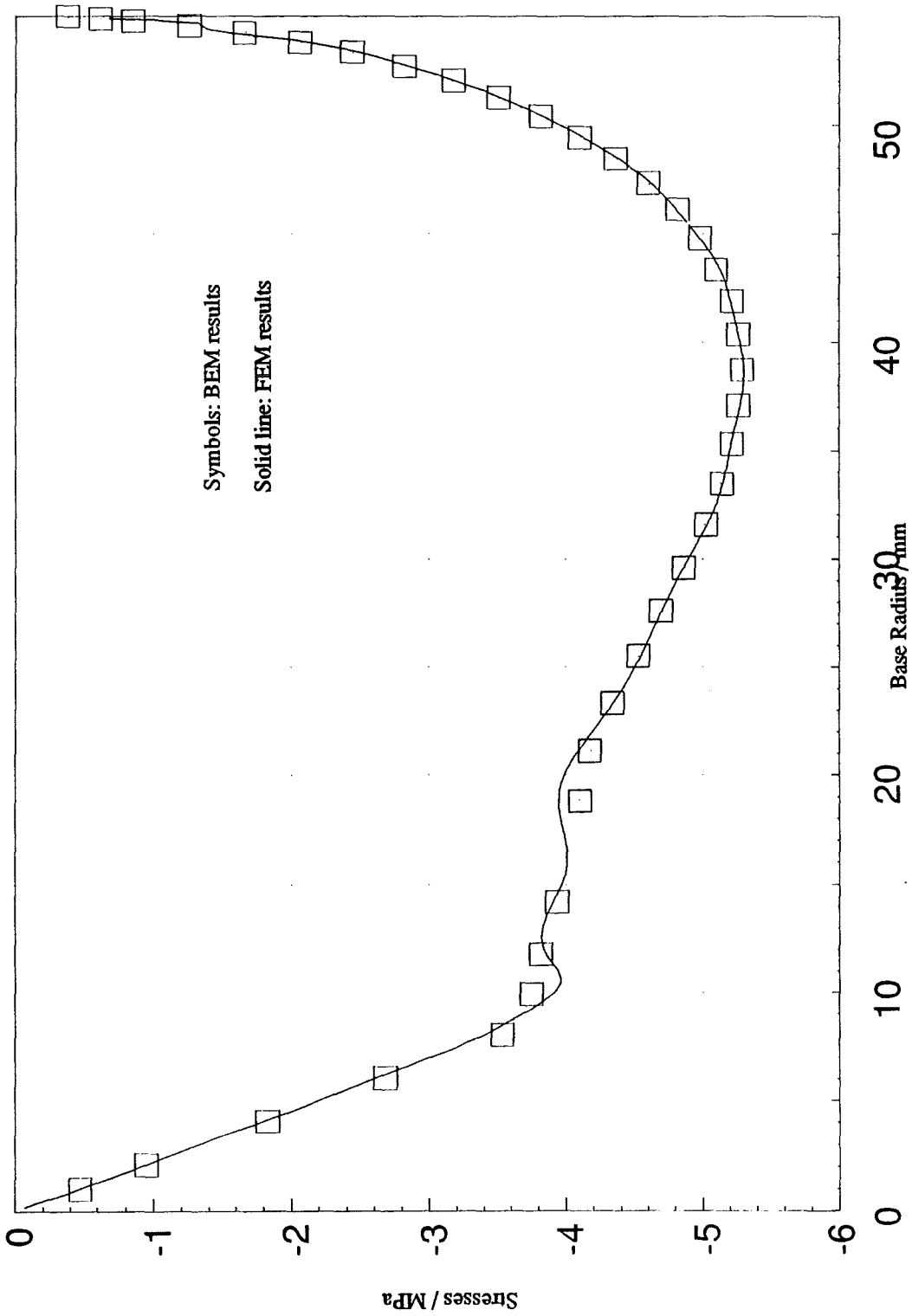

Figure 6.33: Comparison of BEM and FEM shear stress σ_{13} along the inner surface. (Wall thickness = 5mm)

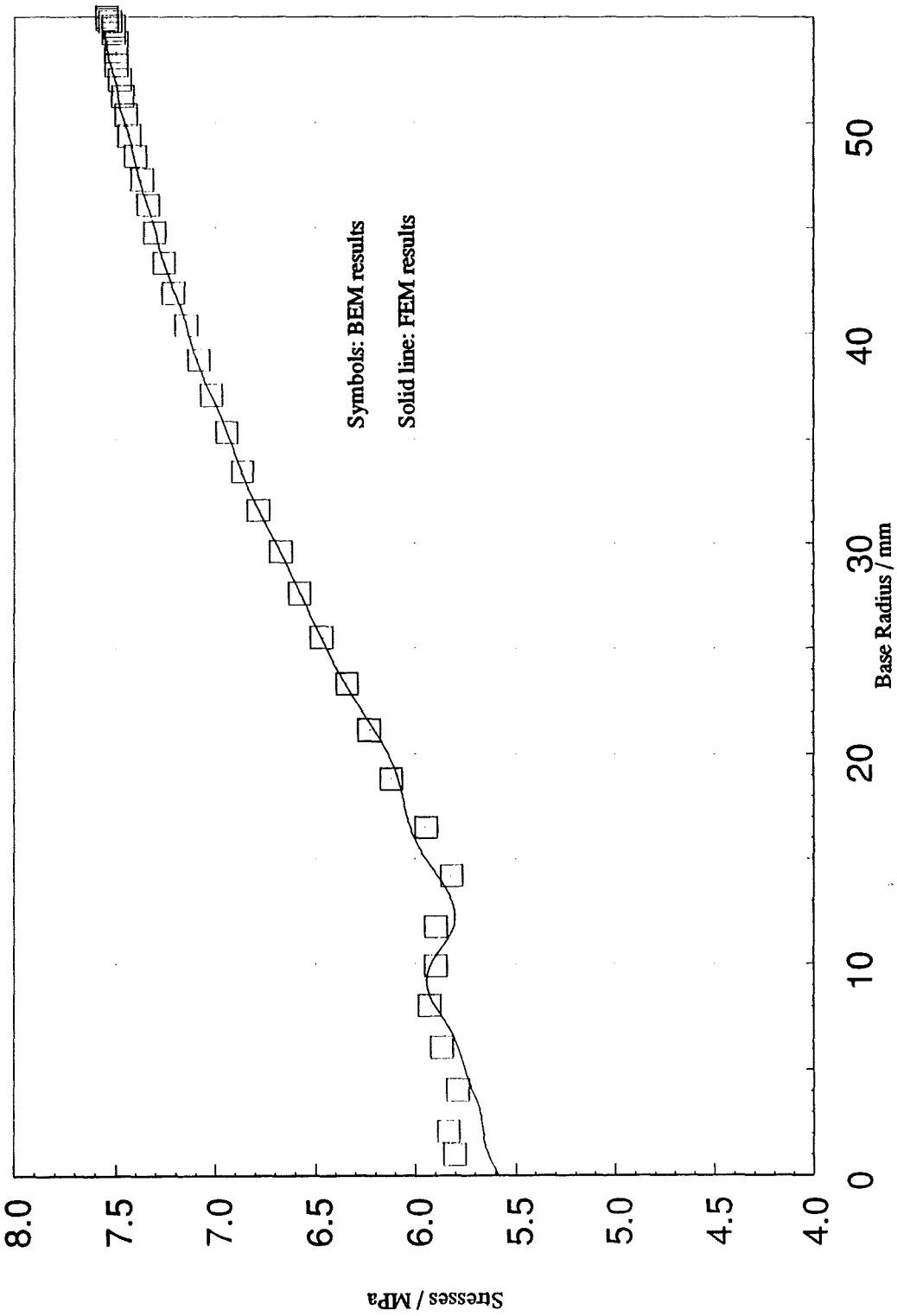

Figure 6.34: Comparison of BEM and FEM Von Mises stresses along the inner surface. (Wall thickness = 5mm)

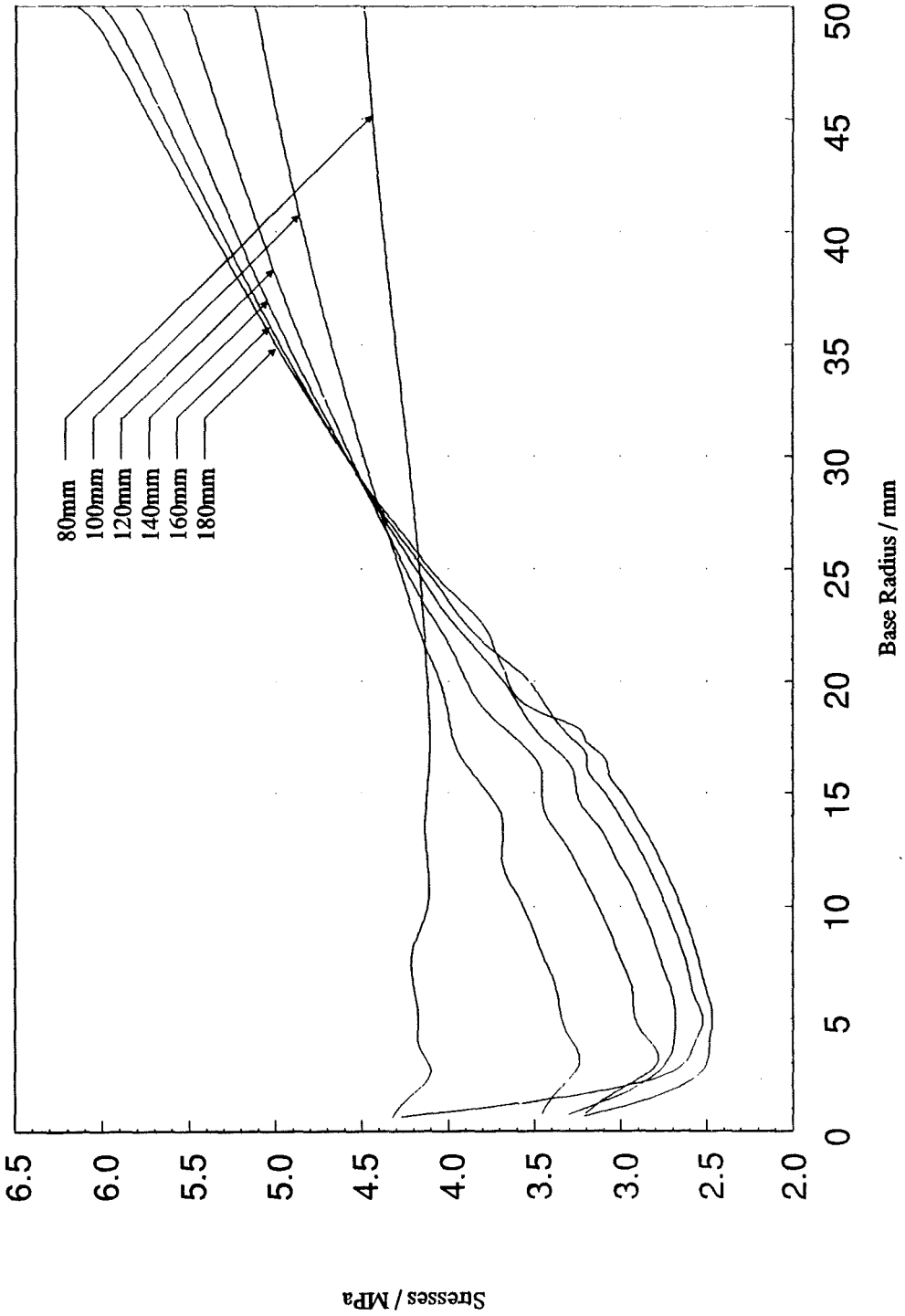

Figure 6.35: BEM hoop stresses $\sigma_{\varphi\varphi}$ along the inner surface for various cone heights. (Wall thickness = 10mm, Outer base radius= 60mm)

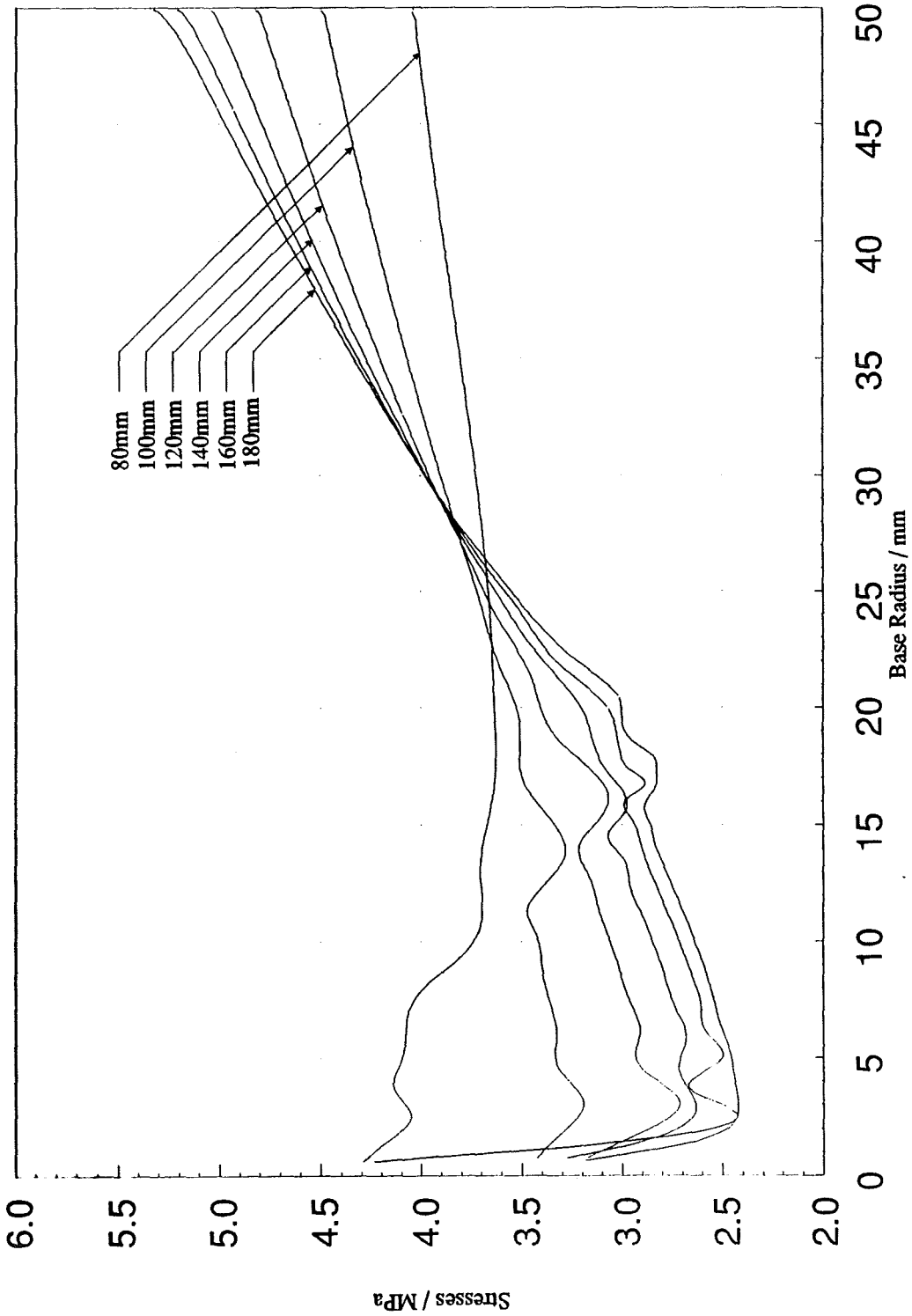

Figure 6.36: BEM Von Mises σ_v stresses along the inner surface for various cone heights. (Wall thickness = 10mm, Outer base radius= 60mm)

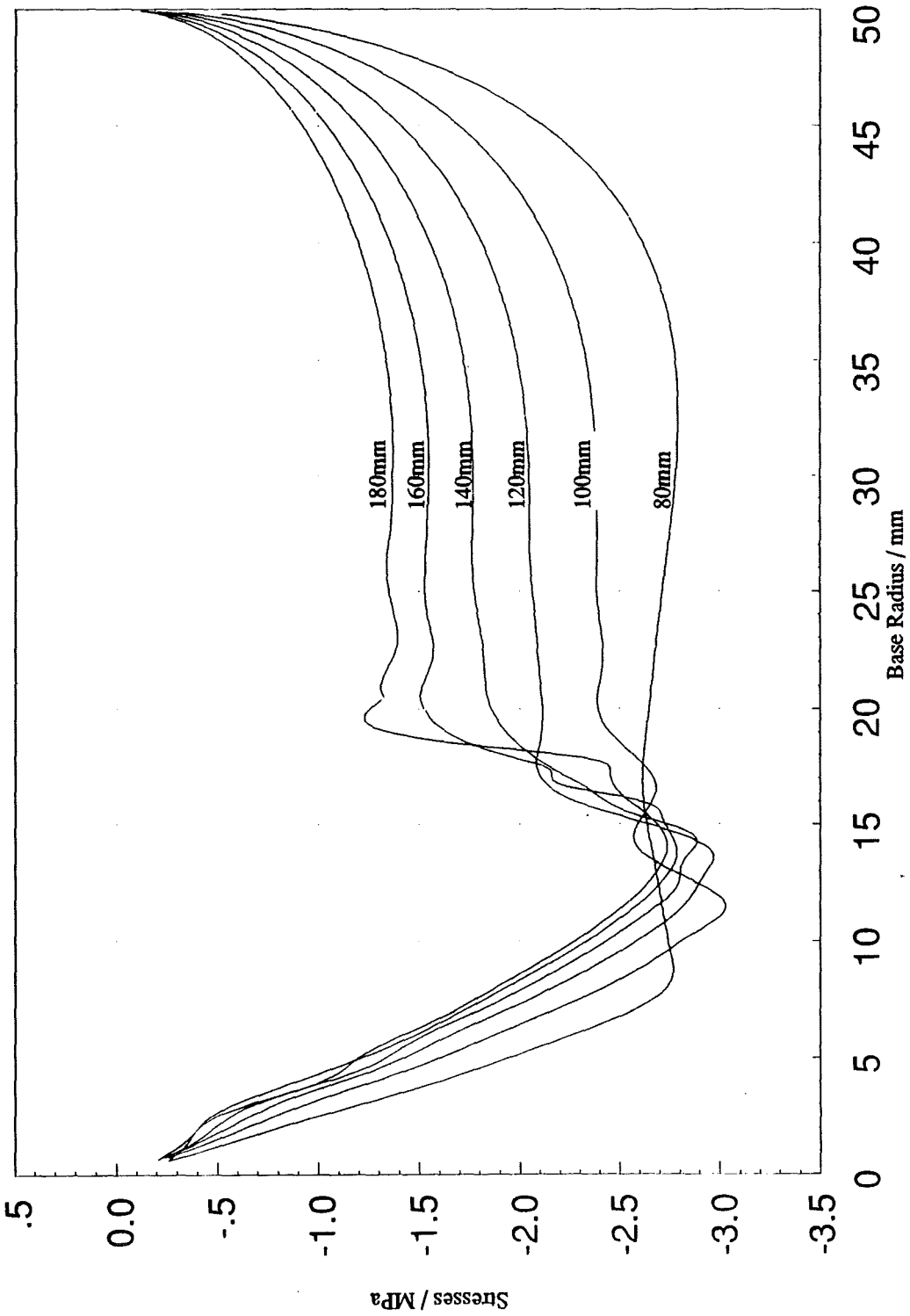

Figure 6.37: BEM Shear stresses σ_{13} along the inner surface for various cone heights. (Wall thickness = 10mm, Outer base radius= 60mm)

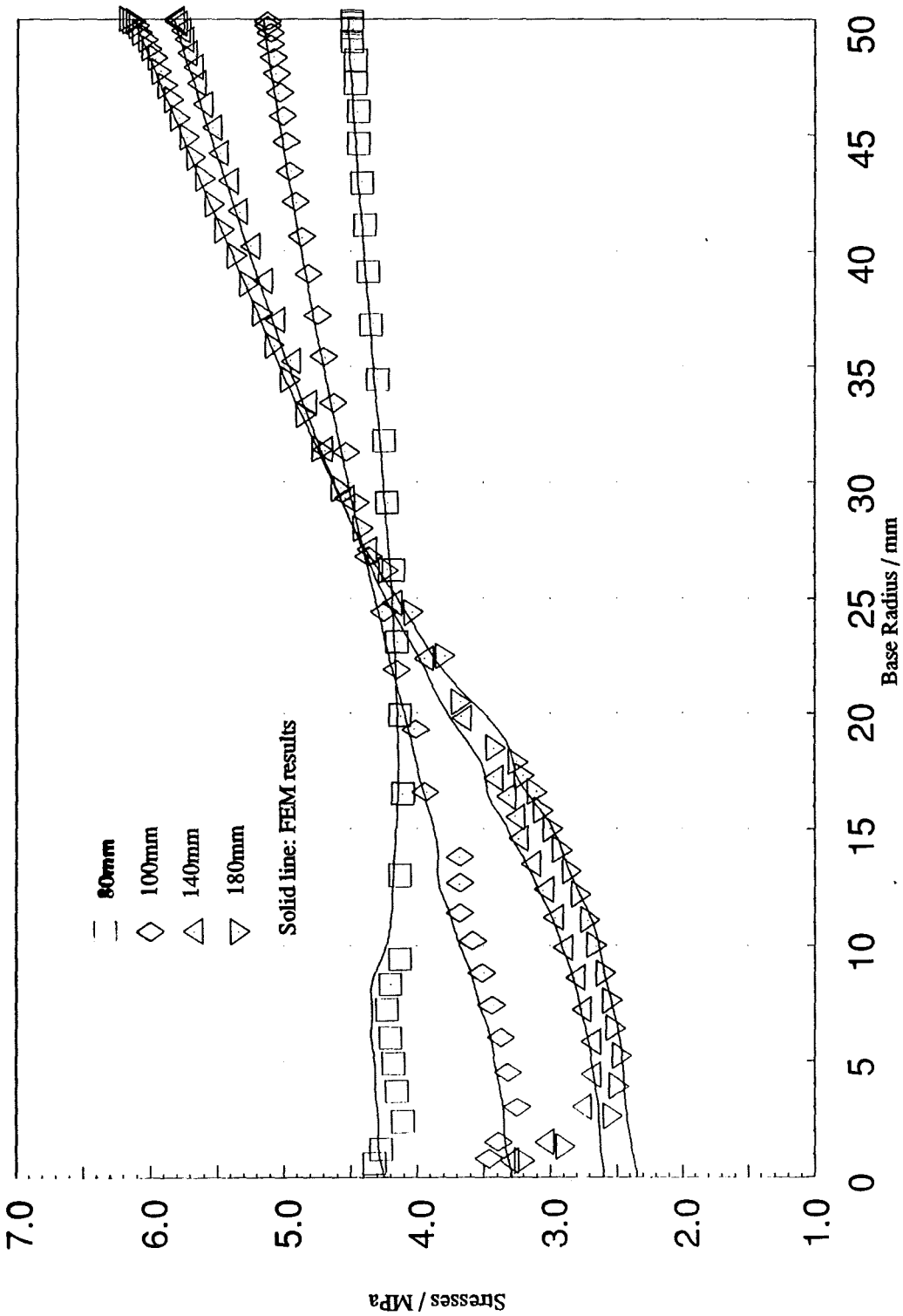

Figure 6.38: Comparison of BEM and FEM hoop stresses $\sigma_{\varphi\varphi}$ along the inner surface for various cone heights. (Wall thickness = 10mm, Outer base radius= 60mm)

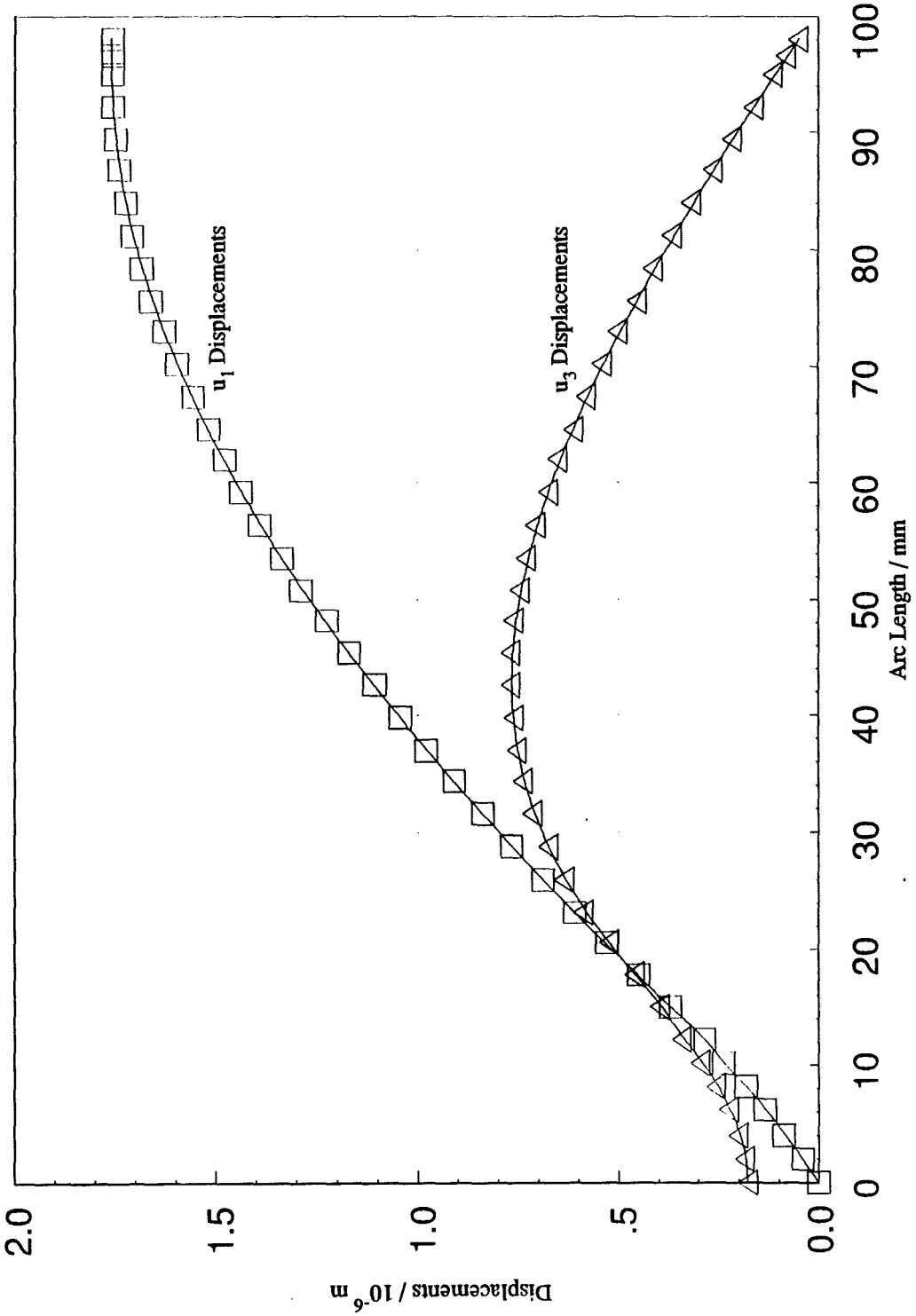

Figure 6.28: Spline fit of the displacements on the inner surface. (Wall thickness = 5mm)

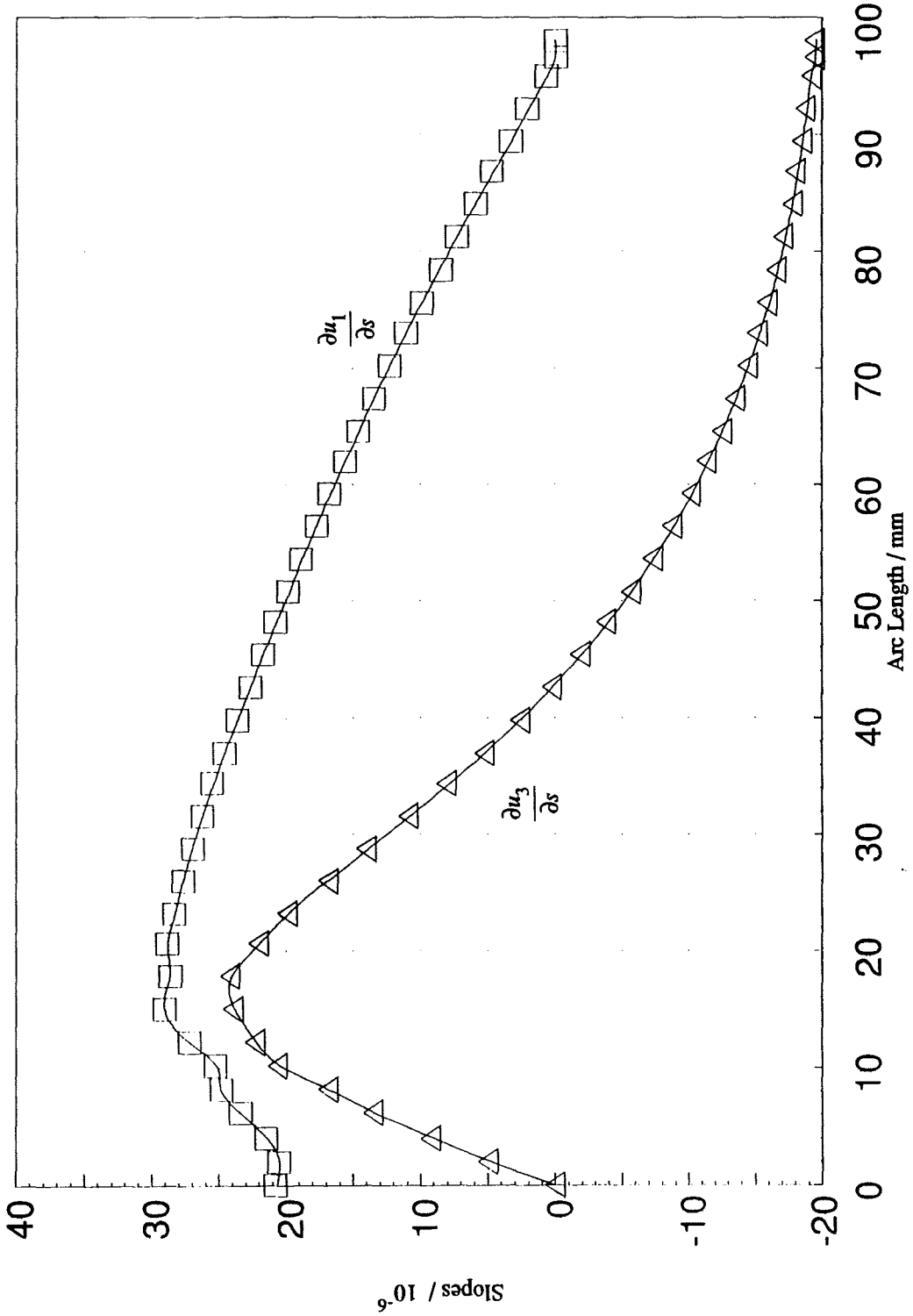

Figure 6.29: Derivatives of the displacments on the inner surface using spline. (Wall thickness = 5mm)

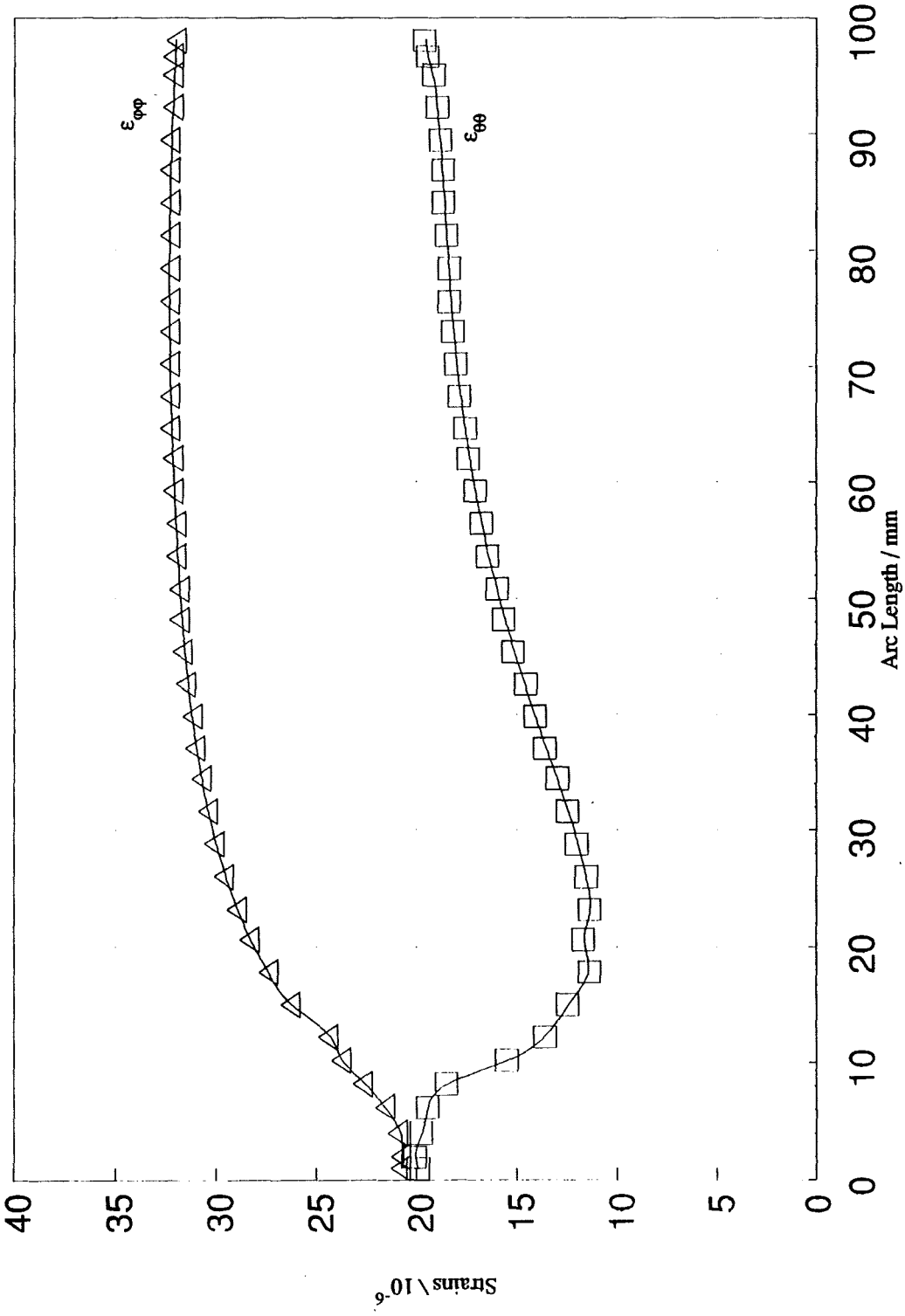

Figure 6.30: BEM hoop (tangential) strains along the inner surface S_3. (Wall thickness = 5mm)

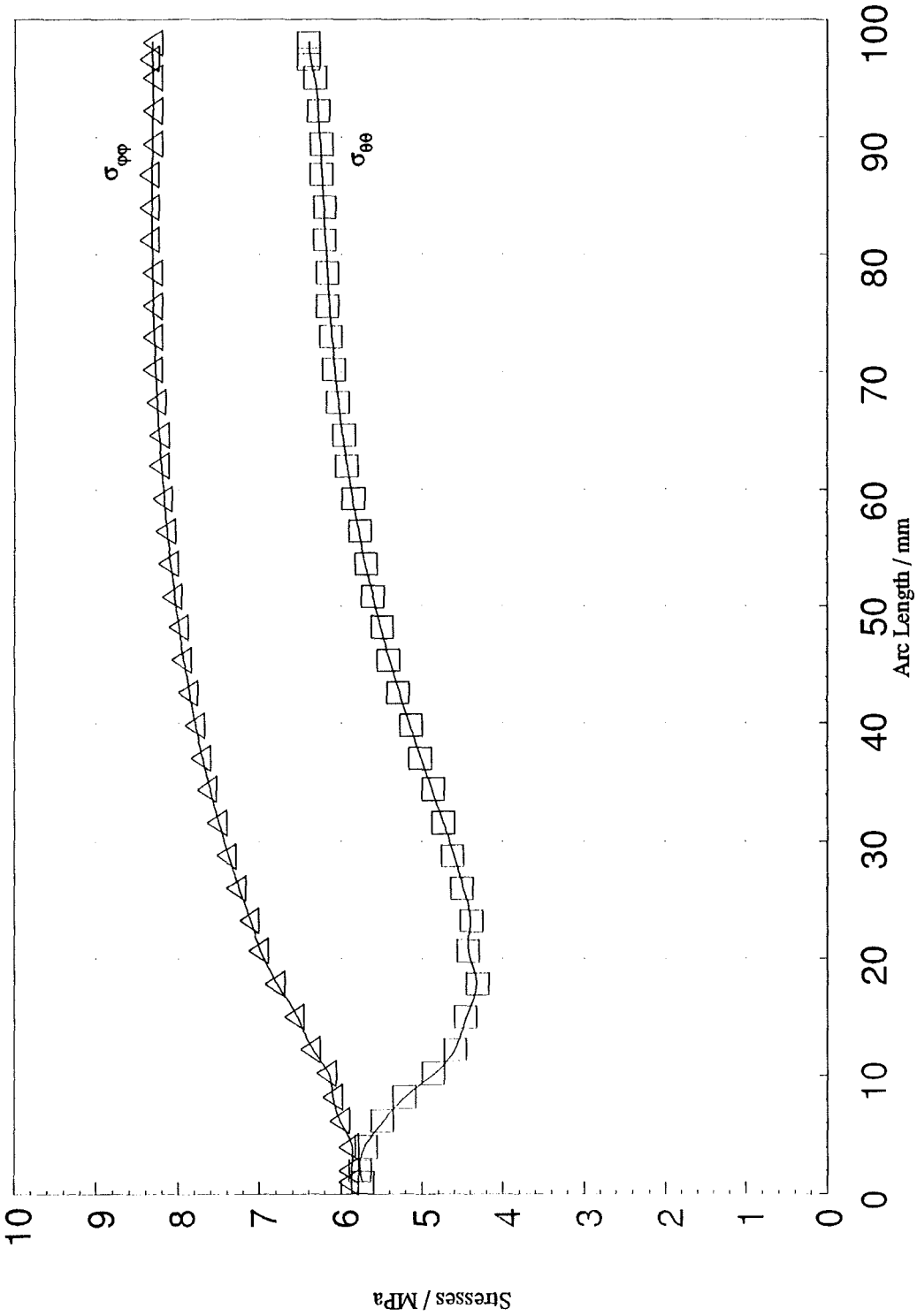

Figure 6.31: BEM hoop (tangential) stresses $\sigma_{\theta\theta}$ and $\sigma_{\varphi\varphi}$ on the inner surface. (Wall thickness = 5mm)

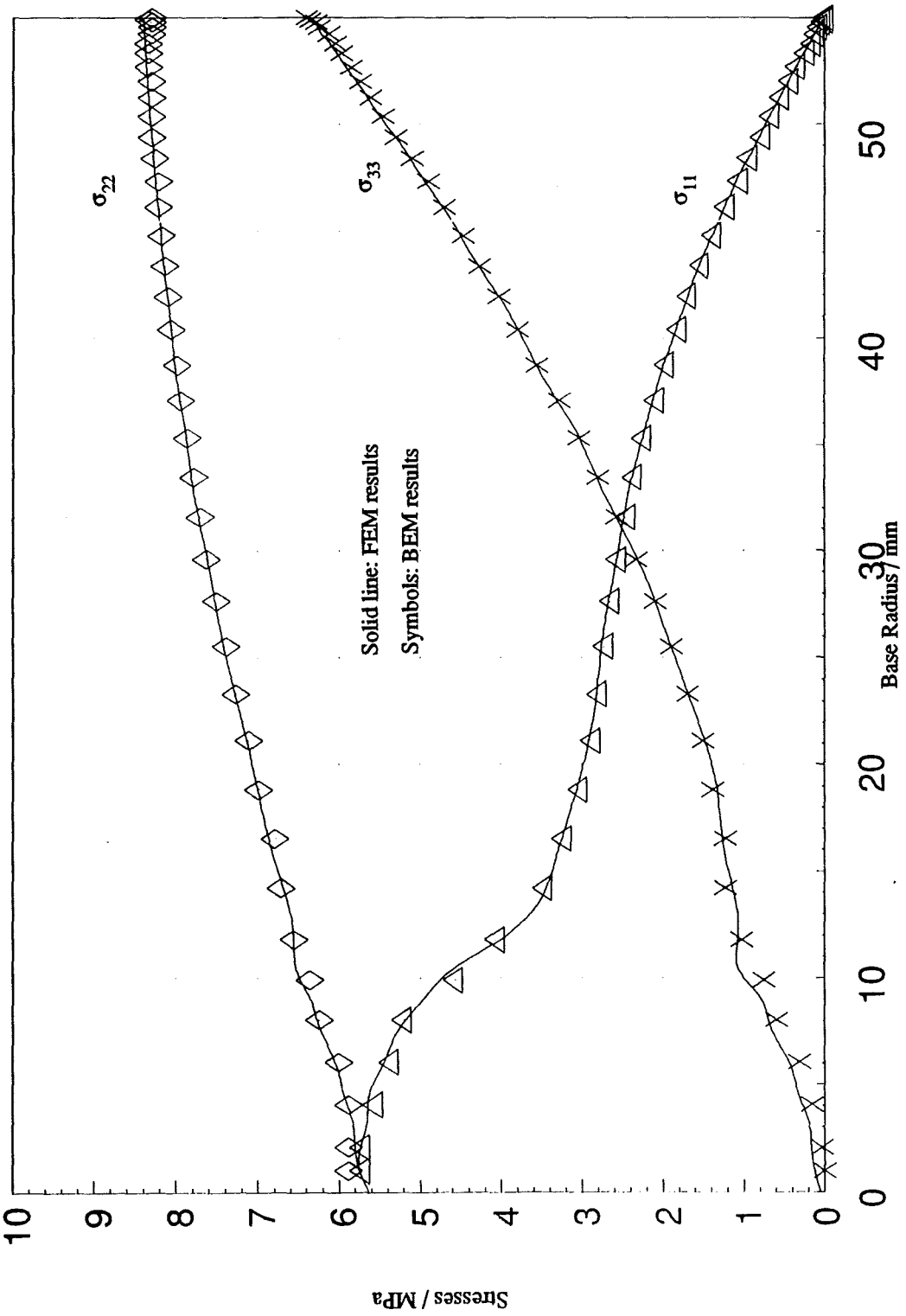

Figure 6.32: Comparison of BEM and FEM stresses along the inner surface. (Wall thickness = 5mm)

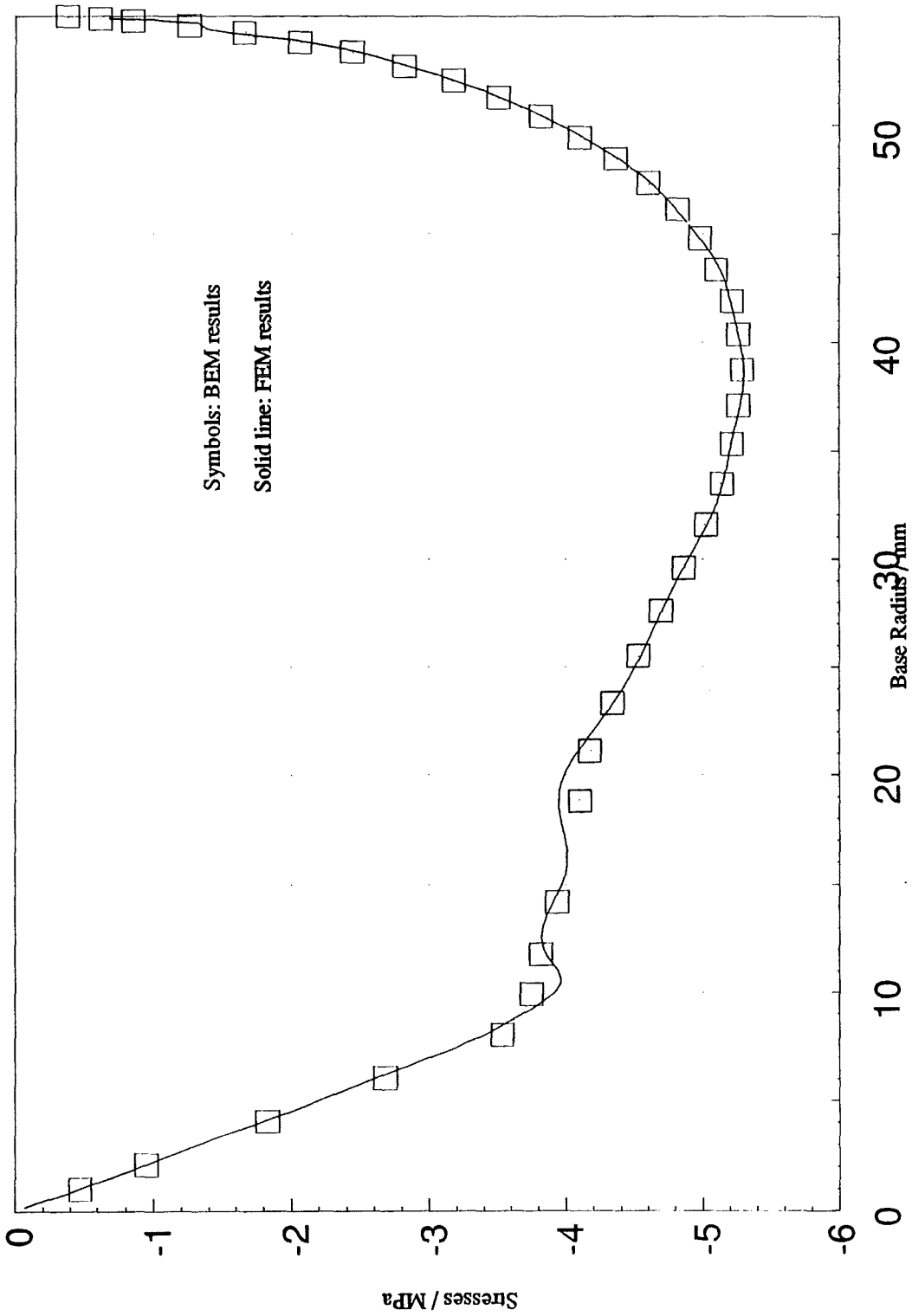

Figure 6.33: Comparison of BEM and FEM shear stress σ_{13} along the inner surface. (Wall thickness = 5mm)

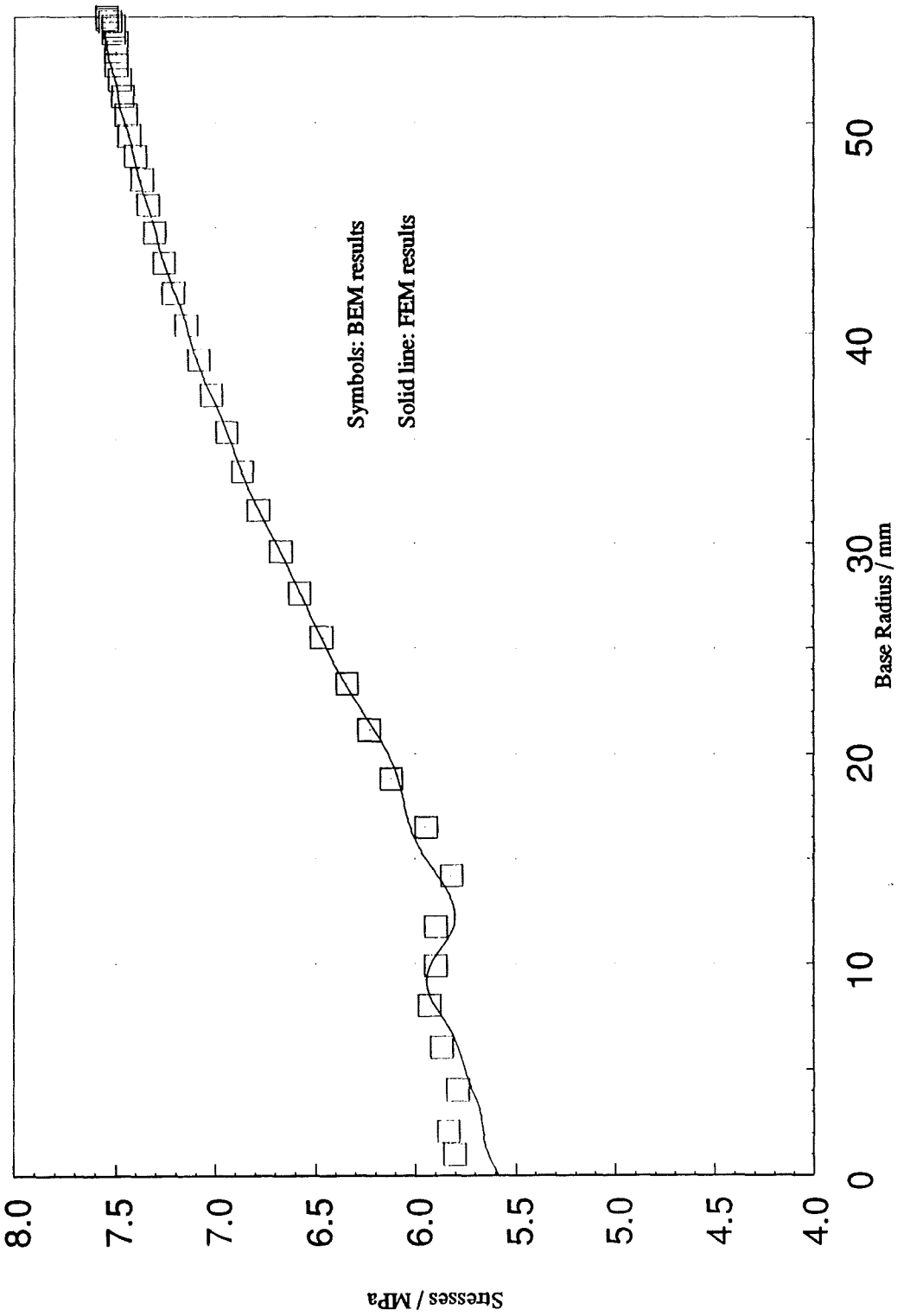

Figure 6.34: Comparison of BEM and FEM Von Mises stresses along the inner surface. (Wall thickness = 5mm)

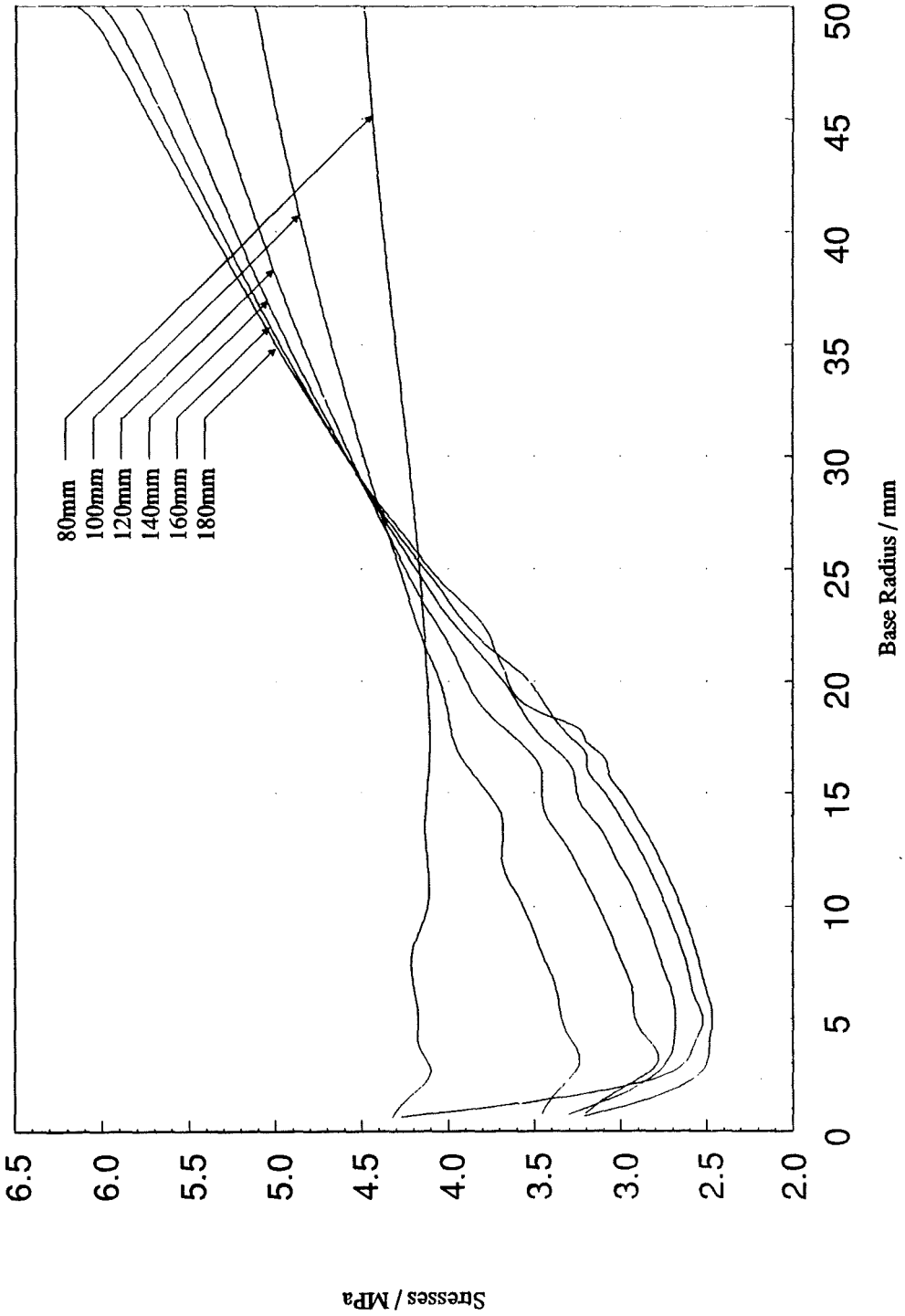

Figure 6.35: BEM hoop stresses $\sigma_{\varphi\varphi}$ along the inner surface for various cone heights. (Wall thickness = 10mm, Outer base radius= 60mm)

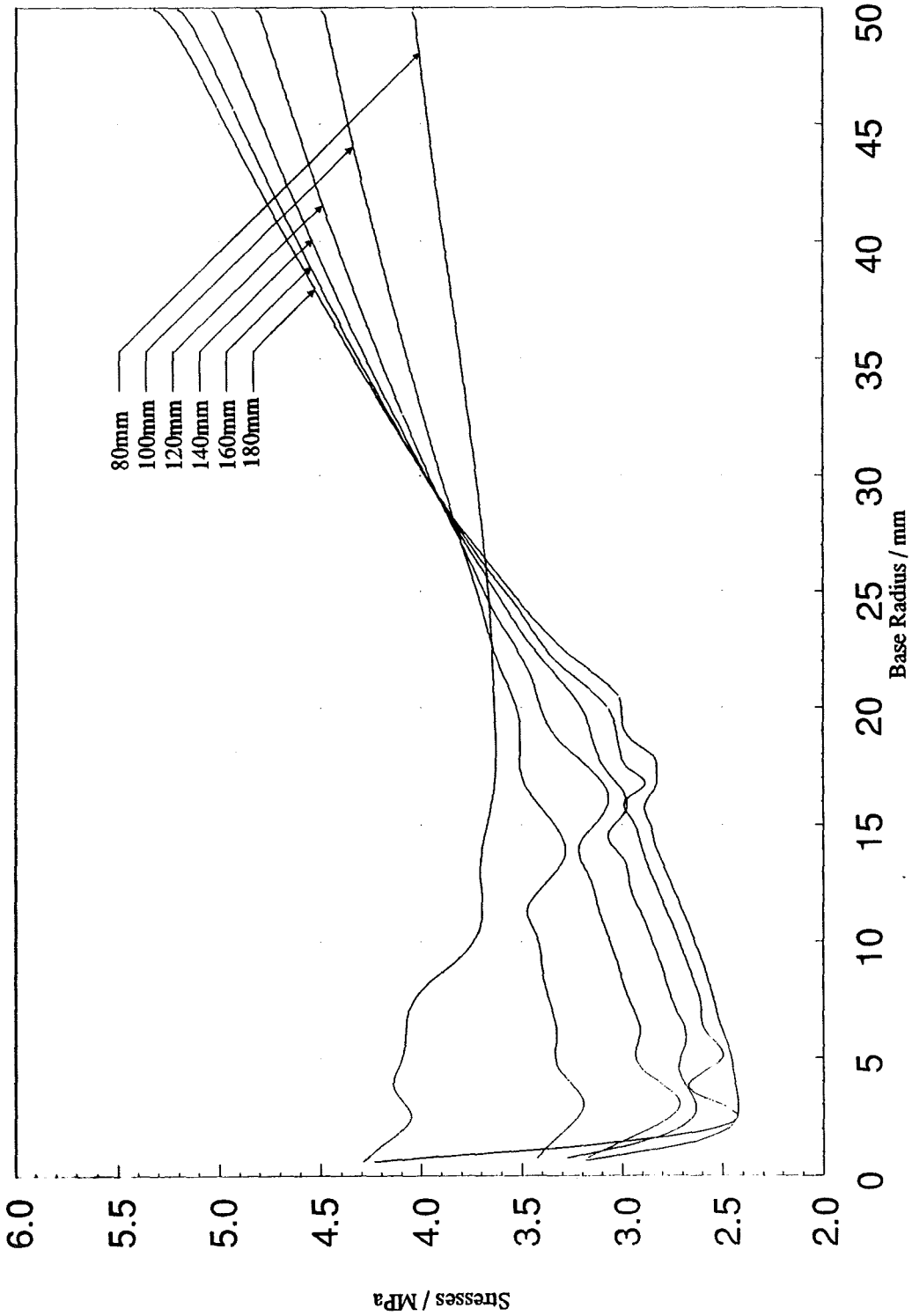

Figure 6.36: BEM Von Mises σ_v stresses along the inner surface for various cone heights. (Wall thickness = 10mm, Outer base radius= 60mm)

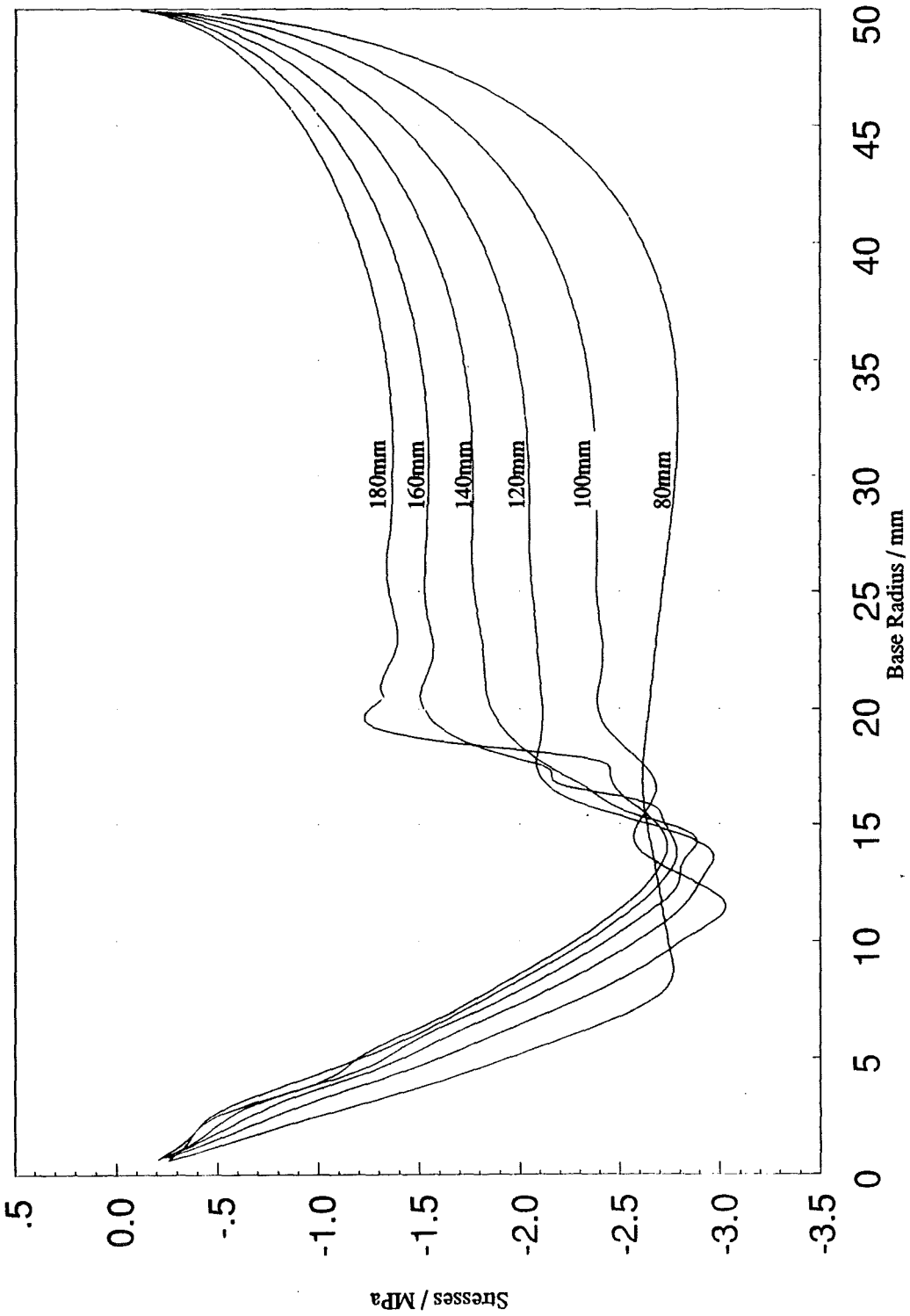

Figure 6.37: BEM Shear stresses σ_{13} along the inner surface for various cone heights. (Wall thickness = 10mm, Outer base radius= 60mm)

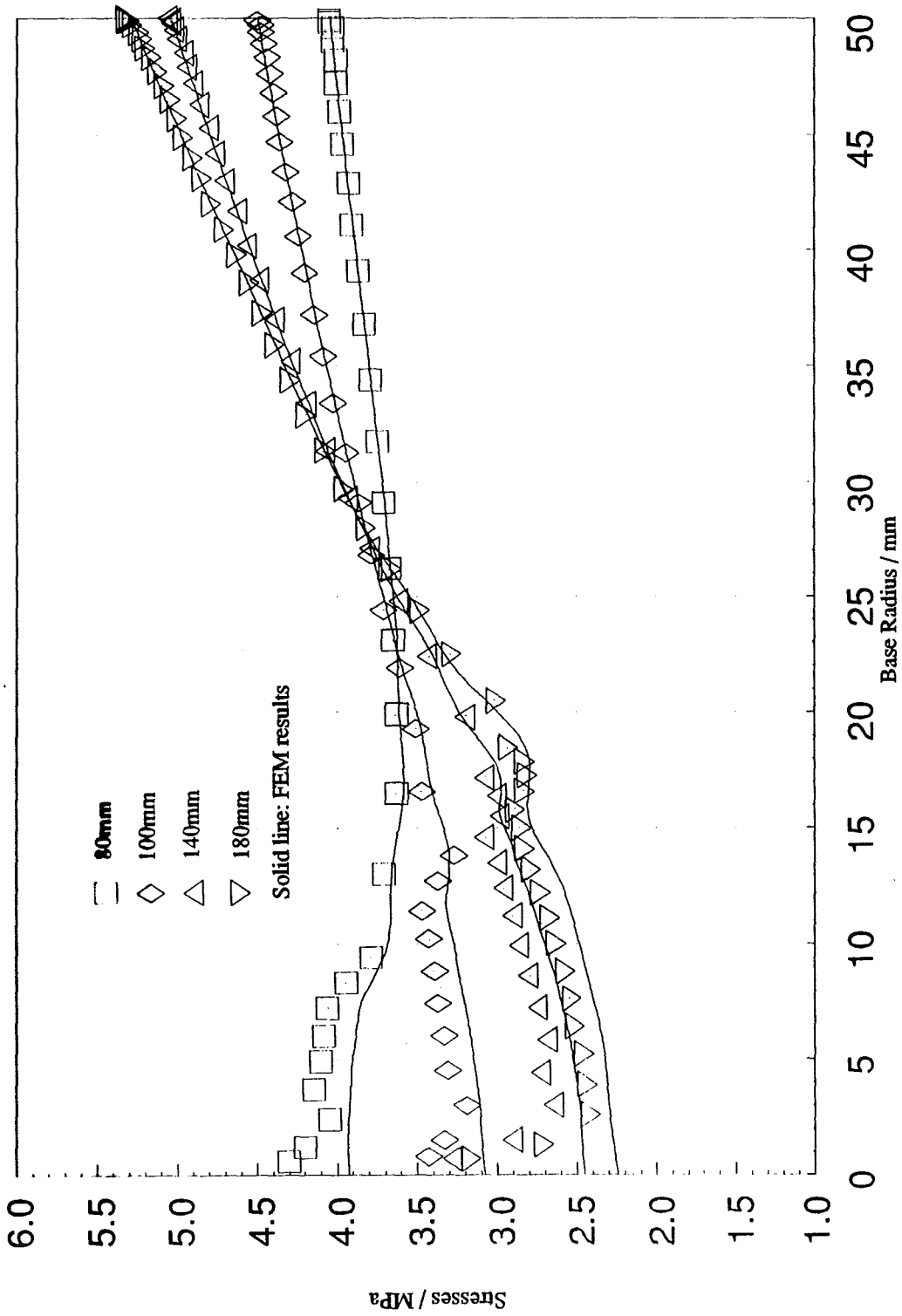

Figure 6.39: Comparison of BEM and FEM Von Mises stresses σ_v along the inner surface for various cone heights. (Wall thickness = 10mm, Outer base radius= 60mm)

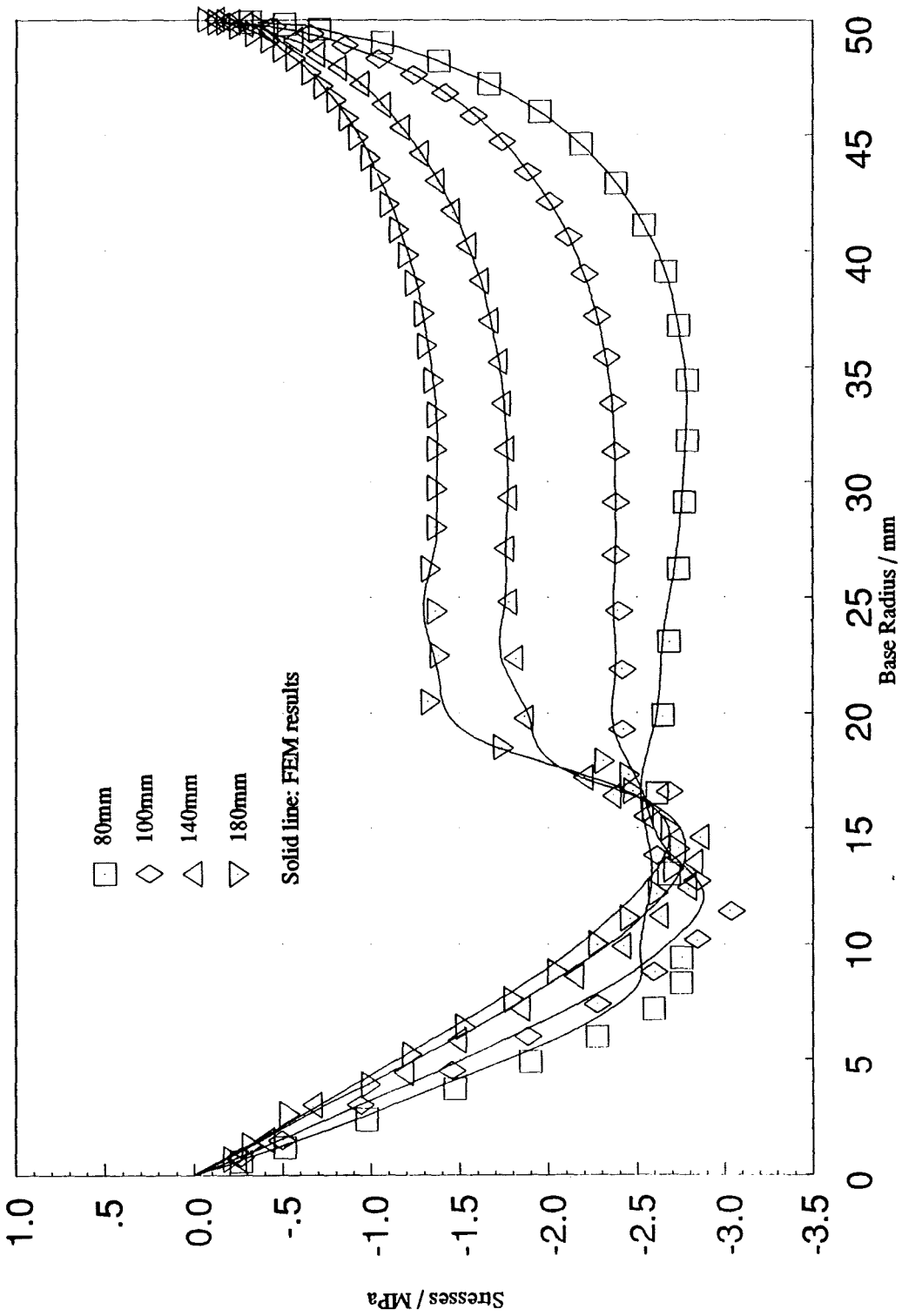

Figure 6.40: Comparison of BEM and FEM Shear stresses σ_{13} along the inner surface for various cone heights. (Wall thickness = 10mm, Outer base radius= 60mm)

Chapter

7

Further Developments

"Only in men's imagination does every truth find an effective and undeniable existence. Imagination, not invention, is the supreme master of art as of life."

Joseph Conrad

1912

7.1 - INTRODUCTION

In this chapter, investigations to take the present work one step further are discussed. One of the areas in need of further investigation is to increase the ability of BEM to deal more efficiently with long and slender sections. It is shown in this work that by having two surfaces very close together, similar rows are obtained in the system matrices which cause singular solutions. This is due to the fact that as the geometrical position of the nodes on two different surfaces becomes similar, the resulting coefficients also become similar, and hence this results in similar rows in the system matrices. This type of limitation also appears in fracture mechanics, where the nodes on both surfaces of a crack often share the same special location when the crack is closed. One way to get around this problem is suggested by Portela et. al. (1991) where a different formulation is used for each of the crack surfaces. This method is known as the Dual Boundary Element Method (DBEM).

7.2 - DBEM APPLIED TO CRACK PROBLEMS

The DBEM uses two independent equations. In Portela's case, the displacement and the traction boundary integral equations are used. One of these equations is used for one side of the crack and the other equation is used for the other side of the crack.

The displacement equation is given in Equation (2.60) and it is repeated here, for the benefit of the reader, without the body force term.

$$\tfrac{1}{2}\, u_l(x') + \int_S p^*_{lk}(x',x)\, u_k(x)\, dS(x) = \int_S w^*_{lk}(x',x)\, \mathrm{P}_k\, dS(x) \tag{7.1}$$

The stress equation for a boundary point x', derived by Cruse (1977), in the absence of the body forces, is:

$$\tfrac{1}{2}\, \sigma_{ij}(x') + \int_S S_{kij}(x',x)\, u_k(x)\, dS(x) = \int_S D_{kij}\, p_k\, dS(x) \tag{7.2}$$

By using the relationship given in Equation (2.2), the traction equation is written as follows:

$$\tfrac{1}{2}\, \mathrm{P}_i(x') + n_j(x') \int_S S_{kij}(x',x)\, u_k(x)\, dS(x) = n_j(x') \int_S D_{kij}\, p_k\, dS(x) \tag{7.3}$$

where $n_j(x')$ denotes the j component of the outward normal to the surface, at the point x'. Equation (7.1) and (7.3) form the bases of the DBEM formulation.

7.3 - DBEM APPLIED TO CONE

These two equations were used to model the cone geometry discussed in Chapter 6. Equation (7.1) was used to formulate the outer and base surfaces, S_1 and S_2. The surface S_3 was formulated using Equation (7.3). However, on the inner surface, S_3, there were no tractions and therefore, Equation (7.3) was simplified to:

$$n_j(x') \int_{S_3} S_{kij}(x',x)\, u_k(x)\, dS(x) = 0 \tag{7.4}$$

Equation (7.1) was already implemented for the surfaces S_1 and S_2 using quadratic elements. The integration routines were also successfully implemented. In Equation (7.4), the kernel S_{kij} exhibits a hypersingularity of the order $\frac{1}{r^3}$. Hypersingular kernels arise whenever the normal derivative of a conventional boundary integral is taken. This is due to the fact that hypersingular integral equations involve the derivatives of already strongly singular kernels.

The existing *Composite Mapping* integration was developed for a singularity of order $\frac{1}{r^2}$ and when the integral was transformed into polar coordinates, the order of the integral reduced by one. This process is detailed in Chapter 3. The same procedure can be applied to the integral in Equation (7.4) which will make the integral a finite-part integral of order 2 (see Kutt, 1975) and is also equivalent to the Hadamard principal-value, provided the integrand is C^2 continuous (see Portela, 1992) . To maintain the C^2 continuity requirement on the integral Equation (7. 4), elements of cubic variation were used on the inner surface and quadratic on the other two surfaces.

However, at this stage, it was decided to test the convergence of the integral Equation (7.4) on a singular element on the inner surface of a hollow hemisphere by using the refinement technique illustrated in Chapter 3. However, convergence of the Equation (7.4) over a singular element was not achieved using the refinement type integration. The same test was also tested with discontinuous quadratic elements which satisfied the continuity requirements, but no improvements on the results were seen.

Although the DBEM method is reported to work well on 2D applications (Portela et. al., 1992), difficulty in the evaluation of the hypersingular integrals of order $\frac{1}{r^3}$ present in 3D applications has been a limiting factor in this study. Further investigation into this problem is necessary and perhaps a more advanced integration scheme can be developed employing

a Kutt type formulation with $\lambda = 2$. It is worth noting here that a Kutt formulation of this order will have complex abscissas in the formulation and complex number manipulations will be necessary in the programming.

7.4 - NEW INTEGRATION METHODS

Recently, attempts have been made to solve the hypersingular integrals, which appear in the BEM formulation, directly. Gray et. al. (1990) used a direct analytical integration with a limiting process on flat elements. Another way was proposed by Krishnasamy et. al. (1990), who interpreted the hypersingular integrals in terms of the Hadamard finite-part integrals and then converted these into regular line and surface integrals through a use of Stoke's theorem. Since no integration by parts was performed, the problem was still formulated in terms of the original variables.

Guiggiani et. al. (1991a, 1991b, 1991c), showed that all hypersingular integrals arising in the BEM could be directly transformed into ordinary integrals in the local plane of the intrinsic coordinates through simple but rigorous manipulations. Firstly, it was shown that no unbounded terms arise in the limiting process. This process was then translated in terms of intrinsic coordinates and through some suitable expansions, all of the singular integrals were evaluated analytically and the limit was carried out exactly. The remaining regular integrals were then integrated using an ordinary Gauss quadrature of low order. It was also shown that the method provides good results even on curved elements.

By using these methods described above, it would be possible to overcome some of the problems outlined in this thesis. For example, it would be to possible evaluate problems with thin sections using BDEM and also to determine the whole stress tensor directly on the boundary.

Chapter

8

Conclusions

"Mathematics, rightly viewed, possesses not only truth, but supreme beauty - a beauty cold and austere, like that of sculpture."

Bertrand Russel
1918

In this thesis, Boundary Element Method formulation and its application in three dimensional elasticity analysis have been presented by making use of Elements of linear and quadratic variations. However, it was found that a quadratic element formulation, which turned out to be easier to implement, gave more accurate results. The main object of this study has been the application of the BEM for a nose cone which concentrated on several key areas of the method.

Calculation of the diagonal terms of the system matrix was done explicitly so improvements on the integration of singular integrals could be made. Two different integration methods were tested. *Convergence Method* was based on dividing the singular elements into smaller areas and summing the results until they converged within a predescribed percentage of

error. With the *Accelerated Convergence Method* developed here, where the element division factor was increased from 2 to 10, the number of iterations necessary to produce the same percentage of error was dropped from 7 to 4 which saved considerable CPU time. Further increases in the element division number was possible, but the danger of approaching the singular point too quickly and reaching the limit of the computer was increasing. With a division number of 50, the number of iterations were reduced to 3 but the risk of having a premature end to the program execution was far too great. Therefore, it was decided to keep the number of iterations to 4. Throughout this research work, a division number of 10 was used.

Another integration method, *Composite Mapping*, which was used to integrate singular double integrals was also used. This method used both Gauss and Kutt quadratures. The rectangular elements were divided into triangular elements and *Composite Mapping* was then applied to evaluate the integral without any iteration. The Kutt integration method is based on the finite- part integral formulation and this was implemented in the BEM.

The result was that *Composite Mapping* was found to be more efficient than the *Accelerated Convergence Method* and it was used to evaluate the singular integrals on the inner and outer surfaces. On the flat surface, S_2, the singular integrals were evaluated using the *Accelerated Convergence Method*.

However, in circumstances where the validity of the numerical answer is uncertain, such as the **A(2,1)** coefficient of the system matrix, a convergence type integration method would be more advantageous because it would be possible to monitor the convergence of such coefficient, whereas the Kutt type integration method would fail to indicate non-convergence.

Using unequal size elements caused some problems in the determination of the surface displacements in the solid sphere analysis. This problem was solved by subdividing the larger singular element concerned and performing the integration on the now two identical

sized elements and then adding the contribution coming from the excess area separately. This method significantly improved the accuracy of a mesh that contained unequally spaced elements.

For the solid sphere of radius 1 metre, good results with internal displacement errors under 0.5% were achieved at nodes as close as 0.003 metres to the surface. However, for the internal stresses, accurate results at nodes so close to the surface could not be achieved. For example, in the solid sphere case, the direct stress σ_{33} was determined at 5.4% at a distance of 0.98 metres. This was due to the more severe singularity presence in the calculation of the third order tensors multiplying the displacements.

Investigation into the corner problems revealed some interesting results. Initially a double node approach was implemented to solve these problems. However, the results obtained, showed that two nodes sharing the same geometrical space, with some of the variables at these nodes eliminated from the system matrices, was not suitable. Therefore, another alternative was tried. This was to use two semi-continuous elements at the corners and a hollow hemisphere was used to develop this method. The corner node of a continuous quadratic element sharing the corner was pulled back into the element slightly to form a semi-continuous element. The midside node position was adjusted accordingly.

The position of the corner node was optimized experimentally for a fixed quadrature order. The tests were done using a 16 by 16 rule and it was found that the most accurate results were obtained when the corner node was placed between 60% and 70% of the element length. i.e.when $t = 0.6 - 0.7$. Further tests were done to link the position of the gauss points and the position of the corner node to the accuracy of the surface displacements. It was found that there is an optimum position of the corner node which coincided with the gauss point. For Gauss order of 16, this was at t=0.64 and for quadrature order of 12, the best results were obtained when t=0.56.

An investigation into the relationship between the element size and the wall thickness for a hollow geometry was conducted. For a long and slender section, like the hollow sphere and the cone geometries used in this work, in the presence of small wall thicknesses such as 5mm or less, it was discovered that the element size should be made the same size as the wall thickness (SOT=1.0). Under these conditions the errors determined on all the surface results were less than 0.5%.

The selection of the SOT ratio was confirmed in two tests. In the first test, the inner and the outer radii were kept constant at 45mm and 50mm respectively. The number of elements on the inner and outer surfaces were adjusted to determine the SOT ratios. SOT ratios of 1.0 to 3.5 were tested. The best result was obtained when the SOT ratio was 1.0, which resulted in errors less than 0.5%. At larger SOT values, the nodal values on the inner and outer surfaces showed considerable errors but when averaged, these dropped to acceptable levels. In case of SOT=3.5, the outer surface displacement at the corner node gave 28% error but when the outer surface displacements were averaged, this resulted in only 4% error. For SOT ratios greater than 1.0, all the results showed greater errors at the corner nodes.

In the second test, the outer radius was kept constant at 50mm but the inner radius dimension was varied between 30mm and 49mm. The SOT ratio was kept constant by altering the element numbers on the inner and outer surfaces. The tests showed that for a fairly thick walled sphere (50mm outer radius, 20mm wall thickness), an SOT ratio of 0.8 gave around 1% error and took 2.3 minutes of CPU time. When the wall thickness was reduced to 3mm, errors of less than 0.5% were recorded but the CPU time went upto 77 minutes.

It was also found in the second test that there was no increase in the errors at the nodes near or at the corners from 20mm thickness down to 3mm wall thickness. This shows that although very accurate results can be achieved, SOT value of 1.0 can be expensive especially in three dimensional analysis which was implemented here. However, this

approach can significantly improve the results in 2-D and axisymmetric analysis dealing with long and slender sections with and without the sharp corners.

The wall thickness that was the main concern in this study was 5mm. When test results of SOT=1.0 were compared with SOT=0.8, no significant increase in the results were seen compared to the large increase in the CPU time of 16 minutes to 42 minutes.

An attempt was made to push the BEM model to 1mm and 2mm wall thicknesses but this was not successful. For the 2mm case, the system matrix obtained after 134 minutes was singular due to very similar rows being achieved. The main reason for this was that the elements on the flat surface, S_2, were getting too small, especially with the corner nodes being pulled towards the inside of the element. At this stage this problem could have been avoided by using just one element on the flat surface, but the CPU time of 134 minutes and solving a matrix of 320 by 320 was not practical. The elements on the inner and outer surfaces were also getting too close together which would cause instability problems in the system matrix as the two surfaces came closer. For the 1mm wall thickness, data storage problems were encountered and the analysis was not continued as negative results were anticipated.

It is shown in this study that the BEM can handle long and slender sections as long as the SOT ratio of 1.0 is maintained. The only disadvantage may be the larger CPU time but with the new developments in the computer technology in mind, this may not be an issue in the very near future; at least for small scale problems.

For the cone analysis, an SOT ratio of 1.0 was maintained and for the semi-continuous elements, the factor t was set to 0.56 throughout the analysis as gauss order of 12 was used for the integration of the corner elements. Cone results were compared with the results obtained from FEM analysis.

The initial comparisons included the surface displacements and tractions for cones with a 10mm wall thickness and a 5mm wall thickness. The BEM results agreed well with the

FEM results. This was then extended to internal points where BEM results were obtained at various distances along the wall of the cones. The internal displacements obtained for the cone with 10mm wall showed oscillatory results at 1mm away from the inner and outer surfaces and gave good results everywhere else. For a 5mm wall thickness, better internal displacement results were achieved at distances as close as 1mm from the surfaces.

However, the internal stresses gave a much different picture. Hoop and Von Mises stresses compared at the mid-wall of the cones agreed well with the FEM results but large errors occurred at nodes close to the surfaces. The oscillations were a lot more severe than the internal displacements at the same nodes. This was believed to be due to the higher order of the singularity present in the stress formulations.

For the results obtained through direct evaluation, good agreement was seen between the BEM and the FEM results. However, the surface stresses were determined using the surface displacements as the present formulation was not suitable for the direct calculation of these stresses.

It is shown in this study that by using a cubic spline fit through the displacements, improved results can be obtained as the first derivative required for strain calculations would be continuous. If quadratic variation was used as in the BEM formulation, there would be discontinuities in the strains and this would be reflected in the stresses.

As the maximum stresses were expected to be on the inner surface, these stresses were compared with the FEM results. For the 5mm wall thickness, excellent results were obtained in all of the stresses. However,there was a slight disagreement at the tip of the cone.

To see the variation of the stresses on the inner surface as the cone height increased with a fixed base radius, several cones of 10mm thick walls were tested and compared with the FEM results. Cone heights of upto 180mm were tested which was three times the size of the base radius. Hoop, Von Mises and the shear stresses were calculated on the inner surface

for all the cones. For hoop and Von Mises stresses, as the cone height varied, the stress curves turned in an anticlockwise direction as if they were pivoted about 28mm away from the origin. These stresses were deliberately plotted against the base radius which was common to all the cones, regardless of their height. The maximum of these stresses occurred at the base. The shear stress became maximum where the two arcs of the surface met. These results were also confirmed by the FEM.

The slight disagreement with the FEM results which was seen on the stresses calculated for the 5mm wall, was also present for the 10mm wall but it was more pronounced. As the cone height increased, the BEM results for the hoop and Von Mises stresses gave higher stress values at the tip of the cone. However this disagreement was confined only to the first element on the tip.

Appendix

A

Linear Interpolation Formula

The linear interpolation formula used in Chapter 3 is based on a straight line equation,

$$v = m\,\theta + c \tag{A.1}$$

To find the slope m and the intercept c, two equations must be written and solved simultaneously.

$$\theta = \theta_j \quad ; \quad v = v^j \qquad \Rightarrow \qquad v^j = m\,\theta_j + c \tag{A.2}$$

$$\theta = \theta_{j+1} \quad ; \quad v = v^{j+1} \qquad \Rightarrow \qquad v^{j+1} = m\,\theta_{j+1} + c \tag{A.3}$$

Subtracting Equation (A.2) from Equation (A.3):

$$v^{j+1} - v^j = m\,(\theta_{j+1} - \theta_j) \tag{A.4}$$

$$m = \frac{(v^{j+1} - v^j)}{(\theta_{j+1} - \theta_j)} \tag{A.5}$$

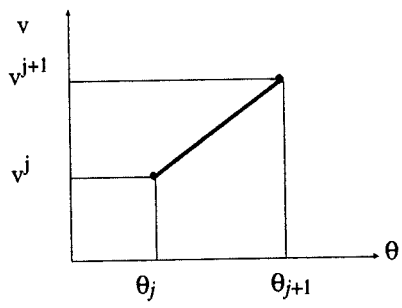

$$A.2 \times \theta_{j+1} \quad \Rightarrow \quad v^{j}\theta_{j+1} = m\,\theta_{j}\,\theta_{j+1} + c\,\theta_{j+1} \tag{A.6}$$

$$A.3 \times \theta_{j} \quad \Rightarrow \quad v^{j+1}\theta_{j} = m\,\theta_{j+1}\,\theta_{j} + c\,\theta_{j} \tag{A.7}$$

Subtracting Equation (A.7) from Equation (A.6) gives:

$$v^{j}\theta_{j+1} - v^{j+1}\theta_{j} = c\,(\theta_{j+1} - \theta_{j)} \tag{A.8}$$

$$c = \frac{(v^{j}\theta_{j+1} - v^{j+1}\theta_{j})}{(\theta_{j+1} - \theta_{j})} \tag{A.9}$$

Now substituting the Equations (A.5) and (A.9) into the general equation (A.1) give:

$$v = \left(\frac{v^{j+1} - v^{j}}{\theta_{j+1} - \theta_{j}}\right)\theta + \left(\frac{v^{j}\theta_{j+1} - v^{j+1}\theta_{j}}{\theta_{j+1} - \theta_{j}}\right) \tag{A.10}$$

Equation (A.10) can be re-written in the following form:

$$v = v^{j+1}\frac{(\theta - \theta_{j})}{(\theta_{j+1} - \theta_{j})} + v^{j}\frac{(\theta_{j+1} - \theta)}{(\theta_{j+1} - \theta_{j})} \tag{A.11}$$

Appendix

B

Formulation Of The Cone Geometry

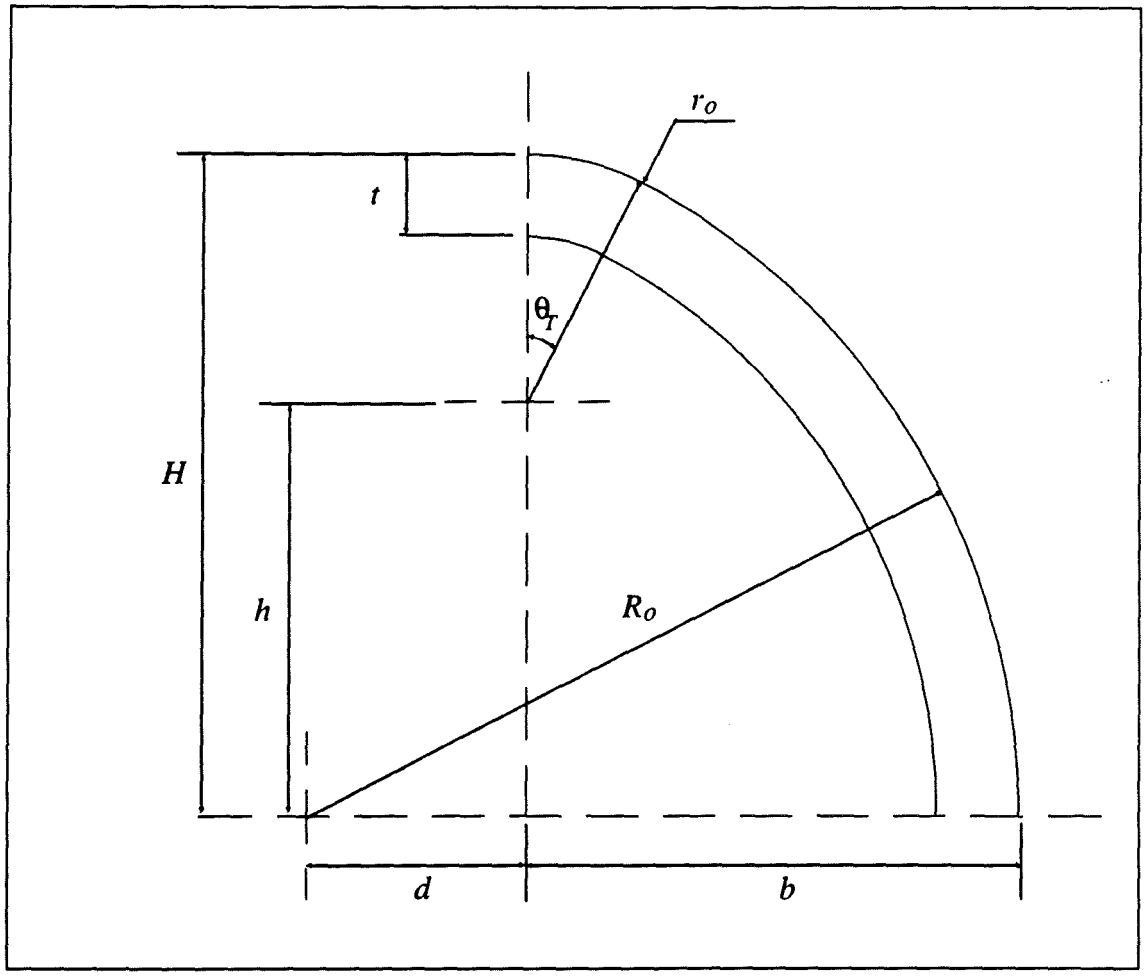

Figure B.1: Parameters used in the determination of the cone geometry.

The profile of the cones to be generated in this thesis is made by joining two arcs of two different circles. An arc of a small circle is used to make the tip and another arc of a much larger circle is used to form the rest of the cone. The two curves are merged at an angle where they have a common tangent.

Normally, the base radius, b, cone height, H, the tip radius, r_o and the wall thickness, t, are given and the rest of the parameters are calculated from the following relationships.

Given r_o, H, b and t:

$$h = H - r_o \tag{B.1}$$

$$(R_o - r_o)^2 = d^2 + h^2 \tag{B.2}$$

$$(R_o - r_o)^2 = (R_o - b)^2 + h^2 \tag{B.3}$$

$$R_o^2 - 2r_oR_o + r_o^2 = R_o^2 - 2R_ob + b^2 + h^2 \tag{B.4}$$

$$2R_o(b - r_o) = b^2 + h^2 - r_o^2 \tag{B.5}$$

$$\therefore \qquad R_o = \frac{b^2 + h^2 - r_o^2}{2(b - r_o^2)} \tag{B.6}$$

Having determined the radius of the outer large arc, R_o, then;

$$d = R_o - b \tag{B.7}$$

$$\theta_T = \tan^{-1}\frac{d}{h} \tag{B.8}$$

Equations (B.1), (B.6), (B.7) and (B.8) are used to generate the profile of the outer surface. Subtraction of thickness t from R_o and r_o gives the R_i and r_i for the inner profile.

Appendix

C

Effect Of Quadratic Elements

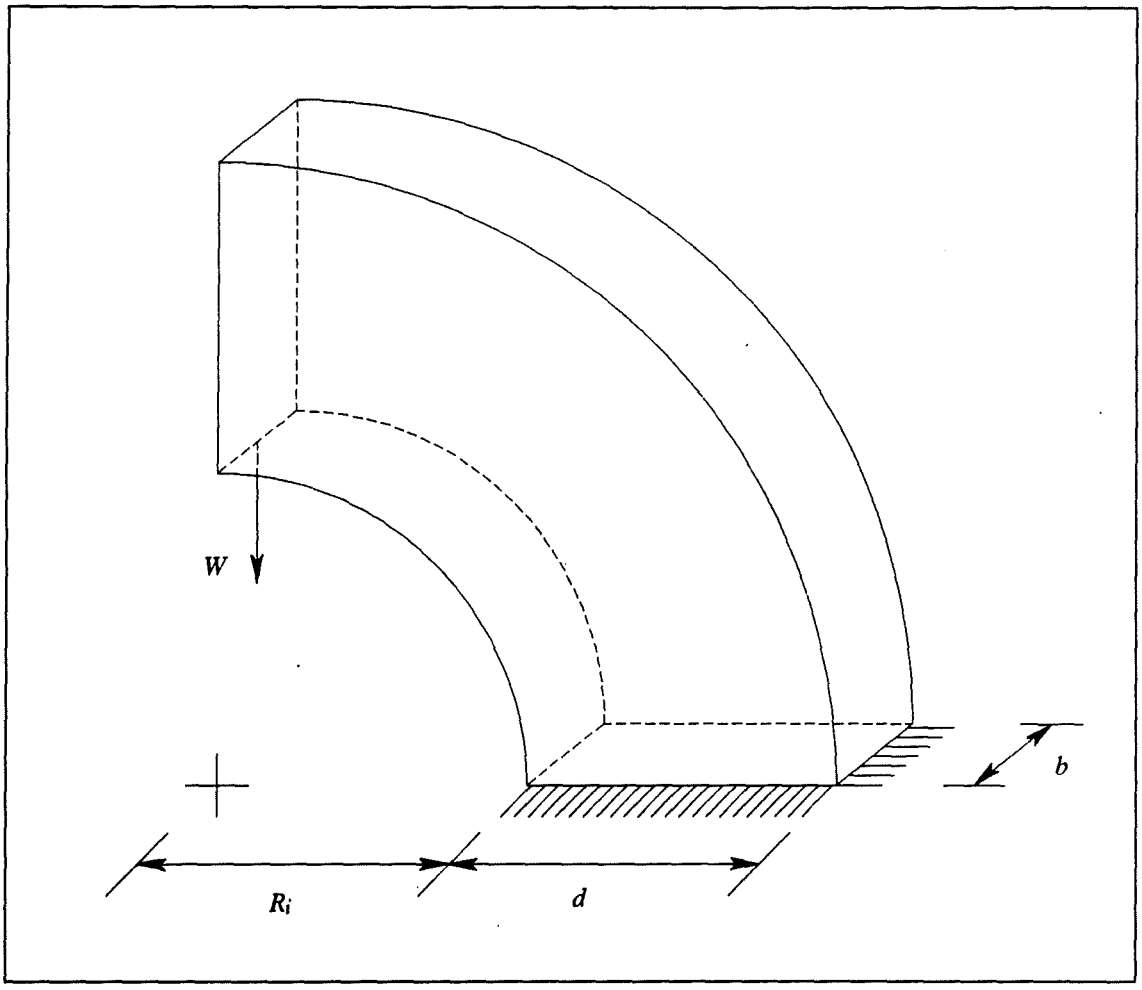

Figure C.1: A Curved beam used for the comparison of tangential stress σ_{tt} at angle $\theta = 45°$.

Figure C.1 shows a curved beam with an inner radius R_i= 0.2m, outer radius R_o = 0.4m, b = 0.1m and d = 0.2m. The beam is subjected to a point load W = 0.2 MN. Comparison of the stress due to bending involved the theory developed by Winkler and the numerical analysis by the BEM.

The inner surface of the beam was decretized into five quadratic elements, the outer surface into six quadratic elements and the ends at θ = 0° and θ = 90° into two quadratic elements each.

The object of this analysis is to compare the stresses at a distance p measured from the inner wall at θ = 45° and show the effect of seeking stresses at an end node of a quadratic element which is also shared by a neighbouring element.

From the Winkler theory (Beswick, 1992), the tangential stress along mean radius R is given by:

$$\sigma_{tt} = W \sin\theta \frac{y}{J} \tag{C.1}$$

where,

$$J = -R^2 bd + R^3 \ln\left\{\frac{(R+\frac{d}{2})}{(R-\frac{d}{2})}\right\} \tag{C.2}$$

Table C.1: Results of Winkler stress for the curved beam at θ = 45°.

p (metres)	0.0	0.02	0.04	0.06	0.08	0.10	0.12	0.14	0.16	0.18	0.20
Winkler Stress (MN/m^2)	-89.0	-64.7	-44.5	-27.4	-12.7	0.0	11.2	20.9	29.7	37.5	44.5
BEM Stress (MN/m^2)	-92.1	-64.2	-43.6	-26.7	-12.5	-0.26	10.6	20.3	29.3	37.7	47.7

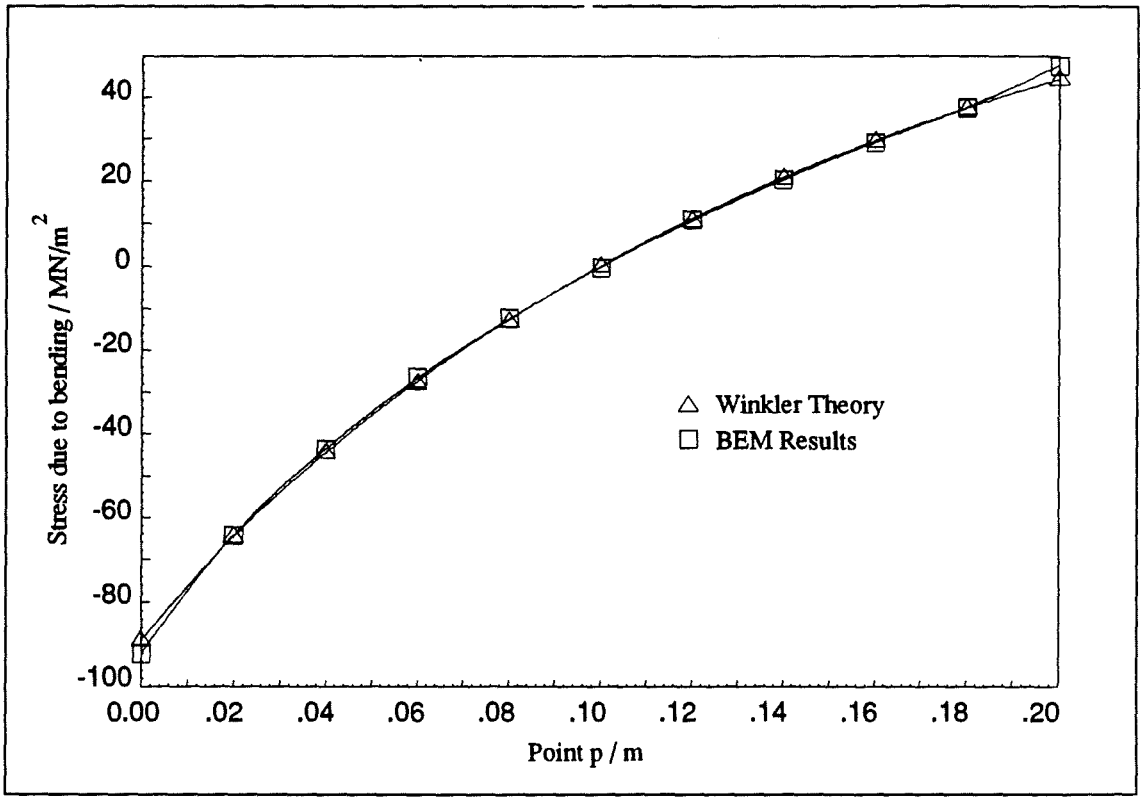

Figure C.2: Comparison of stress due to bending at $\theta = 45°$.

The results given in Table C.1 are also plotted in Figure C.2. The stresses at the internal points compare well but the surface nodes have 3.4% error on the inner surface and 7.2% error on the outer surface. When the mesh for the BEM model was arranged in such a way that the nodes on the inner and outer surfaces at $\theta = 45°$, corresponded to a mid-point, the errors at the end nodes were seen to reduce to the similar order of the error on the internal nodes.

Appendix

D

Stress Transformations

Determining σ_{11}:

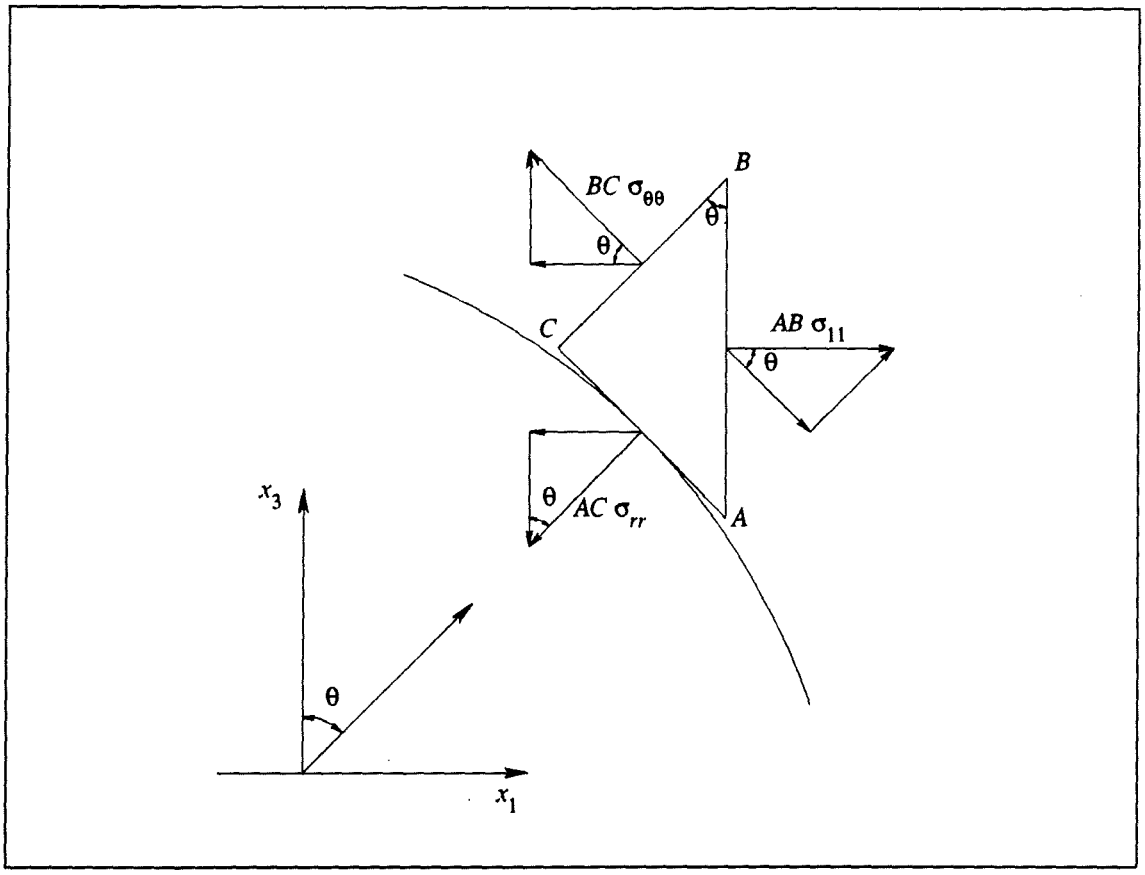

Figure D.1: Resolving forces to determine the stress σ_{11} in terms of the tangential stress $\sigma_{\theta\theta}$.

On the inner surface there is no pressure, therefore on the surface, the radial stress σ_{rr} is zero. By equating the horizontal forces from F igure D.1:

$$CB\,\sigma_{\theta\theta}\cos\theta = AB\,\sigma_{11} \tag{D.1}$$

However, from the triangle ABC,

$$CB = AB\cos\theta \tag{D.2}$$

Substituting Equation (D.2) into Equation (D.1) and simplifying,

$$\sigma_{11} = \sigma_{\theta\theta}\cos^2\theta \tag{D.3}$$

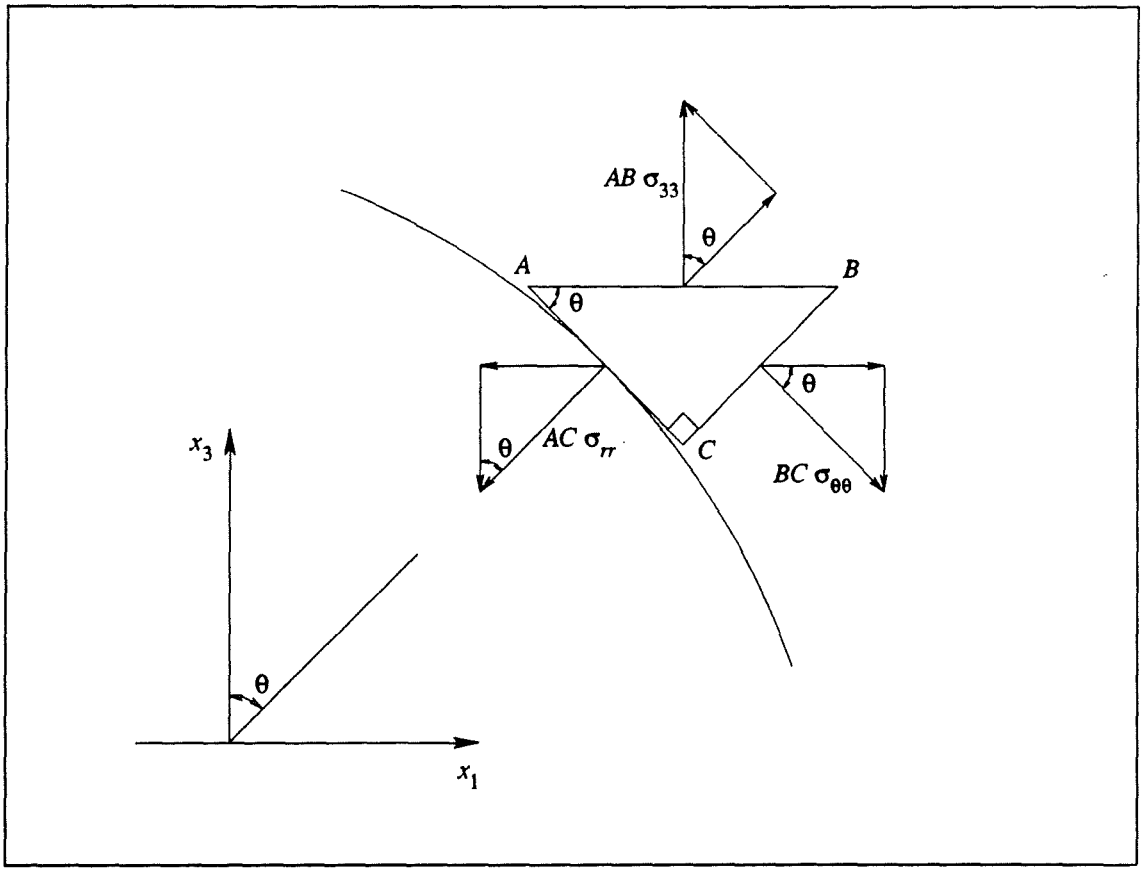

Figure D.2: Resolving forces to determine the stress σ_{33} in terms of the tangential stress $\sigma_{\theta\theta}$.

Determining σ_{33}:

The stress σ_{33} similarly can be determined by resolving forces and equating the vertical components. From Figure D.2,

$$AB\ \sigma_{33} = BC\ \sigma_{\theta\theta} \sin\theta \tag{D.4}$$

From the triangle ABC,

$$BC = AB \sin\theta \tag{D.5}$$

Substituiting Equation (D.5) into Equation (D.4) and simplifying,

$$\sigma_{33} = \sigma_{\theta\theta} \sin^2\theta \tag{D.6}$$

Determining σ_{13}:

The shear stress σ_{13} can be expressed in terms of the direct stresses σ_{11} and σ_{33}. These stresses are turned into forces and resolved as shown in Figure D.3. Equating the perpandicular forces to the surface,

$$AC\ \sigma_{rr} = AB\ \sigma_{33} \cos\theta + AB\ \sigma_{13} \sin\theta + BC\ \sigma_{11} \sin\theta + BC\ \sigma_{13} \cos\theta \tag{D.7}$$

By using the relationships from the triangle ABC in Figure D.3,

$$AB = AC \cos\theta \tag{D.8}$$

$$BC = AC \sin\theta \tag{D.9}$$

Substituiting Equations (D.8) and (D.9) into Equation (D.7),

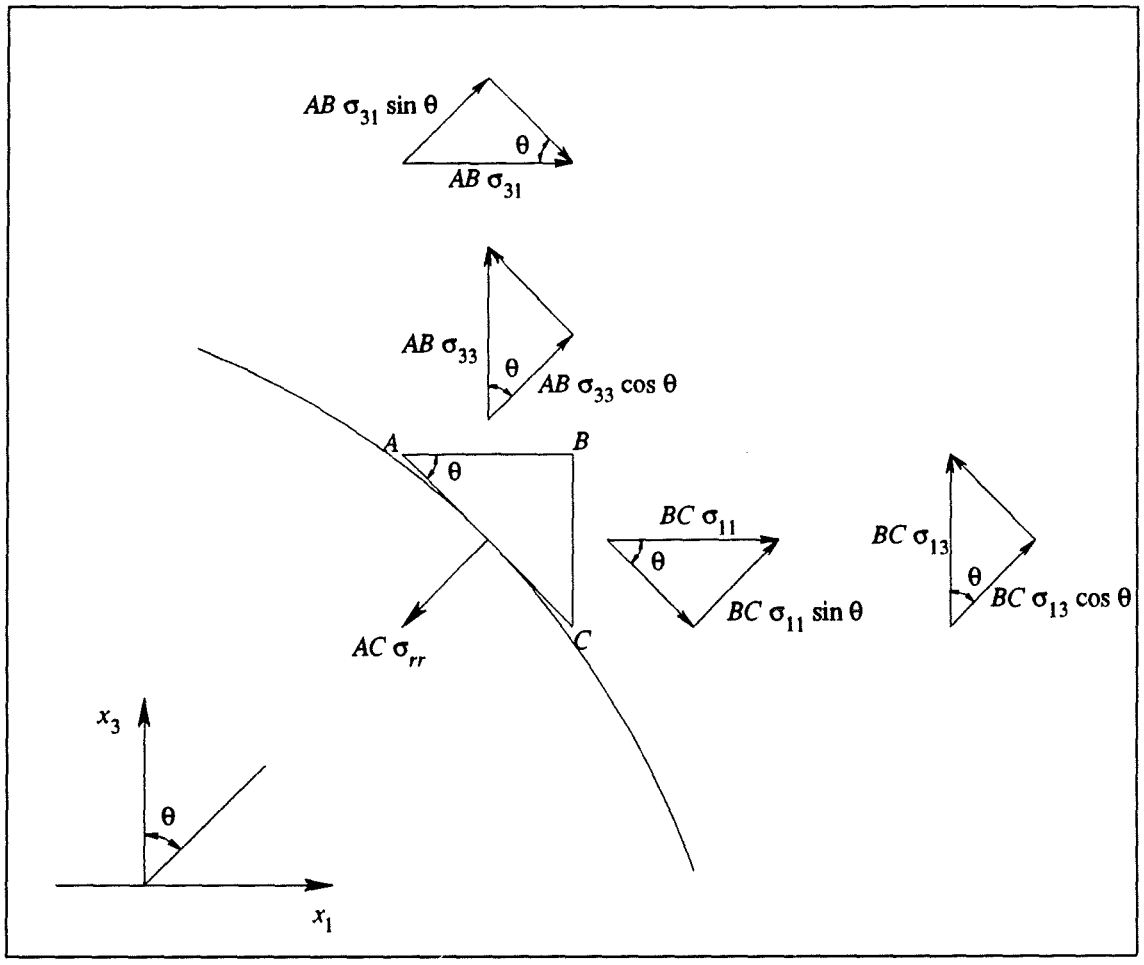

Figure D.2: Resolving forces to determine the shear stress σ_{13} in terms of the direct stresses σ_{11} and σ_{33}.

$$\sigma_{rr} = \sigma_{33} \cos^2\theta + \sigma_{31} \sin\theta \cos\theta + \sigma_{11} \sin^2\theta + \sigma_{13} \sin\theta \cos\theta \qquad \text{(D.10)}$$

However, due to symmetry, the shear stresses

$$\sigma_{13} = \sigma_{31} \qquad \text{(D.11)}$$

Hence,

$$\sigma_{rr} = \sigma_{11} \sin^2\theta + \sigma_{33} \cos^2\theta + 2\,\sigma_{13} \sin\theta \cos\theta \qquad \text{(D.12)}$$

There is no pressure applied onto the inner surface, therefore the radial stress σ_{rr} is zero.

Hence,

$$\sigma_{13} = \frac{-\sigma_{11}\sin^2\theta - \sigma_{33}\cos^2\theta}{2\sin\theta\cos\theta} \tag{D.13}$$

$$\sigma_{13} = \frac{-\sigma_{11}\sin^2\theta - \sigma_{33}\cos^2\theta}{\sin 2\theta} \tag{D.14}$$

Appendix

E

Further Results

This appendix holds some of the graphs which their results are used in Chapter 6. All the figures are for a cone with 60mm base radius, 80mm cone height and 10mm wall thickness. Gauss order used for the semi-continuous elements on the S_2 surface are 12x12. Number of elements on arc1, arc2, arc3 and arc4 are 4, 10, 10 and 4 respectively. For the figures E.1-E.4 the number of elements on the S_2 surface is 2 and for the figures E.5-E.7 the number of elements on S_2 is 4.

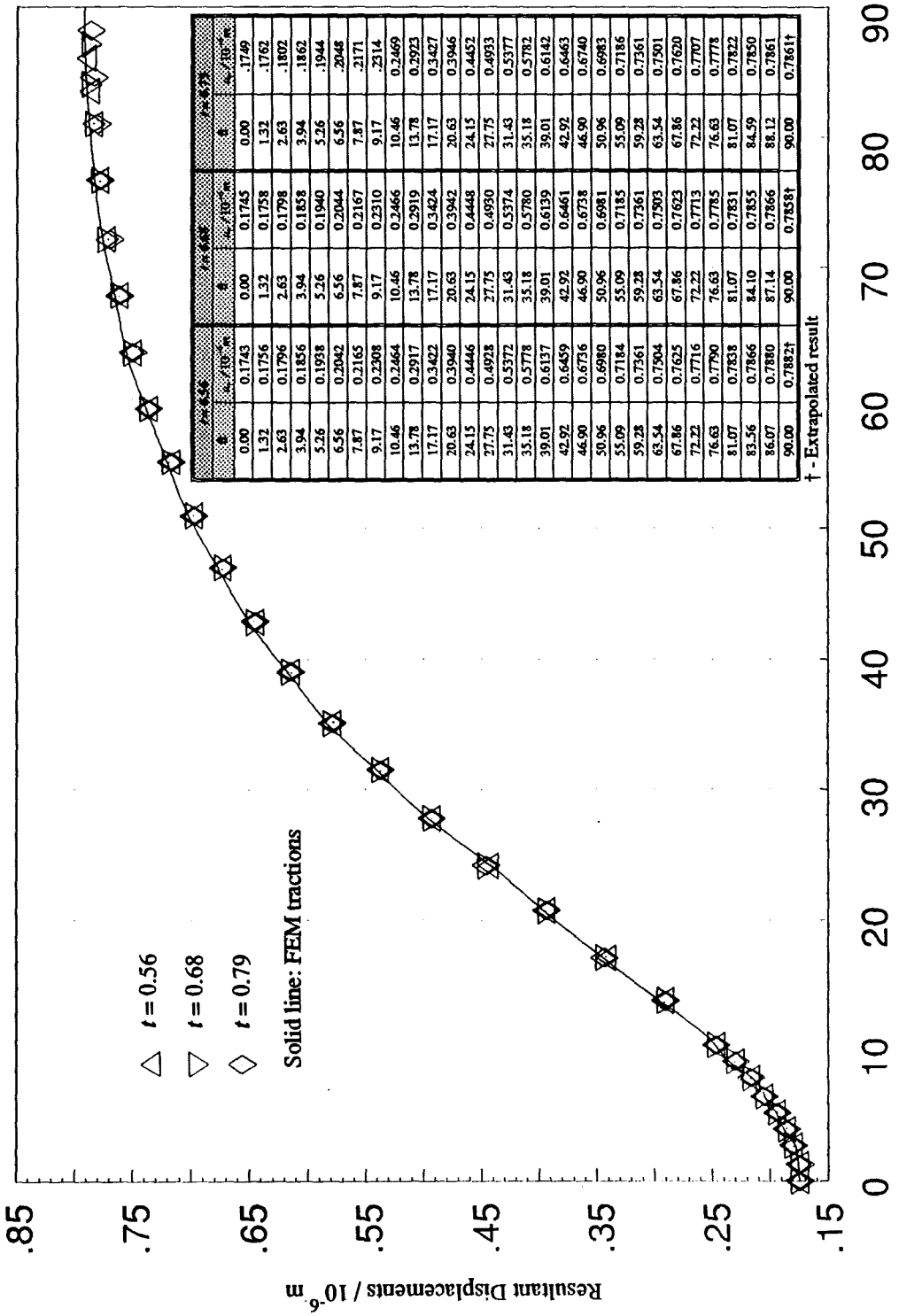

θ	t = 0.56 u_r / 10^{-6} m	θ	t = 0.68 u_r / 10^{-6} m	θ	t = 0.79 u_r / 10^{-6} m
0.00	0.1743	0.00	0.1745	0.00	.1749
1.32	0.1756	1.32	0.1758	1.32	.1762
2.63	0.1796	2.63	0.1798	2.63	.1802
3.94	0.1856	3.94	0.1858	3.94	.1862
5.26	0.1938	5.26	0.1940	5.26	.1944
6.56	0.2042	6.56	0.2044	6.56	.2045
7.87	0.2165	7.87	0.2167	7.87	.2171
9.17	0.2308	9.17	0.2310	9.17	.2314
10.46	0.2464	10.46	0.2466	10.46	0.2469
13.78	0.2917	13.78	0.2919	13.78	0.2923
17.17	0.3422	17.17	0.3424	17.17	0.3427
20.63	0.3940	20.63	0.3942	20.63	0.3946
24.15	0.4446	24.15	0.4448	24.15	0.4452
27.75	0.4928	27.75	0.4930	27.75	0.4933
31.43	0.5372	31.43	0.5374	31.43	0.5377
35.18	0.5778	35.18	0.5780	35.18	0.5782
39.01	0.6137	39.01	0.6139	39.01	0.6142
42.92	0.6459	42.92	0.6461	42.92	0.6463
46.90	0.6736	46.90	0.6738	46.90	0.6740
50.96	0.6980	50.96	0.6981	50.96	0.6983
55.09	0.7184	55.09	0.7185	55.09	0.7186
59.28	0.7361	59.28	0.7361	59.28	0.7361
63.54	0.7504	63.54	0.7503	63.54	0.7501
67.86	0.7625	67.86	0.7623	67.86	0.7620
72.22	0.7716	72.22	0.7713	72.22	0.7707
76.63	0.7790	76.63	0.7785	76.63	0.7778
81.07	0.7838	81.07	0.7831	81.07	0.7822
83.56	0.7866	84.10	0.7855	84.59	0.7850
86.07	0.7880	87.14	0.7866	88.12	0.7861
90.00	0.7882†	90.00	0.7858†	90.00	0.7861†

† - Extrapolated result

Figure E.1: Resultant displacements on surfaces S_1 of the cone with various t values corresponding to the Gauss points compared with the FEM results. (Wall thickness = 10mm, No. of elements on S_2 = 2)

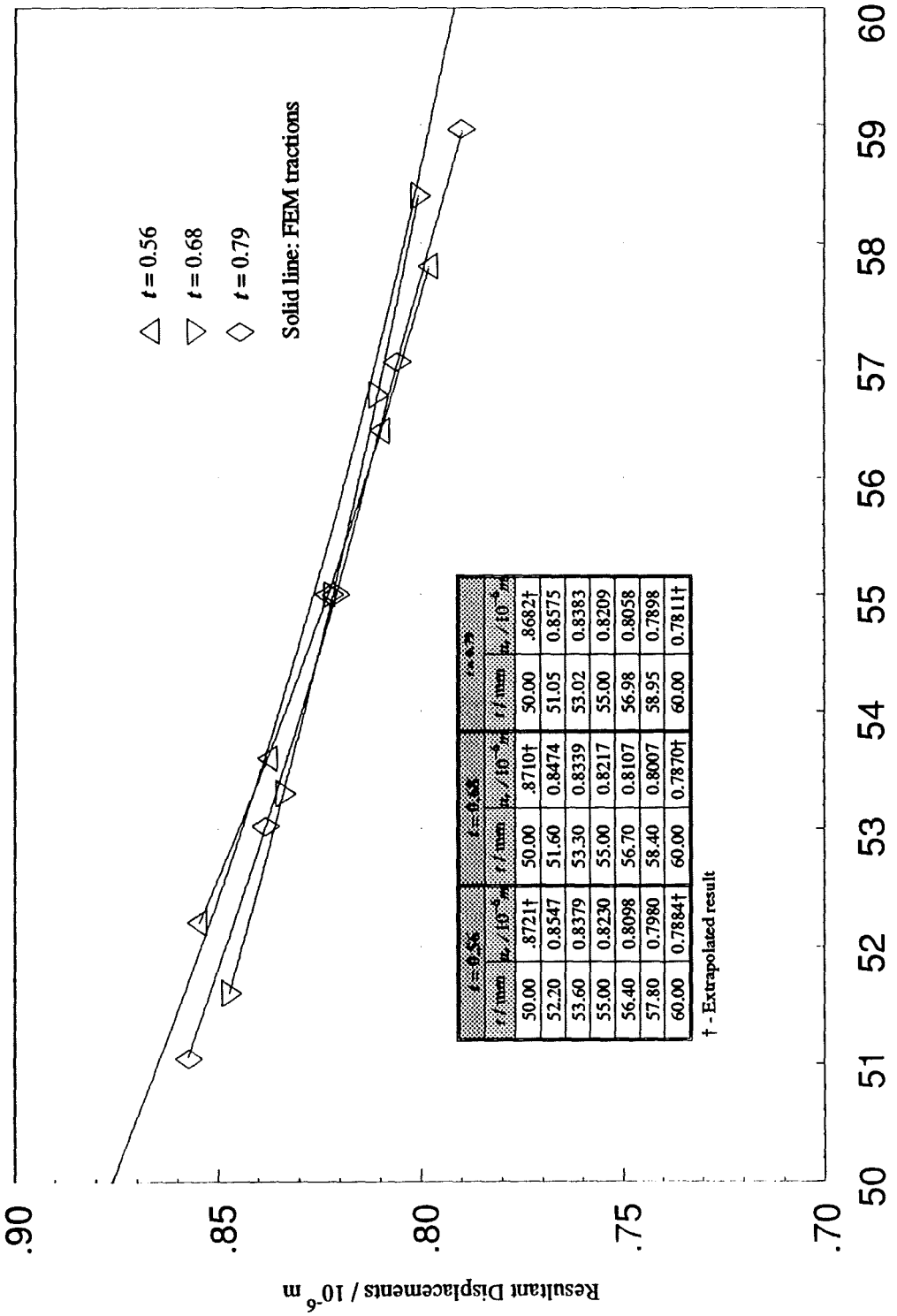

$t = 0.56$		$t = 0.68$		$t = 0.79$	
r / mm	μ_r / 10^{-6} m	r / mm	μ_r / 10^{-6} m	r / mm	μ_r / 10^{-6} m
50.00	.8721†	50.00	.8710†	50.00	.8682†
52.20	0.8547	51.60	0.8474	51.05	0.8575
53.60	0.8379	53.30	0.8339	53.02	0.8383
55.00	0.8230	55.00	0.8217	55.00	0.8209
56.40	0.8098	56.70	0.8107	56.98	0.8058
57.80	0.7980	58.40	0.8007	58.95	0.7898
60.00	0.7884†	60.00	0.7870†	60.00	0.7811†

† - Extrapolated result

Figure E.2: Resultant displacements on surfaces S_2 of the cone with various t values corresponding to the Gauss points compared with the FEM results.(Wall thickness = 10mm, No. of elements on S_2 = 2)

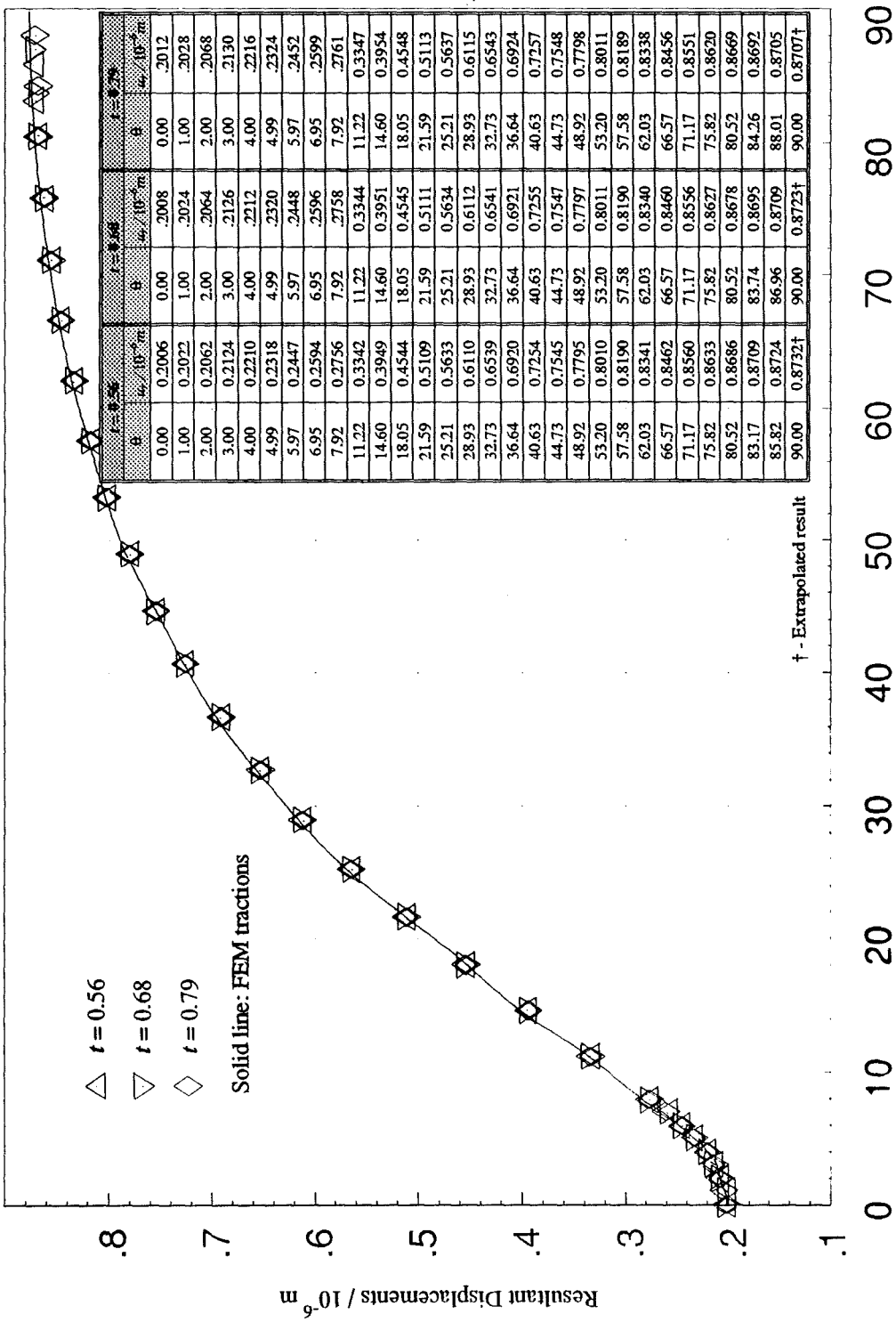

$t = 0.56$		$t = 0.68$		$t = 0.79$	
θ	w / 10^{-6} m	θ	w / 10^{-6} m	θ	w / 10^{-6} m
0.00	0.2006	0.00	.2008	0.00	.2012
1.00	0.2022	1.00	.2024	1.00	.2028
2.00	0.2062	2.00	.2064	2.00	.2068
3.00	0.2124	3.00	.2126	3.00	.2130
4.00	0.2210	4.00	.2212	4.00	.2216
4.99	0.2318	4.99	.2320	4.99	.2324
5.97	0.2447	5.97	.2448	5.97	.2452
6.95	0.2594	6.95	.2596	6.95	.2599
7.92	0.2756	7.92	.2758	7.92	.2761
11.22	0.3342	11.22	0.3344	11.22	0.3347
14.60	0.3949	14.60	0.3951	14.60	0.3954
18.05	0.4544	18.05	0.4545	18.05	0.4548
21.59	0.5109	21.59	0.5111	21.59	0.5113
25.21	0.5633	25.21	0.5634	25.21	0.5637
28.93	0.6110	28.93	0.6112	28.93	0.6115
32.73	0.6539	32.73	0.6541	32.73	0.6543
36.64	0.6920	36.64	0.6921	36.64	0.6924
40.63	0.7254	40.63	0.7255	40.63	0.7257
44.73	0.7545	44.73	0.7547	44.73	0.7548
48.92	0.7795	48.92	0.7797	48.92	0.7798
53.20	0.8010	53.20	0.8011	53.20	0.8011
57.58	0.8190	57.58	0.8190	57.58	0.8189
62.03	0.8341	62.03	0.8340	62.03	0.8338
66.57	0.8462	66.57	0.8460	66.57	0.8456
71.17	0.8560	71.17	0.8556	71.17	0.8551
75.82	0.8633	75.82	0.8627	75.82	0.8620
80.52	0.8686	80.52	0.8678	80.52	0.8669
83.17	0.8709	83.74	0.8695	84.26	0.8692
85.82	0.8724	86.96	0.8709	88.01	0.8705
90.00	0.8732†	90.00	0.8723†	90.00	0.8707†

Figure E.3: Resultant displacements on surfaces S_1 of the cone with various t values corresponding to the Gauss points compared with the FEM results. (Wall thickness = 10mm, No. of elements on S_2 = 2)

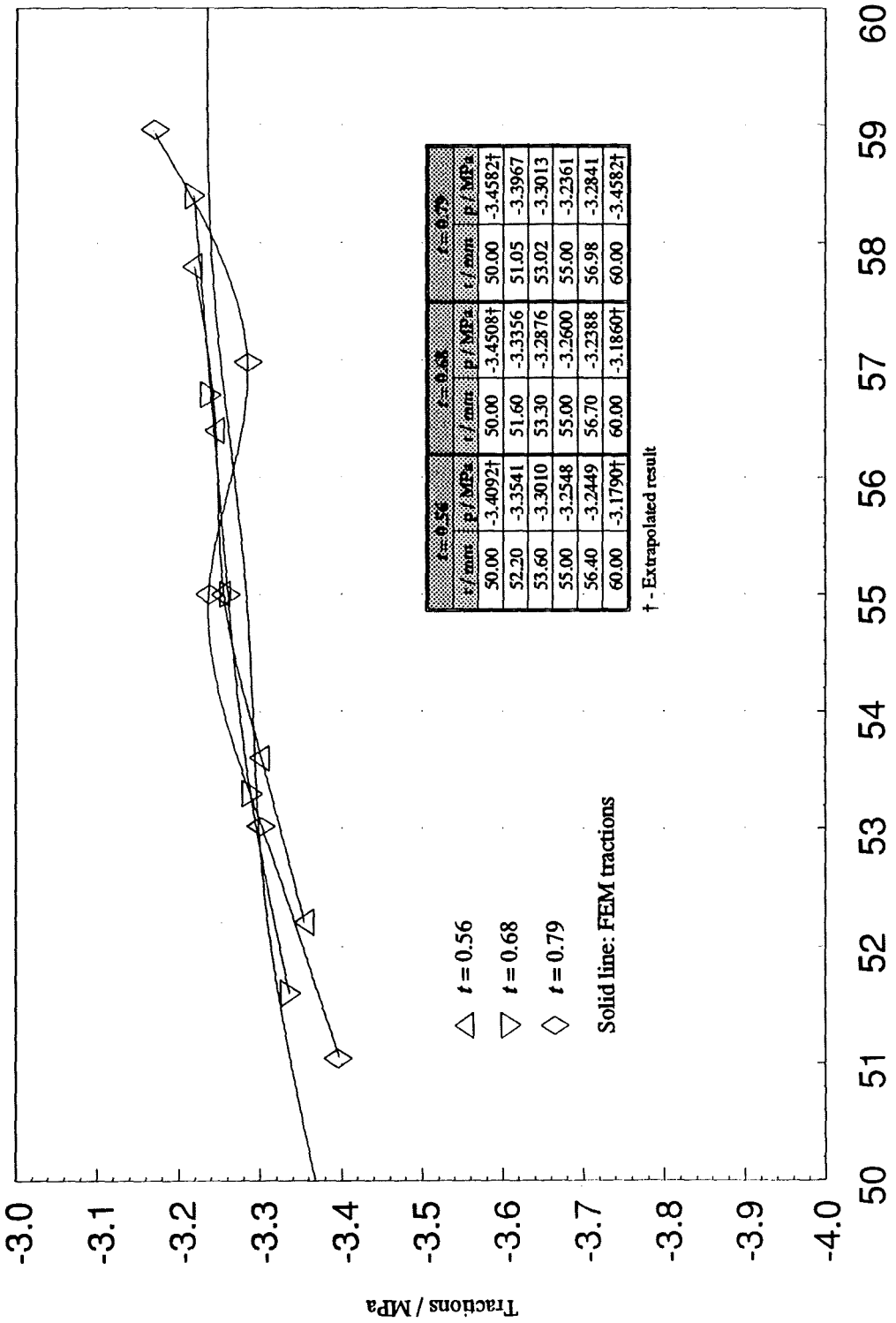

t = 0.56		t = 0.68		t = 0.79	
r / mm	p / MPa	r / mm	p / MPa	r / mm	p / MPa
50.00	-3.4092†	50.00	-3.4508†	50.00	-3.4582†
52.20	-3.3541	51.60	-3.3356	51.05	-3.3967
53.60	-3.3010	53.30	-3.2876	53.02	-3.3013
55.00	-3.2548	55.00	-3.2600	55.00	-3.2361
56.40	-3.2449	56.70	-3.2388	56.98	-3.2841
60.00	-3.1790†	60.00	-3.1860†	60.00	-3.4582†

† - Extrapolated result

Figure E.4: Tractions on surface S_2 of the cone with various t values corresponding to the Gauss points compared with the FEM results. (Wall thickness = 10mm, No. of elements on S_2 = 2)

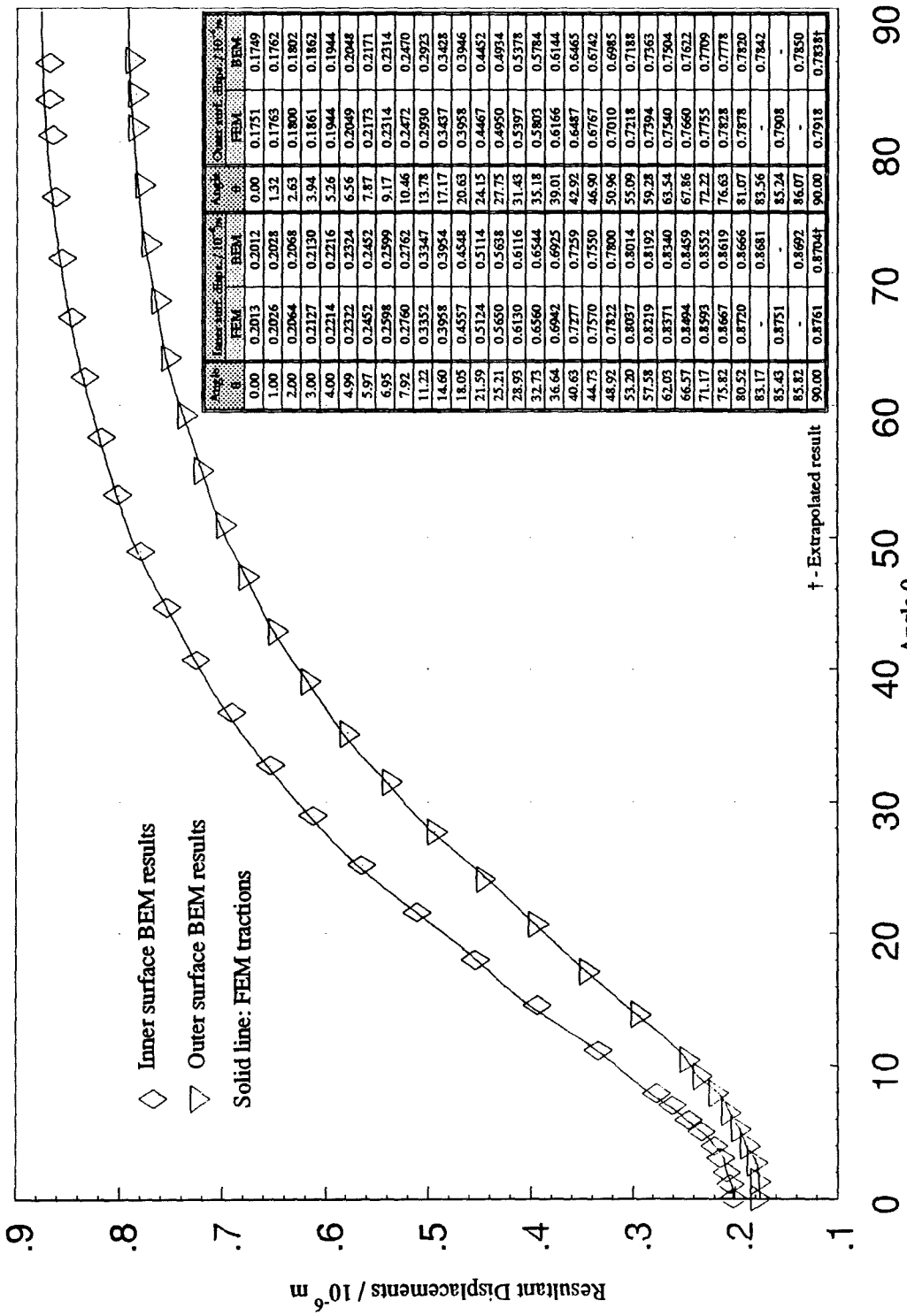

Angle θ	Inner surf. disp. / 10^{-6} m FEM	Inner surf. disp. / 10^{-6} m BEM	Angle θ	Outer surf. disp. / 10^{-6} m FEM	Outer surf. disp. / 10^{-6} m BEM
0.00	0.2013	0.2012	0.00	0.1751	0.1749
1.00	0.2026	0.2028	1.32	0.1763	0.1762
2.00	0.2064	0.2068	2.63	0.1800	0.1802
3.00	0.2127	0.2130	3.94	0.1861	0.1862
4.00	0.2214	0.2216	5.26	0.1944	0.1944
4.99	0.2322	0.2324	6.56	0.2049	0.2048
5.97	0.2452	0.2452	7.87	0.2173	0.2171
6.95	0.2598	0.2599	9.17	0.2314	0.2314
7.92	0.2760	0.2762	10.46	0.2472	0.2470
11.22	0.3352	0.3347	13.78	0.2930	0.2923
14.60	0.3958	0.3954	17.17	0.3437	0.3428
18.05	0.4557	0.4548	20.63	0.3958	0.3946
21.59	0.5124	0.5114	24.15	0.4467	0.4452
25.21	0.5650	0.5638	27.75	0.4950	0.4934
28.93	0.6130	0.6116	31.43	0.5397	0.5378
32.73	0.6560	0.6544	35.18	0.5803	0.5784
36.64	0.6942	0.6925	39.01	0.6166	0.6144
40.63	0.7277	0.7259	42.92	0.6487	0.6465
44.73	0.7570	0.7550	46.90	0.6767	0.6742
48.92	0.7822	0.7800	50.96	0.7010	0.6985
53.20	0.8037	0.8014	55.09	0.7218	0.7188
57.58	0.8219	0.8192	59.28	0.7394	0.7363
62.03	0.8371	0.8340	63.54	0.7540	0.7504
66.57	0.8494	0.8459	67.86	0.7660	0.7622
71.17	0.8593	0.8552	72.22	0.7755	0.7709
75.82	0.8667	0.8619	76.63	0.7828	0.7778
80.52	0.8720	0.8666	81.07	0.7878	0.7820
83.17	-	0.8681	83.56	-	0.7842
85.43	0.8751	-	85.24	0.7908	-
85.82	-	0.8692	86.07	-	0.7850
90.00	0.8761	0.8704†	90.00	0.7918	0.7835†

† - Extrapolated result

Figure E.5: Resultant displacements on surfaces S_1 and S_3 of the cone with t = 0.56. (Wall thickness = 10mm, No. of elements on S_2 = 4)

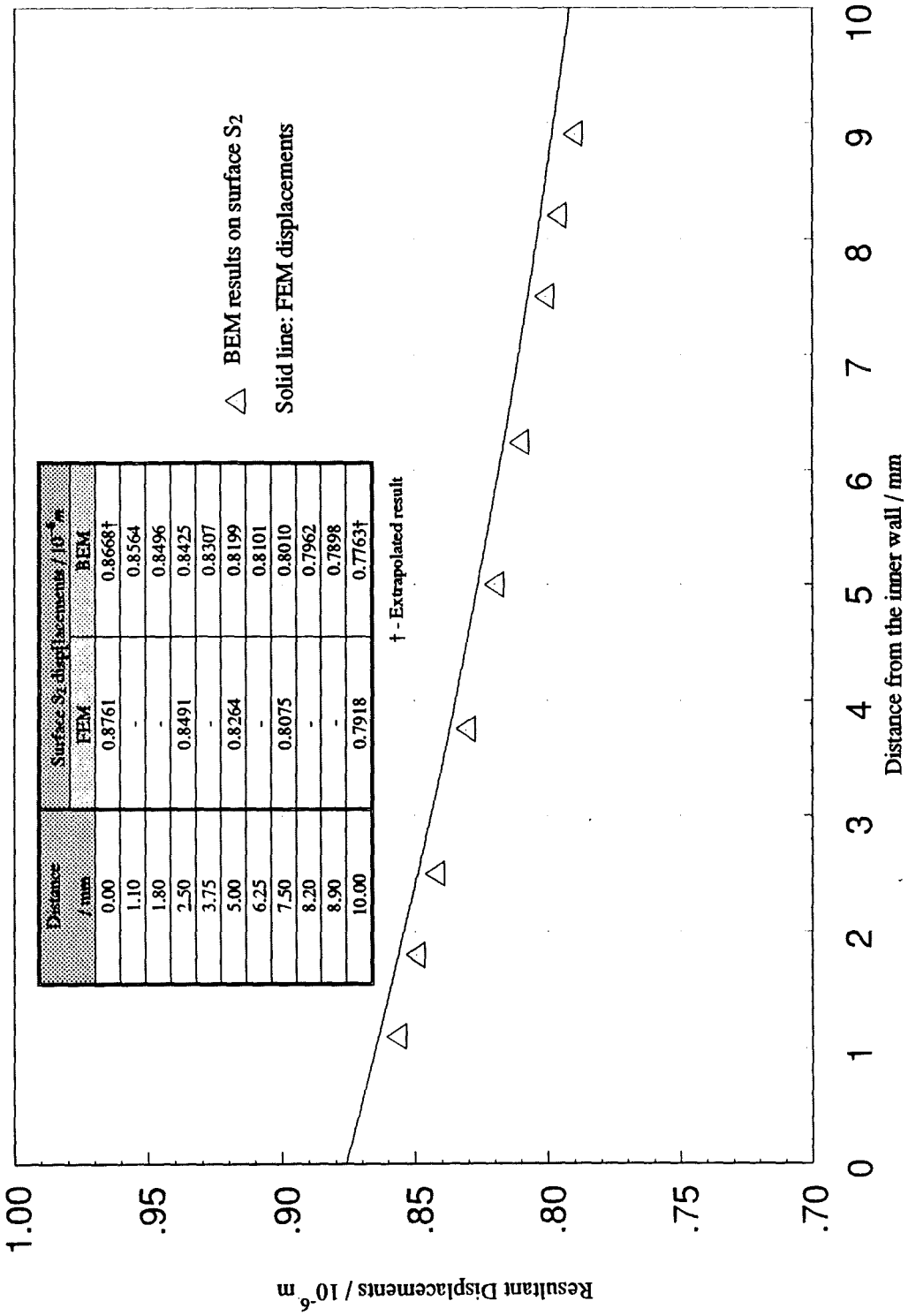

Distance / mm	Surface S_2 displacements / 10^{-6} m	
	FEM	BEM
0.00	0.8761	0.8668†
1.10	-	0.8564
1.80	-	0.8496
2.50	0.8491	0.8425
3.75	-	0.8307
5.00	0.8264	0.8199
6.25	-	0.8101
7.50	0.8075	0.8010
8.20	-	0.7962
8.90	-	0.7898
10.00	0.7918	0.7763†

Figure E.6: Resultant displacements on surfaces S_2 of the cone with $t = 0.56$. (Wall thickness = 10mm, No. of elements on $S_2 = 4$)

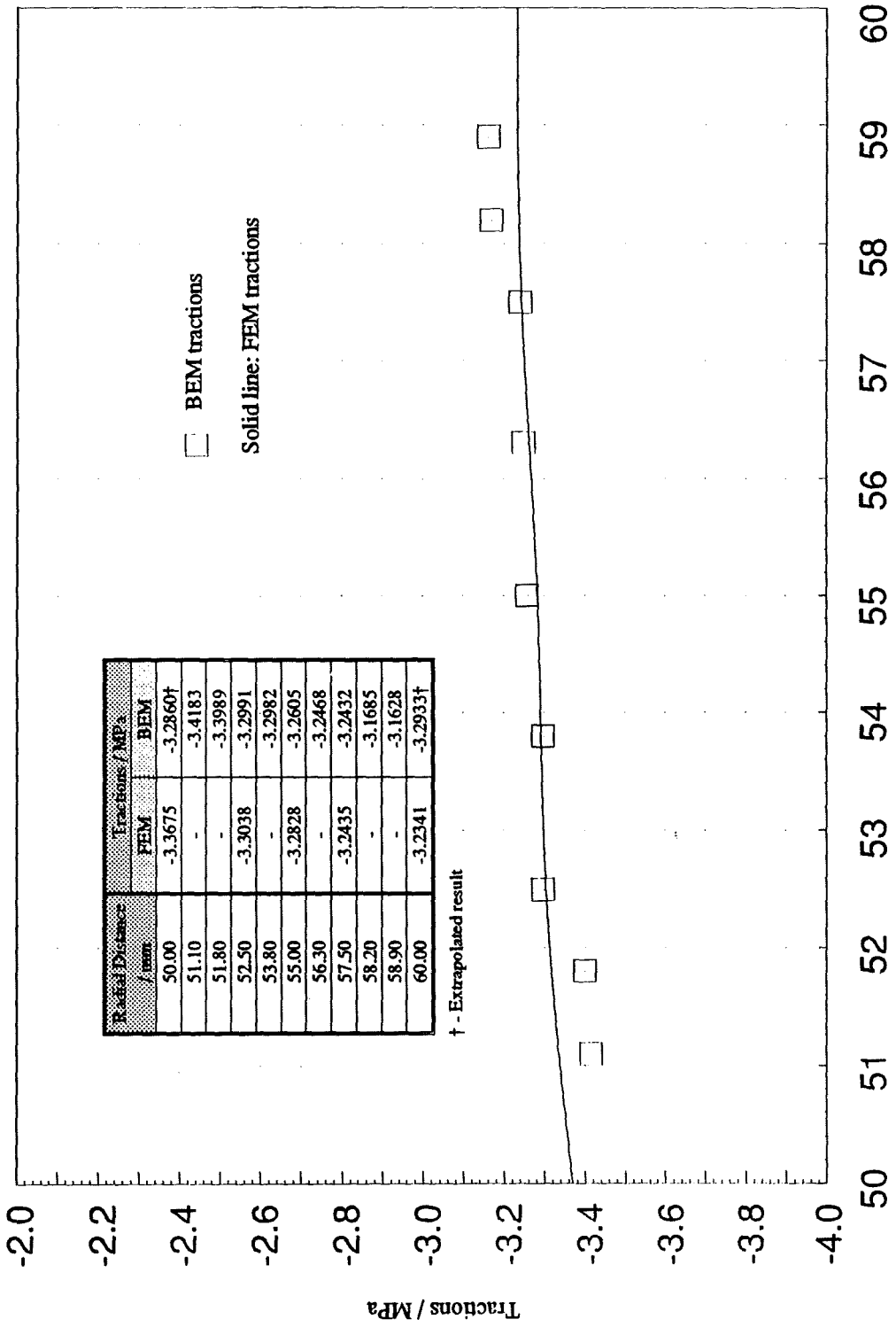

Radial Distance / mm	Tractions / MPa	
	FEM	BEM
50.00	-3.3675	-3.2860†
51.10	-	-3.4183
51.80	-	-3.3989
52.50	-3.3038	-3.2991
53.80	-	-3.2982
55.00	-3.2828	-3.2605
56.30	-	-3.2468
57.50	-3.2435	-3.2432
58.20	-	-3.1685
58.90	-	-3.1628
60.00	-3.2341	-3.2933†

† - Extrapolated result

Figure E.7: Comparison of BEM and FEM tractions on surface S_2 of the cone with $t = 0.56$. (Wall thickness = 10mm, No. of elements on $S_2 = 4$)

References

Banarjee, P.K. and R.Butterfield (1981) *Boundary Element Methods In Engineering Science*, McGraw-Hill Book Co. (UK) Ltd., London.

Bakr (Becker), A.A.G. (1983) 'Boundary integral equation analysis of axisymmetric stress and potential problems', PhD Thesis, University of London, UK.

Beswick, G.E. (1992a) 'Application of BEM to Linear Structures', PhD Thesis, Imperial College, University of London, UK.

Beswick, G.E. (1992b) *Elements of Modern Linear Elastic Stress Analysis*, Pentech Press, Hendon, UK.

Brebbia, C.A. and S.Walker (1980) *Boundary Element Techniques In Engineering*, Newness - Butterworths, London.

Brebbia, C.A. (1984) *The Boundary Element Method For Engineers*, Pentech Press, London .

Brebbia , C.A. and J. Dominguez (1989) *Boundary Elements : An Introductory Course*, Computational Mechanics, Southampton.

Cerrolaza, M. and E. Alarcon, J. Molina (1989a) 'Accurate integration of singular kernels in boundary element method', in *Advances in Boundary Elements: Computations and Fundamentals*, Vol. 1, C.A. Brebbia and J.J. Connors (eds.), pp. 227-240.

Cerrolaza, M. (1989b) 'A bi-cubic transformation for the numerical evaluation of cauchy principal value integrals in boundary methods', *Int. J. Numer. Meth. in Engng*, vol. 28, pp. 987-999.

Chaudonneret, M. (1978) 'On the discontinuity of the stress vector in the boundary integral equation method for elastic analysis', in *Recent Advances in Boundary Element Methods*, C.A. Brebbia (ed.), Pentech Press.

Cook, R.D, D.S. Malkus and M.E. Plesha (1989) *Concepts and Applications of Finite Element Analysis*, John Wiley & Sons, New York.

Cookson, R.A. and A. El-Zafrany (1986) 'State of the art review of the boundary element method', in *Advances in the Use of Boundary Element Method for Stress Analysis*, The Institution of Mechanical Engineers, London.

Cruse, T.A. (1977) 'Mathematical foundations of the boundary integral equation method in solid mechanics', Internal Report No: AFOSR-TR-77-1002, Pratt and Whitney Aircraft Group.

Floyd, C.G. (1984) 'The determination of stresses using a combined theoretical and experimental analysis approach', *Proc. Second Int. Conf. on Computational Methods and Experimental Measurements*, C.A. Brebbia and G.A. Karamidas (eds.), CML Publications, Southampton, section 6, pp. 67-82.

Gray, L.J., L.F. Martha and A.R. Ingraffea (1990) 'Hypersingular integrals in boundary element fracture analysis', *Int. J. Numer. Meth. in Engng*, vol. 29, pp. 1135-1158.

Guiggiani, M. and P.Casalini (1987) 'Direct computation of cauchy principal value integrals in advanced boundary elements ', *Int. J. Numer. Meth. in Engng*, vol. 24, pp. 1711-1720.

Guiggiani, M. (1988) 'The evaluation of cauchy principal value integrals in the boundary element method - a review', *Computers and Mathematics with Applications*, Special Issue on BIEM/BEM.

Guiggiani, M., G. Krishnasamy, T.J. Rudolphi and F.J. Rizzo (1991a) 'A general algorithm for the numerical solution of hypersingular boundary integral equations', *J. Appl. Mechanics, Trans. ASME.*

Guiggiani, M. and G. Krishnasamy, F.J. Rizzo, T.J. Rudolphi (1991b) 'Hypersingular boundary integral equations: a new approach to their numerical treatment', *Proc. IABEM-90 Conf.*, October 15-19, Rome, Italy, Springer-Verlag (in press).

Guiggiani, M. (1991c) 'Direct evaluation of hypersingular integrals in 2D BEM', *Proc. Seventh GAMM Seminar on Numerical Techniques for Boundary Element Methods*, January 25-27, 1991,Kiel, (to appear in Notes in Numerical Fluid Mechanics), Vieweg-Verlag.

Higashimachi, T., Y. Ezawa, N. Okamoto and T. Aizawa (1986) 'Highly accurate boundary element method and its application to structural analysis', *Bulletin of JSME*, vol. 29, pp. 1096-1103.

Jaswon, M.A. (1963) 'Integral equation methods in potential theory - I', *Proc. Roy. Soc. Lond.*, A275, pp. 23-32

Jun, L., G. Beer and J.L. Meek (1985a) 'Efficient evaluation of integral of order $1/r$, $1/r^2$, $1/r^3$ using gauss quadrature', *Engineering Analysis*, 2, pp. 118-123.

Jun, L., G. Beer and J.L. Meek (1985) 'The application of double exponential formulas in the boundary element method', *Proc. Seventh Int. Conf. on Boundary Element Methods*, Vol. 2, C.A. Brebbia and G. Maier (eds.), Springer Verlag, section 13, pp. 3-16.

Karamanoglu, M. and G.E. Beswick (1991), 'Improving the accuracy of BEM in the use of non-equidistant elements', *Proc. Sixth Int. Conf. on Boundary Element Technology*, C.A. Brebbia (ed), Computational Mechanics Publications, Southampton, pp. 321-334

Krishnasamy, G., L.W. Schmerr, T.J. Rudolphi and F.J. Rizzo (1990) 'Hypersingular boundary integral equations: Some applications in acoustic and elastic wave scattering', *J. Appl. Mechanics, Trans. ASME*, vol. 57, pp. 404-414.

Kutt, H.R. (1975) 'Quadrature formulae for finite-part integrals', *CSIR Special Report, WISK 178*, National Research Institute for Mathematical Science, Pretoria, South Africa.

Labeyrie, J. and M. Blanc (1985) 'A new integration scheme in the bem to fracture mechanics problems', *Proc. Seventh Int. Conf. on Boundary Element Methods*, Vol. 2, C.A. Brebbia and G. Maier (eds.), CML Publications, section 8, pp. 47-56.

Lachat, J.C. (1975) 'A further development of the boundary integral technique for elastostatics', PhD Thesis, Southampton University, UK.

Lera, S.G, E. Paris and E. Alarcon (1982) 'Treatment of singularities in 2-D domain using BIEM', *Appl. Math. Modelling*, vol. 6, pp. 111-118.

Massonnet, C.E. and P. Morelle (1987) 'The origin of the boundary element method and its variants', *Proc. Ninth Int. Conf. on Boundary Element Methods*, Vol. 1, W.L. Wendl and C.A.Brebbia (eds.), CML Publications, pp. 1-10.

Pafec (1975) *Pafec 75: Theory, Results*, Pafec Limited, Nottingham.

Portela, A., M.H. Aliabadi and D.P. Rooke (1991), 'Dual boundary element analysis of pin-loaded lugs', *Proc. Sixth Int. Conf. on Boundary Element Technology* , C.A. Brebbia (ed), Computational Mechanics Publications, Southampton, pp. 381-392.

Portela, A., M.H. Aliabadi and D.P. Rooke (1992), 'Dual boundary element analysis of linear crack problems', in *Advances in BEM for Fracture Mechanics*, Computational Mechanics Publications, Southampton.

Prescot, J. (1961) *Applied Elasticity*, 2nd ed., Dover.

Rees, D.W.A. (1990) *Mechanics of Solids and Structures*, McGraw-Hill, London.

Riccardella, P. (1973) 'An implimentation of the boundary integral technique for plane problems in elasticity and elastoplasticity', PhD Thesis, Carnegie-Mellon University, Pittsburg.

Stoer, J. and R. Bulirsh (1983) *Introduction to Numerical Analysis*, Springer-Verlag, Berlin.

Stroud, A.H. and D. Secrest (1966) *Gaussian Quadrature Formulas*, Prentice Hall.

Symm, G.T. (1963) 'Integral equation methods in potential theory - II', *Proc. Roy. Soc. Lond.*, vol. A275, pp. 33-46

Telles, J.C.F. (1987) 'A self-adaptive co-ordinate transformation for efficient numerical evaluation of general boundary element integrals', *Int. J. Num. Meth. in Engng*, vol. 24, pp. 959-973.

Xu, J.M. and C.A. Brebbia (1986) 'Optimum positions for the nodes in discontinuous boundary elements', *Proc. Eighth Int. Conf. on Boundary Element Methods*, Vol. 2, M. Tanaka and C.A. Brebbia (eds.), CML Publications, pp. 751-767.